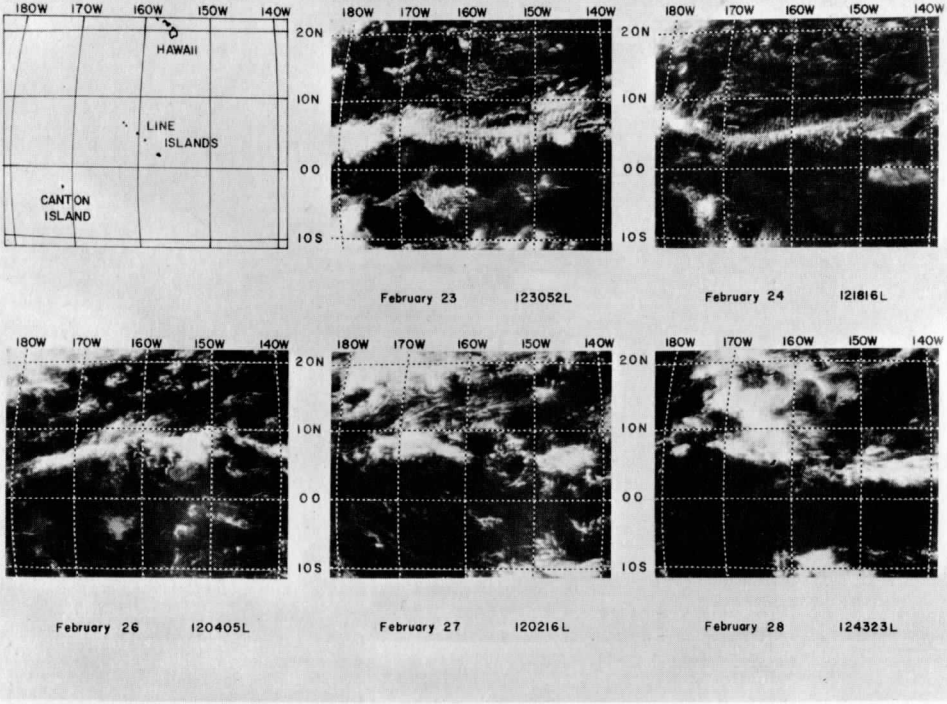

Studies in Atmospheric Energetics Based on Aerospace Probings

Annual Report-1967

Department of Meteorology,
The University of Wisconsin

MAY, 1968

COVER PHOTOGRAPH

A part of the program of calibration and testing of the ATS-1 camera was the Line Island Experiment (LIE) conducted by NCAR. We are including the cover photograph of typical cloud pictures of the Line Island region. In addition, the Appendix of this Report contains cloud cover pictures for each day of the LIE. These pictures have been enlarged and a grid included for the convenience of the reader. The Appendix also contains a summary of the available LIE data.

Department of Meteorology
The University of Wisconsin
Madison, Wisconsin

STUDIES IN ATMOSPHERIC ENERGETICS BASED ON AEROSPACE PROBINGS

Annual Report on

WBG-27

1967

The research reported in this document has been supported by the National Environmental Satellite Center of the Environmental Science Services Administration.

May, 1968

400-282

Scanner's note:

This page is blank.

PRINCIPAL INVESTIGATOR

Verner E. Suomi

CONTRIBUTIONS BY

S. Cox
K. Hanson
F. Hasler
M. Johnson
J. Kornfield
D. Nelson
R. Parent
D. Sargeant
U. Shafrir
E. Smith
V. Suomi
T. Vonder Haar
T. Yonker
J. Young

University of Wisconsin

Scanner's note:

This page is blank.

CONTENTS

Scanner's note:

This page is blank.

PREFACE

Most but not all of the contents of this report are related to the use of ATS-I spin scan camera data as a means to better understand the heat transfer of the tropics. This is mainly a report on the development and testing of techniques for using the ATS-I pictures in a quantitative way. During the last half of the year a means to quantify the heat transfer of convective systems and other similar data analysis for meteorological content was well underway but had not yet reached the state of completion required for a report like this.

Again I wish to thank my associates for their contributions.

V. E. Suomi
Principal Investigator

Scanner's note:

This page is blank.

A PHOTOGRAMMETRIC TECHNIQUE FOR FINDING WINDS FROM SATELLITE PHOTOS

by

Michael H. Johnson

ABSTRACT

This development introduces a technique for measuring cloud velocities from sequences of ATS photos. A comparison is made between cloud velocity measurements and corresponding rawinsonde wind measurements to test the usefulness of the technique of determining the wind velocities from selected cloud velocities.

TABLE OF CONTENTS

1. INTRODUCTION

Cloud photos represent the basic information from which pressure, moisture and wind fields may be inferred (this is not to say measured). Wind fields have been inferred from cloud features, but few methods have been demonstrated as yet to measure winds to a desirable accuracy directly by remote sensing.

Current work is being done at the University of Wisconsin to abstract information from the picture elements in the photos taken by the ATS series of satellites. For instance, cloud displacement can be uniquely determined in a series of ATS photos because the satellite's orbit period is equal to that of the earth's rotation.

The purpose of this work is to introduce a simple and economical means of quantifying selected cloud velocities from a set of satellite photos. The "cloud velocity" is obtained by the measurement of a cloud displacement from a sequence of ATS photos. Not all clouds are suitable for wind measurement. Orographic clouds and those which are related to the phase velocity of horizontal-transverse wave motions will not yield to the wind. Similarly we avoid measuring cumulonimbus clouds that do not move with the simple wind field and other clouds that are rapidly changing structure at their boundaries or are otherwise structurely active.

2. MATERIALS AND METHODS USED FOR MEASURING CLOUD DISPLACEMENTS

The satellite photographs used for the thesis research are sequences of ATS-1, 8 × 10 photographs. The ATS pictures are taken in a fairly uniform time sequence. Two pictures used in series allow one to measure a displacement of a cloud system and, thus, calculate a velocity.

The satellite itself is essentially fixed above one spot on the earth. Therefore, the ATS picture sequences show the same sub-satellite point of the earth's image. Cloud pictures, taken from the satellite, record the movement of clouds much as one sees a stick floating on the water while sitting on a high bank overlooking a brook.

a. Equipment Required

The equipment needed in the measurement of cloud displacement are: 1) a stereoscope, and 2) a plastic measuring device called a "stereo wind graph."

The stereoscope is conventionally used for air photogrammetry. One places two pictures side by side under the proper position until the elements appear as a single image. Objects viewed through a stereoscope show a change in apparent altitude if these objects have a relative displacement with respect to a fixed background in the image.

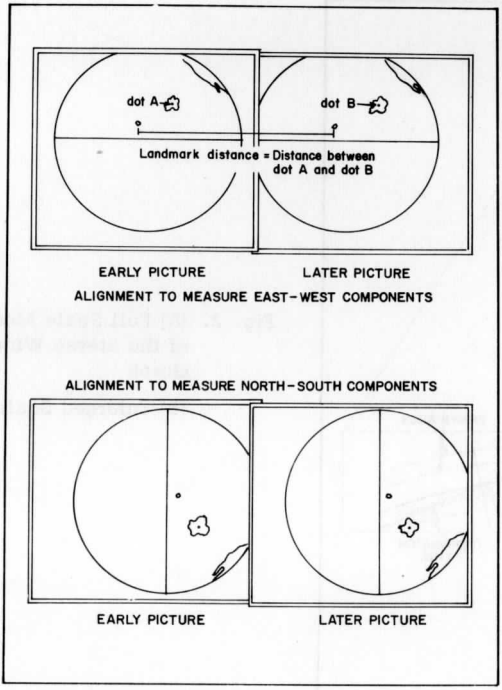

Fig. 1. Alignment to Measure East-West and North-South Components

Cloud system displacements can be studied in a sequence of photos under a stereoscope since the earth represents a "fixed" background in ATS pictures. Two pictures properly positioned under the stereoscope allows one to measure the change in cloud position surprisingly accurately.

Pictures placed side by side (equators in line) allow one to measure the East-West components of the cloud displacements. When the photos are aligned with the earth's axis in line, one measures the North-South components of cloud displacements (Fig. 1).

A second device required for measuring cloud displacements is a stereo wind graph (Fig. 2A). It is a clear plastic strip with which one can measure minute cloud displacements on two ATS pictures in a sequence.

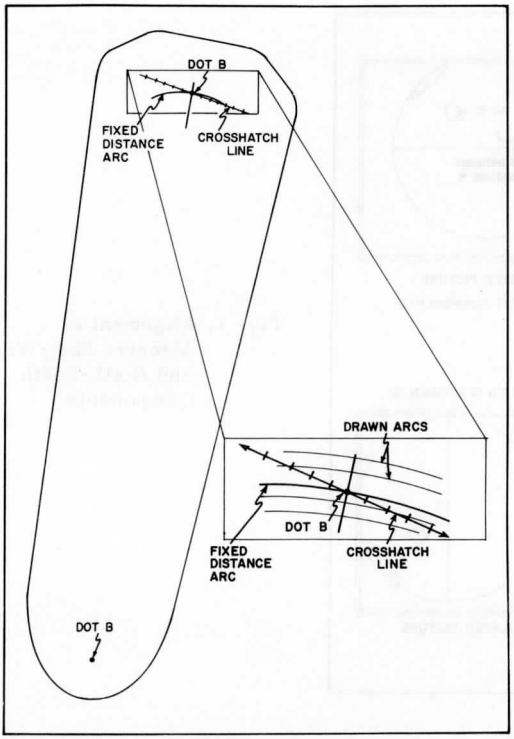

Fig. 2. (A) Full Scale Model of the Stereo Wind Graph

(B) Enlarged Scale

b. Construction of the Stereo Wind Graph

The objective of the stereo wind graph device is to relate a displacement in the photos to a "velocity" on the disk of the earth's image. One therefore chooses a distance on the device appropriate to a convenient velocity on the photos. These distances will be different depending on the properties of the stereoscope and the size of the individual ATS photo enlargements.

The stereo wind graph (SWG) can be constructed to fit each individual's needs. Etch two dots, A and B (see Fig. 2A), on a plastic strip such that they overlay the same landmarks on a pair of ATS photos carefully positioned under the stereoscope. Scratch an arc passing through dot B with dot A serving as the center of radius of the arc. Dot B is called the "dot of exact separation," and the arc with dot B on it is called the "fixed distance arc." Now draw carefully (a microscope could assist) successive arcs at a constant displacement to the left and to the right of the fixed distance arc using dot A again as

the center of radius of the arcs. For example, 0.5 mm is very nearly 11 meters per second when photos are 46.6 minutes apart and the apparent diameter of the disk is 203.3 mm. Then etch an arbitrary straight line, called a measuring line, going through the dot of zero displacement on the fixed distance arc so that it crosses the other arcs on the sheet at a small arbitrary angle (Fig. 2B). Finally, etch small crosshatch lines at every point where the measuring line intersects an arc and erase all the arcs drawn. Each etch mark along the measuring line now represents the equivalent displacement perpendicular from the zero displacement arc. These distances and separations are chosen to represent convenient wind values.

c. Use of the Stereo Wind Graph

Picture alignment, so the landmasses measure no displacement on the SWG (i.e. dots A and B are on the same landmark) in a sequence of ATS pictures, is the most tedious part of using the SWG. The basic limitation in accuracy of cloud displacement measurement depends to a large degree on the accuracy with which the photos are aligned under the stereoscope. The best way of adjusting the pictures is the use of a "jig." The jig is a plane with a rectangular grid and pre-set holes into which alignment pins can be inserted.

The three displacements involved in aligning the pictures are: a) latitude orientation, b) rotation (or twist) of pictures, and c) longitude orientation. Latitude orientation involves aligning ONE landmark in both pictures so that it lies on the same horizontal line of the jig grid and is properly related in the North-South direction. Since ATS pictures are of standard size, rotation of the pictures into alignment can be accomplished by orientation of TWO or more landmarks, preferably ones far apart, such that each lies on its own respective horizontal line of the jig grid. To align the longitudes, the jigs vertical lines are used to set the East-West distances between the same landmark in the two photos to be equal to the distance separating dots A and B on the SWG (see Fig. 1). This whole alignment procedure should be repeated several times to insure accurate picture alignment. One can then insert the pins through the predetermined landmarks into the pre-set holes to hold the pictures in place. Finally, measurements of cloud displacements by the SWG can be made on the pictures with respect to a "fixed" earth background.

d. Measuring Technique

In order to measure cloud displacement one must place dot A of the SWG on a cloud image in the earlier pictures and rotate the SWG using dot A as a pivot until the measuring line intersects the same cloud image in the later pictures (see Fig. 3 sequence). As one looks at the cloud through the stereoscope, it will appear as though dot A is superimposed on the measuring line some distance from the dot of exact separation (dot B). This is, then, the equivalent displacement for one coordinate component of the cloud from the fixed distance arc. For example, Fig. 3C shows an equivalent displacement of plus 1.5 millimeters in the X latitude direction on the SWG.

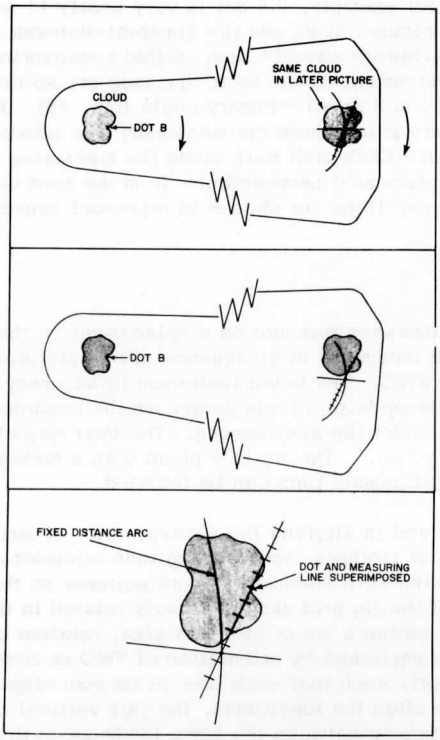

Fig. 3. Stereo Wind Graph showing:
(A) Rotating,
(B) Positioned,
(C) Enlarged Image.

3. CONVERSION OF CLOUD DISPLACEMENT TO CLOUD VELOCITY

Up to now we have only considered cloud displacement on the earth's image in a sequence of ATS photos. Because of a fairly uniform time difference between ATS pictures, we can actually think of the cloud displacement as velocity with respect to the real earth. In order for the velocity to have any meaning, we have to consider:

1. A comparison of scales of the earth's image to that of the real earth.

2. A correction involving rectification of the measured velocity off the earth's flat disk in the photos converted to velocities with respect to the real spherical earth.

3. A series of corrections to the picture image has to be made under the

title of aspect ratio. The aspect ratio corrects for a number of sources of distortion such as improper scan line spacing, the lack of parallelism between the negative and the photo paper used in the enlarging process, the earth's departure from a sphere and photo paper stretching.

4. There is no convenient way to account for nonlinearity in the horizontal or vertical deflection of the imaging device.

a. Comparison of Scales

Translating cloud displacement with respect to time into cloud velocity relative to earth requires a translation from picture scale to real earth scale:

1. Earth's real diameter = 12,742 km at the equator.

2. Earth's picture image diameter = 203.23 mm at the equator.

3. Picture scale of 1 mm = 62.7 km at the subsatellite point.

4. Since 1 km/hr = 0.2778 m/sec, then displacement of 1 mm/hr = 62.7 km/hr = 17.4 m/sec at the subsatellite point (SSP).

Table 1A shows a table of velocities for a common group of standard times between ATS photo sequences for a base displacement of one twentieth of a millimeter on the SWG. This base was used because 1/20 mm is nearly the distance between scan lines in an ATS picture with an eight inch equator diameter, and thus, is the lower limit of measuring the North-South displacement. So, for example, a measured displacement of 0.5 mm can be simply thought of as a velocity of 11.2 meters/sec at the subsatellite point (SSP) for a set of ATS pictures with a 46.5 minute time difference.

Ordinarily ATS pictures are obtained 23.3 minutes apart so that an alternating sequence, found best for research, is 46.6 minutes apart. But, sometimes the set is not exactly 46.6 minutes apart, so some different speed for a base displacement of 1/20 mm must be applied. Table 1B shows the formula and an example that evaluates a different base speed.

b. Rectification Geometry

We are looking at an oblate spheroid projected onto a flat plane of an ATS picture. As a result, geometry shows that a distortion of distance is introduced at all points on the picture, except the subsatellite point. To simplify the geometry we can assume the earth is spherical (introducing an error of only 2 in 600 parts).

The object is to correct for the distortion of distance in the photo so that one may obtain a real measurement of velocity with respect to the spherical earth.

Table 1A

Table of Speed to Standard Time Differences Between ATS Photos for Base Displacement 1/20 Millimeter on Eight Inch Equator Diameter Pictures. Speed in Meters Per Second at Subsatellite Point (SSP)

Minutes	Seconds	Speed	Minutes	Seconds	Speed
23	15	2.25	46	30	1.12
23	20	2.24	46	35	1.12
23	25	2.23	46	40	1.12
23	30	2.22	46	45	1.12
23	35	2.22	46	50	1.12
23	40	2.21	46	55	1.11
23	45	2.20	47	00	1.11
23	50	2.19	47	05	1.11
23	55	2.19	47	10	1.11
24	00	2.10	47	15	1.11

Table 1B

Formula for Base Velocity Evaluations with 1/20 mm Displacement for Nonstandard Time Pictures

$$\text{Basic speed} = 1.12 \frac{m}{sec} - .00031 \frac{m}{sec^2} (\Delta t)$$

Where Δt is time difference in seconds from 46:36 (standard time).

For example, for ATS pictures with 60:00 time difference $\Delta t = 804$ seconds.

$$\text{Base speed} = 1.12 - (.00031) \times 804 \frac{m}{sec^2} \times \text{sec} = .87 \frac{m}{sec}.$$

A computer program was used to measure cloud displacement by the change in angle B caused by cloud displacement between pictures (Fig. 4). A new program was developed to determine what displacements tangent to the real earth at various points a fixed angle would view from the ATS satellite. The displacement covered by the fixed angle was set to equal one millimeter at the subsatellite point of the earth's image (or D = equal to 62.7 km at the subsatellite point on the real earth) (Fig. 5).

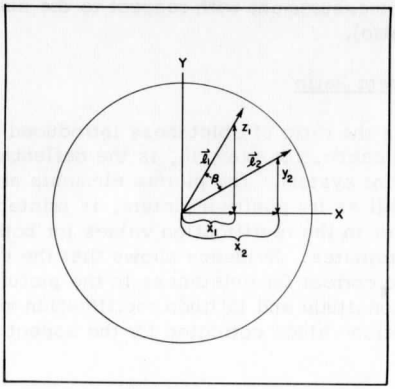

Fig. 4. β = Angle Between Cloud in Picture 1 and Picture 2.

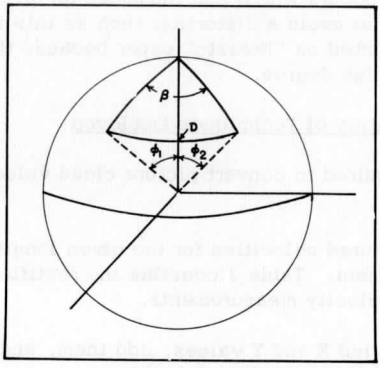

Fig. 5.

The computer program calculated displacements for the fixed angle in the X direction (left to right) and in the Y direction (bottom to top) at every grid point intersection (i.e. longitude line and a latitude line of five degrees) for a grid overlay of ATS picture. The ratio of the calculated X and Y displacements at the grid points to the X and Y displacement at the subsatellite point yielded rectification values at the given longitude and latitude intersections considered. See Table 2 for the results.

The object is to multiply the measured velocity of the stereo wind graph by the rectification values in Table 2 at a given longitude and latitude to obtain an equivalent velocity measurement with respect to the subsatellite point (uncorrected for aspect ratio).

c. Correction for Aspect Ratio

The aspect ratio is the ratio of oblateness introduced into the printed ATS picture. One specific cause, for example, is the deflection of the electronic beam in the display print system. The picture elements are "squeezed" together and the negative as well as its positive picture, is printed oblately. The oblateness introduces an error in the rectification values for both the X and Y (longitude and latitude) coordinates. Evidence shows that the typical value of the aspect ratio is 3.3%. To correct for oblateness in the picture, we multiply the aspect ratio with the longitude and latitude rectification values given in Table 2. The resulting rectification values corrected for the aspect ratio are given in Table 3.

d. Print Paper Distortion

When the photos are printed on ordinary photo paper, paper stretching from the developing process occurs which can introduce an error in measuring cloud displacement. In order to avoid a distortion such as this for accurate work, one should have pictures printed on "Resisto" paper because this type of photo paper resists stretching to a high degree.

e. Summary of Application of Techniques Employed

Three steps are required to convert picture cloud velocity to a velocity real to earth:

1. Rectify the measured velocities for the given longitudes and latitudes of the point of measurement. Table 3 contains the rectification values to multiply with the X and Y velocity measurements.

2. Square the rectified X and Y values, add them, and find the square root of the sum to obtain the total rectified velocity:

$$V_R = (X_R^2 + Y_R^2)^{1/2}$$

Table 2

Rectification Values for Subsatellite Point 150°W, 00'N
(No correction for aspectration)

West Long.	N or S Lat.	X	Y	West Long.	N or S Lat.	X	Y
150°	00	1.000	1.000	160° or 140°	00	1.024	1.003
"	10	1.003	1.024	"	10	1.028	1.028
"	20	1.011	1.101	"	20	1.036	1.107
"	30	1.024	1.257	"	30	1.052	1.270
"	40	1.043	1.533	"	40	1.076	1.573
"	50	1.064	2.001	"	50	1.101	2.050
170° or 130°	00	1.104	1.011	180° East or 120° West	00	1.257	1.024
"	10	1.108	1.039	"	10	1.262	1.059
"	20	1.120	1.126	"	20	1.271	1.166
"	30	1.141	1.307	"	30	1.300	1.378
"	40	1.172	1.614	"	40	1.349	1.732
"	50	1.208	2.166	"	50	1.410	2.374
170° East or 110° West	00	1.528	1.043	160° East or 100° West	00	2.020	1.065
"	10	1.535	1.092	"	10	2.040	1.142
"	20	1.551	1.239	"	20	2.107	1.374
"	30	1.614	1.558	"	30	2.228	1.811
"	40	1.697	2.010	"	40	2.517	2.680
"	50	1.821	2.903	"	50	-	-

Table 3

Rectification for Subsatellite Point 150°W 00°N Corrected for Oblateness Caused by Aspect Ratio

Long	N or S Lat.	X	Y	Long	N or S Lat	X	Y
150W	00	1.000	1.000	140W or 160W	00	1.024	1.003
"	05	1.001	1.006	"	05	1.025	1.009
"	10	1.003	1.026	"	10	1.028	1.029
"	15	1.006	1.059	"	15	1.032	1.064
"	20	1.012	1.108	"	20	1.037	1.115
"	25	1.018	1.180	"	25	1.046	1.190
"	30	1.026	1.280	"	30	1.055	1.294
"	35	1.035	1.410	"	35	1.066	1.431
"	40	1.046	1.600	"	40	1.082	1.642
"	45	1.058	1.851	"	45	1.098	1.897
"	50	1.070	2.173	"	50	1.112	2.236
130 W or 170 W	00	1.104	1.011	120W or 180°	00	1.257	1.024
"	05	1.106	1.019	"	05	1.260	1.034
"	10	1.109	1.041	"	10	1.263	1.062
"	15	1.116	1.081	"	15	1.268	1.110
"	20	1.122	1.135	"	20	1.276	1.178
"	25	1.131	1.218	"	25	1.289	1.272
"	30	1.147	1.335	"	30	1.313	1.414
"	35	1.168	1.491	"	35	1.349	1.605
"	40	1.185	1.689	"	40	1.380	1.830
"	45	1.216	2.015	"	45	1.427	2.213
"	50	1.237	2.388	"	50	1.480	2.671
110W or 170 E	00	1.528	1.043	100W or 160E	00	2.020	1.065
"	05	1.531	1.056	"	05	2.028	1.085
"	10	1.538	1.095	"	10	2.048	1.148
"	15	1.552	1.160	"	15	2.080	1.249
"	20	1.563	1.256	"	20	2.142	1.405
"	25	1.599	1.393	"	25	2.227	1.630
"	30	1.649	1.585	"	30	2.330	1.920
"	35	1.704	1.830	"	35	2.542	2.403
"	40	1.780	2.177	"	40	2.825	3.103
"	45	1.896	2.751	"	45	2.991	3.884
"	50	2.022	3.456	"	50	-	-

3. Find the direction of cloud motion by simple vector addition of the raw X and Y values on a grid at the given longitude and latitude of the cloud measured.

4. A COMPARISON OF CLOUD VELOCITY MEASUREMENT WITH RAWINSONDE WIND

The purpose of the test observations is to compare the cloud displacements converted to "wind" velocity, with radiosonde wind data to evaluate the usefulness of the stereoscopic method for measuring cloud velocity. In this test we must assume that clouds move with the wind field. We are trying to ascertain the correlation of the stereoscopic method of measuring cloud displacement to the measured Rawinsonde wind velocity over a given station at a cloud level for a given period of time.

Cloud displacement measurement requires sufficient contrast of brightness between the cloud and the earth. Whenever cloud sizes are below the resolution of the ATS picture (about two miles) and if there are too few clouds of a larger size within a radius of one hundred kilometers of a station, then the contrast in the picture is too low and a measurement of cloud displacement cannot be made in a picture sequence. Conversely, if there is uniform cloud cover over a given point and a hole, notch, streak in the clouds is less than two miles, then the cloud system will not show enough contrast in brightness for one to measure a displacement.

Cloud pressure altitude must be designated for the comparison of cloud velocities with the rawinsonde winds to the nearest mandatory pressure level unless one has detailed soundings available. The soundings' dew points are used to determine the level of cloud tops (and base). If the significant level is more than 30 millibars (or 40 mb at lower level) from a mandatory level, then the test data includes both of the mandatory level reports that the significant level was found between.

Lastly, jet stream areas should be avoided because of the large wind shears that occur at a given level.

a. Availability of Rawinsonde Data

A set of radiosonde stations were selected in the North Pacific that could be used to compare the resultant cloud velocity measurements (i.e., corrected by the rectification tables) to the stations' upper wind data. The stations shown in Fig. 6 are diverse enough to give a meaningful test of the rectification tables.

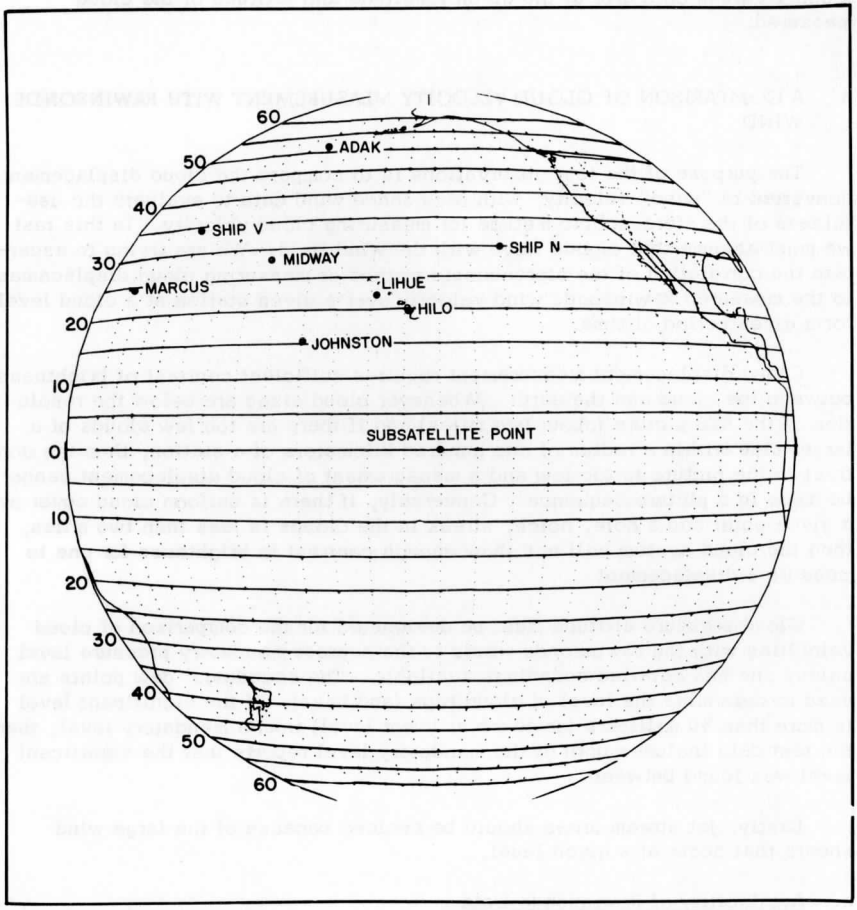

Fig. 6. Station Locations and Grid

Eleven days were studied in three separate groups, corresponding to radiosonde data for 007, April 9-12 (007 picture days 109-112), May 7-10 (007 picture days 127-130), and June 19-21 (picture days 170-172). Of the eleven days, six days had an average time between pictures of 46.5 minutes and five days had an average time between pictures of 23.3 minutes. Because of the lack of availability of pictures, the mean time of some picture sequences (not to be confused with the time between the pictures themselves) differ by up to two hours before (May 8, pictures 127-7-212811 and 127-7-221451) or one and one-half hours after (May 9, pictures 129-7-004736 and 129-7-011100) rawinsonde ascent time (23:15 to 007).

b. Correlation of Measured Velocities with Observed Winds

Sixty-one useful sets of observations for intercomparison were available. Of these, 55 showed good agreement and the remainder showed an undesirable variation between the calculated cloud velocity and the comparable rawinsonde wind. The remaining six observations were low wind velocities or had a great time difference between mean picture sequence time and mean radiosonde airborne time. These errors are probably a result of not only the variability in direction of low wind velocities with time, but also of a weakness in the system of vector addition. For example, if the measured displacement is plus one-twentieth of a millimeter in the X coordinate in a picture sequence 23.3 minutes apart, this would be evaluated as a wind of two meters per second from about 270°. But one could not measure a displacement of a cloud in the Y coordinate unless it was one-twentieth of a millimeter or more. This would mean that an actual cloud displacement at 2m/second from 250° could not have a measured Y displacement and would be calculated by vector addition at 270°, giving an automatic 20° error.

The standard deviation for the direction difference between the calculated directions (by vector addition) and the radiosonde wind data for the 61 cases is 21° (see Fig. 7). Of these, four large differences resulted probably because of the variability of direction of low wind velocities and/or a big enough time difference between the pictures and the rawinsonde data to allow for direction change. For example, observation #31 showed an 80° difference between calculated cloud velocity and the rawinsonde data, but here the reported rawinsonde wind velocity was only four meters per second and the picture times were 003957 and 010317. Likewise, observation #47, with a 40° difference, showed a velocity of only two meters per second and the picture times were 004735 and 011100. Observation #44 and observation #48 are examples of high wind velocities for which calculated and observed winds differ, but both have a large enough time difference from the radiosonde data to warrant some change in wind direction. If we were to discard just these four "poor" observations, then the standard deviation between the calculated direction and radiosonde wind data for 57 cases is only 15°.

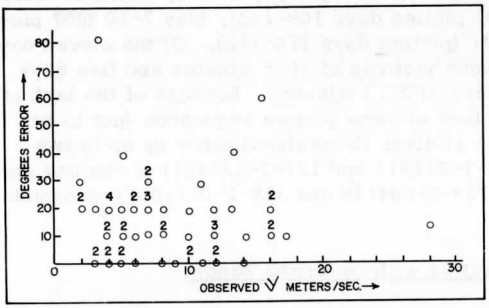

Fig. 7. Distribution of Directional Differences Between Observed and Calculated Wind Directions.

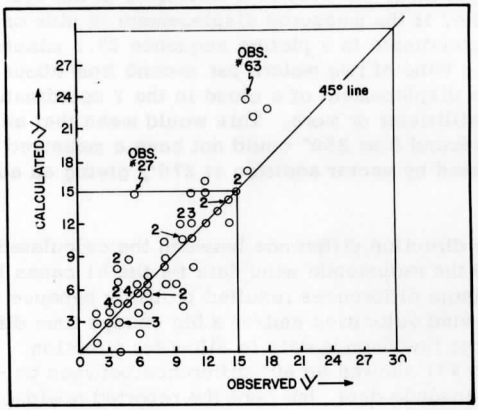

Fig. 8. Distribution of Speed Differences Between Observed and Calculated Wind Speed.

The standard deviation for velocities between calculated and rawinsonde data is 2.7 meters per second for all 61 cases (see Fig. 8). Again, some large differences resulted between calculated and observed data. Observation #27 had a difference of 10 meters per second and probably was caused by an error in recording. Observation #63 had a difference of 8 meters per second, but in this case, the picture time was 23:35 apart, meaning that one can measure to an accuracy of only 2 meters per second at subsatellite point for a one-twentieth of a millimeter displacement because of the picture resolutions. However, if an error of one-twentieth of a millimeter measurement were made over

a point by Ship V in the ATS photo, the rectification values from Table 2, multiplied by the velocity value from Table 1, would give a resulting error of 4 meters per second and this would explain half of the difference that resulted in comparing the calculated-to-observed velocity in observation #63. If we were to exclude just observations #27 and #63 as "bad" data, then the standard deviation between the calculated and radiosonde velocities would be 2.2 meters per second.

c. Comments on Procedure

For the test data involved, making displacement measurements on pictures averaging 46.5 minutes apart is superior to making measurements on pictures 23.3 minutes apart. To begin with, one can ideally measure a cloud displacement in an 8"equator ATS sequence to an accuracy equivalent to one meter per second velocity near the subsatellite point (compared to 2 m/sec in a 23.3 minute sequence). Although the standard deviation between calculated and radiosonde velocities for pictures 46.5 minutes apart (represented by observations 1-26, 37-44, and 67-74) was 2.2 m/sec for all locations in the picture, 22 of the 32 46.5 minute cases had a difference of no more than 1 m/sec between the calculated and radiosonde velocities.

Secondly, it takes from two to four times longer to measure the displacement in pictures averaging 23.3 minutes apart. One is pressured into being much more careful by the fact that one-twentieth of a millimeter error in displacement measurements will mean at least a 2 m/sec error in the resulting velocity calculation in a 23.3 minute sequence.

The picture sequences which had mean times somewhat different from rawinsonde ascent times showed that we can assume continuity of wind patterns for one or two hours in areas not affected by a developing cyclone (note May 7-9, June 19-21) or fronts.

5. SUMMARY AND GENERAL CONCLUSIONS

Section 2 introduces a simple stereoscope method of measuring cloud displacements from a sequence of ATS photos. Section 3 discusses the means to convert these measurements into velocities relative to the earth. Displacement measurements of one-twentieth of a millimeter can be made, ideally, near the subsatellite point for pictures about 46.5 minutes apart, which will permit evaluation to a velocity of one meter per second. If an accuracy of one meter per second velocity can be made near the subsatellite point, then the accuracy of the velocities at the other points in the picture is a function of the rectification values for the given longitude and latitude.

In Section 4, comparisons are made of calculated cloud velocity to upper wind data and show a surprisingly good relation for selected clouds for a short

period of time. The test shows that if one selects appropriate clouds, then cloud velocities can be used to determine wind velocity at cloud level.

In conclusion, the method of measuring cloud velocities should be simple enough to allow for operational studies to be made in the future by anyone with good eyes and a minimum of training. The time involved in measuring a group of cloud displacements (for both X and Y coordinates) is typically one and one-half hours for the recommended 46.5 minute picture sequences (and twice as long on a 23.3 minute sequence), which is economical enough on a labor standpoint to allow for a series of operational studies.

6. REFERENCES

COSPAR WG IV, 1967, Remote Sensing of Meteorological Parameters with Satellites, Panel 2, COSPAR Transactions No. 3, Status Report of the Applications of Space Technology to the World Weather Watch, June, 1967. Part 7, Cloud Observations.

7. ACKNOWLEDGMENTS

I wish to express my appreciation to Dr. Verner Suomi for his guidance and assistance in the preparation of this work.

Appreciation is also expressed to Dr. Frank Sechrist for his helpful comments and suggestions and to Larry Jensen who provided much help in developing the computer programs.

This work was supported by the U.S. Department of Commerce, ESSA under WBG-27.

CLOUD MOTION AND OTHER PARAMETERS FROM ATS-1 DIGITAL DATA

by

Kirby J. Hanson and Thomas H. Vonder Haar

CONTENTS

1. INTRODUCTION

The ATS-1 digital data recording system is designed to provide the maximum amount of quantitative brightness information from the ATS-1 cloud camera. This is accomplished by storing cloud brightness data in a matrix which has the dimensions of approximately 2018 scan lines by 8196 picture elements. At each picture element in this matrix the cloud brightness is digitized on a scale from 0-255. Clearly, there is considerably more information on the ATS digital data than we are accustomed to seeing in the usual ATS pictures which are produced in real time at the NASA ground station and are intended to serve as a signal monitor.

Whitney, et al. (1968) have used the digital data to show the quality of cloud brightness data stored in this form, and have demonstrated the capability of discriminating clouds at various brightness thresholds. In addition, Bristor, et al. (1968) have examined the possibility of determining cloud displacement and growth using picture pairs of ATS digital data.

The purpose of this work is to give meteorologists a better idea of information in the digital data that may be useful to them in discriminating cloud motion

and parameterizing cloud features. We have done this by treating examples of familiar clouds.

The first section of the paper treats low level cumulus embedded in the tropical easterlies. The cloud boundaries are discriminated using the digital data; cloud velocity and divergence fields are determined from a picture pair. The second section of the paper examines cloud ensembles in the tropics which are much brighter than low-level cumulus, and apparently are composed of deep convection. The cloud ensembles appear as rings or polygons, connected somewhat as a chain. The horizontal dimensions of a typical polygon shaped cloud ensemble are given, assuming a certain cloud model. The last section of the paper illustrates the brightness contours of typhoon Sarah in the mid-Pacific on September 11, 1967.

Throughout this paper the ATS-1 digital data have been displayed using techniques developed at the Space Science and Engineering Center, University of Wisconsin. These programs are discussed in detail in this Report by Smith and Vonder Haar.

2. TROPICAL CLOUD MOTION AND DIVERGENCE

ATS-1 digital data have been used to derive the wind field from cloud motions over a region of the equatorial Pacific. An area near the Line Islands on April 19, 1967 was chosen in order to compare the computed winds with observed winds from the same period. Two cloud maps of the same area were prepared from ATS-1 pictures obtained at 2124 and 2148Z. These maps were constructed from digitized ATS-1 measurements using a character display technique for computer output. On both maps the brightness threshold used to define cloud from no-cloud areas was set at 50 digital counts which are proportional to brightness. This relationship is discussed by Peekna et al. (1968) and by Hanson and Suomi (1968).

In this test case the wind direction and speed were inferred from the movement of clouds. However, because of slight changes in satellite attitude relative to the earth, ATS-1 pictures obtained only minutes apart do not view precisely the same areas. This causes an alignment problem between any two pictures which can significantly affect computed winds by adding an unreal component to cloud displacements. In another paper in this Report, Hanson et al. have shown the ATS-1 measurements can be correctly positioned without the aid of a land feature and that near the subsatellite point attitude changes cause primarily a north-south shift in the observed features. Using their technique, the two cloud maps were properly superimposed. Christmas Island is recognized on both maps and serves as an additional alignment check.

On the ATS-1 photo in Fig. 1, the area (2-6°N; 157-163°W) in which the wind field was derived is shown in the small rectangular area. Figure 2

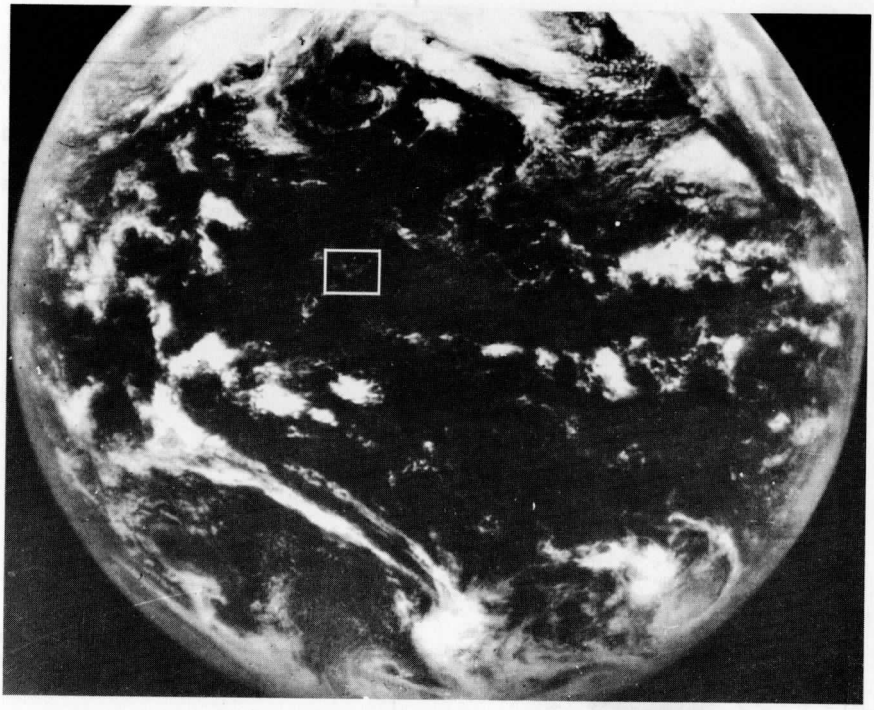

Fig. 1. ATS-1 picture for 2148GMT, April 19, 1967.

illustrates the cloud patterns and Christmas Island as seen on the digital maps of this area. Solid lines mark the cloud boundaries on the 2124Z picture and dashed lines indicate the boundaries 24 minutes later. Differences between the two patterns can be caused by any combination of:

a) cloud motion
b) changing cloud size
c) changing cloud brightness

An overall movement of the clouds toward the west is apparent in Fig. 2. In order to remove the random effects of (b) and (c), mean cloud displacements within each 1 × 1 degree latitude area were derived from many hand measurements of the apparent movement of cloud centers and edges. These displacements were converted into normal components of the wind within each 60 n. mi.

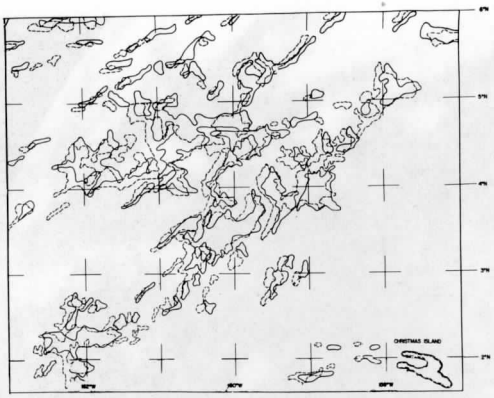

Fig. 2. Cloudiness in the Line Island Region (Fig. 1). Solid cloud boundaries are for 2124GMT and dashed boundaries for 2148GMT, April 19, 1967.

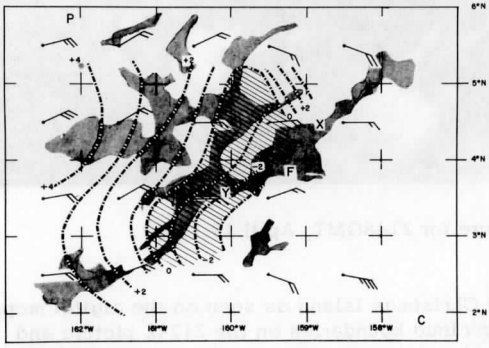

Fig. 3. Clouds, winds and divergence pattern based on cloud motion of Fig. 2. Divergence units are 10^{-5} sec^{-1}.

square area. For this test case, it is assumed that these values represent the average wind direction and speed within the cloud layer.

Figure 3 shows the computed winds and the divergence field derived from the u and v wind components. Of course, no winds are obtained from cloud-free areas. On the same illustration, a sketch of the major cloud regions is shown. Although the cloud systems are probably better related to convergence patterns in the sub-cloud layer, the general alignment of clouds and features of the wind field is good. Together they depict a weak wave embedded in the

easterly flow. Subsequent ATS pictures show that the cloud pattern retained its shape and intensified west of the test area during the next 24 hours. Computed winds ranged from 15 to 25 knots and from 60 to 110 degrees. These values together with others derived near the border of the area shown were used to compute divergence magnitudes of $\pm 3 \times 10^{-5}$ sec^{-1}.

Normally, very few standard meteorological observations are available for this region. On April 19, 1967, however, the Line Island Experiment (LIE) was still in progress and some surface, upper air and aircraft data were obtained at various locations within our test area. (A data summary of the LIE is given in the Appendix of this Report.) Thus, it was possible to assess the computed winds against observed.

Synoptic data obtained within three hours of the picture times are available and at some locations aircraft wind measurements are available for more than one level. Both surface and aircraft (B-47) observations reported only cumulus clouds over the area with bases at 2000-2500 feet. Aircraft data at points X, Y and P on Fig. 3 placed the top of the primary cloud layer near 6000 feet. At Y scattered cumulonimbus towers reaching 22,000 feet were also reported.

Because these data indicate measured cloud displacements pertain to the troposphere, wind observations below 6000 feet near P, F and C were used to check the computed winds. The comparison in Table 1 contains both windspeed in knots (VV) and direction in degrees (DDD). Computed and observed winds are in close agreement considering the uncertainty in altitude determination.

Table 1

Computed and Observed Windspeeds and Directions

La. (deg. N)	(deg. W)	Observed Speed (VV)	Observed Direction (DDD)	Computed Speed (VV)	Computed Direction (DDD)
5.5	162.0	15	080	22	075
3.5	160.0	15	095	15	080
2.0	158.5	Missing	110	35	100

Since the above comparison is limited by the representativeness of the observed data, perhaps a better test of the computed winds is the overall meteorological situation they depict. Figure 3 shows a weak wave embedded in moderate easterly flow with cloud regions lying along the wave axis and greatest vertical development found at the location of maximum low level convergence.

Neither the scattered meteorological observations, nor individual cloud pictures, could provide such a complete description of the typical tropical conditions which are evident from displacement and divergence patterns which two pictures allow. This test case demonstrates the usefulness of wind and divergence fields computed from the ATS digital data for the study of mesoscale weather patterns. It also suggests that a more automated technique using digital data cloud yield realistic winds on an operational basis.

The latter application is currently under investigation and tests not reported here but similar to that described in this study have shown that:

a) strong vertical wind shear can be detected from the ATS digital data,

b) changing cloud brightness or size may obscure cloud motions when the time period between two views of the same area exceeds one and one-half hours,

c) optimum cloud brightness thresholds or gradients must be derived to adequately represent the presence or absence of clouds.

Further work in these areas and on operationally registering the digital pictures will allow us to make maximum use of these high resolution, quantitative digital data for remote wind measurements.

3. TROPICAL CLOUD STRUCTURE

a. Polygon Shaped Cloud Ensembles

In looking at cloudiness of the tropical Pacific on ATS-1 pictures, one is struck by the great amount of organization to the clouds. In one of the lower scales of organization discernible in the ATS pictures, we notice a great deal of the cloudiness forms into polygons of various shapes and distortions. Typical examples of polygon shaped cloud ensembles are seen in Fig. 4. In that picture one can see that not only clouds within the white-bordered area are organized in this way, but many of the remaining clouds as well. In the present study, however, we have considered only clouds in the enclosed area of Fig. 4. These clouds are depicted by computer display of the digital data and are shown in Fig. 5. In that illustration, clouds appear as the whitest areas. The lower brightness contour which outlines the cloud has a value of 54 digital counts and the higher contour 63 digital counts. The various cloud ensembles in Fig. 5 have been designated 1, 2 and 3 to facilitate discussing them.

Cloud ensemble 1 is a relatively large cloud group in which the northern section of the cloud ring is absent. Perhaps this shape results from moderate vertical wind shear which tends to form such U-shaped cloud cells (Rogers,

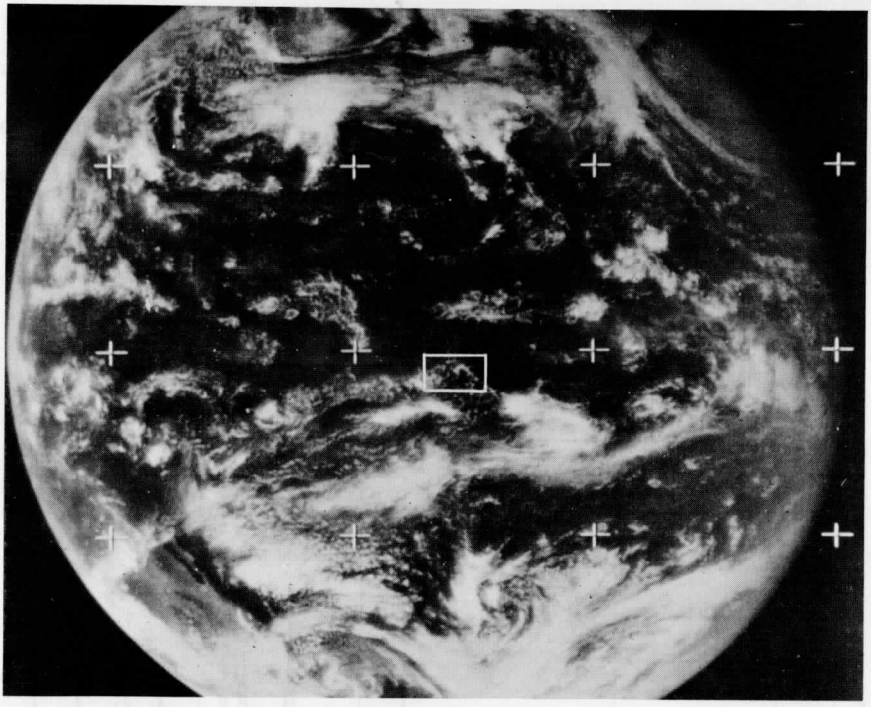

Fig. 4. ATS-1 picture for 202700GMT, April 26, 1967.

1965). The horizontal brightness gradient is very steep along the edges of the cloud band. This is evident in Fig. 6, for example, which shows the brightness cross section of scan line 970. It is clear that brightness values within the polygon are about 25 but increase to over 100 at the cloud edge. In Fig. 7 we have contoured the brightness of this cloud ensemble from a lowest contour of 50, which outlines the cloud, to a highest contour of 175 which appears as the smallest closed contours within the "tic" marked areas. The contour with "tic" marks is 125. From this illustration it is clear that such ensembles are made up of organized deep convection and that there is continuity of brightness associated with this convection. Clearly, it is possible to identify the brightest areas in such polygon shaped cloud ensembles and thereby identify the deepest convective elements that make up the polygon.

Two other cloud groups, ensembles 2 and 3 of Fig. 5, are contoured in greater detail in Fig. 8. These ensembles appear to have somewhat smaller horizontal dimensions than ensemble 1.

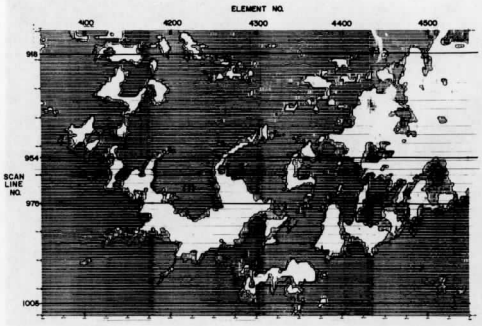

Fig. 5. ATS digital data depiction of cloud structure in enclosed area of Fig. 4. Heavy horizontal lines correspond to the scan lines in Fig. 6. The three cloud ensembles noted in this illustration are shown in greater detail in other illustrations.

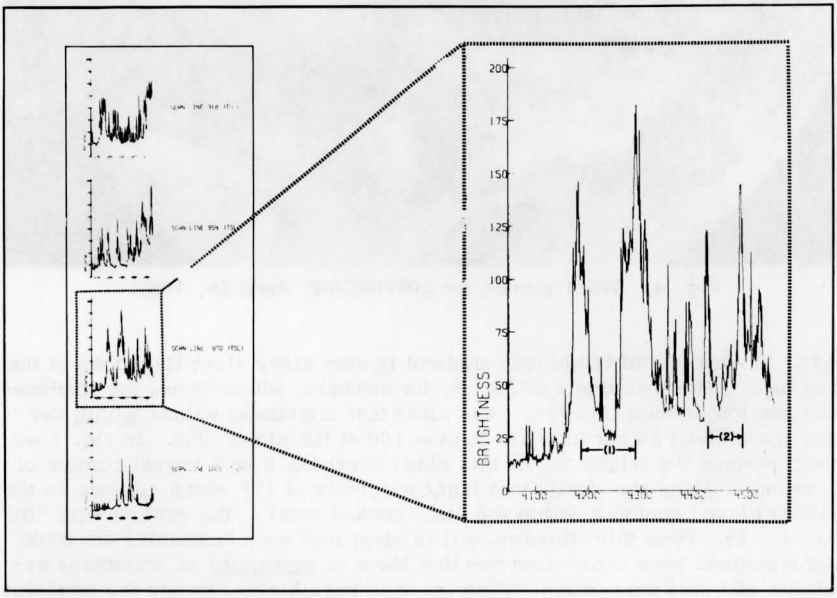

Fig. 6. Brightness plots for scan lines in Fig. 5.

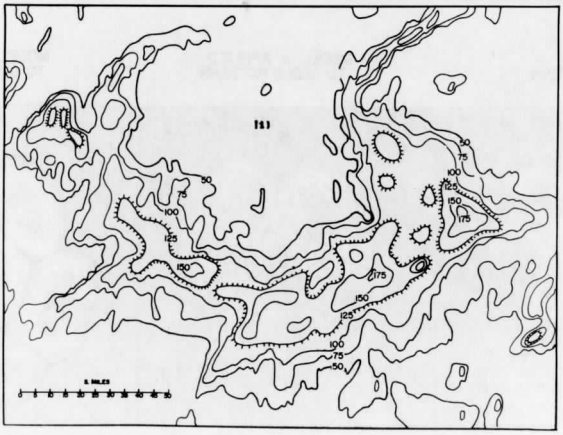

Fig. 7. Brightness contours for cloud ensemble 1 shown in Fig. 5. Scan lines 954 and 970 in Fig. 6 show a brightness cross-section of this cloud ensemble. Minimum brightness contour is 50. Maximum contour is 175 digital counts.

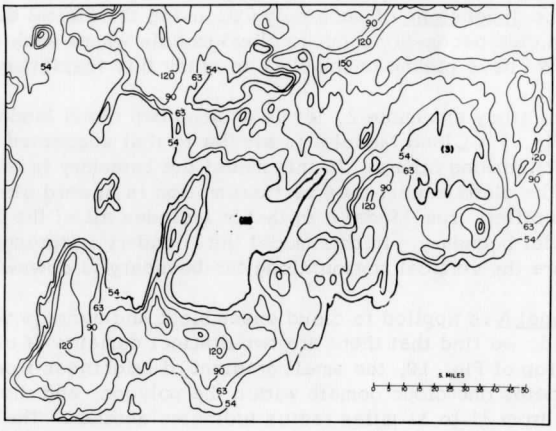

Fig. 8. Brightness contours for cloud ensembles 2 and 3 in Fig. 5. Scan line 970 in Fig. 6 shows the brightness cross-section through cloud ensemble 2. Minimum brightness contour is 54. Maximum brightness contour is 150 digital counts.

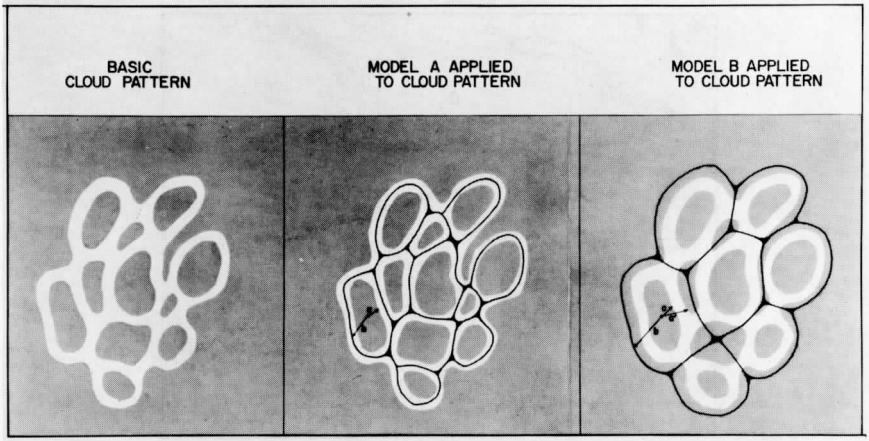

Fig. 9. Definition of cloud modeling parameters for two models. Light areas indicate cloud bands.

If much of the convection in the tropics is organized into polygons, as it appears to be in ATS pictures, then it is important to determine the feasibility of obtaining the dimensions of such polygons using the digital data. These dimensions provide necessary input to cloud models where such parameterization is required. We have picked ensemble 2 to study this feasibility.

In order to study ensemble 2, let us assume two cloud Models, A and B, as shown in Fig. 9. Cloud Model A is similar to that suggested by Kuo (1961), and Asai (1967), among others. In this model the boundary is taken through the center of the cloud bands; thus vertical motion is upward along the boundary. Model B differs from Model A in that it includes all of the cloud ensemble within the model boundary. In this model the boundary is through the cloudless areas; therefore the vertical motion along the boundary is downward.

When Model A is applied to cloud ensemble 2 and average values of a and b are computed, we find that there are two distinct domains of cloudiness. As shown in the top of Fig. 10, the small gradient of brightness from radius 0 to 21 miles indicates one cloud domain within the polygon, and the greater brightness gradient from 21 to 31 miles radius indicates another. The second apparently is deep convection in the polygon cloud ring. The calculated values of a and b do not depend, to any significant extent, on a precise selection of the polygon "center," providing the central point is located somewhere near the visual center of the polygon.

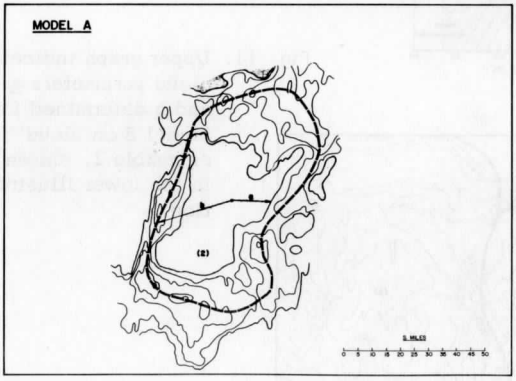

Fig. 10. Upper graph indicates cloud parameters a and b determined for Model A on cloud ensemble 2, shown in the lower illustration.

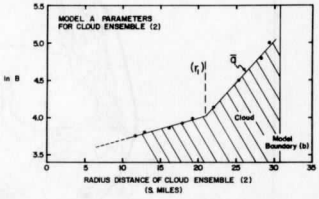

When Model B is applied to ensemble 2, we are able to observe the average brightness cross section for the entire ensemble; this is shown in the top of Fig. 11. It is apparent that the horizontal brightness slope on the inside ($\bar{a}$) and outside ($\bar{a}'$) of the polygon are very similar. Furthermore, there appears to be discernible domains of cloudiness outside the polygon, as well as inside. Thus, parameters r_1 and r_2 in Fig. 11 are useful for defining the horizontal dimensions of such cloud ensembles. These parameters can be determined from brightness gradient alone; absolute values of brightness are not required.

For certain cloud models, such as that given by Asai (1967), it is useful to determine the parameters a and b, as defined in Model A. We have obtained these constants by planimetering the "clear" area of ensemble 2 in Fig. 10 corresponding to brightness values less than that associated with the cloud domain boundary, r_1, and also by planimetering the total area within the model boundary. The results, given in Table 2, show the inner "clear" area covers 48 percent and the outer cloud area 52 percent of the total area. This is in general agreement with the areas covered by clouds in cellular cloud patterns, reported by Krueger and Fritz (1961). They observed cellular patterns with horizontal diameters as large as 30-50 miles and with "clear" centers bounded by cloud

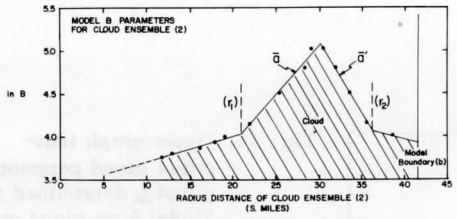

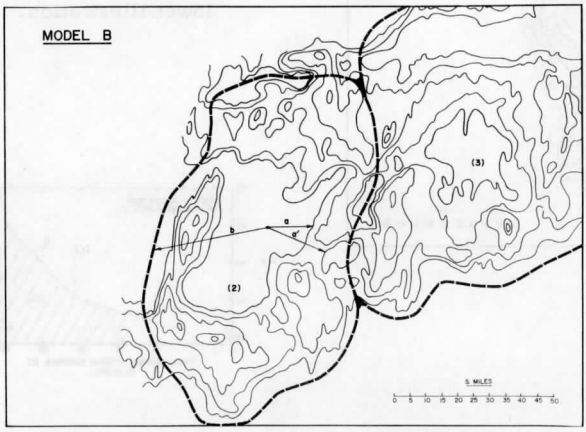

Fig. 11. Upper graph indicates cloud parameters a and b determined for Model B on cloud ensemble 2, shown in the lower illustration.

Table 2

Parameters	Values
$(a/b)^2$	0.48
(a/b)	0.69

elements about 10-15 miles wide. Such cellular patterns would have cloud areas which average about 53 percent of the total area. Both these observations of polygon shaped cloud ensembles indicate considerably more cloudiness than suggested by theoretical considerations for maximum heat transport (3 to 16 percent) by Asai (1967). However, Asai's Model has the opposite circulation to that reported here, and by Krueger and Fritz.

The data in Figs. 10 and 11 indicate that ATS digital data can be used to determine a variety of descriptive parameters for defining the horizontal dimensions of tropical cloud ensembles. In addition, brightness values may also give the clouds' vertical dimensions. Perhaps the most important capability of

the ATS-1 data is that growth and decay of clouds can be studied in great detail using pictures at 20 minute intervals.

b. Typhoon Sarah

Typhoon Sarah was a mature tropical disturbance in 1818GMT on September 11, 1967, several days before she struck Wake Island. The ATS picture of Typhoon Sarah at the time is shown in Fig. 12. The enclosed area is also

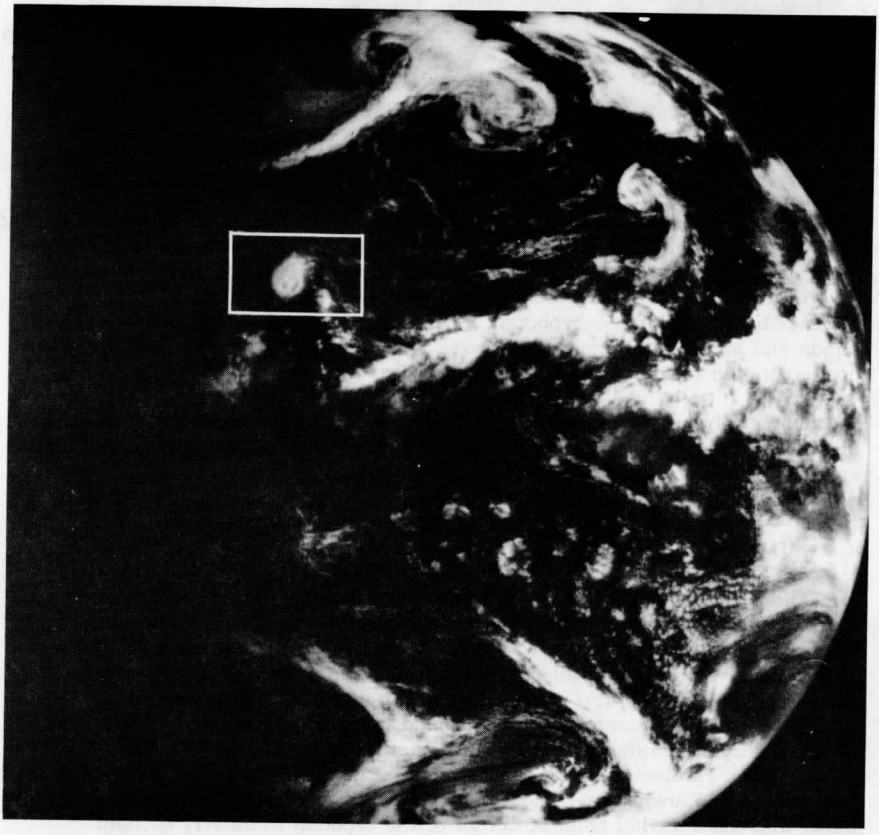

Fig. 12. ATS-1 picture for 1818GMT, September 11, 1967. Typhoon Sarah is visible in the enclosed area located about 100 miles southwest of Honolulu, Hawaii, near 18° North, 165° West.

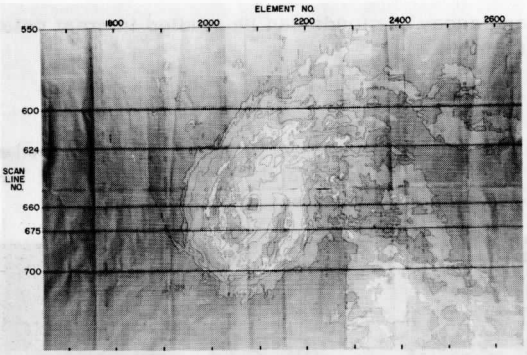

Fig. 13. Typhoon Sarah at 1818GMT, September 11, 1967. The dark horizontal lines are scan lines which in Fig. 14 show brightness cross sections of Typhoon Sarah.

illustrated in the computer produced digital data display of Fig. 13. The lowest brightness contour there is 16 and the highest is 48. The structure of cloud bands in the typhoon is clearly discernible. Brightness cross sections of Typhoon Sarah are given in Fig. 14. The cloud band structure of the storm is also evident in these cross sections. For example, scan line 675 shows three distinct bands within the typhoon. Scan line 660 is through the eye of the typhoon and shows a minimum brightness in the eye and also a brightness peak corresponding to the illuminated west wall of the eye.

Obviously, there is considerable information in the digital data on band structure of the typhoon in spite of the fact that the storm was near the terminator at the time of the picture.

4. SUMMARY

The ATS digital data have been used to determine cloud displacement and divergence of low-level convection in the tropics. Both the speed and direction of the winds agree quite well with wind measurements below and within the cloud layer. The digital data have also been used to determine parameters for defining the horizontal dimensions of cloud ensembles which are made up of deep tropical convection. It was found that such ensembles can be parameterized by examining the horizontal brightness gradient and integration of cloud area. Parameters for a typical polygon shaped cloud ensemble have been determined and are presented. Typhoon Sarah is illustrated with the digital data, and the detailed band structure of the typhoon is clearly evident.

These three applications of ATS-1 digital data show that quantitative, high-resolution measurements from a geosynchronous satellite provide a data resource that promises to be of value for operational wind calculations and for studies of cloud physics and dynamics.

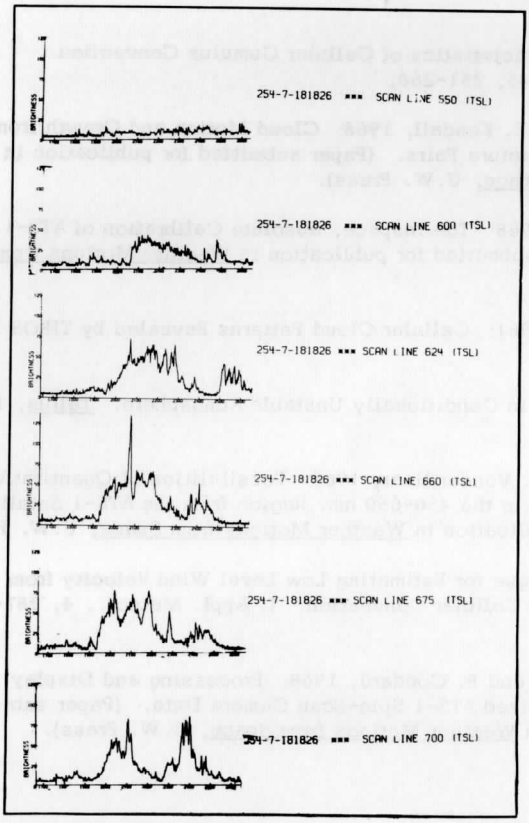

Fig. 14. Brightness cross sections of Typhoon Sarah in Fig. 13.

5. ACKNOWLEDGMENTS

This research was supported by grants from ESSA and NASA. The computer programs used to display the ATS data were written by Mr. Eric Smith and Mrs. Marilyn Mantei.

6. REFERENCES

Asai, T., 1967: On the Characteristics of Cellular Cumulus Convection. J. Meteor. Soc. Japan, 45, 251-260.

Bristor, C., M. Frankel and E. Kendall, 1968: Cloud Motion and Growth from ATS-1 Digitized ATS-1 Picture Pairs. (Paper submitted for publication in Weather Motions from Space, U.W. Press).

Hanson, K. and V. Suomi, 1968: The Inspace, absolute Calibration of ATS-1 Cloud Camera. (Paper submitted for publication in Weather Motions from Space, U.W. Press).

Krueger, A., and S. Fritz, 1961: Cellular Cloud Patterns Revealed by TIROS 1. Tellus, 13, 1-7.

Kuo, H., 1961: Convection in Conditionally Unstable Atmosphere. Tellus, 13, 441-459.

Peekna, S., R. Parent and T. Vonder Haar, 1968: Possibilities of Quantitative Radiance Measurements in the 450-650 nm. Region from the ATS-1 Satellite. (Paper submitted for publication in Weather Motions from Space, U.W. Press).

Rogers, C., 1965: A Technique for Estimating Low Level Wind Velocity from Satellite Photographs of Cellular Convection. J. Appl. Meteor., 4, 387-393.

Whitney, M., R. Doolittle, and B. Goddard, 1968: Processing and Display Experiments using Digitized ATS-1 Spin-Scan Camera Data. (Paper submitted for publication in Weather Motions from Space, U.W. Press).

PHENOMENOLOGY OF CONVECTIVE RING CLOUDS IN THE TROPICS DERIVED FROM GEOSYNCHRONOUS SATELLITE OBSERVATIONS

by

T. Vonder Haar, K. Hanson[1], V. Suomi and U. Shafrir[2]
The University of Wisconsin

1. INTRODUCTION

Since the first meteorological observations from a geosynchronous satellite became available late in 1966, many kinds of interesting cloud patterns have been observed in sequences of high resolution photographs. One of the first features that drew our attention was the apparent organization of convective clouds within the tropical convergence zones into ring-like patterns. This scale of organization differs from the well-known line or isolated tower pattern. Clusters of these rings have been noted during all seasons and at a variety of longitudes across the central and eastern Pacific Ocean. They have been found in both hemispheres and are generally imbedded in, and moving with the easterly winds near the equator. In time-lapse movies made from ATS pictures, the ring patterns appear to develop and dissipate and often portions of the ring clusters are obscured by cirrus blow-off from the convective clouds. When ring clusters are located within a sun glint region, the clear ring centers have a mirror-like brightness that indicates a calm sea. Figure 1 is an ATS-1 photograph in which the ring-like cloud ensembles can be observed in several regions of the tropical Pacific.

Because convective clouds play an extremely important role in the energy budget of the tropics by transporting energy into the upper troposphere for eventual poleward advection, much more information about these clouds is needed to allow parameterization and eventual incorporation into numerical models of the atmospheric circulation (GARP, 1967). This paper is a preliminary study of the

[1] National Environmental Satellite Center, ESSA, Madison, Wisconsin.

[2] On leave from the Institute of Planetary and Space Science, Tel-Aviv University, Ramat-Aviv, Israel.

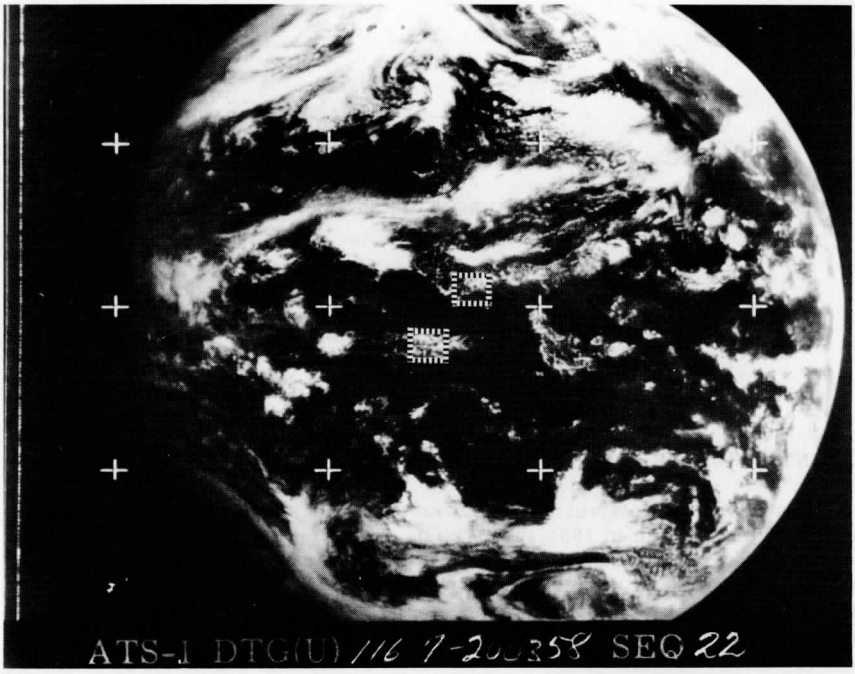

Fig. 1. An ATS-1 photograph taken at 2004Z on April 25, 1967. The enclosed areas are the ring-cloud regions studied in this paper. The Northern area is termed Case 1 and the Southern area Case 2.

spatial and temporal variation of the ring-like patterns formed by the convective clouds. It is hoped that such information can be applied to studies of individual cells and also in subsequent work relating and occurrence of such convective regions to the large-scale atmospheric circulation.

The measurements used in this study are digitized samples of the video signal obtained from the Spin-Scan Camera on ATS-1. These measurements are directly proportional to the shortwave radiation reflected from the clouds, the atmosphere and the ocean (Peekna et al., 1968). The camera has a nominal areal resolution of 2 n.mi. from geosynchronous altitude, and observations over the same region were obtained at 23 minute intervals during the daylight hours.

2. TYPICAL RING CLOUD SIZE AND COMPOSITION

In a paper in this annual Report, Hanson and Vonder Haar have used ATS digital data from one picture to examine the ring clouds in detail. They studied the northernmost enclosed region in Fig. 1 (this area will be termed Case 1 in the present study and the other enclosed region Case 2), and found that the apparent clear centers could be discriminated from the cloudiness of the rings by a sharp horizontal brightness (reflected energy) gradient. In addition, the brightness contours indicated that within the ring itself, small bright regions, apparently the deeper convective elements, could be identified. This first study also showed that the ratio of the inside to the outside diameters of a typical ring was about 0.7 and thus the area of the cloudy regions was nearly the same as that of the clear centers.

Each of these features can be seen in the brightness contour analyses[1] for Cases 1 and 2 in Figs. 2 and 3. (Dark ocean regions are cross-hatched.) Five brightness levels are shown, and the fourth (second-brightest) level is accentuated with "tic" marks. These levels were chosen at equal intervals and, for illustration, correspond roughly to "albedo" values ranging from 10 to 60 percent.

Within each Case, three ring regions are indicated and these same areas were studied in detail by using similar brightness analyses at other times during the same day. The displays in Figs. 2 and 3 refer to conditions near 1000 HST. Choosing the second brightness level as the ring boundary, we observe mean inside diameters ranging from 50 km (Case 2, Ring 1) to 75 km (Case 1, Ring 2). Note also that the rings are sometimes distorted, but basically circular. Assuming that level 4 marks the boundary of the deeper convection, it is apparent that some rings (Case 2, Ring 1) are almost completely composed of these elements, while others (Case 2, Ring 2) are not.

3. TIME VARIATIONS

Five observation times at 2-hour intervals (0800-1600 HST) were chosen to study the temporal variation of the six-ring clouds. The five brightness levels were normalized to eliminate the effect of changing insolation between the five observation times. We have not adjusted the brightness values to account for the non-Lambertian reflectance of clouds. While this point needs further study, present-day information suggests that a small bias toward brighter values may occur near local noon for the regions considered in this paper.

---

[1] Brightness contour analyses of this type are discussed by Smith and Vonder Haar in another paper in this Annual Report.

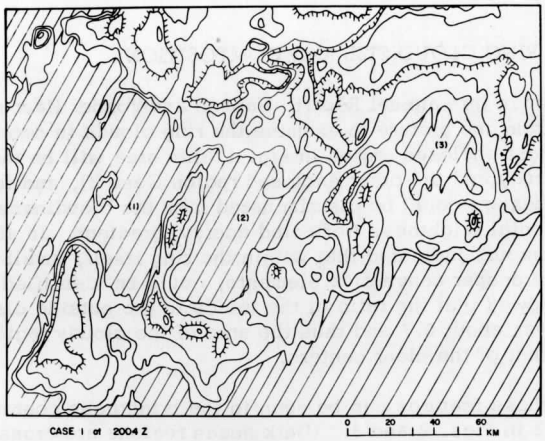

Fig. 2. Brightness pattern of a ring-cloud area with darkest regions cross-hatched and brightest regions noted by "tic" marks. Numbers locate specific cloud rings.

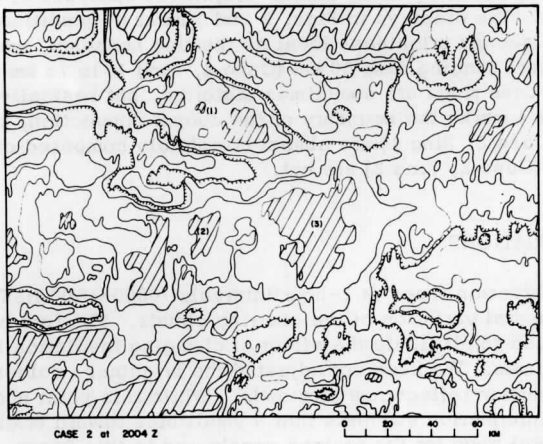

Fig. 3. Brightness pattern of a ring-cloud area with darkest regions cross-hatched and brightest regions noted by "tic" marks. Numbers locate specific cloud rings.

An eight hour record of three descriptive parameters of the ring clouds is shown in Fig. 4. The parameters are:

a) the circular extent of the ring cloud defined by brightness level 2 (from 0 to 360 degrees)
b) the mean inside diameter of the ring cloud (km)
c) the equivalent circular extent of apparent deep convection within the ring of clouds (from 0 to 360 degrees)

Of the six ring cloud areas studied, all seemed to retain a nearly circular shape as long as they could be identified at all. Thus the first parameter above, the extent of the rings, did not drop below 260 degrees during the period of observation. This means there was no extreme fluctuation of various segments of the ring nor did the rings seem to grow or decay in piecemeal fashion.

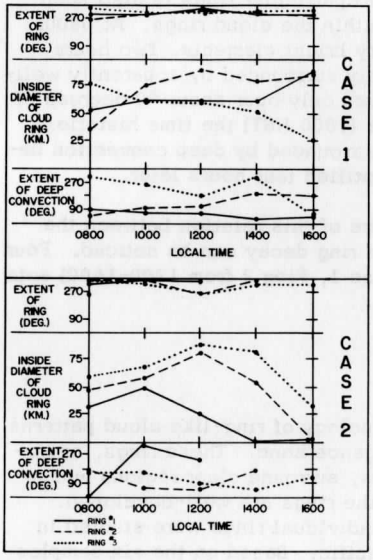

Fig. 4. An eight hour record of three descriptive parameters of the ring-cloud areas noted in Figs. 2 and 3.

However, the inside diameter plots show that two of the rings did disappear during the observation period (Case 2, Rings 1 and 2). In both cases this "death" was preceded by a gradual shrinking of the clear center region (or a widening of the ring cloud) that began four hours previously. The four other rings show histories that range from moderate growth (Case 1, Rings 1 and 2) to apparent constancy with an indication that decay has begun (Case 1, Ring 3 and Case 2, Ring 3).

Assuming these to be typical rings, it appears that a complete life cycle must be longer than our eight hour observation period. An estimate based on all the data of Fig. 3 yields 14-16 hours and thus the four hour decay pattern already noted indicates that the rings may have rather sudden deaths. The need to obtain a more statistically representative sample of these rings is emphasized by the different time variation of Case 2, Ring 1 and Case 1, Ring 2 which were both the same size at 0800 HST.

An interesting difference between these two particular rings is also seen in the plots of the extent of deep convection within the cloud rings. At 0800, less than one-sixth of both rings contained very bright elements. Two hours later, however, Ring 1 in Case 2 was completely surrounded by apparently well-developed cells while the other ring was bounded only over about 90 degrees of arc by these cells. Note that at this very time (1000 HST) the time histories of the two rings became dissimilar. The one surrounded by deep convection began to decay immediately and could not be identified four hours later.

In the six rings under study, other evidence of this relation between the occurrence of deep convection and the onset of ring decay can be noticed. Four rings show the same relation although one (Case 1, Ring 2 from 1200-1600) acts in the opposite manner.

4. CONCLUSIONS

We have presented a preliminary phenomenology of ring-like cloud patterns frequently observed within the tropical convergence zone. These rings, apparently composed of individual convective clouds, surround clear regions whose diameters vary from 30 to 90 kilometers when the rings are well-developed. These phenomena occur in clusters and three individual rings were studied in each of two separate regions in the tropical Pacific. Based on the six samples an estimate of the life-cycle of a typical ring is 14-16 hours, much longer than that of any individual convective cell. The decay of these ring-like patterns seems to be preceded by the extensive development of deep convection within the rings.

Of course, a larger sample of these phenomena should be studied to obtain better statistics. However, this semi-quantitative study of the time variations of the ring clouds is a first step beyond observation and study at only one point

in time. These results also demonstrate the usefulness of very high resolution satellite data in studies such as this, and should provide some basic parameters to guide physical and numerical investigations of tropical convective processes.

5. ACKNOWLEDGMENTS

This study was supported by ESSA Grant WBG-27. It was presented at the International Conference on Cloud Physics, Toronto, 1968.

6. REFERENCES

GARP, Global Atmospheric Research Program, Report of the Study Conference held at Stockholm, 28 June - 11 July 1967: ICSU/IUGG Committee on Atmospheric Sciences, COSPAR, WMO.

Peekna, S., R. Parent and T. Vonder Haar, 1968: Possibilities for quantitative radiance measurements in the 450-650 nm region from the ATS-1 satellite. (Paper submitted for publication in Cloud Motions from Space, U. W. Press)

Scanner's note:

This page is blank.

ON THE DOUBLE STRUCTURE OF CLOUD DISTRIBUTION IN THE EQUATORIAL PACIFIC

by

Jack Kornfield and Kirby Hanson

INTRODUCTION

The circulation and cloud structure of the equatorial atmosphere have been studied because of their roles in the first stage of the atmospheric heat engine. Fletcher (1945), Palmer (1952), Riehl (1954), Flohn (1955), and others have provided the framework of knowledge by describing the general circulation of the equatorial atmosphere. Alpert (1945), Simpson (1947), Malkus et al. (1961), among others, have added a great deal of information by describing the atmospheric behavior in regional studies of the Pacific. These early studies were based primarily on observations taken in the sparse network of Pacific Ocean weather stations, and on rawinsonde and aircraft observations. More recently, Sadler (1963a, b) has used TIROS satellite observations to reveal much about the local circulation and typhoon movement in the Eastern Pacific.

In the past year, two technological advances have provided new possibilities to further our knowledge of the Pacific atmosphere: the computer-produced global cloud mosaics developed by the National Environmental Satellite Center of ESSA, which provide a single "daily" picture of the global cloudiness, and the acquisition of high quality pictures from synchronous altitude of nearly the entire Pacific Ocean, which was first achieved by the ATS-1 Spin-Scan Camera. Because of these two technological advancements, we now have the means for gathering data for the tropical region on a scale never before possible. This paper discusses one of the newly discovered features of the cloud distribution over the Pacific Ocean.

PROCEDURE

In order to study the cloud distribution over the equatorial Pacific, we have employed two techniques to give mean cloud patterns.

One technique provides photographic averaging of a series of pictures. The individual pictures in the series are imaged, one at a time, on a single sheet of photographic film. This single picture represents an average of all the individual pictures of the series. This technique is described by Kornfield and Hasler (1968). Photographic averages of the ATS-1 pictures have been obtained in this manner for monthly and half-monthly periods. The monthly "mean" pictures with a grid superimposed manually are displayed in Fig. 1. Each monthly average is derived from about thirty pictures.

The second technique is used to determine frequency of occurrence of band-type cloudiness. This type of cloudiness is defined as those clouds which appear to be organized into lines or bands having a width of two degrees latitude or greater. One picture per day was used to determine the frequency of occurrence of this type of cloudiness for monthly periods. Each daily ATS-1 picture was overlain with a 5 by 5 degree latitude-longitude grid, and the presence or absence of line-type cloudiness in these boxes was determined. Seldomly did two cloud lines appear in a single block. The frequency of line-organized cloudiness was then determined for monthly periods and hand analyzed. These are plotted in Fig. 2.

Although Figs. 1 and 2 show the same general cloud structure in the Tropics, it is apparent that the hand nephanalysis used does not reveal the full structure of the cloud bands as do the photographic averages which can record clouds of smaller size and without a previously defined definite organization.

DISCUSSION

The most striking features revealed in Figs. 1 and 2 are two zones of convective activity north and south of the equator in the early spring and late winter months and a persistent storm track which runs diagonally across the southern hemisphere (Fig. 4). Here we shall limit ourselves to a short discussion of the equatorial "doublet."

On each monthly picture the cloud bands have a restricted range on latitude. The centers of these cloud bands appear to range only five to ten degrees latitude from the equator. The northern band extends across nearly the entire Pacific while the intensity, longitudinal position and extent of the cloud band south of the equator undergoes greater changes.

The greater frequency of convective activity that permits the observation of the cloud bands may find its origin in both the mass and moisture convergence to be associated with the classical ITC or with warmer surface waters supplied by ocean currents.

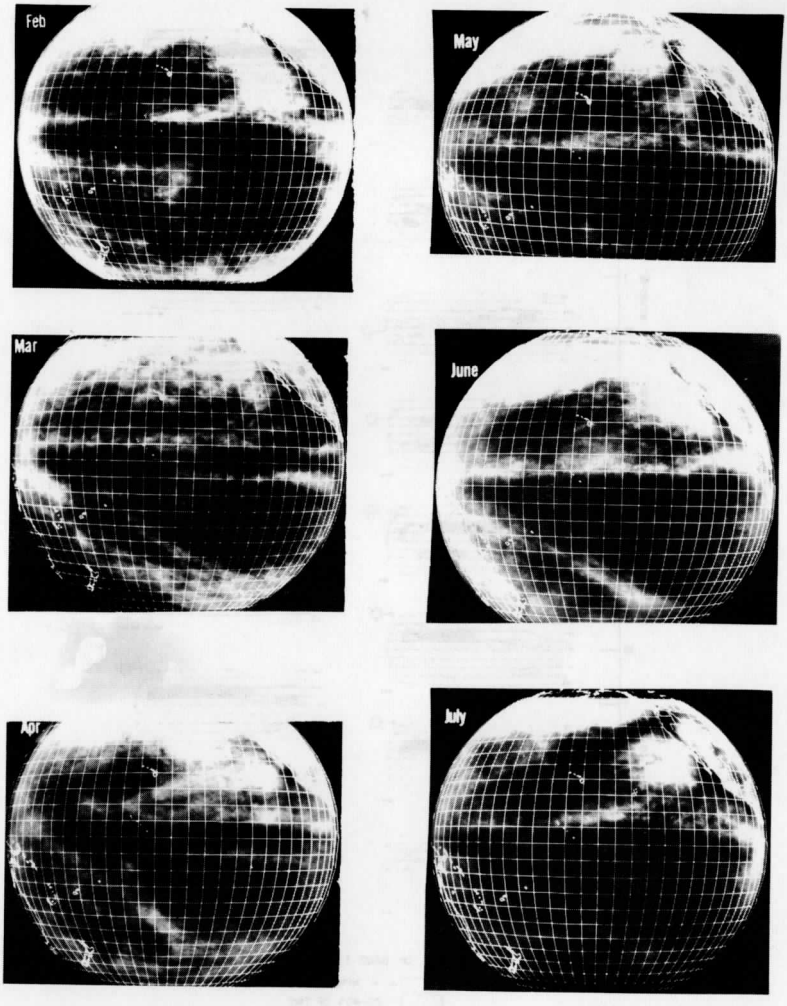

Fig. 1. "Mean" Monthly ATS-1 pictures, 1967.

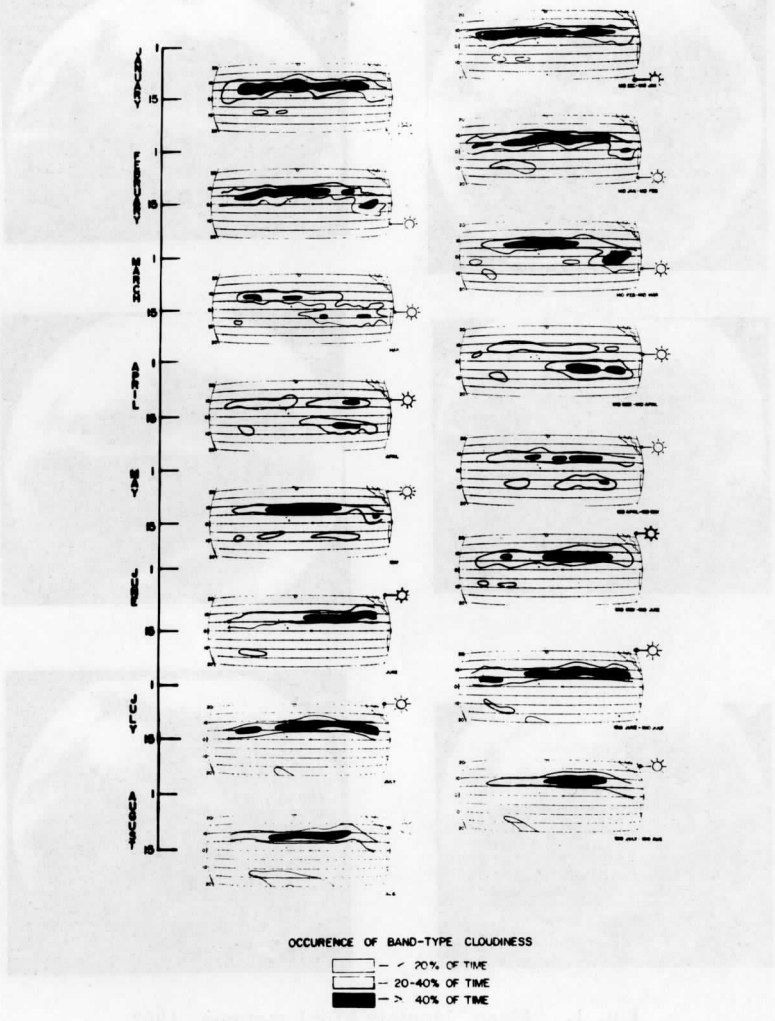

Fig. 2. Monthly frequency of occurrence of band-type cloudiness, 1967.

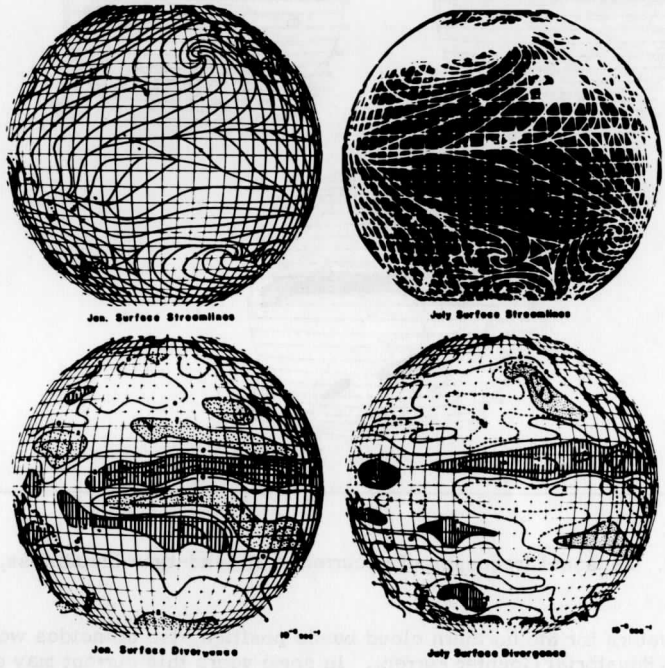

Fig. 3. July and January mean streamlines and divergence of the surface wind, from Mintz and Dean, 1952.

In Fig. 3, we have used Mintz and Dean's (1952) studies of the general circulation to illustrate convergence in the equatorial regions. The directional convergence between the Northern and Southern Hemisphere trades in July coincides well with the northern cloud band. Though convergence lines cross the equator in January, the northern cloud band remains in vertically the same position as may be seen by comparing Figs. 1 and 2 with Fig. 3. This suggests that the convective bands which originate in the southern flanks of the subtropical high and migrate toward the equator may persist in regions of warmer

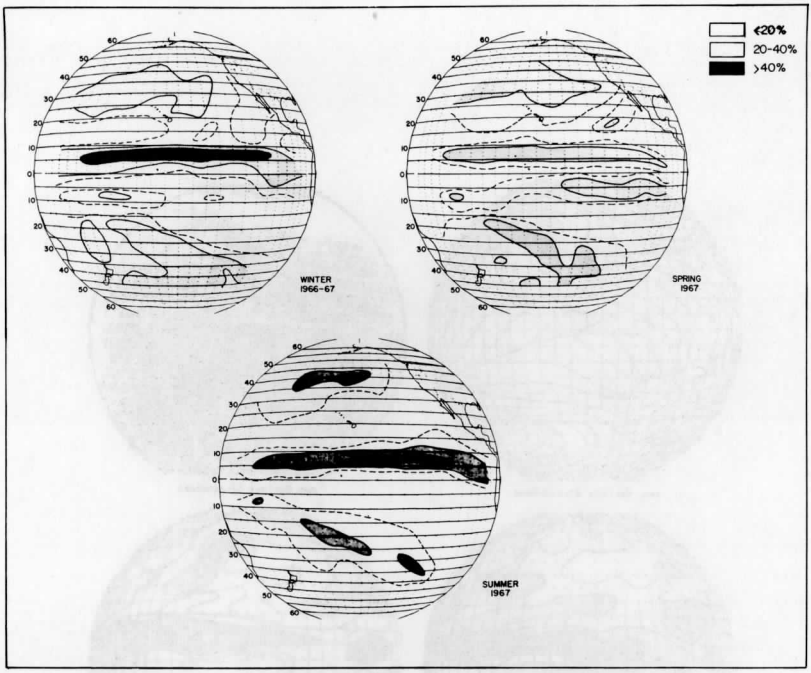

Fig. 4. Seasonal frequency of occurrence of band-type cloudiness, 1967.

surface waters for the northern cloud bands position also coincides well with the North Equatorial Counter current. In some years this current may cross into the southern hemisphere in the Eastern Pacific during the late winter and early spring (Bjerknes, 1966). Wyrtki (1966) indicates that warm waters are usually present in the eastern Pacific at this time.

Cloud bands on the ESSA "averages" (not shown here) also show a similar double structure; in the region west of Central and South America, a complicated structure exists from February through April. During the month of March, similar pictures also show an equatorial doublet in the Indian Ocean west of Africa. In that location, a Northern and Southern ITC has been reported previously (Gentilli, 1958).

The northern cloud band is observed to be relatively stationary west of about 120° West longitude; east of the meridian, however, there does appear

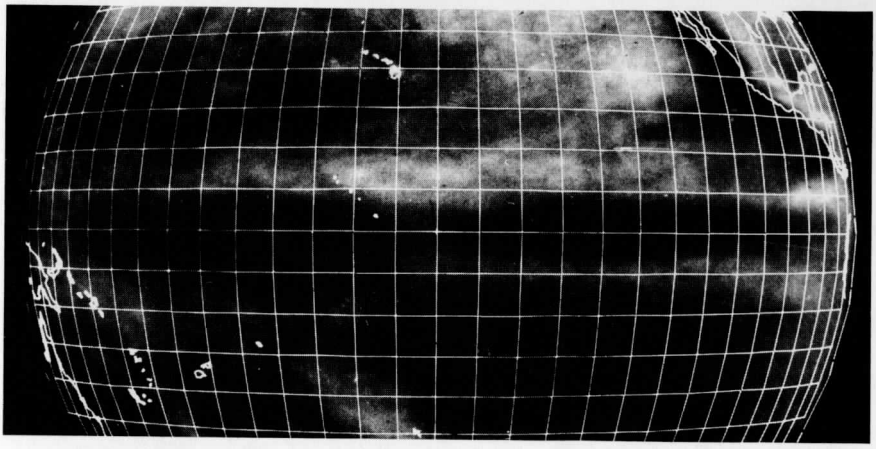

Fig. 5. March - April - May, 1967 "Mean" ATS-1 picture.

to be a seasonal displacement. The displacement of the ITC was studied earlier by Alpert (1942) over the limited region between 90 and 95° West. The mean position of the cloud band has been estimated in the same region from the ATS and ESSA monthly cloud "averages" and appears to be similar to that previously observed for the ITC by Alpert from February to July, i.e., the ITC was farthest south in February and then moved northward as the year progressed.

The equatorial cloud doublet in the eastern-central Pacific Ocean seems to be a characteristic of the atmosphere's general circulation.[1] It appears almost symmetrically about the Equator over the Pacific Ocean (Fig. 5) and apparently also exists in the Indian Ocean, too. The doublet's seasonal intensification around the world is most likely due to regional effects on convective cloud production. The sharp decrease in cloudiness west of 150° West indicated that in the eastern Central Pacific, the Southern Hemisphere cloud band is associated in some way with the subtropical high off the coast of South America. In the western equatorial Pacific the doublet's intensification may be associated with the seasonal variation in surface wind convergence, as suggested by the streamlines of Mintz and Dean. The extremely narrow latitudinal extent of the cloud bands North and South of the Equator, with their longitudinal growth and the cloud-free regions on either side, also suggests the earth's rotation has a strong influence on organized convective activity in the tropics. The ease with which one may view the clear zone over the Pacific Ocean as compared to the

[1] The equatorial doublet appears to exist in the spring of 1968.

Indian Ocean also suggests that the subsurface, cold water, Cromwell current, which is centered on the Equator, contributes substantially to the clear area between the cloud bands in the equatorial Pacific. A recent theoretical paper by Charney discusses the role of the coriolis effect and the Cromwell current on the equatorial convergence zone.

SUMMARY

This study has employed a photographic and manual technique to analyze ATS-1 cloud information. An equatorial cloud doublet is observed in the East Central Pacific region. It is best developed in March and April. The cloud bands have a preferred location between 5 and 10 degrees North and South of the Equator, and the northern band extends across nearly the entire Pacific Ocean. There is only minor latitudinal displacement of the northern band west of 120° West longitude. East of the meridian there is a seasonal displacement. The intensity, longitudinal position, and extent of the southern band varies with season. The doublet may be closely associated with warmer surface waters in the eastern Pacific in the early spring.

ACKNOWLEDGMENT

This research was supported by the U.S. Department of Commerce, ESSA, under WBG-27.

REFERENCES

Alpert, A.C. 1945: The Intertropical Convergence Zone of the Eastern Pacific Region (I). Bull. Amer. Meteor. Soc., 26, 426-432.

Bjerknes, J., 1966: A Possible Response of the Atmosphere Hadley Circulation to Equatorial Anomalies of Ocean Temperature. Tellus, 18: 820-829.

Charney, J., 1968: Intertropical Convergence Zone and the Hadley Circulation of the Atmosphere. (Submitted for publication in Weather Motions from Space, U.W. Press)

Fletcher, R.D., 1945: The General Circulation of the Tropical and Equatorial Atmosphere, J. Meteor., 2, 167-174.

Flohn, H., 1955: Tropical Circulation Patterns. WMO Tech. Notes, 9.

Gentilli, J., 1958: A Geography of Climate, The University of Western Australia Press, Perth, Western Australia.

Kornfield, J. and A. Hasler, 1968: Photographic Cloud Averages. (Submitted for publication in Weather Motions from Space, U.W. Press)

Malkus, J.S., H. Riehl, C. Ronne, and W. S. Gray, 1961: Cloud Structure and Distribution over the Tropical Pacific, Part II, Woods Hole Ocean. Inst. Ref. No. 61-24.

Mintz, Y., and G. Dean, 1952: The Observed Mean Field of Motion of the Atmosphere. Geophys. Res. P., 17, GRD, AFCRL, Cambridge, Mass.

Palmer, C. E. Tropical Meteorology, Quarterly Journal of the Royal Meteorological Society, Vol. 78, 1952, 126-164.

Riehl, H., 1954: Tropical Meteorology, McGraw-Hill, New York.

Sadler, J., 1963a: Utilization of Meteorological Satellite Cloud Data in Tropical Meteorology. Proceedings of First International Symposium on Rocket and Satellite Meteorology. Northland Publ. Co., Amsterdam, 335-356.

Sadler, J., 1963b: TIROS Observations of the Summer Circulation and Weather Patterns of the Eastern North Pacific. Symposium on Tropical Meteorology, Rotorus, New Zealand.

Simpson, R.H., 1947: Synoptical Aspects of the Intertropical Convergence Near Central and South America. Bull. Amer. Meteor. Soc., 28, 335-346.

Wyrtki, K. 1966: Oceanography of the Eastern Equatorial Pacific Ocean. Oceanogr. Mar. Biol. Ann. Rev., 4, 33-68.

Scanner's note:

This page is blank.

PHOTOGRAPHIC CLOUD CLIMATOLOGY FROM ESSA III AND V

COMPUTER PRODUCED MOSAICS

by

J. Kornfield, A. F. Hasler, K. J. Hanson and V. E. Suomi

(Published in: Bulletin of the American Meteorological Society, Vol. 48, No. 12, December, 1967, pp. 878-883)

A simple photographic technique using multiple exposures is being developed at the University of Wisconsin to enhance the salient features exhibited by the cloud field on ATS-I photographs [1]. Photographic film is exposed equally to a daily series of satellite pictures taken of the same geographic area and at the same local time. This technique has also been applied to ESSA computer produced mosaics[1] [2]. The resulting photographs provide a measure of the entire Earth's "average" cloud cover for selected time periods as well as information about the distribution of snow, ice and vegetation. First examples of the multiple exposure technique applied to the ESSA mosaics are shown in Figs. 1-4. Each picture shows the "average" cloud condition for one-half month. February and July were chosen as interesting examples because these months represent extreme seasonal differences in both hemispheres.

In the upper part of Fig. 1, which shows the Northern Hemisphere, the large dark area appearing in the center of the picture is the north-polar region which is not illuminated by the Sun in February. Comparing the February and July pictures in Fig. 1, a most striking increase of cloudiness is evident over India; this change is associated with the monsoonal circulation. Equally interesting is the cloud free area, over the Western Atlantic in February which extends to the Mediterranean Sea and the Middle East in July.

In February parts of the snow and ice fields which blanket the continental polar regions are visible. Snow and clouds on the ranges of the Alps, Caucasus,

[1] The computer mosaics are produced by NESC, ESSA [3] on a daily basis from video data obtained from ESSA satellites. The particular data used in this study are from ESSA III and V satellites which are in a 3 p.m. local Sun time orbit. Thus, the photographic "averages" presented in this paper represent average conditions over the Earth for 3 p.m.

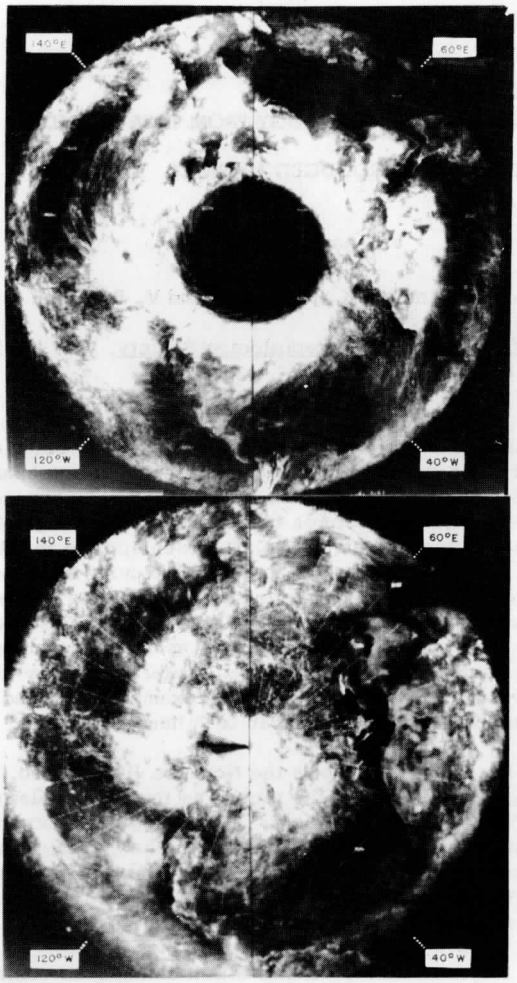

Fig. 1. Northern Hemisphere multiple exposure "averages" from ESSA III and V computer produced mosaics.

Zagros, Himalayas, Andes and Rockies mark their positions. The Greenland ice cap is easily seen in the July "average." The brightness of the Arctic ice pack in the July picture is less than that of the Greenland ice cap, which could be due to melt water on the ice packs' surface.

In Fig. 2, showing the Southern Hemisphere, the summertime increase of cloudiness of the Pampas of Argentina and the Kalahari Desert of Southwest Africa is plainly evident. The snow and ice of Antarctica and the Andes Mountains also stand out clearly in the February picture.

Figure 3 is a mercator projection of the equatorial region, from 40N to 30S, centered on the Atlantic Ocean and Africa. An equatorial cloud band is located over the Atlantic at approximately 3N during January and 7N during July. Cumulus activity, over the continental areas, is much more intense on the "summer side" of the equatorial cloud band. This is well illustrated by comparing winter and summer cloudiness over Brazil and the region in Africa from approximately 7 to 15N. In cloud free, continental areas, such as North Africa, the dark spots which are observed are thought to be due to topography. One of these dark areas coincides very closely in location and shape with the Tibesti Mountain Range in the Republic of Chad.

Figure 4 is a mercator projection showing the equatorial region, centered on the Pacific Ocean. An outstanding feature of the March picture is a paid of cloud bands which parallel the equator in both hemispheres. These cloud bands are separated by an equatorial dry zone. Preliminary observations indicate that these bands are relatively stationary and vary in intensity rather than migrate across the equator. The northern cloud band remains quite strong through the six month period January-July (complete data are not given here), whereas the southern band varies in intensity. The southern band is strongest near the vernal equinox in March, but is practically non-existent in June (not shown) and January. A more detailed treatment of the equatorial doublet will be given in [4]. (There are also indications of a weak doublet and dry zone about the equator in Fig. 3.) Another interesting cloud feature of the Pacific, revealed in Fig. 4, is a preferred storm-track which appears as a broad band of cloudiness extending from the New Guinea and Solomon Islands region, southeastward toward Antarctica.

The examples illustrated in Figs. 1-4 show that a simple photographic method of averaging satellite pictures can be used to obtain climatological information. The "averages" provide a measure of the cloud, snow, and ice cover over the entire Earth. A complete set of "averages," although not provided here, reveals climatological changes over the course of a year. The "averages" provide a quick and inexpensive method of summarizing some of the photographic information available to the meteorologist.

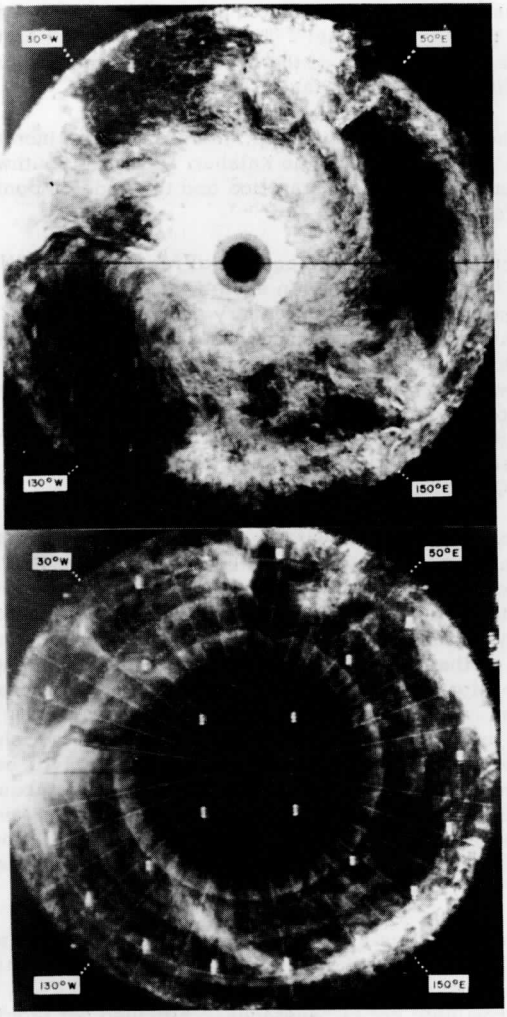

SOUTHERN HEMISPHERE

FEBRUARY 1-15, 1967

SOUTHERN HEMISPHERE

JULY 1-15, 1967

Fig. 2

Fig. 2. Southern Hemisphere multiple exposure "averages" from ESSA III and V computer produced mosaics.

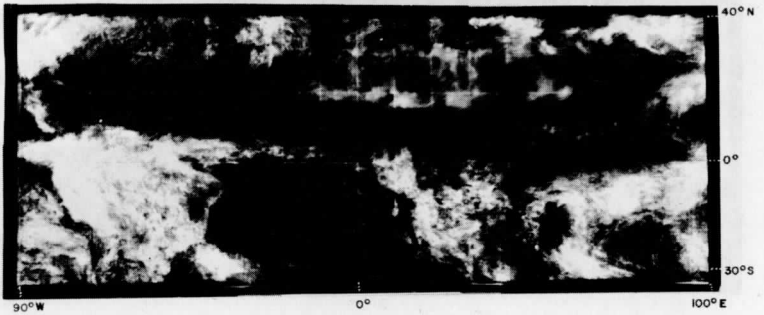

MERCATOR PROJECTION
JANUARY 1-15, 1967

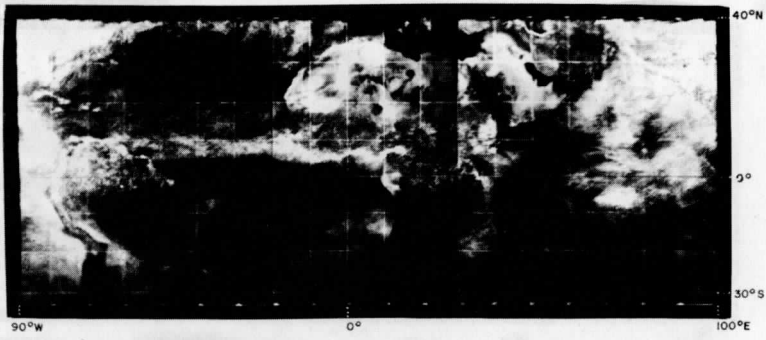

MERCATOR PROJECTION
JULY 1-15, 1967

Fig. 3

Fig. 3. Mercator projection (90W-100E) multiple exposure "averages" from ESSA III and V computer produced mosaics.

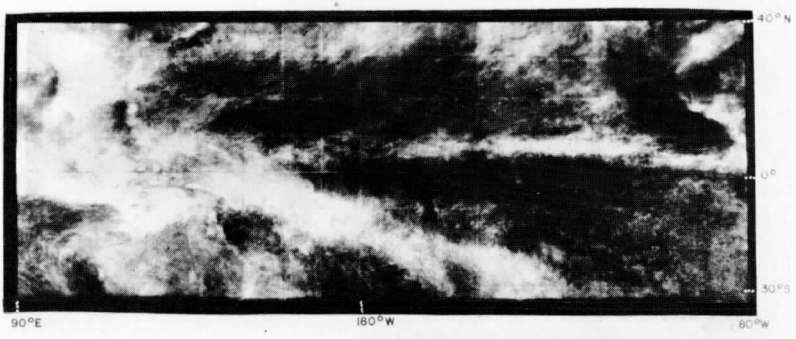

MERCATOR PROJECTION
JANUARY 16-31, 1967

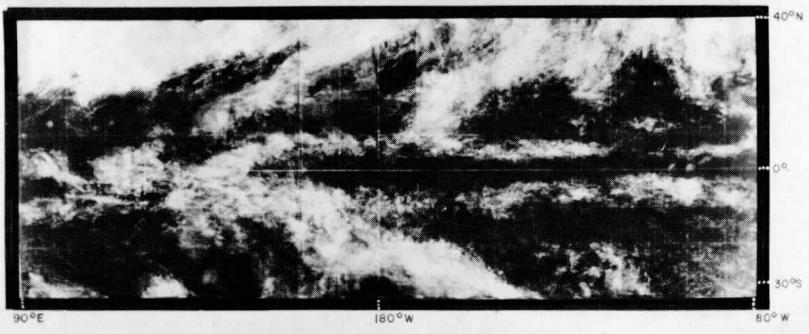

MERCATOR PROJECTION
MARCH 16-31, 1967

Fig. 4

Fig. 4. Mercator projection (90E-80W) multiple exposure "averages" from ESSA III and V computer produced mosaics.

ACKNOWLEDGMENTS

The writers are grateful to the team at ESSA for making these computer mosaics available to us, and to Dave Cadle, University of Wisconsin, for photographic assistance.

The research was supported by the U.S. Department of Commerce, ESSA, under WBG-27.

REFERENCES

1. Kornfield, J., and A. F. Hasler: Photographic cloud averages. (Submitted for publication in Weather Motions from Space. U.W. Press)

2. ESSA computer produced mosaics are available in both polar and mercator projection from the National Weather Records Center, Asheville, N.C.

3. Bristor, C. L., W. M. Callicott and R. E. Bradford, 1966: Operational processing of satellite cloud pictures by computer. Mon. Wea. Rev., 94, 515-527.

4. Kornfield, J., and K. J. Hanson: On the Double Structure of Cloud Distribution in the Equatorial Pacific. (Submitted for publication in Weather Motions from Space, U.W. Press)

Scanner's note:

This page is blank.

RAY ANALYSIS OF THE REFRACTION OF MICROWAVES PROPAGATED BETWEEN SATELLITES IN A SPHERICALLY STRATIFIED ATMOSPHERE

(A PRELIMINARY REPORT)

by

D. H. Sargeant

ABSTRACT:

The following is a preliminary report which develops the analytical foundation necessary for evaluating a remote probing technique using microwave refraction.

Section I derives exact expressions for basic ray theory parameters under the assumption of local spherical stratification.

Section II evaluates the various expressions for an ideal exponential atmosphere. The accuracy requirements of both the formulas and possible measurements are estimated, and the general features of inversion are sketched. The exact expressions of I allow a rigorous evaluation of errors in the formulas. A method allowing the ray variables for the ideal atmosphere to be calculated with arbitrary accuracy is developed.

Section III provides graphical presentations of the salient properties of the solutions. The sensitivity of the ray parameters to the profile parameters is investigated in detail. Weighting functions which show the relative contribution of different portions of a single ray path are also developed.

CONTENTS

LIST OF PRINCIPAL SYMBOLS

Coordinates

(r, θ)	general point on a ray
$(r, 0)$	point of closest approach
$(r_{a, b, s}; \theta_{a, b, s})$	satellite coordinates
Θ	angular satellite separation
r_0	earth radius
$h = r - r_0$	height above earth
$R = r - \hat{r}$	height above low point of ray
$t = (t - \hat{r})/H$	normalized low point of ray
$d = r \sin \theta$	horizontal coordinate (from closest approach)
$x = d/(2rH)^{\frac{1}{2}}$	normalized coordinate (from closest approach)

Profile Parameters

n	refractive index
$N = n - 1$	refractivity $\times 10^{-6}$

N_0	surface value of N
H	scale height
$\beta = 1/H$	Inverse scale height

Ray Variables

S	arc length from closest approach
α	angle between ray and refractivity isopleths
ϵ	bending angle from closest approach
L	ray (optical) path length
$\mathcal{L}$	portion of L expressible as an elementary function of ϵ
$\ell = L - \mathcal{L}$	remainder of L (approximately the retardation effect)
$L_e = L - d$	"excess" path length
$L_\epsilon = \mathcal{L} - d$	bending contribution to "excess" path length
ℓ^*	true retardation effect
E_ϵ, E_ℓ, E_L	error terms due to approximate integrations
W_ϵ, W_ℓ, $W_{L\epsilon}$, W_L	weighting functions (see section III. D)

Conventions

$\hat{X}$	value of X at $\hat{r}$
X_S	value of X at satellite

I. THE BASIC EQUATIONS

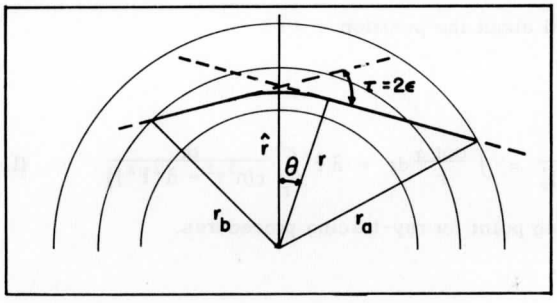

r_a, r_b: satellite locations

r: closest approach of ray

τ: total bending of ray

$n = n(r)$

A. Ray Equation

The ray path is assumed to satisfy Fermat's principle. In spherical coordinates, the problem is to minimize

$$\int n(r)ds(r) = \int n(r)[1 + r^2 (\frac{d\theta}{dr})^2]^{\frac{1}{2}} dr \equiv \int F(r, \theta, \theta')dr; \text{ where } \theta' \equiv \frac{d\theta}{dr}$$

From the calculus of variations, the Euler equation is

$$\frac{d}{dr}\frac{\partial F}{\partial \theta'} - \frac{\partial F}{\partial \theta} = \frac{d}{dr}[n(r)\frac{\partial}{\partial \theta'}(1 + r^2\theta'^2)] = 0$$

Thus $r^2\theta' n(r)(1 + r^2\theta'^2)^{-\frac{1}{2}} = C_1$, a constant for the path. (Note that C_1 has the sign of θ'. For convenience, measure θ from the minimum value of r, and consider C_1 positive.)

Geometrical Interpretation

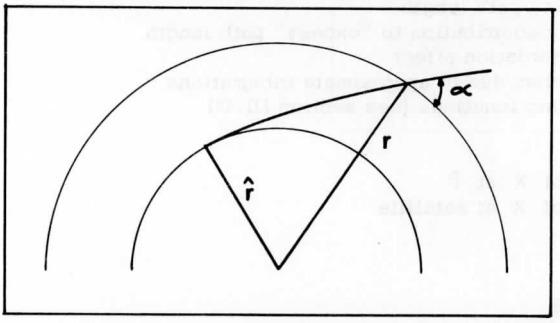

$$r\theta' = C_1/(n^2r^2 - C_1^2)^{\frac{1}{2}} = \cot\alpha$$

Thus $C_1 = n\, r \cos\alpha$, which is Snell's law for spherical stratification. In particular, $C_1 = n(\hat{r})\,\hat{r}\cos(0) = \hat{n}\,\hat{r}$.

The ray path is symmetrical about the position $r = \hat{r}$.

Integral Expression

$$\theta(r) = \int \frac{c_1\, dr}{r(n^2r^2 - c_1^2)^{\frac{1}{2}}} = \int \frac{\cot\alpha}{r}dr = \hat{n}\,\hat{r}\int_{\hat{r}}^{r} \frac{dr}{r(n^2r^2 - \hat{n}^2\hat{r}^2)^{\frac{1}{2}}} \qquad (1.1)$$

This equation is the starting point for ray-tracing procedures.

B. Bending Equation

It is convenient to isolate that portion of the θ variation due to bending of the ray. Analytically, this is accomplished by setting $u = nr$, $du = ndr + rn'(r)dr$. Then (1.1) becomes

$$\theta(r) = \hat{n}\,\hat{r}\int_{\hat{n}\,\hat{r}}^{n(r)r} \frac{du}{u(u^2 - \hat{n}^2\hat{r}^2)^{\frac{1}{2}}} - nr\int_{\hat{r}}^{r} \frac{n'(r)dr}{n(r)(n^2r^2 - \hat{n}^2\hat{r}^2)^{\frac{1}{2}}}$$

$$= \cos^{-1}\left(\frac{\hat{n}\,\hat{r}}{n\mathcal{r}}\right) - n\,r\int_{\hat{r}}^{\mathcal{r}} \frac{n'(r)dr}{n(r)(n^2r^2 - \hat{n}^2\hat{r}^2)^{\frac{1}{2}}} \qquad (1.2)$$

Geometrical Interpretation

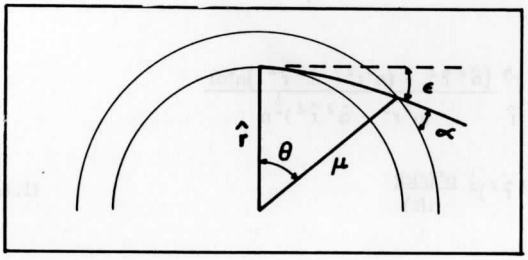

$$\cos^{-1}\left(\frac{\hat{n}\,\hat{r}}{n\mathcal{r}}\right) = \alpha(\mathcal{r})$$

$$\theta = \alpha + \epsilon$$

$$\frac{d\epsilon}{dr} = \frac{d\theta}{dr} - \frac{d\alpha}{dr}$$

From Snell's law,

$$\frac{d\alpha}{dr} = \cos\alpha\left(\frac{1}{n}\frac{dn}{dr} + \frac{1}{r}\right),$$

so that

$$\frac{d\epsilon}{dr} = \frac{\cot\alpha}{r} - \frac{d\alpha}{dr} = -\frac{\cot\alpha}{n}\frac{dn}{dr}$$

$$\epsilon(\mathcal{r}) = -\int \frac{c_1 n'(r)dr}{n(n^2r^2 - c_1^2)^{\frac{1}{2}}} = -\int \cot\alpha\,\frac{dn}{n} = -\hat{n}\,\hat{r}\int_{\hat{r}}^{\mathcal{r}} \frac{n'(r)dr}{n(r)(n^2r^2 - \hat{n}^2\hat{r}^2)^{\frac{1}{2}}}$$

(1.3)

C. Path Length Equation

The ray path length is given by

$$L(\mathcal{r}) = \int n(r)ds(r) = \int n(1 + r^2\theta'^2)^{\frac{1}{2}}dr$$

$$= \int \frac{n^2 r\,dr}{(n^2r^2 - c_1^2)^{\frac{1}{2}}} = \int \frac{n\,dr}{\sin\alpha} = \int_{\hat{r}}^{\mathcal{r}} \frac{n^2(r)r\,dr}{(n^2r^2 - \hat{n}^2\hat{r}^2)^{\frac{1}{2}}} \qquad (1.4)$$

Applying the transformation used to obtain (1.2) yields

$$L(\hbar) = \int_{\hat{n}\,\hat{r}}^{n\hbar} \frac{u\,du}{(u^2 - \hat{n}^2\hat{r}^2)^{\frac{1}{2}}} - \int_{\hat{r}}^{\hbar} \frac{r^2\, n\, n'\, dr}{(n^2r^2 - \hat{n}^2\hat{r}^2)^{\frac{1}{2}}}$$

$$= (n^2\hbar^2 - \hat{n}^2\hat{r}^2)^{\frac{1}{2}} - \int_{\hat{r}}^{\hbar} \frac{r^2 n(r) n'(r) dr}{(n^2r^2 - \hat{n}^2\hat{r}^2)^{\frac{1}{2}}} \qquad (1.5)$$

Also

$$- \int_{\hat{r}}^{\hbar} \frac{r^2\, n\, n'\, dr}{(n^2r^2 - \hat{n}^2\hat{r}^2)^{\frac{1}{2}}} = - \int_{\hat{r}}^{\hbar} \frac{[\hat{n}^2\hat{r}^2 + (n^2r^2 - \hat{n}^2\hat{r}^2)]n'dr}{(n^2r^2 - \hat{n}^2\hat{r}^2)^{\frac{1}{2}} n}$$

$$= \hat{n}\,\hat{r}\,\epsilon(\hbar) - \int_{\hat{r}}^{\hbar} (n^2r^2 - \hat{n}^2\hat{r}^2)^{\frac{1}{2}} \frac{n'(r)dr}{n(r)} \qquad (1.6)$$

Thus

$$L(\hbar) = (n^2\hbar^2 - \hat{n}^2\hat{r}^2)^{\frac{1}{2}} + \hat{n}\,\hat{r}\,\epsilon(\hbar) - \int_{\hat{r}}^{\hbar} (n^2r^2 - \hat{n}^2\hat{r}^2)^{\frac{1}{2}} \frac{n'(r)}{n(r)}\, dr. \qquad (1.7)$$

Geometrical Interpretation

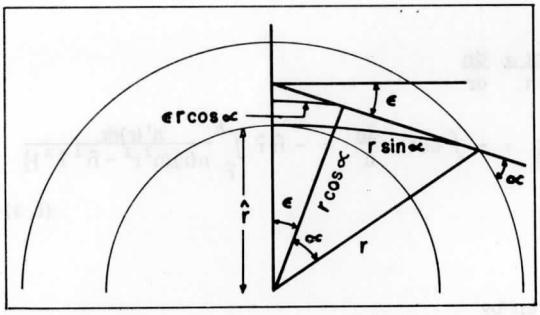

$(n^2r^2 - \hat{n}^2\hat{r}^2)^{\frac{1}{2}} = n(r)r \sin\alpha = \hat{n}\,\hat{r} \tan\alpha$

$\hat{n}\,\hat{r}\,\epsilon(r) = n(r)\epsilon(r)r \cos\alpha$

The first term is the optical path length to the (different) point of closest approach for a straight ray tangential to the actual ray at r but propagating in a medium of constant index n(r). The second term is also shown in the figure above.

It is useful to combine the first two terms of (1.7):

$$= \cos^{-1}\left(\frac{\hat{n}\,\hat{r}}{n\mathcal{r}}\right) - n\,r\int_{\hat{r}}^{\mathcal{r}} \frac{n'(r)dr}{n(r)(n^2r^2 - \hat{n}^2\hat{r}^2)^{\frac{1}{2}}} \tag{1.2}$$

Geometrical Interpretation

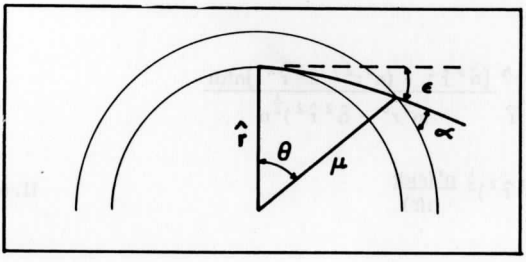

$$\cos^{-1}\left(\frac{\hat{n}\,\hat{r}}{n\mathcal{r}}\right) = \alpha(\mathcal{r})$$

$$\theta = \alpha + \epsilon$$

$$\frac{d\epsilon}{dr} = \frac{d\theta}{dr} - \frac{d\alpha}{dr}$$

From Snell's law,

$$\frac{d\alpha}{dr} = \cos\alpha\left(\frac{1}{n}\frac{dn}{dr} + \frac{1}{r}\right),$$

so that

$$\frac{d\epsilon}{dr} = \frac{\cot\alpha}{r} - \frac{d\alpha}{dr} = -\frac{\cot\alpha}{n}\frac{dn}{dr}$$

$$\epsilon(\mathcal{r}) = -\int \frac{c_1 n'(r)dr}{n(n^2r^2 - c_1^2)^{\frac{1}{2}}} = -\int \cot\alpha\,\frac{dn}{n} = -\hat{n}\,\hat{r}\int_{\hat{r}}^{\mathcal{r}} \frac{n'(r)dr}{n(r)(n^2r^2 - \hat{n}^2\hat{r}^2)^{\frac{1}{2}}}$$

(1.3)

C. Path Length Equation

The ray path length is given by

$$L(\mathcal{r}) = \int n(r)ds(r) = \int n(1 + r^2\theta'^2)^{\frac{1}{2}}dr$$

$$= \int \frac{n^2 r\,dr}{(n^2r^2 - c_1^2)^{\frac{1}{2}}} = \int \frac{n\,dr}{\sin\alpha} = \int_{\hat{r}}^{\mathcal{r}} \frac{n^2(r)r\,dr}{(n^2r^2 - \hat{n}^2\hat{r}^2)^{\frac{1}{2}}} \tag{1.4}$$

Applying the transformation used to obtain (1.2) yields

$$\mathcal{L}(r) \equiv [n^2(r)r^2 - \hat{n}^2\hat{r}^2]^{\frac{1}{2}} + \hat{n}\hat{r}\,\epsilon(r)$$

$$= nr \sin\alpha + \epsilon\, nr \cos\alpha$$

$$= nr[\sin\theta\cos\epsilon - \cos\theta\sin\epsilon + \epsilon(\cos\theta\cos\epsilon + \sin\theta\sin\epsilon)]$$

$$= nr[\sin\theta(\cos\epsilon + \epsilon\sin\epsilon) - \cos\theta(\sin\epsilon - \epsilon\cos\epsilon)]$$

$$= nr[\sin\theta(1 + \epsilon^2/2 - \epsilon^4/8 + \ldots) - \cos\theta(\epsilon^3/3 - \epsilon^5/30 + \ldots)] \qquad (1.8)$$

Geometrical Interpretation

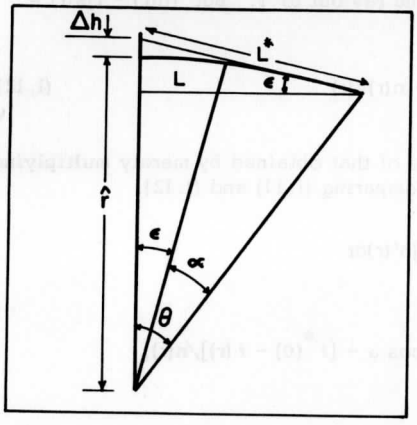

$$L^* = r\sin\alpha + r\cos\alpha\tan\epsilon$$

$$L^* - \mathcal{L}/n = r\cos\alpha(\tan\epsilon - \epsilon)$$

$$= r\cos(\theta-\epsilon)(\epsilon^3/3 + \epsilon^5/15 + \ldots)$$

(1.9)

Thus, when ϵ is small, $\mathcal{L}(r)$ is approximately equal to the optical path length of the straight ray tangential to the actual ray at r, in a medium of uniform n(r), and traversing the actual angle θ.

The height difference Δh between this approximate ray and the actual ray as given by

$$\Delta h = r\cos\alpha\sec\epsilon - (n/\hat{n})r\cos\alpha = r\cos(\theta - \epsilon)(\sec\epsilon - n/\hat{n})$$

$$= r\cos\theta\{1 - (n/\hat{n})\cos\epsilon + \tan\theta[\tan\epsilon - (n/\hat{n})\sin\epsilon]\}$$

$$= r\cos\theta[(1 - n/\hat{n})(1 + \epsilon\tan\theta) + \tfrac{1}{2}\epsilon^2(n/\hat{n}) + \ldots] \qquad (1.10)$$

The final integral in (1.7) can be roughly interpreted in terms of phase retardation. Let

$$\ell(\mathcal{R}) \equiv -\int_{\hat{r}}^{\mathcal{R}} (n^2 r^2 - \hat{n}^2 \hat{r}^2)^{\frac{1}{2}} \frac{n'(r)}{n(r)}\, dr = -\int_{\hat{r}}^{\mathcal{R}} r \sin\alpha\, n'(r) dr \tag{1.11}$$

Since $\ell(r) = L(r) - \mathcal{L}(r) \doteq L(r) - n(r)L^*(r)$, $\ell(r)$ must be approximately equal to the apparent path lengthening due to phase retardation suffered in regions having refractive index exceeding $n(r)$. Let the total retardation effect be denoted

$$L_R(r) = \int_0^{s(r)} [n(\mathcal{R}) - 1] ds(\mathcal{R}) = [n(r) - 1]s(r) - \int_{\hat{r}}^{r} s(\mathcal{R}) n'(\mathcal{R}) d\mathcal{R},$$

where $s(r)$ is the geometrical length of the ray out to r. But $[n(r) - 1]s(r) = n(r)s(r) - [L(r) - L_R(r)]$, so that

$$\ell^*(r) \equiv -\int_{\hat{r}}^{r} s(\mathcal{R}) n'(\mathcal{R}) dr = L(r) - n(r)s(r) \tag{1.12}$$

which is exactly the retardation in excess of that obtained by merely multiplying the actual geometrical length by $n(r)$. Comparing (1.11) and (1.12),

$$\ell^*(\mathcal{R}) - \ell(\mathcal{R}) = -\int_{\hat{r}}^{\mathcal{R}} [s(r) - r \sin\alpha] n'(r) dr$$

and using

$$s(r) = [L(r) - \ell^*(r)]/n(r) = r \sin\alpha + \epsilon r \cos\alpha - [\ell^*(0) - \ell(r)]/n(r),$$

$$\ell^* - \ell = -\int_{\hat{r}}^{\mathcal{R}} [\epsilon r \cos\alpha - \frac{\ell^* - \ell}{n}] n' dr$$

Letting $f(r) = \ell^*(r) - \ell(r)$, this becomes

$$f(r) - \int_{\hat{r}}^{r} \frac{f n'}{n} d\mathcal{R} = -\int_{\hat{r}}^{r} \epsilon \mathcal{R} \cos\alpha\, n' d\mathcal{R}, \text{ and differentiating,}$$

$$f' - f n'/n = n \frac{d}{dr}(\frac{f}{n}) = -\epsilon r \cos\alpha\, n'.$$

Finally,

$$f(r) = \ell^*(r) - \ell(r) = -n(r) \int_{\hat{r}}^{r} \epsilon \mathcal{R} \cos\alpha \frac{n'}{n} d\mathcal{R} = -\hat{n}\hat{r}\, n(r) \int_{\hat{r}}^{r} \frac{\epsilon(\mathcal{R}) n'(\mathcal{R})}{n^2(\mathcal{R})} dr \tag{1.13}$$

When n decreases monotonically with r,

$$-\int_{\hat{r}}^{r}\frac{\epsilon n'}{n^2}\,d\hbar \;<\; -\int_{\hat{r}}^{r}\epsilon\, n'\,d\hbar \;=\; \int_{\hat{r}}^{r} n\epsilon'\,d\hbar - \epsilon(r)n(r) \;=\; \int_{\hat{r}}^{r}(n-1)\epsilon'\,d\hbar - \epsilon(r)[n(r)-1]$$

so that

$$\ell^{*}(r) - \ell(r) \;<\; \hat{n}\,\hat{r}\,n(r)\int_{\hat{r}}^{r}(n-1)\,\epsilon'\,d\hbar \;<\; n(r)\hat{n}\,\hat{r}\,\epsilon(r)(\hat{n}-1). \tag{1.14}$$

These bounds should be very close to the actual value when $n \doteq 1$, as in the earth's troposphere.

Note: The basic equation for path length (1.7) derived in this section can also be obtained conveniently using the geometrical variables. Starting with (1.4) and Snell's Law,

$$L = \int\frac{n\,dr}{\sin\alpha} = \int\frac{nr}{\cos\alpha}\,d\theta = \hat{n}\,\hat{r}\int\frac{d\alpha + d\epsilon}{\cos^2\alpha} = \hat{n}\,\hat{r}\tan\alpha + \hat{n}\,\hat{r}\int(1+\tan^2\alpha)d\epsilon$$

$$= \hat{n}\,\hat{r}\tan\alpha + \hat{n}\,\hat{r}\,\epsilon - \int r\sin\alpha\,dn, \text{ using (1.3).}$$

D. Ray Curvature

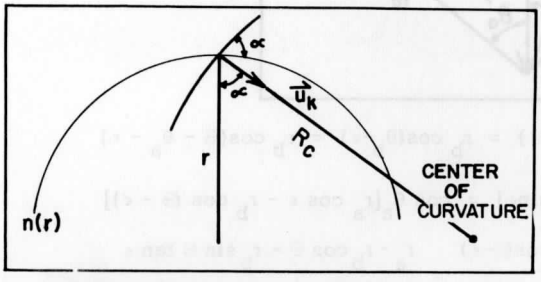

$$\frac{1}{R_C} = \vec{u}_K\cdot\frac{\nabla n}{n} = -\frac{n'(r)}{n(r)}\cos\alpha = -\frac{\hat{n}\,\hat{r}}{n^2 r}\,n'(r). \tag{1.15}$$

$$\epsilon = \int \frac{dr}{R_C \sin\alpha} = \int \frac{ds}{R_C}$$

$$L = \int n R_C \, d\epsilon$$

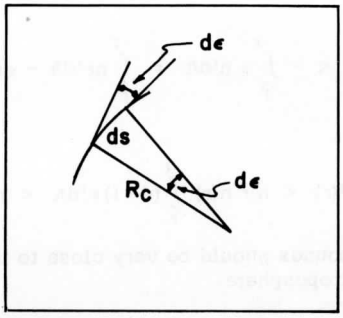

$d\epsilon = ds/R_C$

E. Closest Approach

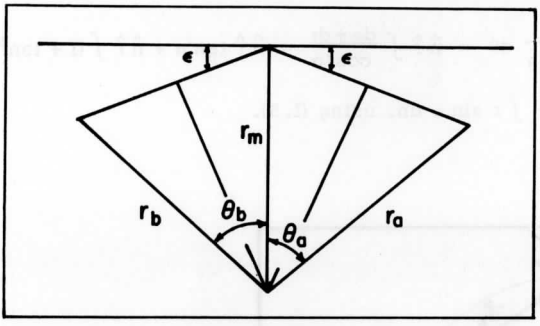

r_a, r_b, and $\Theta = \theta_a + \theta_b$ are assumed known from the orbital data. It is necessary to relate θ_a, θ_b and ϵ in order to determine $\hat{r}$.

$$r_m \cos\epsilon = r_a \cos(\theta_a - \epsilon) = r_b \cos(\theta_b - \epsilon) = r_b \cos(\Theta - \theta_a - \epsilon)$$

$$\sin\theta_a [r_b \sin(\Theta - \epsilon) - r_a \sin\epsilon] = \cos\theta_a [r_a \cos\epsilon - r_b \cos(\Theta - \epsilon)]$$

$$\tan\theta_a = \frac{r_a \cos\epsilon - r_b \cos(\Theta - \epsilon)}{r_b \sin(\Theta - \epsilon) - r_a \sin\epsilon} = \frac{r_a - r_b \cos\Theta - r_b \sin\Theta \tan\epsilon}{r_b \sin\Theta - (r_a + r_b \cos\Theta)\tan\epsilon} \qquad (1.16)$$

Special Cases:

$$\epsilon = 0: \quad \tan\theta_a = \frac{r_a - r_b \cos\Theta}{r_b \sin\Theta}$$

$$\epsilon \text{ small}: \quad \tan\theta_a \doteq \frac{r_a - r_b \cos\Theta - \epsilon r_b \sin\Theta}{r_b \sin\Theta - \epsilon (r_a + r_b \cos\Theta)}$$

$$r_a = r_b : \tan\theta_a = \frac{1 - \cos\Theta - \sin\Theta\tan\epsilon}{\sin\Theta - (1+\cos\Theta)\tan\epsilon} = \tan(\Theta/2), \text{ independent of } \epsilon.$$

$$r_m = r_a \cos(\theta_a - \epsilon)/\cos\epsilon = r_a \cos\theta_a (1 + \tan\theta_a \tan\epsilon)$$

$$\hat{n}\,\hat{r} = r_m \cos\epsilon = r_a \cos(\theta_a - \epsilon) \tag{1.17}$$

Let $\theta_e \equiv \theta_a - \Theta/2 \equiv \theta_a - \vartheta$

$$\tan\theta_e = \frac{\sin(\theta_a - \vartheta)}{\cos(\theta_a - \vartheta)} = \frac{2\sin(\theta_a - \vartheta)\sin(\vartheta - \epsilon)\cos(\vartheta - \epsilon)}{2\cos(\theta_a - \vartheta)\cos(\vartheta - \epsilon)\sin(\vartheta - \epsilon)}$$

$$= \frac{\cos(\theta_a + \epsilon - 2\vartheta) - \cos(\theta_a - \epsilon)}{\cos(\theta_a + \epsilon - 2\vartheta) + \cos(\theta_a - \epsilon)} \cot(\vartheta - \epsilon)$$

But

$$r_a \cos(\theta_a - \epsilon) = r_b \cos[\Theta - (\theta_a + \epsilon)] = r_b \cos(\theta_a + \epsilon - 2\vartheta),$$

so that

$$\tan\theta_e = \tan(\theta_a - \Theta/2) = \left(\frac{r_a - r_b}{r_a + r_b}\right) \cot(\Theta/2 - \epsilon) \tag{1.18}$$

Let $\theta_E \equiv \theta_a - \theta_a(\epsilon = 0)$

$$\tan\theta_E = \frac{[(r_a - r_b\cos\Theta) - r_b\sin\Theta\tan\epsilon]r_b\sin\Theta - (r_a - r_b\cos\Theta)[r_b\sin\Theta - (r_a + r_b\cos\Theta\tan\epsilon]}{r_b\sin\Theta[r_b\sin\Theta - (r_a + r_b\cos\Theta)\tan\epsilon] + (r_a - r_b\cos\Theta)[(r_a - r_b\cos\Theta) - r_b\sin\Theta\tan\epsilon]}$$

$$\tan\theta_E = \frac{(r_a^2 - r_b^2)\tan\epsilon}{r_a^2 + r_b^2 - 2r_a r_b(\cos\Theta + \sin\Theta\tan\epsilon)} = \frac{(r_a^2 - r_b^2)\tan\epsilon}{r_a^2 + r_b^2 - 2r_a r_b\cos(\Theta - \epsilon)/\cos\epsilon} \tag{1.19}$$

F. Summary of Equations

S1.

$$n(r)r\cos\alpha(r) = \hat{n}\,\hat{r}\,; \qquad \alpha(r) = \cos^{-1}(\hat{n}\,\hat{r}/nr)$$

S2.

$$\theta(r) = \alpha(r) + \epsilon(r) = \int \frac{\cot\alpha\, dr}{r} = \hat{n}\hat{r}\int_{\hat{r}}^{r} \frac{d\rho}{\rho(n^2\rho^2 - \hat{n}^2\hat{r}^2)^{\frac{1}{2}}}$$

S3.

$$\epsilon(r) = \int \frac{ds}{R_C} = -\int \cot\alpha \frac{dn}{n} = -\hat{n}\hat{r}\int_{\hat{r}}^{r} \frac{n'(\rho)d\rho}{n(\rho)(n^2\rho^2 - \hat{n}^2\hat{r}^2)^{\frac{1}{2}}}$$

S4.

$$L(r) = \mathcal{L}(r) + \ell(r) = \int \frac{n\, dr}{\sin\alpha} = \int_{\hat{r}}^{r} \frac{n^2(\rho)\rho\, d\rho}{(n^2\rho^2 - \hat{n}^2\hat{r}^2)^{\frac{1}{2}}}$$

S5.

$$\mathcal{L}(r) = (n^2r^2 - \hat{n}^2\hat{r}^2)^{\frac{1}{2}} + \hat{n}\hat{r}\,\epsilon(r)$$

$$= \hat{n}\hat{r}[\tan\alpha + \epsilon(r)] = n(r)r[\sin\alpha + \epsilon(r)\cos\alpha]$$

$$= n\,r\sin\theta[(1 + \epsilon^2/2 - \epsilon^4/8 + \ldots) - \cot\theta(\epsilon^3/3 - \epsilon^5/30 + \ldots)]$$

S6.

$$\ell(r) = -\int r\sin\alpha\, dn = -\int_{\hat{r}}^{r} (n^2\rho^2 - \hat{n}^2\hat{r}^2)^{\frac{1}{2}} \frac{n'(r)}{n(r)} dr$$

S7.

$$L^*(r) - \mathcal{L}(r)/n(r) = r\cos\alpha\,(\tan\epsilon - \epsilon) = r\cos(\theta-\epsilon)(\epsilon^3/3 + 2\epsilon^5/15 + \ldots)$$

$$= r\cos\theta[\epsilon^3/3 - \epsilon^5/30 + \ldots + \tan\theta(\epsilon^4/3 - 4\epsilon^6/45 + \ldots)]$$

S8.

$$\Delta h = r\cos\alpha(\sec\epsilon - n/\hat{n}) = r\cos\theta[(1-n/\hat{n})(1 + \epsilon\tan\theta) + \tfrac{1}{2}\epsilon^2(n/\hat{n}) + \ldots]$$

S9.

$$\ell^*(r) - \ell(r) < \hat{n}\hat{r}\, n(r)\int_{\hat{r}}^{r} [n(r) - 1]\epsilon'(\rho)d\rho$$

S10.

$$1/R_C = -\frac{n'(r)}{n(r)}\cos\alpha(r) = -\frac{\hat{n}\hat{r}}{n^2r}\, n'(r)$$

S11.

$$\tan \theta_a = \frac{r_a \cos \epsilon - r_b \cos(\Theta - \epsilon)}{r_b \sin(\Theta - \epsilon) - r_a \sin \epsilon}$$

S12.

$$\hat{n}\,\hat{r} = r_a \cos[\theta_a - \epsilon(r_a)]$$

S13.

$$\tan(\theta_a - \Theta/2) = \left(\frac{r_a - r_b}{r_a + r_b}\right) \cot(\Theta/2 - \epsilon)$$

S14.

$$\tan(\theta_a - \theta_{ao}) = \frac{(r_a^2 - r_b^2)\tan \epsilon}{r_a^2 + r_b^2 - 2r_a r_b \cos(\Theta - \epsilon)/\cos \epsilon}$$

where $\theta_{ao} = \theta_a$ when $\epsilon = 0$.

II. EVALUATION FOR AN EXPONENTIAL REFRACTIVITY PROFILE

A. Refractivity Profile

$n(r) \equiv 1 + N(r)$ (note absence of 10^{-6} factor)

$N(r) = N_0 e^{-\beta(r - r_0)} = Ne^{-\beta(r - \hat{r})}$, where $\beta = 1/H$

$$n'(r) = N'(r) = -\beta N(r) \tag{2.1}$$

B. Evaluation of the Integrals for ϵ, ℓ, $\ell^* - \ell$

$$\epsilon(r) = -\hat{n}\,\hat{r} \int_{\hat{r}}^{r} \frac{n'(\mathcal{r})d\mathcal{r}}{n(\mathcal{r})(n^2 r^2 - \hat{n}^2\hat{r}^2)^{\frac{1}{2}}} = \hat{n}\,\hat{N}\beta\,\hat{r} \int_{\hat{r}}^{r} \frac{e^{-\beta(\mathcal{r} - \hat{r})}d\mathcal{r}}{n(n^2 r^2 - \hat{n}^2\hat{r}^2)^{\frac{1}{2}}}$$

$$= \hat{n}\,\hat{N}\beta\,\hat{r} \int_{0}^{r-\hat{r}} \frac{e^{-\beta x}dx}{n^2(\hat{r} + x)[2\hat{r}x + x^2 - (\hat{n}^2 - n^2)\hat{r}^2/n^2]^{\frac{1}{2}}} \tag{2.2}$$

$$\ell(r) = -\int_{\hat{r}}^{r} (n^2\mathcal{r}^2 - \hat{n}^2\hat{r}^2)^{\frac{1}{2}} \frac{n'(\mathcal{r})}{n(\mathcal{r})} d\mathcal{r} = \hat{N}\beta \int_{0}^{r-\hat{r}} [2\hat{r}x + x^2 - (\hat{n}^2 n^2)\hat{r}^2/n^2]^{\frac{1}{2}} e^{-\beta x}dx \tag{2.3}$$

$$\ell^*(r) - \ell(r) < \hat{n}\,\hat{r}\,n(r) \int_{\hat{r}}^{r} (n-1)\epsilon'(\hbar)d\hbar$$

$$< (\hat{n}\,\hat{r})^2 n(r)\,\hat{N}^2\beta \int_0^{r-\hat{r}} \frac{e^{-2\beta x}dx}{[2\hat{r}x + x^2 - (\hat{n}^2-n^2)\hat{r}^2/n^2]^{\frac{1}{2}}} \tag{2.4}$$

First Approximation ($n \doteq 1$, $x << 2r$)

Let $R = r - r$, r_s = satellite position.

$$\epsilon(r) \doteq \hat{N}\beta\hat{r} \int_0^{r-\hat{r}} \frac{e^{-\beta x}dx}{(2\hat{r}x)^{\frac{1}{2}}} = \hat{N}\,(\frac{\pi\beta\hat{r}}{2})^{\frac{1}{2}}(\frac{\beta}{\pi})^{\frac{1}{2}} \int_0^R x^{-\frac{1}{2}}\, e^{-\beta x}dx,$$

but

$$(\frac{\beta}{\pi})^{\frac{1}{2}} \int_0^R x^{-\frac{1}{2}}\, e^{-\beta x}dx = \frac{2}{\sqrt{\pi}} \int_0^{\sqrt{\beta R}} e^{-t^2}dt \equiv \mathrm{erf}\sqrt{\beta R}$$

Thus

$$\epsilon(r) \doteq \hat{N}\,(\frac{\pi\beta\hat{r}}{2})^{\frac{1}{2}}\,\mathrm{erf}[\beta(r-\hat{r})]^{\frac{1}{2}} \tag{2.5}$$

$$\epsilon(r_s) \doteq \hat{N}\,(\frac{\pi\beta\hat{r}}{2})^{\frac{1}{2}} \tag{2.6}$$

$$\ell(r) \doteq \int_0^R (2\hat{r}x)^{\frac{1}{2}} e^{-\beta x} = \hat{N}\,(\frac{\pi\hat{r}}{2\beta})^{\frac{1}{2}}\, 2\beta(\frac{\beta}{\pi})^{\frac{1}{2}} \int_0^R x^{\frac{1}{2}}\, e^{-\beta x}dx$$

but

$$2\beta(\frac{\beta}{\pi})^{\frac{1}{2}} \int_0^R x^{\frac{1}{2}}\, e^{-\beta x}dx = \frac{2}{\sqrt{\pi}} \int_0^{\beta R} t^{\frac{1}{2}}\, e^{-t}dt = \mathrm{erf}\sqrt{\beta R} - 2(\frac{\beta R}{\pi})^{\frac{1}{2}} e^{-\beta R}.$$

Thus

$$\ell(r) \doteq \hat{N}\,(\frac{\pi\hat{r}}{2\beta})^{\frac{1}{2}} \{\mathrm{erf}[\beta(r-\hat{r})]^{\frac{1}{2}} - 2[\frac{\beta(r-\hat{r})}{\pi}]^{\frac{1}{2}} e^{-\beta(r-\hat{r})}\} \tag{2.7}$$

$$\ell(r_s) \doteq \hat{N}(\frac{\pi\hat{r}}{2\beta})^{\frac{1}{2}} \doteq \epsilon(r_s)/\beta \tag{2.8}$$

$$\ell^*(r_s) - \ell(r_s) \lesssim \hat{r}^2\hat{N}^2\beta \int_0^{\infty} \frac{e^{-2\beta x}}{(2\hat{r}x)^{\frac{1}{2}}}dx = \hat{N}^2\hat{r}^2\beta(\frac{\pi}{\Delta\beta\hat{r}})^{\frac{1}{2}}$$

$$= \frac{\hat{N}^2\hat{r}}{2}(\pi\beta\hat{r})^{\frac{1}{2}} \doteq \frac{\hat{N}\hat{r}}{\sqrt{2}}\epsilon(r_s) \doteq \frac{\hat{N}\beta\hat{r}}{\sqrt{2}}\ell(r_s). \qquad (2.9)$$

C. Numerical Estimates (Earth's Atmosphere)

$\pi\hat{r}/2 \doteq 10^4$ km; $H \doteq 8$ km; $N_0 \doteq 3(10^{-4})$; $R_s \doteq 300$ km

$\epsilon(r) \doteq 10^2\,\hat{N}\,\beta^{\frac{1}{2}}\,\mathrm{erf}\sqrt{\beta R}$ (see 2.5)

$\epsilon(r_s) \doteq (10^2/H^{\frac{1}{2}})\hat{N} \doteq 35\hat{N} \doteq 10$ mrad for $\hat{r} \doteq r_0$ (see 2.6)

$\ell(r_s) \doteq H\epsilon(r_s) \doteq 80$m (see 2.8)

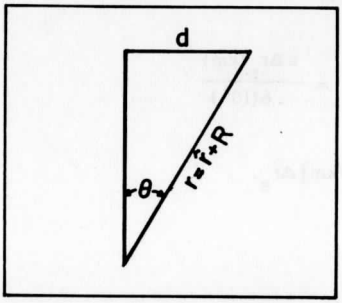

$d \equiv r\sin\theta \doteq (2\hat{r}R+R^2)^{\frac{1}{2}} \doteq (2\hat{r}R)^{\frac{1}{2}}$

$d_s \doteq 2000$ km

$\theta_s \doteq 20°$

$\cos\theta_s \doteq 0.95$; $\tan\theta_s \doteq 0.3$

$\mathcal{L}(r_s) \doteq d_s(1 + \epsilon_s^2/2 - \cot\theta_s\,\epsilon_s^3/3)$ (see S.7)

$d_s\,\epsilon^2/2 \doteq 100$ m

$r_s\cos\theta_s\epsilon^3/3 \doteq 2$ m

$\hat{n}\,\hat{r}\,\epsilon(r_s) \doteq 65$ km (see S.5)

$L^*(r_s) - \mathcal{L}(r_s) \doteq r_s\cos\theta_s\,\epsilon^3/3 \doteq 2$m (see S.7)

$\Delta h_s \doteq r_s\cos\theta_s(1 - n_s/\hat{n} + \epsilon^2/2) \doteq r_0(\hat{N} + \epsilon^2/2) \doteq 2$ km (see S.8)

$\ell^*(r_s) - \ell(r_s) \doteq \hat{N}\beta\,\hat{r}\,\ell(r_s)/\sqrt{2} \doteq 15$ m $\doteq 0.2\,\ell(r_s)$ (see 2.9)

$1/R_c \doteq -n'(r) = \beta N(r) \doteq N/H$ (see S.10)

$$R_{C0} \doteq H/N_0 \doteq 2.5(10^4)\text{km} = 4r_0$$

$$\tan(\theta_a - \Theta/2) = \left(\frac{r_a - r_b}{r_a + r_b}\right)\frac{1 + \tan\Theta/2\,\tan\epsilon}{\tan\Theta/2 - \tan\epsilon} \qquad \text{(see S.13)}$$

$$\doteq \frac{\Delta r_s}{2r_0}\,\frac{1 + \epsilon\,\tan\theta_s}{\tan\theta_s - \epsilon} \doteq \frac{\Delta r_s}{2\,d_s} \doteq \frac{\Delta r_s\,(\text{km})}{4(10^3)}\,, \text{ so for } \Delta r_s \text{ small,}$$

$$\theta_a - \Theta/2 \doteq (.25\ \text{mrad/km})\Delta r_s \doteq (.014°/\text{km})\Delta r_s$$

$$\tan(\theta_a - \theta_{ao}) = \frac{(r_a^2 - r_b^2)\tan\epsilon}{r_a^2 + r_b^2 - 2r_a r_b\cos(\Theta - \epsilon)/\cos\epsilon} \qquad \text{(see S.14)}$$

$$\doteq \frac{\Delta r_s\,\epsilon}{r_s(1 - \cos 2\theta_s)} = \frac{\Delta r_s\,\epsilon}{2r_s\sin^2\theta_s} = \frac{\Delta r_s\,\epsilon}{2d\,\sin\theta_s} \doteq \frac{\epsilon\,\Delta r_s\,(\text{km})}{.6(10^3)}$$

$$\theta_a - \theta_{ao} \doteq (.017\ \text{mrad/km})\Delta r_s \doteq [0.95(10^{-4})°/\text{km}]\,\Delta r_s.$$

D. Accuracy Considerations

In applying the equations derived above to real propagation in the Earth's atmosphere, several sources of error should be considered.

(1) The medium is assumed to be spherically stratified with refractivity decreasing exponentially throughout the region of propagation. There are no inversions, no ducts, no "blobs," no ionosphere. However, the basic character of the real atmosphere is retained, and the assumptions allow an analytical treatment of moderate complexity. The method readily extends to admit large-scale features by assuming local spherical stratification, i.e., a variable origin of coordinates; and by considering piecewise exponential profiles with discretely varying scale height. The assumptions about the medium can be greatly relaxed for testing specific cases by using ray-tracing procedures. However, ray-tracing is a "forward" procedure (structure must be specified initially), and it is therefore difficult to apply to the inversion of propagation data.

(2) The propagation has been characterized by a direct-ray theory. Ground-reflected signals and resulting interference are ignored, although these could be treated by extended ray techniques using reflection and defocusing coefficients. In fact, all amplitude variations in space and time have been ignored. Some features, such as diffraction by the earth, could be calculated separately.

(3) Although the equations derived in section I are exact under the assumptions (1) and (2) above, approximate formulas were derived for ϵ and ℓ in terms of the parameters of the exponential medium and the minimum height of the ray. The errors in these formulas will be investigated below in IIE.

(4) When the equations are applied, some of the quantities will be known, measured or assumed, and the others will be deduced by some procedure. The sensitivity of the deduced variables to variations and errors in the initial variables will in large part determine which quantities are desirable to measure, what measurement and formula accuracies are required, and which equations and procedures are acceptable for practical calculations. Some of these considerations will be explored below.

The candidates for remote measurement are the phase path length $L(\hat{h}, \hat{N}, H)$, and the angle of arrival $\epsilon(\hat{h}, \hat{N}, H)$, although accurate absolute measurements of these variables may be impractical. In addition, the quantities r_a, r_b, Θ of section I.E. must be deduced from orbital data. Note that these latter quantities are not merely position coordinates relative to a fixed point on the earth, but are determined relative to the local center of curvature of the atmospheric strata traversed.

For some combination of values of the above "measured" variables, obtained using two or more satellites, it is desired to deduce the large-scale horizontal and vertical distribution of meteorological variables (e.g., ρ, p, T, e) on a global basis. The more specific problem of the deduction of $\hat{N}$, H, $\hat{h}$ can be studied using the equations derived above.

The Basic Equations

$$\epsilon_s \doteq \hat{N}\left(\frac{\pi \hat{r}}{2H}\right)^{\frac{1}{2}} \doteq N_0\left(\frac{\pi r_0}{2H}\right)^{\frac{1}{2}} e^{-\beta\hat{h}}(1 + \hat{h}/r_0) \doteq \epsilon_0(N_0, H)e^{-\beta\hat{h}} \tag{2.10}$$

$$\ell_s \doteq \hat{N}\left(\frac{\pi \hat{r} H}{2}\right)^{\frac{1}{2}} \doteq H\epsilon_s \doteq \ell_0(N_0, H)e^{-\beta\hat{h}} \tag{2.11}$$

$$\mathcal{L}_s = (n_s^2 r_s^2 - \hat{n}^2\hat{r}^2)^{\frac{1}{2}} + \hat{n}\hat{r}\epsilon_s$$

$$= n_s r_s \sin\theta_s[1 + \epsilon_s^2/2 - \epsilon_s^4/8 + \ldots - \cot\theta_s(\epsilon_s^3/3 - \ldots)] \tag{S.5}$$

The latter equations can be simplified without significant error. First, $n_s = 1 + N_s$, where $N_s \doteq N_0\rho(h_s)/\rho_0 \doteq 3(10^{-4})(3.6)(10^{-11})/1.2 \doteq 10^{-14}$ when $h_s = 300$ km, using density values from the U.S. Standard Atmosphere, 1962. Also,

$d_s \epsilon_s^4/8 \doteq 0.25$ cm, and $r_s \cos\theta_s \epsilon_s^3/3 \doteq 2$m, so that

$$\mathcal{L}_s = (r_s^2 - \hat{n}^2\hat{r}^2)^{\frac{1}{2}} + \hat{n}\hat{r}\epsilon_s \qquad (2.12_a)$$

$$\doteq d_s(1 + \epsilon_s^2/2) - r_s \cos\theta_s \epsilon_s^3/3 \qquad (2.12_b)$$

Eq. (2.12_a) is virtually exact, and (2.12_b) is accurate to within 1 cm using both terms, and within 2m neglecting the last term. Eq. (2.12_b) is much more tolerant of errors when calculating $\mathcal{L}_s$.

$$\Delta\mathcal{L}_s \doteq \hat{r}\Delta\epsilon_s + (r_s/d_s)\Delta h_s - (r_s/d_s - \epsilon_s)\Delta(\hat{n}\hat{r})$$

$$\doteq r_0 \Delta\epsilon_s + \Delta\hat{h}_s/\sin\theta_s - \Delta\hat{h}/\sin\theta_s - r_0\Delta N/\sin\theta_s \text{ from } (2.12_a)$$

while

$$\Delta\mathcal{L}_s \doteq \epsilon_s d_s \Delta\epsilon_s + \Delta d_s \text{ from } (2.12_b).$$

Thus, using (2.12_a), a 1 m error in $\mathcal{L}_s$ results from an error of 1.5 (10^{-4}) mrad in ϵ_s, 0.3 m is h_s or $\hat{h}$, or 0.05 N units in $\hat{N}$. Using (2.12b), 1 m error in $\mathcal{L}_s$ requires about .05 mrad error ϵ, 1 m in d_s, and neither $\hat{N}$ nor $\hat{h}$ need be specified.

In the rest of this discussion, the subscripts will be understood and suppressed.

Sensitivity to Desired Variations. How sensitive are the measurement candidates to the "signal," i.e. changes in $\hat{h}$, $\hat{N}$, H?

$$\left.\begin{aligned}
\left(\frac{\partial\epsilon}{\partial\hat{h}}\right)_{H,N_0} &\doteq -\frac{\epsilon}{H} \doteq -1.2\, e^{-\beta\hat{h}} \text{ mrad/km} \\
\left(\frac{\partial\epsilon}{\partial\hat{N}}\right)_{H,N_0} &\doteq \frac{\epsilon}{\hat{N}} \doteq \frac{\epsilon_0}{N_0} \doteq 0.03 \text{ mrad/N unit} \\
\left(\frac{\partial\epsilon}{\partial\hat{p}}\right)_{H,N_0} &\doteq \frac{\epsilon}{p} = \frac{\epsilon_0}{p_0} \doteq 0.01 \text{ mrad/mb} \\
\left(\frac{\partial\epsilon}{\partial H}\right)_{\hat{h},\hat{N}} &\doteq \frac{-\epsilon}{2H} \doteq -0.6\, e^{-\beta\hat{h}} \text{ mrad/km}
\end{aligned}\right\} \qquad (2.13)$$

$$\left(\frac{\partial \epsilon}{\partial H}\right)_{\hat{h}, N_0} \doteq \frac{-\epsilon}{2H}\left(1 - \frac{2\hat{h}}{H}\right) \doteq -0.6\, e^{-\beta\hat{h}}(1 - 2\hat{h}/H)\text{mrad/km}$$

$$\left(\frac{\partial \epsilon}{\partial \hat{h}}\right)_{H, \hat{N}} \doteq \frac{\epsilon}{2\hat{r}} \doteq .78(10^{-3})e^{-\beta\hat{h}}\ \text{mrad/km}$$

Also, using $L \doteq d(1 + \epsilon^2/2 - \cot\theta_s \epsilon^3/3) + H\epsilon$

$$\left(\frac{\partial L}{\partial \hat{h}}\right)_{H, N_0} \doteq [\epsilon d(1 - \epsilon \cot\theta_s) + H](-\epsilon/H) \doteq -\left(1 + \frac{\epsilon d}{H}\right)\epsilon$$

$$\doteq -(1 + 2.5e^{-\beta\hat{h}})10^{-2}e^{-\beta\hat{h}} = -(1 + 2.5e^{-\beta\hat{h}})\, e^{-\beta\hat{h}}\ \text{cm/m}$$

$$\left(\frac{\partial L}{\partial \hat{N}}\right)_{H, N_0} \doteq \left(1 + \frac{\epsilon d}{H}\right)\frac{\epsilon H}{\hat{N}} \doteq (1 + 2.5e^{-\beta\hat{h}})25\ \text{cm/N unit}$$

$$\left(\frac{\partial L}{\partial \hat{p}}\right)_{H, N_0} \doteq \left(1 + \frac{\epsilon d}{H}\right)\frac{\epsilon H}{p} \doteq (1 + 2.5\, e^{-\beta\hat{h}})8\ \text{cm/mb} \qquad (2.14)$$

$$\left(\frac{\partial L}{\partial H}\right)_{\hat{h}, \hat{N}} \doteq -\left(1 + \frac{\epsilon d}{H}\right)\frac{\epsilon}{2} + \epsilon \doteq (1 - 2.5\, e^{-\beta\hat{h}})(.5)\, e^{-\beta\hat{h}}\ \text{cm/m}$$

$$\left(\frac{\partial L}{\partial H}\right)_{\hat{h}, N_0} \doteq -\left(1 + \frac{\epsilon d}{H}\right)\left(1 - \frac{2\hat{h}}{H}\right)\frac{\epsilon}{2} + \epsilon \doteq [1 + 2\beta\hat{h} - 2.5e^{-\beta\hat{h}}(1 - 2\beta\hat{h})](.5)e^{-\beta\hat{h}}\text{cm/m}$$

$$\left(\frac{\partial L}{\partial \hat{h}}\right)_{H, \hat{N}} \doteq (\epsilon d + H)\frac{\epsilon}{2r} \doteq (1 + 2.5\, e^{-\beta\hat{h}})(.625)\, e^{-\beta\hat{h}}\text{cm/km}$$

These results are summarized as follows:

			Response		Relative Sensitivity
X	ΔX	Fixed	ΔL(cm)	$\Delta\epsilon$ (mrad)	$\Delta L/\Delta\epsilon$ (m/mrad)
$\hat{h}$	10m	H, N_0	$-(25e^{-\beta\hat{h}} + 10)e^{-\beta\hat{h}}$	$-.012e^{-\beta\hat{h}}$	$20e^{-\beta\hat{h}} + 8$
$\hat{h}$	10m	$H, \hat{N}$	$(16e^{-\beta\hat{h}} + 6)10^{-3}e^{-\beta\hat{h}}$	$8(10^{-6})e^{-\beta\hat{h}}$	"
$\hat{N}$	1 N	H, N_0	$62e^{-\beta\hat{h}} + 25$	.03	"
$\hat{p}$	1mb	H, N_0	$20e^{-\beta\hat{h}} + 8$	.01	"
H	10m	$\hat{h}, \hat{N}$	$(-12.5e^{-\beta\hat{h}} + 5)e^{-\beta\hat{h}}$	$-6(10^{-3})e^{-\beta\hat{h}}$	$20e^{-\beta\hat{h}} - 8$
H	10m	$\hat{h}, N_0$	$(-12.5e^{-\beta\hat{h}} + 5)e^{-\beta\hat{h}}$ $+(25e^{-\beta\hat{h}} + 10)\beta\hat{h}e^{-\beta\hat{h}}$	$-6(10^{-3})e^{-\beta\hat{h}}$ $+12(10^{-3})\beta\hat{h}e^{-\beta\hat{h}}$	$20e^{-\beta\hat{h}} - 8\frac{(1 + 2\beta\hat{h})}{(1 - 2\beta\hat{h})}$

							$\hat{N}$ fixed		N_0 fixed	
$\hat{p}$(mb)	$\beta\hat{h}$	$\hat{h}$(km)	$\Delta\hat{h}$/m	$\Delta\hat{h}$/0.1 mrad	$\Delta\hat{N}$/m	$\Delta\hat{p}$/m	ΔH/m	ΔH/0.1 mrad	ΔH/m	ΔH/0.1 mrad
1000	0	0	-29m	-80m	1.1N	3.6mb	-133m	-160m	-133m	-160m
850	.163	1.5	-38	-94	1.2	4.0	-209	-188	-2.23km	-279
700	.357	3	-52	-114	1.4	4.5	-382	-229	+236m	-801
500	.693	5.5	-89	-160	1.7	5.5	-1.60km	-320	+140	+830
300	1.205	10	-191	-267	2.1	7.1	+2.66	-533	+149	+378
150	1.90	15	-485	-533	2.7	9.1	+2.13	-1.07km	+228	+381
50	3.00	25	-1.78km	-1.60	3.3	10.1	+4.57	-3.20	+525	+640

Note: $\Delta\epsilon = 0.1$ mrad results from $\Delta\hat{N} = 3N$ units or $\Delta p = 10$mb, independent of $\hat{h}$.

The second table gives the parameter changes necessary to produce 1 m change in L or 0.1 mrad change in ϵ, for various heights. Several features are revealed by these calculations. First, to resolve differences of 1% in tropospheric refractivity (or density) at the probe height ($\hat{h}$) requires a measurement resolution of better than 1 m in path length, and better than .05 mrad in angle of arrival. Second, the sensitivity of ϵ to changes in $\hat{N}$ is independent of height in an exponential atmosphere, and the sensitivity of L decreases exponentially toward a constant value about 30% of the surface value. Thus the resolvable fraction of the ambient value increases approximately exponentially with height.

Both ϵ and L depend on scale height (H) also. The height dependence of the sensitivity to changes in H is more complicated because of competing effects. First, consider the simplest case of ϵ with $\hat{N}$ and $\hat{h}$ fixed, which considers only the effect of changing the scale height in the region actually traversed by a ray with a particular lowest height. The sensitivity to this kind of change in H decreases exponentially with height. Next, consider N_0 and $\hat{h}$ fixed. Now an increase in H, for example, will increase the value of N at all heights $\hat{h}$ by an amount proportional to $\hat{h}$, so that competing changes occur in the vertical gradient $N' \propto N/H$ at any fixed height $\hat{h}$. For sufficiently large $\hat{h}$, $\Delta N > \Delta H$, so the gradient actually increases. Thus the sensitivity to changes in H with N_0 fixed becomes zero at some height. Increases in H for small $\hat{h}$ will decrease ϵ, but for large $\hat{h}$ will increase ϵ.

The case for L is even more complicated because the bending contributions and the retardation contribution are affected differently by changes in H. For fixed $\hat{N}$ and $\hat{h}$, the former dominates at small heights—the latter at greater heights, again giving a reversal in the sign of the sensitivity. When N_0 and $\hat{h}$ are fixed, the effect described above also occurs, resulting in a rapid change of sensitivity with height in the lowest few km.

The contrasting dependence of ϵ and L on H suggests that H might be isolated by obtaining sufficiently accurate simultaneous values of ϵ and L, and using $L \doteq d + d\epsilon^2/2 + \epsilon H$. This approach will be analyzed below.

Another striking feature of the preceding calculations is the almost total insensitivity of equations (2.10, 11, 12b) to the particular physical height to which $\hat{N}$ applies. A fairly crude guess for $\hat{h}$ does not degrade the relationship between the other variables. The fundamental relation determining the probe height $\hat{h}$ is Snell's law, which may be written

$$(1 + \hat{N})(r_0 + \hat{h}) = r_s \cos(\vartheta - \epsilon_s) \qquad (2.15)$$

From this,

$$\frac{\partial \epsilon_s}{\partial h} \doteq (1 - r_0 \hat{N}/H)/ds$$

$$\doteq .5 - .12e^{-\beta \hat{h}} \text{ mrad/km} \qquad (2.16)$$

Thus, to resolve height to 10 m, a resolution in ϵ of about 5 (10^{-3}) mrad is required. If ϵ is to be deduced from measurements of L,

$$\frac{\partial L}{\partial \epsilon} \doteq \epsilon d + H = 8 + 20e^{-\beta \hat{h}} \text{ m/mrad} \qquad (2.17)$$

The resolution requirement for L becomes about 15 cm at low levels and about 10 cm at mid-troposphere.

Sensitivity to Errors. How accurate must the various quantities be in order to allow the required deductions ?

Adequate sensitivity is a necessary condition, but not sufficient. The deduction procedures must also be relatively insensitive to unavoidable errors in the input variables. The basic relations suggested by the proceeding analysis were (2.10, 11, 12a, 15):

$$L \doteq d + d\epsilon^2/2 + \epsilon H \qquad (B1)$$

$$\epsilon \doteq \hat{N}(\pi \hat{r}/2H)^{\frac{1}{2}} \qquad (B2)$$

$$(1 + \hat{N})(r_0 + \hat{h}) = r_s \cos(\theta_s - \epsilon) \qquad (B3)$$

where $\hat{N}$, $\hat{h}$, and H are to be determined. From these,

$$\Delta L \doteq \Delta d + (\epsilon d + H)\Delta\epsilon + \epsilon \Delta H$$

$$\doteq \Delta d + (8 + 20e^{-\beta \hat{h}})(\text{m/mrad})\Delta\epsilon + 10^{-2} e^{-\beta \hat{h}} \Delta H \qquad (2.18)$$

$$\Delta\epsilon \doteq \epsilon(\Delta\hat{N}/N - \Delta H/2H + \Delta\hat{h}/2\hat{r})$$

$$\doteq \frac{(.03)}{N_{unit}} \Delta\hat{N} - \frac{0.6}{km} e^{-\beta \hat{h}} \Delta H + \frac{0.8}{km}(10^{-3})\, e^{-\beta \hat{h}} \Delta\hat{h} \text{ mrad} \qquad (2.19)$$

$$\Delta\hat{h} \doteq \Delta h_s + d\Delta\epsilon - d\Delta\theta_s - r_0 \Delta\hat{N}$$

$$\doteq \Delta h_s + 2(\text{km/mrad})\Delta\epsilon - 2(\text{km/mrad})\Delta\theta_s - 6(\text{m/N unit})\Delta\hat{N} \qquad (2.20)$$

The following table shows consistent error sets for each basic equation.

Eq.	$\Delta\epsilon$ (mrad)	$\Delta\hat{N}$ (N units)	ΔH (m)	$\Delta\hat{h}$	ΔL or Δd_s
B1	.3		$600 + 240e^{\beta\hat{h}}$		$2.4 + 6\, e^{-\beta\hat{h}}$ cm
	.03		$60 + 24e^{\beta\hat{h}}$		$24 + 60\, e^{-\beta\hat{h}}$ cm
	.003		$6 + 2.4e^{\beta\hat{h}}$		$2.4 + 6\, e^{-\beta\hat{h}}$ cm
				km	
B2	.3	10	$500\, e^{\beta\hat{h}}$	$400\, e^{\beta\hat{h}}$	
	.03	1	$50\, e^{\beta\hat{h}}$	$40\, e^{\beta\hat{h}}$	
	.003	0.1	$5\, e^{\beta\hat{h}}$	$4\, e^{\beta\hat{h}}$	
	$\Delta\epsilon$ or $\Delta\theta_s$			$\Delta\hat{h}$ or Δh_s(m)	Δd_s(m)
B3	.3	100		600	1800
	.03	10		60	180
	.003	1		6	18

(1) Deduction of $\hat{N}$

$\hat{N}$ is rather well specified by values of ϵ and (B2), Crude estimates of $\hat{h}$ will suffice, and values of H are of secondary importance. The major difficulty will probably be in obtaining sufficiently accurate values of ϵ.

(2) Deduction of $\hat{h}$

The probe height $\hat{h}$ can be calculated using (B3) and values of ϵ, $\hat{N}$, and the satellite height and separation h_s, θ_s. The accuracy requirement on $\hat{N}$ is not as demanding as that on ϵ, in view of (B2). The probe height can be defined no better than the satellite height, and the error in half-separation d_s can be about three times larger. These position requirements are not as severe as those required when applying (B1). The accuracy required of ϵ is probably more severe than for (B2).

(3) Deduction of ϵ from L

The high accuracies required of ϵ, particularly for accurate height determination, may well be unfeasible by direct measurement. Fortunately, ϵ can be deduced from measurements of L by using (B1). Errors in L or satellite separation are indistinguishable. Errors in H are of secondary importance, but they become significant when high accuracy in ϵ is required.

(4) Deduction of H

These equations do not uniquely determine H for a single observation of $\hat{h}$, $\hat{N}$ unless ϵ and L are independently determined. Fortunately, deductions of ϵ, $\hat{N}$, $\hat{h}$ from L are not highly sensitive to errors in H. Since H normally varies comparatively slowly with $\hat{h}$, a set of observations having different $\hat{h}$ should yield a well determined set of equations.

If ϵ and L could be independently determined, H could, in principle, be obtained for a single $\hat{h}$ by using (B1) alone. However, this assumes <u>absolute</u> measurements of ϵ, L and d of the accuracies shown in the table, and this may be technically unfeasible. On the other hand, ϵ and L depend on $\hat{h}$ and H rather differently, so that simultaneous measurements of ϵ and L for various $\hat{h}$ may be useful.

The ancient rules regarding numbers of equations and unknowns should always be contemplated in circumstances such as this. There are three independent equations and five primary variables (ϵ, L, $\hat{N}$, $\hat{h}$, H), in addition to two variables specifying satellite location (r_S, θ_S, or $d_S = r_S \sin \theta_S$). These latter two variables include a possible hidden dependence on the local center curvature of the strata. Additional independent values of any of the variables may help to better determine the entire set. For example, although H can be determined from (B1) only with accurate values of ϵ and d as well as L, d can be determined from measurements of ϵ and L and rather rough values of H.

The preceding error analysis deals with absolute values of all variables. The same general arguments apply to relative measurements of L and ϵ In terms of the relative variables (δX),

$$\delta L \doteq \delta d + (\epsilon d + H)\delta\epsilon + \epsilon\delta H$$

$$\delta\epsilon \doteq \epsilon(\delta\hat{N}/\hat{N} - \delta H/2H + \delta\hat{h}/2\hat{r})$$

$$(1 + \delta\hat{N})(r_0 + \delta\hat{h}) \doteq \delta h_s + (\delta\epsilon)d - (\delta\theta_s)d \qquad \text{and from these,}$$

$$\Delta(\delta L) \doteq \{\Delta(\delta d) + (\epsilon d + H)\Delta(\delta H)\} + [(\delta\epsilon)d + \delta H]\Delta\epsilon + (\delta\epsilon)\Delta H + (\delta\epsilon)\epsilon\Delta d$$

$$\Delta(\delta\epsilon) \doteq \{\epsilon[\Delta(\delta\hat{N})/\hat{N} - \Delta(\delta H)/2H + \Delta(\delta\hat{h})/2\hat{r}]\}$$

$$+ \frac{\delta\epsilon}{\epsilon}\Delta\epsilon - \epsilon\left[\frac{\delta\hat{N}\Delta\hat{N}}{\hat{N}^2} - \frac{\delta H\Delta H}{2H^2} + \frac{\delta\hat{h}\Delta\hat{h}}{2\hat{r}^2}\right]$$

$$\Delta\delta\hat{h} \doteq \{\Delta(\delta h_s) + d\Delta(\delta\epsilon) - d(\Delta\delta\theta_s) - r_0\Delta(\delta\hat{N})\} + (\delta\epsilon - \delta\theta_s)\Delta d$$

The expressions in braces relating the difference variables are identical to (2.18, 19, 20) relating the absolute variables, so the same table applies. The remaining error terms are all smaller than these when the relative variables are sufficiently small compared to the absolute variables, and this is true for all reasonable values of the absolute errors. In return for requiring only accurate changes in the measured parameters, only changes in the deduced variables can be determined accurately. They must be "anchored" by an independent measurement if absolute values are required.

Estimates of attainable absolute L measurements are in order. The round-trip travel time is about 25 m sec, so that absolutes measurements of L within 2 m (or $1:10^6$) would require round-trip timing accuracies of 25 n sec. A phase-lock microwave transponding system could resolve relative changes in L of centimeters, and follow small changes in the profile parameters. An additional pulse-transponding capability could provide absolute values of moderate accuracy.

(5) Determination of r_s and θ_s

It is assumed that the heights and angular separation of the satellites relative to some fixed point in the earth will be provided by orbital data, and that these can be referred to the local center of curvature of the strata to provide r_a, r_b and Θ. Either height can be called r_s, and Θ_s can be determined from (S11). If the satellite heights are essentially equal, S13 or S14 can be used efficiently. (See examples, section IIC.)

E. Error Analysis for the Approximate Integrations

The following similar approximations were made in IIB.

$$\text{For } \epsilon_s\text{: } n\int_0^{r_s-\hat{r}} \frac{e^{-\beta x}dx}{n^2(\hat{r}+x)[2\hat{r}x+x^2-(\hat{n}^2-n^2)\hat{r}^2/n^2]^{\frac{1}{2}}} \doteq \left(\frac{\pi}{2\beta\hat{r}}\right)^{\frac{1}{2}}$$

$$\text{For } \ell_s\text{: } \int_0^{r_s-\hat{r}} [2\hat{r}x+x^2-(\hat{n}^2-n^2)\hat{r}^2/n^2]^{\frac{1}{2}} e^{-\beta x}dx \doteq \left(\frac{\pi\hat{r}}{2\beta^3}\right)^{\frac{1}{2}}$$

It is convenient to consider separately four sources of error in these approximations. They are, in order of seriousness, a) extending the integration limit to ∞, b) assuming $n = 1$ outside the radical (ϵ only), c) neglecting x^2, and d) neglecting the term in $\hat{r}^2$.

a) $r_s - \hat{r} \doteq \infty$

$$I_\epsilon = \int_0^{r-r_s} \frac{e^{-\beta x}dx}{(2\hat{r}x)^{\frac{1}{2}}} = (\frac{\pi}{2\beta\hat{r}})^{\frac{1}{2}}[1 - (\frac{\beta}{\pi})^{\frac{1}{2}} \int_{R_s}^{\infty} \frac{e^{-\beta x}}{x^{\frac{1}{2}}} dx]$$

$$I_\ell = \int_0^{r-r_s} (2\hat{r}x)^{\frac{1}{2}} e^{-\beta x}dx = (\frac{\pi\hat{r}}{2\beta^3})^{\frac{1}{2}} [1 - (\frac{4\beta^3}{\pi})^{\frac{1}{2}} \int_{R_s}^{\infty} x^{\frac{1}{2}} e^{-\beta x}dx]$$

$$(\frac{\beta}{\pi})^{\frac{1}{2}} \int_{R_s}^{\infty} x^{-\frac{1}{2}} e^{-\beta x}dx = \frac{e^{-\beta R_s}}{(\pi\beta R_s)^{\frac{1}{2}}} \int_0^{\infty} (1 + t/\beta R_s)^{-\frac{1}{2}} e^{-t}dt$$

$$= \frac{e^{-\beta R_s}}{(\pi\beta R_s)^{\frac{1}{2}}} [1 - \frac{1}{2\beta R_s} + \frac{3}{4\beta^2 R_s^2} - \ldots]$$

$$(\frac{4\beta^3}{\pi})^{\frac{1}{2}} \int_{R_s}^{\infty} x^{\frac{1}{2}} e^{-\beta x}dx = 2(\frac{\beta R_s}{\pi})^{\frac{1}{2}} e^{-\beta R_s} \int_0^{\infty} (1 + t/\beta R_s)^{\frac{1}{2}} e^{-t}dt$$

$$= 2(\frac{\beta R_s}{\pi})^{\frac{1}{2}} e^{-\beta R_s}[1 + \frac{1}{2\beta R_s} - \frac{1}{4\beta^2 R_s^2} + \ldots]$$

Thus

$$I_\epsilon = (\frac{\pi}{2\beta\hat{r}})^{\frac{1}{2}} [1 - \frac{e^{-\beta R_s}}{(\pi\beta R_s)^{\frac{1}{2}}} (1 - \frac{1}{2\beta R_s} + \frac{3}{4\beta^2 R_s^2} - \ldots)] \qquad (2.21)$$

$$I_\ell = (\frac{\pi\hat{r}}{2\beta^3})^{\frac{1}{2}} [1 - 2(\frac{\beta R_s}{\pi})^{\frac{1}{2}} e^{-\beta R_s}(1 + \frac{1}{2\beta R_s} - \frac{1}{4\beta^2 R_s^2} + \ldots)] \qquad (2.22)$$

Assuming $\beta R_s \geq 300$ km/10 km = 30, the respective error terms are about $10^{-13}/10 = 10^{-14}$ and $5(10^{-13})$, which are totally negligible for any application.

b) n = 1 outside the radical for ϵ

$$I_\epsilon = \hat{n} \int_0^{\infty} \frac{e^{-\beta x}dx}{n^2(\hat{r}+x)(2\hat{r}x)^{\frac{1}{2}}} = \frac{\hat{n}}{(2\hat{r})^{\frac{1}{2}}} \int_0^{\infty} x^{-\frac{1}{2}}(1 + \hat{N}e^{-\beta x})^{-2} e^{-\beta x}dx$$

$$= (\frac{\pi}{2\beta\hat{r}})^{\frac{1}{2}}(1+\hat{N})(1 - \sqrt{2}\hat{N} + \sqrt{3}\hat{N}^2 - \ldots) = (\frac{\pi}{2\beta\hat{r}})^{\frac{1}{2}}(1 - .414\hat{N} + .318\hat{N}^2 - \ldots)$$

(2.23)

As $\hat{N} \leq 3.5(10^{-4})$, the error term is less than $1.5(10^{-4})$, and it decreases exponentially with the probe height.

c) $x^2 << 2\hat{r}x$

$$I_\epsilon = \int_0^\infty \frac{e^{-\beta x}dx}{(2\hat{r}x+x^2)^{\frac{1}{2}}} = \frac{1}{(2\hat{r})^{\frac{1}{2}}}\int_0^\infty x^{-\frac{1}{2}}(1 - \frac{x}{4\hat{r}} + \frac{3x^2}{32\hat{r}^2} - \ldots)e^{-\beta x}dx$$

$$= \frac{1}{(2\hat{r})^{\frac{1}{2}}}[\Gamma(\tfrac{1}{2})\beta^{-\frac{1}{2}} - \frac{1}{4\hat{r}}\Gamma(\tfrac{3}{2})\beta^{-3/2} + \frac{3}{32\hat{r}^2}\Gamma(\tfrac{5}{2})\beta^{-5/2} - \ldots]$$

$$= (\frac{\pi}{2\beta\hat{r}})^{\frac{1}{2}}(1 - \frac{1}{8\beta\hat{r}} + \frac{9}{128\beta^2\hat{r}^2} - \ldots) \qquad (2.24)$$

$$I_\ell = \int_0^\infty (2\hat{r}x + x^2)^{\frac{1}{2}}e^{-\beta x}dx = (2\hat{r})^{\frac{1}{2}}\int_0^\infty x^{\frac{1}{2}}(1 + \frac{x}{4\hat{r}} - \frac{x^2}{32\hat{r}^2} + \ldots)e^{-\beta x}dx$$

$$= (2\hat{r})^{\frac{1}{2}}[\Gamma(\tfrac{3}{2})\beta^{-3/2} + \frac{1}{4\hat{r}}\Gamma(\tfrac{5}{2})\beta^{-5/2} - \frac{1}{32\hat{r}^2}\Gamma(\tfrac{7}{2})\beta^{-7/2} + \ldots]$$

$$= (\frac{\pi\hat{r}}{2\beta^3})^{\frac{1}{2}}(1 + \frac{3}{8\beta\hat{r}} - \frac{15}{128\beta^2\hat{r}^2} + \ldots) \qquad (2.25)$$

As $\beta\hat{r} \doteq 900$, the error terms are about $(1.5)10^{-4}$ for ϵ and $5(10^{-4})$ for ℓ, and they are essentially independent of the probe height.

d) Neglect of term in $\hat{r}^2$

$$\frac{\hat{n}^2 - n^2}{n^2} = \frac{[2 + \hat{N}(1 + e^{-\beta x})](1 - e^{-\beta x})\hat{N}}{(1 + \hat{N}e^{-\beta x})^2} \doteq 2\hat{N}(1 - e^{-\beta x})$$

$$I_\epsilon = \int_0^\infty \frac{e^{-\beta x}dx}{[2\hat{r}x - 2\hat{r}^2\hat{N}(1-e^{-\beta x})]^{\frac{1}{2}}} = \frac{1}{(2\hat{r})^{\frac{1}{2}}}\int_0^\infty x^{-\frac{1}{2}}[1 - \hat{N}\beta\hat{r}(\frac{1-e^{-\beta x}}{\beta x})]^{-\frac{1}{2}}e^{-\beta x}dx$$

$$I_\ell = \int_0^\infty [2\hat{r}x - 2\hat{r}^2\hat{N}(1-e^{-\beta x})]^{\frac{1}{2}}e^{-\beta x}dx = (2\hat{r})^{\frac{1}{2}}\int_0^\infty x^{\frac{1}{2}}[1 - \hat{N}\beta\hat{r}(\frac{1-e^{-\beta x}}{\beta x})]^{\frac{1}{2}}e^{-\beta x}dx$$

As the most significant contribution to the integral occurs near $x = 0$, simple bounds on the error factors are $(1 - \hat{N}\beta\hat{r})^{-\frac{1}{2}}$ for ϵ and $(1 - \hat{N}\beta\hat{r})^{\frac{1}{2}}$ for ℓ. However, $\hat{N}\beta\hat{r} \doteq 10^3 \times \hat{N} \lesssim 0.3$, so that these factors are about $(1 + 0.2)$ and $(1 - 0.2)$, respectively. In view of the largeness of these error terms, it is necessary to undertake a more sophisticated analysis of these integrals.

Let $a \equiv \hat{N}\beta\hat{r}$ and $f(x) = (1 - e^{-\beta x})/\beta x$

$$\int_0^\infty x^{-\frac{1}{2}}[1 - af(x)]^{-\frac{1}{2}} e^{-\beta x} dx = \int_0^\infty x^{-\frac{1}{2}}[1 + \frac{1}{2}af + \frac{1\cdot 3}{2\cdot 4} a^2 f^2 + \ldots] e^{-\beta x} dx$$

$$\int_0^\infty x^{\frac{1}{2}}[1 - af(x)]^{\frac{1}{2}} e^{-\beta x} dx = \int_0^\infty x^{\frac{1}{2}}[1 - \frac{1}{2}af - \frac{1\cdot 1}{2\cdot 4} a^2 f^2 - \frac{1\cdot 1\cdot 3}{2\cdot 4\cdot 6} a^3 f^3] e^{-\beta x} dx$$

It is therefore sufficient to evaluate

$$I_{\epsilon R} = \int_0^\infty x^{-\frac{1}{2}} \left(\frac{1-e^{-\beta x}}{\beta x}\right)^k e^{-\beta x} dx \qquad \text{and}$$

$$I_{\ell R} = \int_0^\infty x^{\frac{1}{2}} \left(\frac{1-e^{-\beta x}}{\beta x}\right)^k e^{-\beta x} dx, \qquad k = 1, 2, 3, \ldots$$

This is possible by k successive integrations by parts.

Let $I_k(\beta, p, m) \equiv \int_0^\infty x^{p-1} \left(\frac{1-e^{-\beta x}}{\beta x}\right)^k e^{-m\beta x} dx$

$$= \frac{x^p e^{-m\beta x}}{p-k} \left(\frac{1-e^{-\beta x}}{\beta x}\right)^k \Bigg]_0^\infty + \frac{1}{k-p} \int_0^\infty x^{p-1} \left(\frac{1-e^{-\beta x}}{\beta x}\right)^{k-1} [(k+m)e^{-\beta x} - m] e^{-m\beta x} dx$$

$$= [(k+m) I_{k-1}(\beta, p, m+1) - m I_{k-1}(\beta, p, m)]/(k-p), \qquad p > 0.$$

Temporarily suppressing the arguments of I_k,

$$I_0 = \Gamma(p)(\beta m)^{-p}$$

$$I_1 = \Gamma(p)\beta^{-p}[(1+m)^{1-p} - m^{1-p}]/(1-p)$$

$$I_2 = \Gamma(p)\beta^{-p}[(2+m)^{2-p} - 2(1+m)^{2-p} + m^{2-p}]/[(1-p)(2-p)]$$

$$I_3 = \Gamma(p)\beta^{-p}[(3+m)^{3-p} - 3(2+m)^{3-p} + 3(1+m)^{3-p} + m^{3-p}]/[(1-p(2-p)(3-p)]$$

$$\vdots$$

$$I_k = \Gamma(p)\beta^{-p}[(k+m)^{k-p} - k(k-1+m)^{k-p} + \ldots + (-1)^j \binom{k}{j}(k-j+m)^{k-p} + \ldots + (-1)^k m^{k-p}]/$$

$$/[(1-p)(2-p)\ldots(k-p)]$$

$$I_{\epsilon k} = I_k(\beta, \tfrac{1}{2}, 1) = (\tfrac{\pi}{\beta})^{\frac{1}{2}}[(k+1)^{k-\frac{1}{2}} - k\,k^{k-\frac{1}{2}} + \ldots + (-1)^k]/[\tfrac{1}{2}\cdot\tfrac{3}{2}\ldots\tfrac{2k-1}{2}]$$

$$I_{\ell k} = I_k(\beta, \tfrac{3}{2}, 1) = \tfrac{1}{2}(\tfrac{\pi}{\beta^3})^{\frac{1}{2}}[(k+1)^{k-3/2} - k\,k^{k-3/2} + \ldots + (-1)^k]/[-\tfrac{1}{2}\cdot\tfrac{1}{2}\ldots\tfrac{2k-3}{2}]$$

$$I_\epsilon \equiv (\frac{\pi}{2\beta\hat{r}})^{\frac{1}{2}}[1 + \sum_{k=1}^{\infty} b_k(\hat{N}\beta\hat{r})^k] \equiv (\frac{\pi}{2\beta\hat{r}})^{\frac{1}{2}}[1 + E_\epsilon(\hat{N}\beta\hat{r})]$$

$$I_\ell \equiv (\frac{\pi\hat{r}}{2\beta^3})^{\frac{1}{2}}[1 + \sum_{k=1}^{\infty} c_k(\hat{N}\beta\hat{r})^k] \equiv (\frac{\pi\hat{r}}{2\beta^3})^{\frac{1}{2}}[1 + E_\ell(\hat{N}\beta\hat{r})]$$

where

$$b_k = \frac{1}{k!}[(k+1)^{k-\frac{1}{2}} - k\,k^{k-\frac{1}{2}} + \ldots + (-1)^j\binom{k}{j}(k-j+1)^{k-\frac{1}{2}} + \ldots + (-1)^k]$$

and

$$c_k = \frac{1}{k!}[(k+1)^{k-3/2} - k\,k^{k-3/2} + \ldots + (-1)^j\binom{k}{j}(k-j+1)^{k-\frac{1}{2}} + \ldots + (-1)^k]$$

k	b_k		c_k	
1	$\sqrt{2} - 1$	0.41421	$\frac{1}{2}\sqrt{2} - 1$	-0.29289
2	$\frac{3}{2}\sqrt{3} - 2\sqrt{2} + \frac{1}{2}$	0.26965	$\frac{1}{2}\sqrt{3} - \sqrt{2} + \frac{1}{2}$	-0.04819
3	$\frac{16}{3} - \frac{9}{2}\sqrt{3} + 2\sqrt{2} - \frac{1}{6}$	0.20086	$\frac{4}{3} - \frac{3}{2}\sqrt{3} + \sqrt{2} - \frac{1}{6}$	-0.01720

$$E_\epsilon(\hat{N}\beta\hat{r}) = (.41421)\hat{N}\beta\hat{r} + (.26965)(\hat{N}\beta\hat{r})^2 + (.20086)(\hat{N}\beta\hat{r})^3 + \ldots \qquad (2.26)$$

$$E_\ell(\hat{N}\beta\hat{r}) = -[(.29289)\hat{N}\beta\hat{r} + (.04819)(\hat{N}\beta\hat{r})^2 + (.01720)(\hat{N}\beta\hat{r})^3 + \ldots] \qquad (2.27)$$

These error terms are plotted vs. the probe height in figures of section IIIA. They are on the order of 10% for low probe heights, and decrease nearly exponentially with $\hat{h}$. Also,

$$\Delta E_\epsilon / E_\epsilon \doteq -\Delta E_\ell / E_\ell \doteq \Delta\hat{N}/\hat{N} - \Delta H/H + \Delta\hat{h}/\hat{r}$$

so that the error terms are practically independent of errors in $\hat{h}$, and have the same percentage error as $\hat{N}$ or H.

The errors in ϵ and ℓ due to the approximate formulas are

$$\Delta\epsilon \doteq \epsilon E_\epsilon \doteq 1e^{-2\beta\hat{h}} \text{ mrad}$$

$$\Delta\ell \doteq \ell E_\ell \doteq -8e^{-2\beta\hat{h}} \text{ m}$$

The equivalent errors in L or d in (B1) can be calculated using

$$L \doteq d + \epsilon^2 d/2 + \ell$$

$$\Delta L \text{ or } \Delta d \doteq E_\epsilon \epsilon^2 d + E_\ell \ell \doteq 20e^{-3\beta\hat{h}} - 8e^{-2\beta\hat{h}} \text{ m}$$

The equivalent error in H due to assuming $\ell = \epsilon H$ is

$$\Delta H \doteq H(E_\ell - E_\epsilon) \doteq -0.7\,\hat{N} r_0 \doteq -1.3\, e^{-\beta\hat{h}} \text{ km}$$

The equivalent errors in $\hat{N}$, H, and $\hat{h}$ due to the approximate formula (B2) are

$$\Delta\hat{N} \doteq E_\epsilon \hat{N} \doteq 30e^{-2\beta\hat{h}} \text{ N units}$$

$$\Delta H \doteq -E_\epsilon 2H \doteq -1.6\, e^{-\beta\hat{h}} \text{ km}$$

$$\Delta\hat{h} \doteq E_\epsilon 2\hat{r} \doteq 600\, e^{-\beta h} \text{ km}$$

The effects of the errors given by (2.23, 24, 25) are only 0.1% to 0.5% as large, and can be neglected in comparison. The errors E_ϵ and E_ℓ cannot be neglected when high accuracy is desired.

F. Summary

The basic working equations derived follow:

$$L_s \doteq d_s + \epsilon_s^2 d_s/2 - r_s \cos\theta_s\, \epsilon_s^3/3 + \ell_s \qquad \text{(W1)}$$

$$\epsilon_s = \left(\frac{\pi\hat{r}}{2H}\right)^{\frac{1}{2}} \hat{N}\,(1 + E_\epsilon) \qquad \text{(W2)}$$

$$\ell_s = \left(\frac{\pi \hat{r} H}{2}\right)^{\frac{1}{2}} \hat{N}(1 \quad E_\ell) \tag{W3}$$

$$E_\epsilon \doteq (.41421)\left(\frac{\hat{N}\hat{r}}{H}\right) + (.26965)\left(\frac{\hat{N}\hat{r}}{H}\right)^2 + (20086)\left(\frac{\hat{N}\hat{r}}{H}\right)^3 \tag{W4}$$

$$E_\ell \doteq -\left[(.29289)\left(\frac{\hat{N}\hat{r}}{H}\right) + (.04819)\left(\frac{\hat{N}\hat{r}}{H}\right)^2 + (.01720)\left(\frac{\hat{N}\hat{r}}{H}\right)^3\right] \tag{W5}$$

$$(1 + \hat{N})\hat{r} = r_s \cos(\theta_s - \epsilon_s) \tag{W6}$$

$$N(r) = \hat{N} \exp\left(-\frac{r - \hat{r}}{H}\right), \tag{W7}$$

where r and $\hat{r}$ are measured from the center of curvature of the strata.

$$d_s = r_s \sin \theta_s \tag{W8}$$

where r_s is the distance of a terminal from the center of curvature, and θ_s is the angle, measured at the center of curvature, between the terminal and the point of closest approach of the ray. The angle θ_s can be determined from the distances of the two terminals, their angular separation and ϵ_s by using (S11), (S13) or (S14) of section I–F.

III. EXAMINATION OF THE RELATIONS — GRAPHS

A. Basic Variables (corrected expressions)

The fundamental propagation variables ϵ_s, ℓ_s and L_s can be calculated using (W2), (W3) and (W1), respectively. It is convenient to consider the excess path length $L_e = L - d$. These variables are plotted versus the minimum height of the ray ($\hat{h}$) in figures 1, 2 and 3. The selected values of surface refractivity N_0 and scale height H should encompass most values occurring in the (large-scale) earth's atmosphere. Neither ϵ_s nor ℓ_s depends on satellite separation. Figure 3 assumes a separation of 4000 km (d_s = 2000 km), which corresponds to an orbital height of about 300 km. Note that $L_e \to \ell$ as $\hat{h}$ increases.

B. Errors due to Approximate Integrations

If the first approximations of II–B were used, the errors described by E_ϵ and E_ℓ in (W4) and (W5) would result. These are plotted in figures 4 and 5

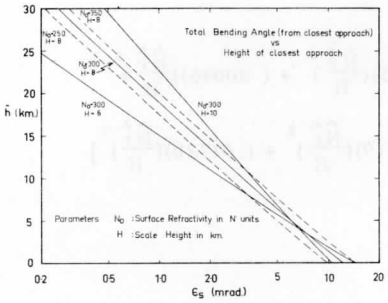

Fig. 1. Total bending angle (ϵ_s) vs. minimum height of ray ($\hat{h}$).

Fig. 2. "Retardation" lengthening (ℓ_s) vs. $\hat{h}$.

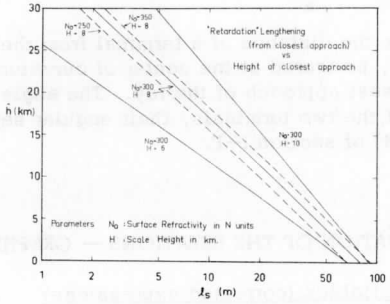

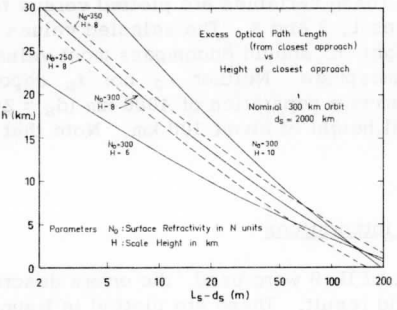

Fig. 3. Excess optical path length ($L_s - d_s$) vs. $\hat{h}$.

for the same parameter values used above. Also plotted in these figures are the errors remaining if only the first correction terms of (W4) and (W5) were used.

The error in L_s due to the errors in ϵ_s and ℓ_s is given by

$$\Delta L_s = \epsilon_s^2 d_s E_\epsilon - r_s \cos\theta_s \epsilon_s^2 E_\epsilon + \ell_s E_\ell$$

Examples are plotted vs. $\hat{h}$ in figure 6. The relative error in excess path length $E_L \equiv \Delta L_s / L_{es}$ is plotted in figure 7. Both figures 6 and 7 assume d_s = 2000 km.

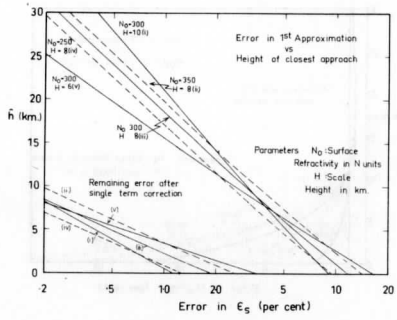

Fig. 4. Errors in ϵ_s (due to approximate integrations) vs. $\hat{h}$.

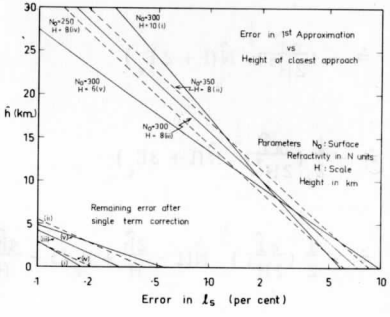

Fig. 5. Errors in ℓ_s vs. $\hat{h}$.

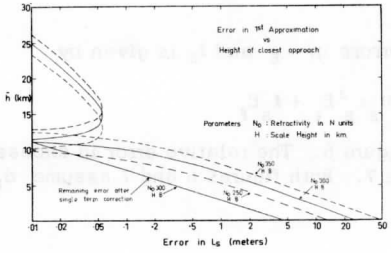

Fig. 6. Absolute errors in L_s vs. $\hat{h}$.

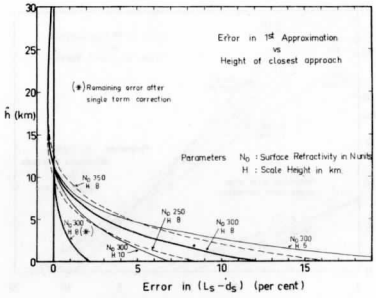

Fig. 7. Relative errors in $(L_s - d_s)$ vs. $\hat{h}$.

C. Sensitivity of the Basic Variables

$$\left(\frac{\partial \epsilon_s}{\partial \hat{h}}\right)_{H, N_0} \doteq -\left(\frac{\pi \hat{r}}{2H^3}\right)^{\frac{1}{2}} \hat{N}(1 + 2E_\epsilon) \tag{3.1}$$

$$\left(\frac{\partial \epsilon_s}{\partial H}\right)_{\hat{h}, \hat{N}} \doteq -\frac{1}{2}\left(\frac{\pi \hat{r}}{2H^3}\right)^{\frac{1}{2}} \hat{N}(1 + 3E_\epsilon) \tag{3.2}$$

$$\left(\frac{\partial \epsilon_s}{\partial H}\right)_{\hat{h}, N_0} \doteq -\frac{1}{2}\left(\frac{\pi \hat{r}}{2H^3}\right)^{\frac{1}{2}} \hat{N}\left[1 - \frac{2\hat{h}}{H} + E_\epsilon\left(3 - \frac{4\hat{h}}{H}\right)\right] \tag{3.3}$$

$$\left(\frac{\partial \epsilon_s}{\partial \hat{N}}\right)_{H, N_0} \doteq \left(\frac{\pi \hat{r}}{2H}\right)^{\frac{1}{2}} (1 + 2E_\epsilon) \tag{3.4}$$

$$\left(\frac{\partial \ell_s}{\partial \hat{h}}\right)_{H, N_0} = -\left(\frac{\pi \hat{r}}{2H}\right)^{\frac{1}{2}} \hat{N}(1 + 2E_\ell) \tag{3.5}$$

$$\left(\frac{\partial \ell_s}{\partial H}\right)_{\hat{h}, \hat{N}} = \frac{1}{2}\left(\frac{\pi \hat{r}}{2H}\right)^{\frac{1}{2}} \hat{N}(1 - E_\ell) \tag{3.6}$$

$$\left(\frac{\partial \ell_s}{\partial H}\right)_{\hat{h}, N_0} = \frac{1}{2}\left(\frac{\pi \hat{r}}{2H}\right)^{\frac{1}{2}} \hat{N}\left[1 + \frac{2\hat{h}}{H} - E_\ell\left(1 - \frac{4\hat{h}}{H}\right)\right] \tag{3.7}$$

$$\left(\frac{\partial \ell_s}{\partial \hat{N}}\right)_{H, N_0} = \left(\frac{\pi \hat{r} H}{2}\right)^{\frac{1}{2}} (1 + 2E_\ell) \tag{3.8}$$

$$\frac{\partial L_s}{\partial X} \doteq \epsilon_s d_s (1 - \epsilon_s \cot \theta_s) \frac{\partial \epsilon_s}{\partial X} + \frac{\partial \ell_s}{\partial X} \tag{3.9}$$

where X denotes $\hat{h}$, H or $\hat{N}$. Note that all sensitivities of L_s approach those of ℓ_s as $\hat{h}$ increases.

Figures 8 and 9 show the sensitivity to changes in $\hat{N}$, the refractive index at the minimum ray height. The primary dependence of the basic variables on the "probe height" $\hat{h}$ occurs implicitly through the dependence of $\hat{N}$ on height. Figures 10 and 11 show the sensitivity to change in $\hat{h}$ for various exponential profiles. As discussed earlier in II. D, the dependence of the variables on scale-height H is somewhat more complicated. The second set of curves in fig. 11 shows the sensitivity of ϵ_s to changes in H in the region traversed by the ray, but with fixed values of $\hat{h}$ and $\hat{N}$. Figure 12 shows the sensitivity to changes in H throughout the entire atmosphere, with N_0 fixed. This latter sensitivity changes sign with height because of competing effect of changes in $\hat{N}$, as described in II. D. Figure 13 shows the sensitivity of ℓ_s and L_s to changes in H for a single typical atmosphere only. Other values of N_0 and H would yield a family of curves as in Fig. 12.

D. Weighting Functions

The measurement candidates are integrals over extended paths. The contribution of various portions of a single ray path will be assessed.

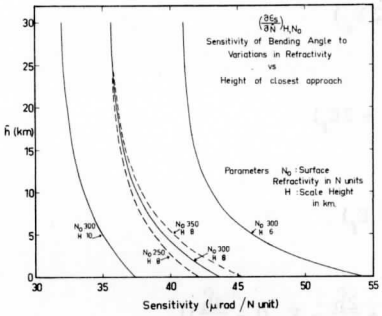

Fig. 8. Sensitivity of ϵ_s to variations in refractivity at $\hat{h}$ ($\hat{N}$) vs. $\hat{h}$.

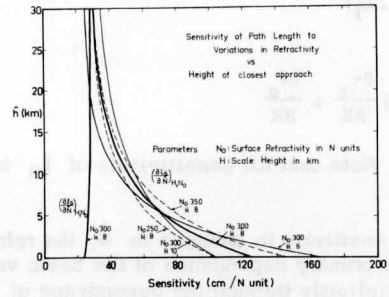

Fig. 9. Sensitivity of L_s and ℓ_s to variations in $\hat{N}$ vs. $\hat{h}$.

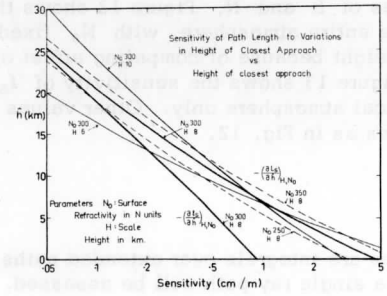

Fig. 10. Sensitivity of L_s and ℓ_s to variations in $\hat{h}$ vs. $\hat{h}$.

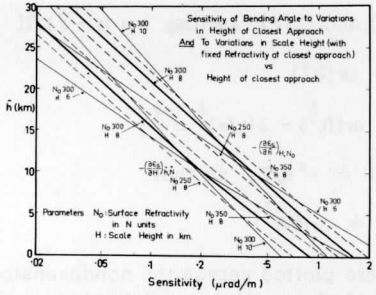

Fig. 11. Sensitivity of ϵ_s to variations in $\hat{h}$ vs. $\hat{h}$; and sensitivity of ϵ_s to variations in scale height (H) vs. $\hat{h}$, ($\hat{N}$ fixed).

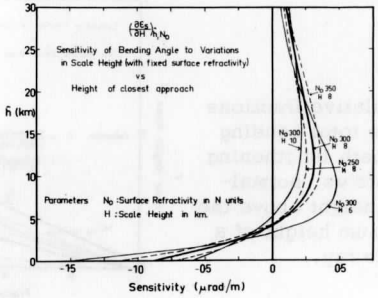

Fig. 12. Sensitivity of ϵ_s to variations in H vs. $\hat{h}$, (N_0 fixed).

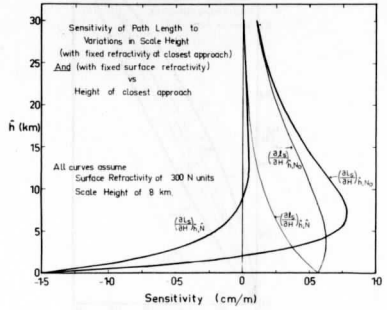

Fig. 13. Sensitivity of L_s and ℓ_s to variations in H vs. $\hat{h}$, ($\hat{N}$ fixed and N_0 fixed).

1. Vertical Dependence

From (2.5) and (2.7), setting $t = (r - \hat{r})/H$

$$\epsilon(r)/\epsilon_s \doteq \mathrm{erf}(t^{\frac{1}{2}}) \tag{3.10}$$

$$\ell(r)/\ell_s \doteq \mathrm{erf}(t^{\frac{1}{2}}) - 2(t/\pi)^{\frac{1}{2}} e^{-t} \tag{3.11}$$

Let $L_\epsilon = \mathscr{L} - d \doteq \epsilon^2 d/2$, so that

$$L_\epsilon(r)/L_{\epsilon s} \doteq \mathrm{erf}^2(t^{\frac{1}{2}}) \tag{3.12}$$

These results are plotted versus the nondimensional height parameter t in figure 14. Figure 15 shows the same data versus $e^{-t} = N/\hat{N}$, which is essentially a pressure or density scale (e.g., $p/\hat{p}$). These results give quantitative meaning to the statement that "most of the effect occurs near the minimum height

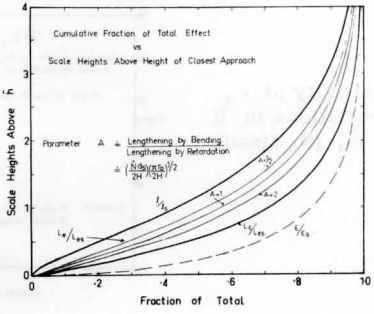

Fig. 14. Cumulative fractions of the total bending and path lengthening effects vs. normalized height above the minimum height of a single ray.

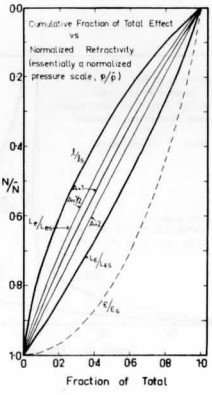

Fig. 15. Cumulative fractions vs. $N/\hat{N}$ (essentially a pressure scale).

of the ray," and allow assessment of the vertical scale of the measurement. For example, figure 14 shows that 50 percent of the bending occurs within H/4 or about 2 km of the low point, and 90 percent occurs in about 10 km. The path lengthening effects, which lie between the two heavy curves of figures 14 and 15, are distributed over a greater height range.

The relative importance of various heights can be seen from the derivatives of the foregoing curves, yielding a type of vertical "weighting function" for these effects.

$$W_\epsilon \equiv \frac{1}{\epsilon_s}\frac{d\epsilon}{dt} \doteq e^{-t}/(\pi t)^{\frac{1}{2}} \tag{3.13}$$

$$W_\ell \equiv \frac{1}{\ell_s}\frac{d\ell_s}{dt} \doteq (2/\pi^{\frac{1}{2}})t^{\frac{1}{2}}\, e^{-t} \tag{3.14}$$

$$W_{L\epsilon} \equiv \frac{1}{L_{\epsilon s}}\frac{dL_\epsilon}{dt} \doteq 2 \operatorname{erf} t^{\frac{1}{2}}\, W_\epsilon \tag{3.15}$$

These results are plotted versus a "height" scale in figure 16, and the corresponding functions (i.e., W/e^{-t}) are plotted versus the "pressure" scale in figure 17. The differences in the heights of importance are striking in these presentations. Especially note that although the total effects ϵ_s and ℓ_s are approximately proportional for different rays (i.e., $\ell_s \doteq H\epsilon_s$), this is by no means true for different points along the same ray. The bending effect ϵ is strongly weighted toward the minimum height, even in terms of mass or pressure internal. The path lengthening is more evenly distributed with height, especially in terms of mass traversed.

The preceding considerations are essentially independent of the satellite geometry, except that satellite separation determines the minimum height of the ray for a given profile. The quantities ϵ/ϵ_s, ℓ/ℓ_s and $L_\epsilon/L_{\epsilon s}$ are essentially independent of the <u>absolute</u> value of $\hat{N}$ or $\hat{h}$, depending only on $(h - \hat{h})/H$, the height above the low point. The total path length L <u>does</u> depend on absolute values, but it is convenient to handle the dependence by introducing a nondimensional parameter A.

$$\text{Let } A = \left(\frac{\hat{N}d_s}{2H}\right)\left(\frac{\pi\hat{r}}{2H}\right)^{\frac{1}{2}}\frac{(1+E_\epsilon)^2}{1+E_\ell} \doteq L_{\epsilon s}/\ell_s \tag{3.16}$$

so that the "excess path length" may be expressed as

$$L_{es} \equiv L_s - d_s \doteq (1+A)\ell_s \tag{3.17}$$

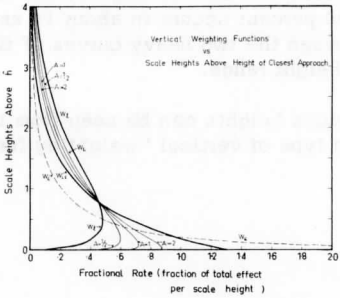

Fig. 16. Vertical weighting functions vs. normalized height above $\hat{h}$.

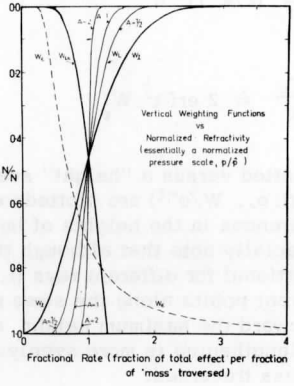

Fig. 17. Vertical weighting functions vs. $N/\hat{N}$.

then
$$\frac{L_e(r)}{L_{es}} = \left(\frac{A}{1+A}\right)\left(\frac{L_\epsilon}{L_{\epsilon s}}\right) + \left(\frac{1}{1+A}\right)\left(\frac{\ell}{\ell_s}\right) \tag{3.18}$$

and
$$W_L \equiv \frac{1}{L_{es}}\frac{dL_e}{dt} = \left(\frac{A}{1+A}\right)W_{L\epsilon} + \left(\frac{1}{1+A}\right)W_\ell \tag{3.19}$$

Thus the pertinent function for L_e are obtained as a weighted average of the corresponding functions for L_ϵ and ℓ.

The parameter A is of order unity for low probe heights, but decreases approximately exponentially toward zero in proportion to $\hat{N}$ (or $\hat{h}$). Reasonable values for A for the earth's atmosphere are shown in figure 18. Examples of the vertical dependence functions (3.18) and (3.19) are included in figures

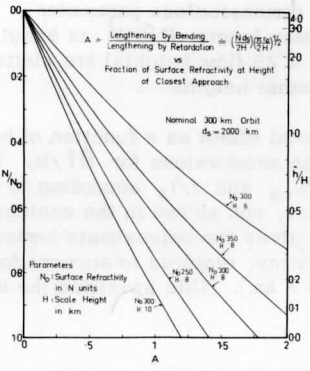

Fig. 18. Dimensionless parameter "A" vs. $\hat{N}/N_0$ (and h/H).

14 - 17 for $A = \frac{1}{2}$, 1, 2. These might correspond, very roughly, to minimum ray heights at 1000 mb, 500 mb, and 300 mb.

Note in particular from figures 15 and 17 that the path lengthening effect is rather uniformly distributed with respect to mass, in striking contrast to the bending effect ϵ. Thus there is much more vertical "smoothing" in a path length measurement. Also, this implies that simultaneous observation of L and ϵ contain information regarding departures of the profile from a pure exponential.

2. Horizontal Dependence

The preceding results can be applied once a relationship between vertical and horizontal ray coordinates is established. Snell's law gives

$$\hat{n}\hat{r} = n r \cos(\theta - \epsilon) = n[(r^2 - d^2)^{\frac{1}{2}} \cos\epsilon + d \sin\epsilon],$$

or $$d^2 - 2(\hat{n}\hat{r} \sin\epsilon/n)d + (\hat{n}\hat{r}/n)^2 - r^2\cos^2\epsilon = 0$$

Since all other quantities are known as a function of height, d may be compared directly:

$$d = \frac{\hat{n}\hat{r}}{n} \sin\epsilon + [2\hat{r}R + R^2 - \hat{r}^2 (\frac{\hat{n}^2}{n^2} - 1)]^{\frac{1}{2}} \cos\epsilon$$

$$\doteq \hat{r}\epsilon + (2\hat{r}R)^{\frac{1}{2}} [1 - \frac{\hat{N}\hat{r}}{R}(1 - e^{-R/H})]^{\frac{1}{2}}$$

It is useful to nondimensionalize using $(2\hat{r}H)^{\frac{1}{2}}$, and $t = R/H$

$$x \equiv \frac{d}{(2\hat{r}H)^{\frac{1}{2}}} \doteq t^{\frac{1}{2}}[1 - \frac{\hat{N}\hat{r}}{H}(\frac{1-e^{-t}}{t})]^{\frac{1}{2}} + (\frac{\pi^{\frac{1}{2}}}{2})(\frac{\hat{N}\hat{r}}{H})(1 + E_\epsilon) \operatorname{erf} t^{\frac{1}{2}}. \qquad (3.20)$$

This expression involves only t and the dimensionless parameter $\hat{N}\hat{r}/H \sim 0.25 \exp(-\hat{h}/H)$. The normalization length $(2\hat{r}H)^{\frac{1}{2}}$ is about 300 km. Curves for $\hat{N}\hat{r}/H = 0$ (great heights) and 0.25 (low heights) are plotted in figure 19, thus bracketing the curves for other heights.

Figure 20 shows the fraction of the total effect as a function of horizontal distance from the low point of a ray for the same values for $\hat{N}\hat{r}/H$. The curves for L_e/L_{es} occur between those for $L_\epsilon/L_{\epsilon s}$ and ℓ/ℓ_s according to the parameter A, exactly as discussed above in D.1, and shown in the analogous figure 15. The scale at the top of figure 20 gives the approximate horizontal distance, centered on the low point of the ray, required to account for a given fraction of the total effect (based on H = 8 km). This specifies the horizontal "scale" of the measurement.

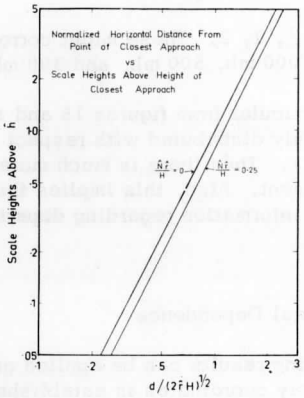

Fig. 19. Normalized horizontal distance from point of closest approach of ray (x) vs. normalized height above $\hat{h}$.

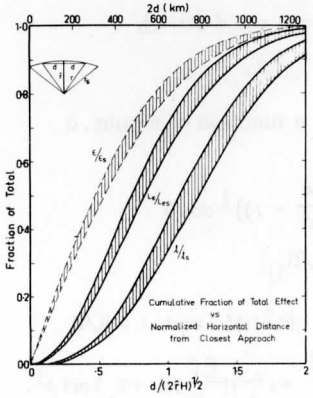

Fig. 20. Cumulative fractions of total bending and path lengthening effects vs. x (and approximate horizontal distance).

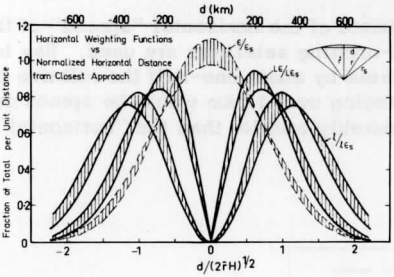

Fig. 21. Horizontal weighting functions vs. x (and approximate horizontal distance)

Figure 21 gives the horizontal weighting functions analogous to the vertical functions of figure 17. They are obtained using

$$W(x) = W(t)/(dx/dt)$$

where x and dx/dt are computed for various t from (3.20), and W(t) is obtained from (3.13, 14, 15). Once again, curves are plotted for $\hat{N}\hat{r}/H = 0$ and 0.25 to bracket the possibilities for various heights , and weighting functions W_L occur between $W_{L\epsilon}$ and W_ℓ according to the values of A. Although W_ϵ, $W_{L\epsilon}$, and W_ℓ all become somewhat "narrower" with increasing height, W_L "broadens" because L_e becomes more like ℓ and less like L_ϵ .

The substantial difference between the important regions for bending and path lengthening is apparent from the figures. In one sense, the difference in the horizontal "scale" of the effects is not as great as might at first appear. For example, half of the bending occurs within about 300 km, centered at the ray low point, while half of the path lengthening occurs within about 400 km, but distributed in two pieces centered symmetrically some 300 km each side of the low point. However, a region of some 700 km in total horizontal extent is still involved.

E. Probe Height versus Satellite Separation

Employing the procedure used to derive (3.20), but with $n_s = 1$,

$$d_s = \hat{n}\hat{r}\sin\epsilon_s + (r_s^2 - \hat{n}^2\hat{r}^2)^{\frac{1}{2}}\cos\epsilon_s$$
$$\doteq (r_0 + \hat{h})\epsilon_s + (h_s - \hat{h} - \hat{N}r_0)^{\frac{1}{2}}(2r_0 + h_s + \hat{h})^{\frac{1}{2}} \qquad (3.21)$$

The relative separation $d_s - d_s(\hat{h} = 0)$ is plotted versus $\hat{h}$ in figure 22 for

satellite heights of 300 and 400 km, assuming a model exponential atmosphere. For comparison, the case for no bending is also plotted for the 300 mb orbit.

Figure 22 also provides an estimate of the horizontal "spread" of the low points of the rays when multiple co-orbiting satellites are used. Ray low-points should be horizontally separated by about one-half the relative satellite separation. Thus, probe heights ranging over 10 km would be spread only about 50 km horizontally, which is considerably smaller than the "horizontal scale" of the measurement.

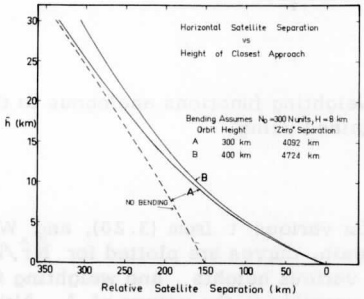

Fig. 22. Horizontal satellite separation vs. minimum ray height.

ACKNOWLEDGMENTS

The author gratefully acknowledges Mr. P. Meyer for assisting with some of the numerical calculations, Miss Y. Smith for typing this manuscript, Mr. B. de Jonk for assisting with some of the drafting, and especially Miss D. Myers for drafting the figures in the text, lettering all of the equations and figures, and generally supervising and editing the preparation of this report.

This research was supported, in part, by the U. S. Department of Commerce, ESSA, under WBG-27.

A COLOR VIEW OF PLANET EARTH

by

Verner E. Suomi and Robert J. Parent

published in

Bulletin of the Amer. Meteor. Soc.
Vol. 49, No. 2, Feb. 1968, pp. 74-83

The cover photo of this issue of the Bulletin is a full color view of the Earth taken by the multicolor spin-scan camera on the applications technology satellite, ATS-3, which is in geosynchronous orbit 22,300 miles over the mouth of the Amazon River. Details of the camera, how it operates and how the color pictures are generated at the Rosman ground station are given in an accompanying article by Wendell Sunderlin, Assistant ATS Project Manager.

This experiment allows us to extend our studies of synoptic and subsynoptic systems of the tropics to the Atlantic as well as the Pacific. Now we also have a superb picture of convective activity over the continental tropics of Central and South America. The purpose of adding the color capability was mainly to help estimate the altitudes of the cloud tops. When one views a cloud in the terminator zone one has a long light path through the atmosphere due to the grazing angle of the solar illumination. Rayleigh scattering causes a change in the ratio of the energy in blue and red portions of the spectrum. Fig. 1 shows observations of this ratio change taken by Kirby Hanson in the clear air above Bancroft Laboratory of the White Mountain Research Station, California. A given blue to red ratio indicates the number of air masses in the path and to convert this to cloud altitude one needs the zenith angle of the radiation to the cloud from the Sun and the zenith angle of the radiation from the cloud to the spacecraft. Both of the angles are known very accurately.

Preliminary results show that the ratios do change in the way expected, but no quantitative estimates of cloud height have yet been made.

A second difference of this camera over the one used in ATS-1 is its wider view angle to include the whole Earth disk. The full view is aesthetically far more pleasing. The full Earth disk also makes accurate navigation on the

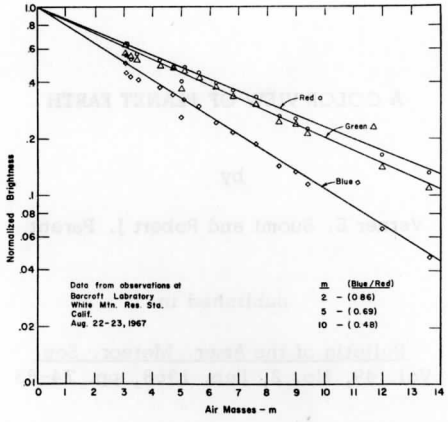

Fig. 1

picture very much easier. One can number the first scan line that intersects the Earth at whichever pole is illuminated. Accurate navigation is essential if one is to measure cloud displacements between pictures in a computer. Displacements of selected clouds can yield winds at cloud level.

In the accompanying article, Dr. Guenter Warnecke has combined photos taken from ATS-1 and ATS-3 into a montage, and has described some of the main weather features which are visible.

We would like to use this opportunity to express our appreciation to the many individuals who made contributions to the camera, the spacecraft, the booster, the launch, the ground station data access, the imaging system, the color photography, and to the program management. These are the individuals who really make these beautiful color photos of the planet Earth possible.

COMPARATIVE PROPERTIES OF SOME TIME-DIFFERENCING SCHEMES FOR LINEAR AND NONLINEAR OSCILLATIONS

by

John A. Young[1]

ABSTRACT

The properties of thirteen computational methods for the integration of first-order differential equations in time are studied. Special attention is given to the representation of periodic fluctuations in a simple spectral baroclinic model of the atmosphere. Errors in the energy, three-dimensional scale, and frequency for linear and nonlinear oscillations are evaluated.

Comparisons of both one-step and two-step methods are made. It is found that the two-step schemes compare favorably with one-step methods only when given the advantage of a smaller time increment. Even then, it is concluded that certain one-step procedures incorporating two or more extrapolations over each constant increment of time produce errors which grow most slowly. With small time increments, these errors are generally made smallest by increasing the number of time extrapolations at each step rather than by decreasing the time increment.

[1] Portions of this study were taken from a Ph. D. thesis submitted to the Department of Meteorology, Massachusetts Institute of Technology.

CONTENTS

1. INTRODUCTION

The continued development of numerical modeling in recent years has produced insight into the mechanisms of various atmospheric phenomena. The broadened spectrum of physical problems has been accompanied by widened investigations into appropriate numerical methods. Impressive advances in the area of space-differencing have resulted [1]. On the other hand, meteorological interest in time-differencing procedures has usually been limited to spectral studies of geophysical circulation models (Bryan [3]; Lorenz [13]; Veronis [17]). However, Lilly [10] has suggested that time-differencing methods will now assume a new significance as a consequence of the advances in space-differencing methods. Developments in this area would appear to be especially important for studies of the large-scale climate and its long-period fluctuations.

The purpose of this paper is to present comparative properties of a number of time-differencing schemes designed to handle atmospheric-like oscillations. To a large extent, the methods considered here supplement those discussed by Kurihara [9] and Lilly [10]. In this paper, major attention is given to "one-step" or "deterministic" schemes whereby the solution at a given time step depends only upon the single state of the system at the preceding time step. Such methods are unlike "multi-step" methods which often produce nonphysical "parasitic" solutions. However, the suppression of truncation errors in one-step methods cannot be accomplished by the use of past solution information, as in the case of multi-step methods. Thus, the deterministic scheme must develop greater accuracy by generating approximate states (usually in the future, through the use of at least one forward-difference). As will be seen later, the extra work often appears to be worth the extra effort for the one-step methods.

In Section 2, the exact linear and nonlinear characteristics of a maximally simplified baroclinic model described by three spectral variables are presented. The comparative performances of ten different one-step computational schemes in this model are given in Section 3. Section 4 demonstrates that reduction of

the time increment Δt is not always the best way to increase accuracy for one-step schemes. Section 5 summarizes the properties of three different two-step methods. Concluding remarks are contained in Section 6.

2. SPECTRAL MODEL OSCILLATIONS

The governing laws for numerical models may often be expressed as a system of first-order ordinary differential equations in time t:

$$\frac{dx_i(t)}{dt} = f_i(x_1, x_2, \ldots, x_M; t) \tag{2.1}$$

Here $i = 1, 2, \ldots M$. The elements x_i denote the dependent variables at specific points in grid-point or wave-number space. Included in the functions f_i are quadratic representations of the energy-conserving advective processes.

With given initial conditions, the finite difference approximation to the system (2.1) yields a solution which eventually departs from the exact solution. A measure of the truncation error is given by the order of the last term in which the Taylor Series expansion of (2.1) and its finite difference form agrees. This order of accuracy characterizes the local generation of error but is not helpful in describing the accumulation of error over a length of time. Instead, we study the computational stability of solutions for a particular numerical model. The stability properties are indicative of integrated errors and hence depend upon the character of the solution itself.

We confine ourselves to studying simple linear and nonlinear systems which exhibit periodic fluctuations. A similar approach has been followed by Lilly [10]. A particularly simple system arises from the spectral form of a two-level quasi-geostrophic model with fixed stability. In the case of adiabatic, frictionless flow, the equations have been given by Lorenz [12]. With slight changes in scaling and definitions, these contain the following energetically complete subset:

$$\frac{d\theta_Z}{dt} = -C(1 + B_Z)^{-1}\theta_W \psi_W$$

$$\frac{d\theta_W}{dt} = +C(1 + B_W)^{-1}(1 + B_Z - B_W)\theta_Z \psi_W$$

$$\frac{d\psi_W}{dt} = -C B_W^{-1}(B_Z - B_W)\theta_Z \theta_W \tag{2.2}$$

Here, ψ and θ are nondimensional representations of the vertically averaged

("barotropic") and vertical shear ("baroclinic") flows, respectively. t is non-dimensional time. The static stability $\bar{\sigma}$ is contained in the parameters $B_Z = \bar{\sigma}\, a_Z^2$ and $B_W = \bar{\sigma}\, a_W^2$, where $a^2 = 1.000$ and $a_W^2 = 1.444444$ are effectively squared wave-numbers. The subscripts Z and W refer to the zonal and wave modes, respectively. C = +0.8002814 is the interaction coefficient for this set.

With $\bar{\sigma} = 0.10$ and initial conditions $\theta_Z(0) = +0.1000$, $\theta_W(0) = +0.0349$, and $\psi_W(0) = 0.0000$, an exact solution to the set (2.2) is given in terms of elliptic functions of time (Lorenz [11]). The solution is

$$\theta_Z(t) = +0.1000\ \mathrm{sn}(ht + K)$$

$$\theta_W(t) = +0.1020\ \mathrm{dn}(ht + K)$$

$$\psi_W(t) = -0.0582\ \mathrm{cn}(ht + K) \qquad (2.3)$$

where K = 2.5046 and h = +0.0406. This solution exhibits growth of the initially small wave disturbance variables θ_W and ψ_W at the expense of θ_Z; θ_Z decreases to zero and then becomes negative. The vertical tilt of the fully developed wave then changes sign, producing a meridional heat flux which brings the system back to its original state after a nondimensional length of time $\frac{4K}{h} = 247.2$.

While this period is the fundamental one for the system, Fourier analysis of the elliptic solutions shows that the nonlinearities produce higher frequencies in abundance (Davis [4]). These high frequencies are associated with transitional time scales much shorter than the fundamental period of oscillation, and arise from the initial wave growth and its subsequent feedback onto the zonal flow. Such sudden changes occurring in the midst of otherwise slow variations provide a stringent test of any computational scheme.

These solutions specify unique amplitudes for each fluctuating variable at all times. For the later computational tests it is convenient to define certain quadratic quantities which do not change in time in the case of the exact solution. The first of these is the sum of the available potential energy and the kinetic energy:

$$E = \frac{1}{2\bar{\sigma}}[\theta_Z^2 + \theta_W^2] + \frac{1}{2}[a_Z^2\theta_Z^2 + a_W^2(\theta_W^2 + \psi_W^2)] \qquad (2.4)$$

The total squared potential vorticity

$$V = [\theta_Z(a_Z^2 + \bar{\sigma}^{-1})]^2 + [\theta_W(a_W^2 + \bar{\sigma}^{-1})]^2 + [\psi_W a_W^2]^2 \qquad (2.5)$$

also a constant, is used with E to define the second quantity S = V/E. S is also invariant; it has the "units" of a_Z^2, a_W^2, or $\bar{\sigma}^{-1}$ and thus is a measure

of the three-dimensional scale of the flow.[2] We see that E and S are physically meaningful parameters which measure the gross amplitude of the system and the spectral distribution of amplitudes, respectively.

It is important to realize that the period of the nonlinear oscillation is not independent of these quantities; with these quadratic interactions, increases in amplitude result in proportionately higher frequencies.[3] To see this, suppose the amplitude of each variable is initially altered by the same multiplicative factor β. Then E and V are altered by β^2, while S remains unchanged. It is evident in the paper by Lorenz [11] that h^2 is proportional to a linear combination of E and V; hence h is increased by the factor β. K is uninfluenced by β. Thus the period $4K/h$ varies as β^{-1}.

The above features are useful tests of computational schemes for a nonlinear system. However, the analysis of a linear system is also helpful, and is more simply accomplished. In the limit $\bar{\sigma} \to \infty$, baroclinic instability of θ_Z is suppressed and the set (2.2) reduces to

$$\frac{d\theta_Z}{dt} = 0$$

$$\frac{d\theta_W}{dt} = -C\left(\frac{a_W^2 - a_Z^2}{a_W^2}\right)\theta_Z\psi_W$$

$$\frac{d\psi_W}{dt} = +C\left(\frac{a_W^2 - a_Z^2}{a_W^2}\right)\theta_Z\theta_W \qquad (2.6)$$

(2.6) is of the linear form

$$\frac{d\chi}{dt} = i\omega\chi \qquad (2.7)$$

where $\chi = \theta_W + i\psi_W$, $i = \sqrt{(-1)}$, and $\omega^2 = C^2\left(\frac{a_W^2 - a_Z^2}{a_W^2}\right)^2\theta_Z^2$.

[2] In barotropic flows such as those considered by Lorenz [11], Lilly [10], and Fjørtoft [5], the "vertical scale" is fixed and S then describes the two-dimensional scale associated with the horizontal flow structure.

[3] This inter-relation appears to provide a mechanism for the rapid growth of errors in the later stages, for by shortening the oscillation period, the amplitude error can grow all the faster having once reached moderate size.

The solution to (2.7) with initial conditions $\chi(0) = \eta$ can be written as $\chi^{(n)} = G^n \eta$ (2.8), where $\chi^{(n)}$ stands for χ evaluated at times $t = t_0 + n\Delta t$. G here has the properties $|G| = 1$ and $\arg(G) = p$. We note that p alone determines the frequency of this linear oscillation; the frequency is thus independent of amplitude $|\eta|$, in contrast to the nonlinear case. $p = (\omega\Delta t)$ is generally small; it measures the constant increment Δt against the period of oscillation $2\pi/\omega$.

Solutions to one-step finite difference analogues of (2.7) are also of the form (2.8), but often exhibit amplification ($|G| > 1$) and a different frequency of oscillation ($\arg(G) \neq p$). For later discussion we define the amplification factor as $|G|$ and the frequency error factor as the leading terms in the expansion of $\arg(G)/p$ in terms of p. $|G|^2$ reflects amplification of energy E, while the scale parameter S in this linear case is a constant.

3. PROPERTIES OF ONE-STEP COMPUTATIONAL METHODS

Table 1 lists and defines the computational methods tested. The names of established methods are stated where known to the author. Nameless methods originated from heuristic considerations and are identified by capital letters. As seen from the table, the first ten methods required information at only one time-step and most were of second order accuracy. Precise estimates of the truncation error, not shown, were usually smaller when the number of evaluations of $f_i(\chi_1, \ldots, \chi_M; t)$ per time-step were increased.

The defining formulas for the methods are indicated in abbreviated form, with $f_i^{(n)}$ standing for $f_i(\chi_1^{(n)}, \ldots, \chi_M^{(n)}; t_0 + n\Delta t)$. Euler's modified method was the only implicit method examined. In practice, a variable number of iterations (4-7) were required to produce convergence of this solution. With one iteration, it reduced to the Heun method, which is the "double-forward" approximation used by Lorenz [13]. The Heun method may also be classified as one of the Runge-Kutta family (Hildebrand [7]).

Method A used the "double-forward" estimate of $\chi_i^{(n+\frac{1}{2})}$ as basis for a subsequent step by a centered-difference rule. Method A' was designed to provide one small time increment $0 \leq \alpha\Delta t \leq \Delta t$ for each fixed double interval $2\Delta t$. In other respects method A' coincided with method A.

Method B was a simplified version of A in that a single forward-difference estimated $\chi_i^{(n+\frac{1}{2})}$, followed by a centered-difference extrapolation. Method C calculated the quadratic terms in f_i following a "geometric-mean" approximation involving $\chi_i^{(n)}$ and a forward-difference estimate of $\chi_i^{(n+1)}$; it differed

Table 1. Defining Characteristics of Some Computational Methods for First-Order Equations. "Steps" denotes the number of initial information time levels required by the procedure. "Order of accuracy" is obtained from a Taylor Series Analysis.

Method (Description)	Steps	Order of Accuracy	Number of f_i Evaluations per Time Step	Formulas or Description	Explicit or Implicit
ONE-STEP METHODS					
1. Euler's modified— (trapezoidal)	1	2	≥ 2	$\chi^{(n+1)} = \chi^{(n)} + \frac{1}{2}[f^{(n)} + f^{(n+1)}]\Delta t$	I
2. Heun— (double forward)	1	2	2	$\chi^{(n+1)*} = \chi^{(n)} + f^{(n)}\Delta t$ $\hat{\chi}^{(n+1)} = \chi^{(n)} + \frac{1}{2}[f^{(n)} + f^{(n+1)*}]\Delta t$	E
3. Method A— (double forward, centered)	1	2	3	$\chi^{(n+\frac{1}{2})*} = \chi^{(n)} + f^{(n)}\Delta t/2$ $\hat{\chi}^{(n+\frac{1}{2})} = \chi^{(n)} + \frac{1}{2}[f^{(n)} + f^{(n+\frac{1}{2})*}]\Delta t/2$ $\tilde{\chi}^{(n+1)} = \chi^{(n)} + \hat{f}^{(n+\frac{1}{2})}\Delta t$	E
4. Method A'— (Method A; Variable Δt)	1	2	3	For even n, $0 \leq \alpha \leq 1$, and $\hat{\chi}$ obtained by Method 2: $\tilde{\chi}^{(n+\alpha)} = \chi^{(n)} + \hat{f}^{(n+\frac{1}{2}\alpha)}\alpha\Delta t$ $\chi^{(n+2)} = \tilde{\chi}^{(n+\alpha)} + \hat{f}^{(n+1+\frac{1}{2}\alpha)}(2-\alpha)\Delta t$	E

(continued on next page)

Table 1 (continued)

Method	Steps	Order of Accuracy	Number of f_i Evaluations per Time Step	Formulas or Description	Explicit or Implicit
5. Method B— (forward, centered)	1	2	2	$\chi^{(n+\frac{1}{2})*} = \chi^{(n)} + f^{(n)}\,\Delta t/2$ $\chi^{(n+1)} = \chi^{(n)} + f^{(n+\frac{1}{2})*}\,\Delta t$	E
6. Method C—	1	2	2	With quadratic $f_i = \sum_{j,k} C_{ijk}\,\chi_j\chi_k$: $\chi_i^{(n+1)} = \chi_i^{(n)} + \frac{1}{2}\sum_{j,k} C_{ijk}[\chi_j^{(n)}\chi_k^{n+1)*} + \chi_j^{(n+1)*}\chi_k^{(n)}]\,\Delta t,$ where $\chi^{(n+1)*} = \chi^{(n)} + f^{(n)}\,\Delta t.$	E
7. Kutta—	1	4	4	$\chi^{(n+\frac{1}{2})*} = \chi^{(n)} + f^{(n)}\,\Delta t/2$ $\bar{\chi}^{(n+\frac{1}{2})} = \chi^{(n)} + f^{(n+\frac{1}{2})*}\,\Delta t/2$ $\chi^{(n+1)**} = \chi^{(n)} + \bar{f}^{(n+\frac{1}{2})}\,\Delta t$ $\chi^{(n+1)} = \chi^{(n)} + \frac{1}{6}[f^{(n)}+2f^{(n+\frac{1}{2})*}+2\bar{f}^{(n+\frac{1}{2})}+f^{(n+1)**}]\Delta t$	E
8. Method D— (two forwards, latest values, reversed variable order)	1	1	2	i assumes successive values i = 1, 2, 3, ... M. $\chi_i^{(n+\frac{1}{2})*} = \chi_i^{(n)} + f_i[\chi_1^{(n+\frac{1}{2})*}, \ldots, \chi_{i-1}^{(n+\frac{1}{2})*}, \chi_i^{(n)}, \ldots, \chi_M^{(n)}]\,\Delta t/2,$ and then with i' = (M+1-i):	E

				$\left\{ x_{i'}^{(n+1)} = x_{i'}^{(n+\frac{1}{2})*} + f_{i'}[x_M^{(n+1)}, \ldots, x_{i'-1}^{(n+1)}, x_{i'}^{(n+\frac{1}{2})*}, \ldots, x_1^{(n+\frac{1}{2})*}] \Delta t/2 \right.$	
9. Method D'—	1	1	2	Same as D except that order of variables assigned to x_i is changed randomly before each new time step.	E
10. Euler— (forward)	1	1	1	$x^{(n+1)} = x^{(n)} + f^{(n)} \Delta t$	E
TWO-STEP METHODS					
11. Adams-Bashforth—	2	2	1	$x^{(n+1)} = x^{(n)} + [\frac{3}{2} f^{(n)} - \frac{1}{2} f^{(n-1)}] \Delta t$	E
12. Centered— (uncorrected)	2	2	1	$x^{(n+1)} = x^{(n-1)} + 2f^{(n)} \Delta t$	
13. Centered— (correction A)	2	2	1	$x^{(n+1)} = x^{(n-1)} + 2f^{(n)} \Delta t$ periodically corrected by method A of Appendix A	E

from the Heun method which used an arithmetic average of these quantities.

The Kutta method used forward-differences, center-differences, and arithmetic averaging to produce a high order of accuracy.

Scheme D consisted of two successive operations at each time step, each similar to a forward difference with time increment $\Delta t/2$. Unlike the simple forward difference, the latest estimates of the variables χ_i were used in evaluating f_i.[4] Thus, in the first operation, f_1 would depend only upon the variables $\chi_1^{(n)}, \ldots, \chi_M^{(n)}$; with $\chi_1^{(n+\frac{1}{2})*}$ determined, f_2 would involve $\chi_1^{(n+\frac{1}{2})*}, \chi_2^{(n)}, \ldots \chi_M^{(n)}$. Finally, $\chi_1^{(n+\frac{1}{2})*}, \ldots \chi_{M-1}^{(n+\frac{1}{2})*}, \chi_M^{(n)}$ would determine f_M and hence $\chi_M^{(n+\frac{1}{2})*}$. The second and final operation consisted of reversing the order in which the variables were solved and then repeating the first operation, starting with the set $\chi_1^{(n+\frac{1}{2})*}, \ldots, \chi_M^{(n+\frac{1}{2})*}$ and obtaining $\chi_1^{(n+1)}, \ldots, \chi_M^{(n+1)}$.

From this description it appears that solutions obtained by method D would usually depend upon the order in which the variables were solved. This could be a disadvantage in a grid-point or wave-number space calculation, for the geometry of the scanning pattern would determine the variable order and hence geometrically bias the solution.

In an attempt to minimize this order bias, scheme D' was invented. It coincided with scheme D except that the order of variables was determined randomly before each new time step. This method appeared to be mainly of academic interest since the programming difficulties would be severe in a system with many degrees of freedom.

The remaining methods shown in Table 1 are well known and are useful in later comparisons. The two-step schemes are discussed in Section 5 and Appendix A.

Let us now examine properties of the one-step schemes as shown in Table 2. Considering the linear oscillation first, we note that amplification factors for many one-step methods involved p to a power at least equal to 4; higher powers corresponded to increased sensitivity of energy errors to a change in Δt. On the other hand, the frequency error was not so sensitive to Δt, except in the highly accurate Kutta scheme.

---

[4] This aspect of method D was related to the Gauss-Seidel iterative method of solving linear systems of algebraic equations.

Most numerical solutions for the nonlinear case were obtained with 24 time increments per period of oscillation. Comparative energy amplification values were found to be in qualitative accord with those of the linear oscillation. However, the shorter internal time scale of the nonlinear solution produced large quantitative differences. Fractional errors in the scale parameter S were much smaller than those in E, but tended to resemble the E errors. Frequency errors exceeded E errors as in the linear case. However, as expected from earlier remarks, comparative frequency errors were not correctly indicated by the linear results; in some cases the fractional frequency error changed significantly with time.

In view of the linear solution properties it is not surprising that the schemes numbered 2, 5, 6 and 10 were inferior to the other more complicated one-step methods when applied to the nonlinear system. Despite its two-part simplicity, scheme D was surprisingly successful in the nonlinear test; as expected, the errors varied with the order in which the three variables were solved. Interestingly, scheme D' with randomized order was comparatively poor.

Results for method A' showed that, given an average value of Δt, the use of variable time increments resulted in increased computational errors for both linear and nonlinear oscillations when applied to method A. Linear analysis suggests that this conclusion is valid for other one-step schemes as well.

Thus, the outstanding one-step methods were those numbered 1, 3, 7 and 8. Further information on these was given by the maximum local errors in E and S. These errors, not shown in Table 2, were confined to the quick-transition periods of the nonlinear solution. They were much larger than the net error in the case of Euler's modified method, despite the increased number of iterations per time step during the transition. On the other hand, the Kutta method exhibited excellent stability in this sense, as expected from its small local truncation error.

4. TIME RESOLUTION VS. COMPLEXITY OF ONE-STEP METHODS

We have noted that those one-step schemes which were most simple calculated at each time step were predictably poor compared to more complicated schemes. However, a natural question is whether a simple one-step scheme used with smaller time increments can compete favorably with these more sophisticated ones.

To test this, four experiments using the simple Euler (forward-difference) method with successively smaller values were performed. With 48 time increments per period, the Euler scheme required about as much computational time as each of the schemes 2, 5, 6, 8 or 9 required with only 24 increments per period. From Table 2 we see that the performance of each of the latter methods

TABLE 2. Properties of one-step computational methods taken from linear analysis and the numerical solutions of nonlinear equations. (Numerical values estimated from linear oscillations with the same period as the nonlinear oscillation are shown in parenthesis. All numerical values are estimates based upon the first several cycles.

Method	Linear Periodic Solution		Nonlinear Periodic Solution						
	Amplification Factor $\|G\|$	Frequency Error Factor	$\frac{\Delta t}{\text{period}}$	$10^3 \times$ Net Fractional Energy Error Per Cycle		$10^3 \times$ Net Fractional Frequency Error per Cycle		$10^4 \times$ Net Fractional Scale Error per Cycle	
1. Euler's modified—	1	$(1 - \frac{p^2}{12} + \ldots)$	1/24	$\leq +.028$	(0)	+46.	(-5.7)	$\leq +.18$	(0)
2. Heun—	$(1 + \frac{p^4}{4})^{\frac{1}{2}}$	$(1 + \frac{p^2}{6} + \ldots)$	1/24	+164.	(+28.)	+162.	(+11.)	+4.9	(0)
			1/48	+13.	(+3.4)	+104.	(+3.)	+0.6	(0)
3. Method A—	$(1 + \frac{p^6}{64})^{1/2}$	$(1 + \frac{p^2}{24} + \ldots)$	1/24	+0.48	(+0.12)	+64.	(+.28)	+0.23	(0)
4. Method A' General α —	$(1 + \frac{\alpha p^6}{64})^{\frac{1}{4}}(1 + \frac{(2-\alpha)p^6}{64})^{\frac{1}{4}}$	$(1 + p^2(\frac{1}{6} - \frac{\alpha}{4} + \frac{\alpha^2}{8}) + \ldots)$	--	----	----	----	----	----	---
$\alpha = 1.0$	$(1 + .0156p^6)^{1/2}$	$(1 + .0417p^2 + \ldots)$	1/24	+0.48	(+0.12)	+64.	(+2.8)	+0.23	(0)
$\alpha = 0.8$	$(1 + .0254p^6 + \ldots)^{1/2}$	$(1 + .0467p^2 + \ldots)$	1/24	+0.75	(+0.19)	+62.	(+3.2)	+0.35	(0)
$\alpha = 0.6$	$(1 + .0592p^6 + \ldots)^{1/2}$	$(1 + .0617p^2 + \ldots)$	1/24	+1.6	(+.45)	+53.	(+4.2)	+0.86	(0)
$\alpha = 0.0$	$(1 + .5000p^6 + \ldots)^{1/2}$	$(1 + .1667p^2 + \ldots)$	1/24	+16.	(+3.8)	{variable: +70. to -180.}	(+11.4)	+7.	(0)
$0 \leq \alpha \leq 1$	$(1 + .1429p^6 + \ldots)^{1/2}$	$(1 + .0834p^2 + \ldots)$	1/24	+14.	(+1.1)	{variable: +90. to -180.}	(+5.7)	+2.3	(0)
5. Method B—	$(1 + \frac{p^4}{4})^{1/2}$	$(1 + \frac{p^2}{6} + \ldots)$	1/24	+158.	(+28.)	+167.	(+11.)	+5.5	(0)

6. Method C—	$(1 + \frac{p^4}{4})^{1/2}$	$(1 + \frac{p^2}{6} + \ldots)$	1/24	+110.	(+28.)	+125.	(+11.)	+5.7	(0)
7. Kutta—	$(1 - \frac{p^6}{72})^{1/2}$	$(1 + \frac{p^4}{8} + \ldots)$	1/24	-0.81	(0.12)	+58.	(+.59)	-0.20	(0)
8. Method D: Order of solution of variables:									
$(\theta_W, \theta_Z, \psi_W)$	1	$(1 + \frac{p^2}{24} + \ldots)$	1/24	+.000	(0)	+54.	(+2.8)	+.000	(0)
$(\psi_W, \theta_W, \theta_Z)$	1	$(1 + \frac{p^2}{24} + \ldots)$	1/24	+.000	(0)	+67.	(+2.8)	+.000	(0)
$(\theta_Z, \psi_W, \theta_W)$	1	$(1 + \frac{p^2}{24} + \ldots)$	1/24	+.000	(0)	+67.	(+2.8)	+.000	(0)
9. Method D': Random Variable Order	1	$(1 + \frac{p^2}{24} + \ldots)$	1/24	+6.7	(0)	+410.	(+2.8)	variably large: ≈ 50	(0)
10. Euler— severe instability commences at:	$(1 + p^2)^{1/2}$	$(1 - p^2/3)$	---	----	---	-----	-----	---	---
cycle 0.7—			1/24	+2,040.	(+3,642.)	+80.	(-22.8)	+300.	(0)
cycle 1.7—			1/48	+1,880.	(+1,200.)	+46.	(-5.7)	+100.	(0)
cycle 2.7—			1/72	+875.	(+690.)	+60.	(-2.5)	+90.	(0)
cycle 4.0—			1/96	+562.	(+480.)	+58.	(-1.4)	+72.	(0)

was clearly superior to the Euler method in this case. Similar equal computational time comparisons made with three-part schemes 3, 4, and 7 lead to the same conclusion. Thus, the Euler method appears inferior to more complex one-step schemes even when it is used with smaller time increments.

An additional experiment was next performed with the Heun method rather than the Euler method. The time resolution was increased to 48 increments per oscillation and results were compared with those of method A used with 24 increments per period. It is seen in Table 2 that method A was superior to the simpler Heun method while demanding only three-quarters as much computational time.

Based on these results it appears that increased time resolution is not the most efficient way to decrease computational errors for one-step schemes. Instead, as suggested by the amplification factors for linear oscillations, accuracy is usually achieved by increasing the number of f_i evaluations per time step.

5. TWO-STEP METHODS

The results discussed in Sections 3 and 4 were confined to one-step methods. To put these in better perspective we now examine the results of similar tests on the commonly used two-step methods defined in Table 1.

We first note that the "extra" time level (n - 1) appeared solely in the function $f_i^{(n-1)}$ for the Adams-Bashforth scheme; only $f_i^{(n)}$ was evaluated in the centered method. This difference was reflected in the solutions to the linear system. For the centered method the solution was

$$\chi^{(n)} = \eta_1 e^{i\theta n} + \eta_2 (-1)^n e^{-i\theta n} \qquad (5.1)$$

where $\tan \theta = p(1 - p^2)^{-1/2}$. η_1 and η_2 were constants which could be determined by $\chi^{(n)}$ and $\chi^{(n-1)}$; Lilly [10] gave their approximate form for a special case.

The first term in (5.1) corresponds to the "physical mode" of the solution, modified by computational errors. The second term is the extraneous "computational mode" introduced by the increased order of the finite-difference method. A characteristic of this mode is its sign alternation at successive time steps. For the centered method, (5.1) shows that the maximum size of the computational mode never decreases as n increases. This is not the case for the Adams-Bashforth method, where the maximum amplitude can be shown to decrease as $(p)^n$. Thus, problems of "starting" and correcting the solution in order to reduce the amplitude of the computational modes appear important only in the case of centered differences. These topics are discussed in Appendix A.

Table 3 presents the quantitative results obtained for the two-step methods. All solutions were started with the values $\chi^{(0)}$ and $\chi^{(1)}$ taken from the exact solution (eqn. 2.3); as discussed in Appendix A, this procedure does not completely exclude the computational mode initially.

We first note that computational mode oscillations (of period $(2\Delta t)$) never appeared in the nonlinear case using the Adams-Bashforth method. On the other hand, such fluctuations in E and S were apparent with the centered methods, and usually exceeded those associated with the physical mode. Correction of the centered method by procedure A did reduce the computational mode, but to a lesser extent than that expected from the linear solutions.

The remainder of Table 3 concerns the characteristics of the physical mode; its errors are the counterparts of those discussed for the one-step schemes in Sections 3 and 4. We first note that the frequency errors exceeded the amplitude errors for linear oscillations as in the one-step methods. This was also true for the nonlinear solutions when the time increments were small; with larger increments the reverse was true, and in two instances severe computational instability resulted.

Comparison with Table 2 shows clearly that, for a given Δt, these two-step methods usually produced larger errors in the physical mode than the one-step schemes. However, considered on an "equal computational time" basis (as in Section 4) the standings of the two-step methods improved. For example, their performance generally surpassed that of the poorer one-step methods 2, 5, 6, or 10. Nevertheless, the two-step methods remained generally inferior to the outstanding one-step methods 3 and 8 in this case.

Table 3 also allows intracomparison of physical mode errors for the two-step methods. In the cases of largest Δt values, the Adams-Bashforth and "corrected-centered" methods were rather poor. However, with smaller Δt values they represented a slight improvement over the "uncorrected-centered method." Considering also the large computational mode errors of the centered schemes, one must conclude that the Adams-Bashforth and "corrected-centered" schemes were superior to the "uncorrected-centered" method.

6. CONCLUDING REMARKS

We have examined the properties of computational schemes applied to a spectral baroclinic model of maximum simplicity whose linear and nonlinear characteristics were known. The performance of computational methods for the linear oscillation was found to be a better indicator of the nonlinear properties than the order of truncation error. However, the truncation error was useful in assessing local errors associated with sudden nonlinear changes in the solution. Largest fractional errors were usually found in the frequency, followed by successively smaller ones in the amplitude and spatial spectrum.

Table 3. Properties of Two-Step Computational Methods Taken From Linear Analysis and the Numerical Solutions of Nonlinear Equations. All numerical values are estimates based upon the first several cycles. Numerical values estimated from linear oscillations with the same period as the nonlinear oscillation are shown in parenthesis. Values for nonlinear oscillation are classified according to estimated "physical mode" and "computational mode" contributions.

Method	Linear Periodic Solution		Nonlinear Periodic Solution									
				Physical Mode						Computational Mode		
	Amplification Factor $\|G\|$	Frequency Error Factor	$\frac{\Delta t}{\text{period}}$	$10^3 \times$ Net Fractional Energy Error per Cycle		$10^3 \times$ Net Fractional Frequency Error per Cycle		$10^4 \times$ Net Fractional Scale Error per Cycle		$10^3 \times$ Max. Fractional Energy Error per Cycle	$10^4 \times$ Max. Fractional Scale Error per Cycle
11. Adams-Bashforth—	$(1 + \frac{p^4}{4} + \ldots)^{1/2}$	$(1 + \frac{5}{12}p^2 + \ldots)$	--	--		--		--		--	--
(severe instability at cycle 1.6)	---	---	1/24	+445.	(+28.)	+158.	(+27.6)	+34.	(0)	0.	0.
			1/48	+25.5	(+3.4)	+101.	(+6.9)	+0.84	(0)	0.	0.
			1/72	+6.45	(+1.0)	+57.	(+3.1)	+0.43	(0)	0.	0.
12. Centered— (uncorrected)	1	$(1 + \frac{p^2}{6})$	--	--		--		--		--	--
(instability beyond cycle 20)	---	---	1/24	bounded by +120.	(0)	+82.	(+11.)	bounded by +65.	(0)	398.	810.
			1/48	bounded by +24.	(0)	+70.2	(+3.)	bounded by +7.5	(0)	190.	410.
			1/72	bounded by +12.	(0)	+62.5	(+1.2)	bounded by +2.5	(0)	110.	230.
13. Centered— (correction A applied each 24 steps)	1	$(1 + \frac{p^2}{6})$	--	--		--		--		--	--
(severe instability at cycle 5.7)	---	---	1/24	bounded by +136.	(0)	+167.	(+11.)	bounded by -50.	(0)	330.	360.
			1/48	bounded by 6.8	(0)	+69.	(+3.)	bounded by -1.36	(0)	53.	110.
			1/72	bounded by +12.0	(0)	+63.	(+1.2)	bounded by +.80	(0)	2.5	77.

For the one-step methods, reduction of long-term errors was usually accomplished most effectively by increasing the number of calculations of the time derivatives at each time step rather than reducing the time increment Δt. The best one-step methods were found to be a four-part Kutta scheme, the three-part scheme A, Euler's modified implicit scheme, and a two-part scheme which utilized the latest values of each ordered variable. Other two-part methods produced larger errors. Also, the use of variable time increments with method A usually resulted in increased local and propagated errors for both types of oscillations.

The two-step methods produced physical-mode errors which were generally larger than most one-step methods with the same time increment. In fact, these two-step schemes compared favorably only when their computational time advantage was sacrificed by using a reduced time increment. In this case, the best of these two-step methods (Adams-Bashforth) was still somewhat inferior to the best one-step methods when compared on an "equal computational time" basis. In all cases both the corrected and uncorrected versions of the centered difference scheme developed relatively large "computational mode" oscillations during the nonlinear phases of the oscillation.

The above conclusions should be accepted with a note of caution. They have been conveniently obtained through study of a small component model. Thus, their validity for systems with many more degrees of freedom is not assured. For example, a large geophysical system undergoing irregular oscillations possesses a variety of individual frequencies which are sustained by nonlinear energy exchanges involving triads of elements similar to that found in section 2. The mechanisms of these transfers are frequency dependent (Phillips [16]), so an accurate portrayal of the fluctuations would demand a numerical scheme with small frequency errors as well as small amplitude errors. Most schemes do not satisfy both of these requirements. This suggests that detailed climatic or energetic studies may require multi-part, one-step schemes, probably from the Runge-Kutta family.

APPENDIX A

STARTING AND CORRECTION PROCEDURES FOR CENTERED DIFFERENCES

The purpose of this appendix is to discuss some procedures for reducing the amplitude of the computational mode associated with the centered difference scheme.

It is convenient to begin with the linear theory. As mentioned in Section 5, η_1 and η_2 are determined by $\chi^{(n)}$, $\chi^{(n-1)}$ and equation (5.1). At the beginning of the computation these relations are given by:

$$\eta_1 = (\chi^{(0)} e^{-i\theta} + \chi^{(1)})/(2 \cos \theta)$$
$$\eta_2 = (\chi^{(0)} e^{+i\theta} - \chi^{(1)})/(2 \cos \theta) \qquad \text{(A.1)}$$

since the initial conditions $\chi^{(0)}$ are known exactly, $\chi^{(1)}$ alone determines η_1 and η_2. The method by which $\chi^{(1)}$ is estimated from $\chi^{(0)}$ may be termed the "starting method."

The tests discussed in Section 5 were all started using the "exact" value of $\chi^{(1)}$; in this way it was believed that initial errors would be minimized. However, this procedure does not eliminate the computational mode completely. This may be seen in the linear case, where the exact solution gives

$$\chi^{(1)} = \chi^{(0)} e^{ip} \qquad \text{(A.2)}$$

Substitution into (A.1) shows that $\eta_2 = \chi^{(0)}(i\frac{p^3}{12} + \ldots)$, and is not zero. This is a characteristic of other multi-step schemes [7, pp. 207], and apparently arises because the phase error $(\theta - p)$ of the centered scheme is not zero. Equations (A.2) and (A.1) also yield $\eta_1 = \chi^{(0)}[1 - i\frac{p^3}{12} + \ldots]$; the associated amplitude error is $O(p^6)$ while the phase error is $O(p^3)$.

These results may be compared with those of the more common starting method which uses a forward-difference to estimate $\chi^{(1)}$:

$$\chi^{(1)} = \chi^{(0)}(1 + ip) \qquad \text{(A.3)}$$

From (A.1) we then obtain

$$\eta_2 = -\chi^{(0)}(\frac{p^2}{4} + \ldots), \qquad \eta_1 = \chi^{(0)}(1 + \frac{p^2}{4} + \ldots).$$

Thus, use of the forward difference in place of the "exact" value produces an initial computational mode amplitude larger by a factor of $(3/p)$. It also produces a larger amplitude error in the physical mode, of $O(p^2)$.

Unfortunately, amplification of the computational mode frequently develops spontaneously in the nonlinear solutions, so that starting procedures alone seem inadequate. In such cases correction procedures may be periodically applied to reduce the computational mode. Two such methods will now be discussed.

"Correction A" was used in the tests discussed in Section 5. It consisted of first averaging the centered-difference solutions $\chi^{(N)}$ and $\chi^{(N-1)}$, followed by forward and backward differences to give the "corrected" values $\hat{\chi}^{(N)}$ and $\hat{\chi}^{(N-1)}$.

$$\hat{\chi}^{(N-\frac{1}{2})} = \frac{1}{2}[\chi^{(N)} + \chi^{(N-1)}]$$

$$\hat{\chi}^{(N)} = \hat{\chi}^{(N-\frac{1}{2})} + \hat{f}^{(N-\frac{1}{2})}\Delta t/2$$

$$\hat{\chi}^{(N-1)} = \hat{\chi}^{(N-\frac{1}{2})} - \hat{f}^{(N-\frac{1}{2})}\Delta t/2 \qquad \text{(A.4)}$$

When (A.4) was applied to the linear system, the "corrected" values η_1 and η_2 were found in terms of the original quantities $\hat{\eta}_1$ and $\hat{\eta}_2$. In this case the results could be expressed as

$$\frac{|\hat{\eta}_2|}{|\eta_2|} < \frac{|\eta_1|}{|\eta_2|}[O(p^3)] + [O(p^4)] \qquad \text{(A.5)}$$

and

$$\frac{|\hat{\eta}_1|}{|\eta_1|} < [1 + O(p^2)] + \frac{|\eta_2|}{|\eta_1|}[O(p)] \qquad \text{(A.6)}$$

(A.5) indicates that the correction would reduce the computational mode amplitude when it was originally large enough ($|\eta_2| > |\eta_1|O(p^3)$). However, this correction could increase the computational mode when it was initially small enough ($|\eta_2| < |\eta_1|O(p^3)$). (A.6) indicates that the correction procedure would usually introduce a small ($O(p^2)$) error into the physical mode.

Let us now consider "correction B," which was not used in Section 5. It consisted of using backward and forward differences from the respective centered-difference solutions $\chi^{(N)}$ and $\chi^{(N-1)}$, followed by averaging of the two estimates then available at each time level:

$$\chi^{(N-1)*} = \chi^{(N)} - f^{(N)}\Delta t$$

$$\chi^{(N)*} = \chi^{(N-1)} + f^{(N-1)}\Delta t$$

$$\hat{\chi}^{(N-1)} = \frac{1}{2}[\chi^{(N-1)} + \chi^{(N-1)*}]$$

$$\hat{\chi}^{(N)} = \frac{1}{2}[\chi^{(N)} + \chi^{(N)*}] \qquad \text{(A.7)}$$

Application of this procedure to the linear system (2.6) gave results nearly the same as those expressed in (A.5, A.6) for correction A.

Finally, corrections A and B were applied to the nonlinear system for the case with 24 time increments per cycle; the results may be seen in Table A1. We first note that both procedures appear to have encouraged a severe compu-

tational instability in the physical mode while suppressing the computational mode. However, this distressing behavior was not true of correction A in cases with smaller time increments (see Section 5).

On the basis of Table A1, correction A appears slightly superior to the correction B in its ability to follow the physical mode. With respect to computational mode oscillations in E and S, correction A was a nearly perfect damping agent. Correction B damped only about 95 percent of these energy oscillations. For this reason, correction A was chosen for the tests of Section 5.

Table A1. Time of Commencement of Severe Computational Instability for Centered Differences Corrected by Methods A and B. Time is given in cycles. $\Delta t = 1/24$ period in all cases.

Number of Steps Between Corrections	Method A	Method B
12	2.8	3.1
24	5.7	3.5
48	10.0	6.1
96	5.3	5.0
192	-	8.3
No correction	> 20.0	> 20.0

ACKNOWLEDGMENTS

Helpful suggestions on portions of this work were received from Prof. N.A. Phillips and Dr. R. T. Williams. Most numerical work was performed in 1964 at the M.I.T. Computation Center. Financial support at M.I.T. was provided by a fellowship from the Ford Foundation. The work at the University of Wisconsin was performed under ESSA grant WBG-27.

REFERENCES

1. A. Arakawa, "Computational Design for Long Term Numerical Integrations of the Equations of Atmospheric Motion," paper presented at 44th Annual Meeting, American Geophysical Union, Washington, D.C., April 1963.

2. F. Baer, "Integration with the Spectral Vorticity Equation," I. Atmos. Sci., Vol. 21, 1964, pp. 260-276.

3. K. Bryan, "A Numerical Integration of Certain Features of the General Circulation," Tellus, Vol. 11, 1959, pp. 163-174.

4. H. T. Davis, Introduction to Nonlinear Differential and Integral Equations, Dover Publications, Inc., New York, N.Y., 1962. 566 pp.

5. R. Fjørtoft, "On the Changes in the Spectral Distribution of Kinetic Energy for Two-Dimensional, Non-Divergent Flow," Tellus, Vol. 5, 1953, pp. 225-230.

6. P. Henrici, Discrete Variable Methods in Ordinary Differential Equations, Wiley and Sons, New York, 1962, 407 pp.

7. F. B. Hildebrand, Introduction to Numerical Analysis, McGraw-Hill Book Co., New York, 1956, 510 pp.

8. R. H. Kraichnan, "A Theory of Turbulent Dynamics," in Second Symp. on Naval Hydrodynamics, ONR, NAS, NRC, Wash., D.C., 1958.

9. Y. Kurihara, "On the Use of Implicit and Iterative Methods for the Time Integration of the Wave Equation," Monthly Weather Review, Vol. 93, No. 1, Jan. 1965, pp. 33-46.

10. D. K. Lilly, "On the Computational Stability of Numerical Solutions of Time Dependent Non-Linear Geophysical Fluid Dynamics Problems," Monthly Weather Review, Vol. 93, No. 1, Jan. 1965, pp. 11-26.

11. E. N. Lorenz, "Maximum Simplification of the Dynamic Equations," Tellus, Vol. 12, 1960, pp. 243-254.

12. E. N. Lorenz, "Simplified Dynamic Equations Applied to the Rotating-Basin Experiments," J. Atmos. Sci., Vol. 19, 1962, pp. 39-51.

13. E. N. Lorenz, "Deterministic Non-Periodic Flow," J. Atmos. Sci., Vol. 20, 1963, pp. 130-141.

14. N. Minorsky, Nonlinear Oscillations, D. Van Nostrand Co., Inc., Princeton, N.J., 1962, 714 pp.

15. J. Pedlosky, "Spectral Considerations in Two-Dimensional Incompressible Flow," Tellus, Vol. 14, 1962, pp. 125-132.

16. O. M. Phillips, The Dynamics of the Upper Ocean, Cambridge at the University Press, Cambridge, 1966, 261 pp.

17. G. Veronis, "An Analysis of Wind-Driven Ocean Circulation with a Limited Number of Fourier Components," J. Atmos. Sci., Vol. 20, 1963, pp. 577-593.

18. J. A. Young, "On the Relation Between Zonal Heating Asymmetries and Large-Scale Atmospheric Fluctuations in Space and Time," Ph. D. Thesis, Dept. of Meteorology, Massachusetts Institute of Technology, 1966, 266 pp.

SOME DISPLAY AND ANALYSIS TECHNIQUES FOR ATS DIGITAL DATA USERS

by

Eric A. Smith and Thomas H. Vonder Haar

CONTENTS

1. INTRODUCTION

This paper describes simple, yet flexible, display and analysis techniques that have been developed for use with the ATS digital data. All of the techniques were designed for scientific applications, although some byproducts are useful for engineering and quality assessment purposes. Standardized programs that can be adapted to any large-core computer allow the scientific user to work directly with the recorded satellite data. Standard data input is from a magnetic tape and the display techniques use an on-line high speed printer and an off-line X-Y plotter. Five types of display and analysis techniques discussed in this paper are shown in the data flow sequence illustrated in Figure 1.

ATS measurements are stored in digital form as brightness values ranging from 0-255 digital counts. These values are directly related to the output voltage of the camera and, in turn, to the effective radiance reflected from the region in view (Peekna et al. (1968)). This same reference and others in Weather Motions From Space discuss the digitizing procedure and other important facts concerning the digital data.

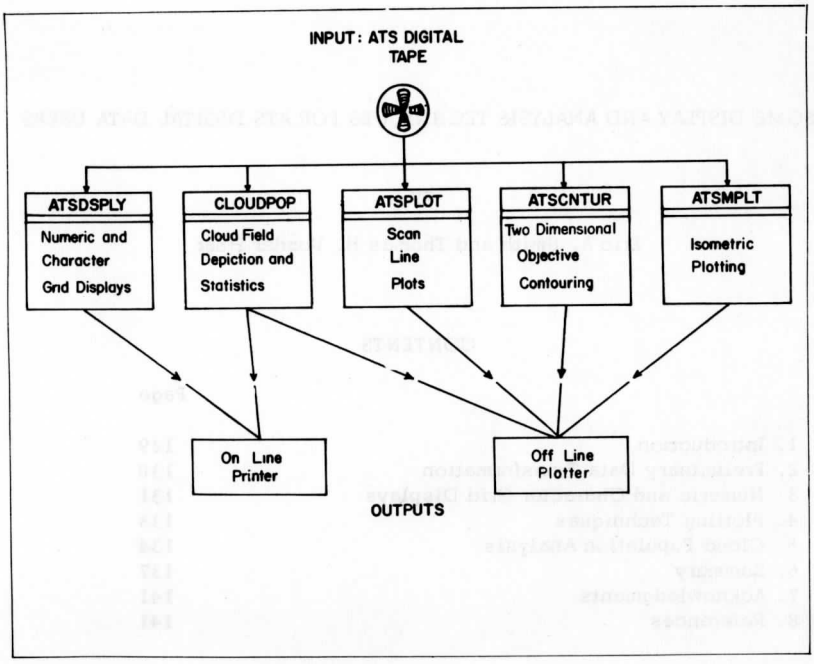

Fig. 1. Data flow sequence for ATS digital data display and analysis programs.

The reference frame used in this paper is the scan line number (increasing from north to south) and the digital element or sample (increasing from west to east).

2. PRELIMINARY DATA TRANSFORMATION

Transformation of the data (from digital counts) is often desired before it is input to the display programs. Methods that are most often required have been integrated in a standardized input package utilized by all the display programs. The features of this "front-end" routine include options to sample or average the data over both elements and scan lines. An enhancement routine is available so that brightness values may be replaced by an enhancement value on a one-to-one basis. This is used not only to improve contrast where needed, but is a method for improving poor quality data if their characteristics are

known. Also available is an option to convert brightness value to their natural logarithm value, which serves to improve separation at the lower end of the brightness scale. Finally, before transferring a prepared data block to a display program, an option is available to output a brightness frequency distribution of the block.

3. NUMERIC AND CHARACTER GRID DISPLAYS

Numeric grid display or numeric posting is a representation of the actual brightness values in a gridded format. The scale size of the output maps is variable, enabling latitude and longitude to be preserved, if required. Although the raw product would not generally be used pictorially, detailed hand analysis can be carried out very effectively because one works with the exact brightness values at camera resolution. Furthermore, if the map is shaded or colored at brightness intervals, or manually contoured at brightness levels, a detailed visual product can be produced.

Character display gridding is another method of displaying the data. In this case printer characters are selected to represent specific brightness intervals so that each data element is displayed by a single character. If the characters are chosen on the basis of size, a very smooth gray scale can be established. In Figure 2 we have displayed a large storm northwest of the Hawaiian Islands. In this illustration we have chosen four brightness levels,

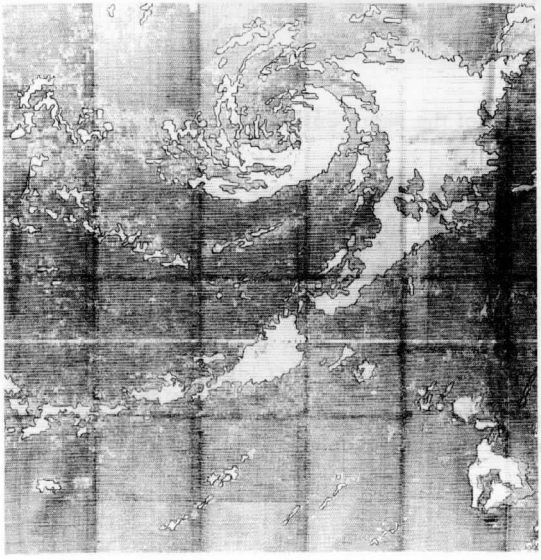

Fig. 2. Character display of a storm to the northwest of the Hawaiian Islands.

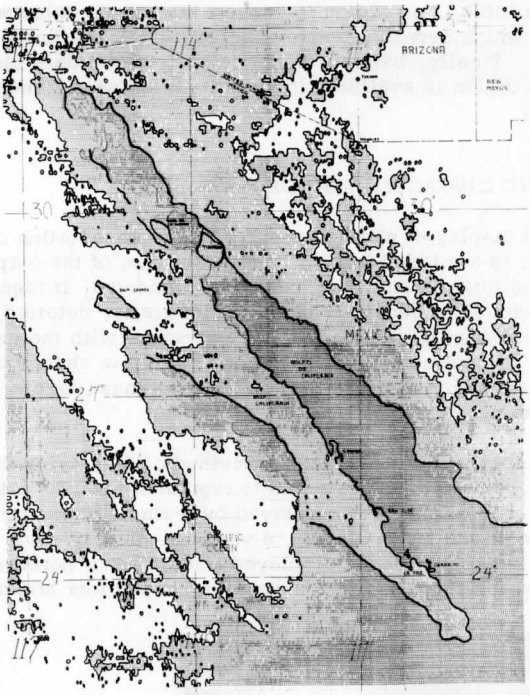

Fig. 3. Character display of the Baja California region.

represented by an asterisk, a slash, a period and a blank. For better contrast, the cloud areas (blanks) have been outlined in black. The cloud-covered islands can be seen in the lower right of the picture and circulation features of the storm are easily spotted. A more carefully analyzed display for the Baja California, region is seen in figure 3. Five brightness intervals have been used, and latitude-longitude lines have been drawn (by hand). A problem with this type of display results from the paper-size factor of the computer product. For example, figure 2 represents 22 sheets of computer paper taped together. The original dimensions of this map were approximately six feet by six feet, which is quite obviously a bulky size to work with. If necessary, this problem can be resolved by use of an off-line X-Y plotting device.

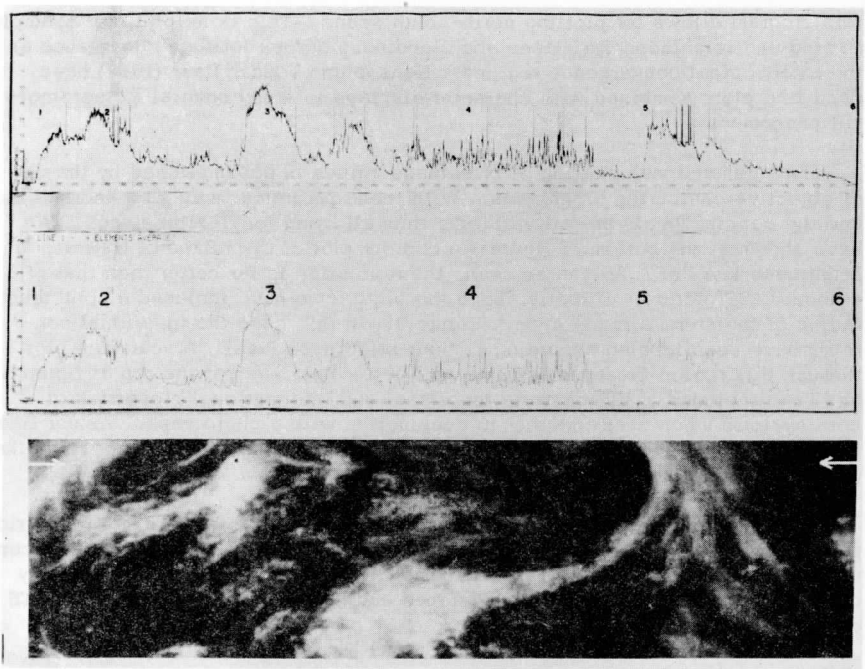

Fig. 4. Scan line plots and photograph of the northern Pacific region

4. PLOTTING TECHNIQUES

In figure 4, an individual scan line (near 60°N) has been displayed by plotting the brightness values of the individual elements. Each sample of the scan line is included in the upper plot, while in the lower plot every four elements were sequentially averaged and the scale expanded for smoothing purposes. The numbered features on the plots correspond to distinctive cloud features on the accompanying enlargement of that ATS photograph. The edge of a cold front moving towards the northwestern coast of the U.S. (feature 5) appears as a sharp rise in brightness, whereas the convective clouds following the front (feature 4) appear as a series of sharp spikes. When used in conjunction with the photographic originals, scan line plots have successfully been used to determine such things as data quality, brightness of characteristic features, and cloud patterns and types. Levanon (1968) is presently able to determine ocean surface characteristics (ultimately winds) from analyzed scan line plots over sun-glint areas of clear or partly cloudy ocean. An option to

this program allows for plotting north-south scans. This is helpful, for example, in studying brightness variations and cloudiness across latitude zones such as the intertropical convergence regions. Hanson and Vonder Haar (1968) have used line plots combined with character displays to study several meteorological phenomena.

Two-dimensional plotting of brightness values is accomplished by the use of objective contouring techniques. With these programs, map size and scaling and the contour levels are all variable, thus allowing for flexible usage. We have shown at the bottom of figure 5 a contour plot of the island of Hawaii, at brightness level 35. As can be seen, the resolution is far better than that of a standard ATS picture. Directly above the picture we have included a contoured region of the storm already seen in figure 2. In this case the individual contours have been labeled according to their brightness level. A scan line plot through this region (heavy black line with lettering), seen at the top of figure 5, has been included to demonstrate the visual and informational properties of both systems when used together in conjunction with a photograph. Vonder Haar et al. (1968) have used the contour maps to study the time variation of ring-like cloud patterns in the tropics.

A three-dimensional technique (in perspective) for plotting an ATS data grid is seen in figure 6. The area represents a typical region of well-developed convection in the tropics. This type of isometric plotting, although qualitatively quite descriptive, is still being developed and has not yet been applied to ATS data in a quantitative fashion.

5. CLOUD POPULATION ANALYSIS

The most versatile program that has been used for quantitative analysis of the digital data utilizes a technique which determines and plots individual cloud boundaries while simultaneously measuring area, mean brightness, and position of these clouds. After the user establishes and inputs the upper and lower brightness threshold values (distinguishing cloud elements from non-cloud elements), the program scans through a data grid, plotting the cloud boundaries and keeping an "information census" on each cloud. Upon completion of the scanning process, individual clouds on the map are given an index number which is referenced in a cloud information program. From this information, a cloud size frequency plot and a cloud mean brightness frequency plot are generated. The percentage of total cloud cover, the mean picture brightness and an element brightness frequency distribution are also computed.

The left of figure 7 shows an area analyzed in this way at three different thresholds. The top map considers as clouds all elements ranging from brightness 35 to 255, the middle map from 50 to 255, the bottom map from 75 to 255. Various cloud masses have been indicated by the letters A-E. In Table 1, we

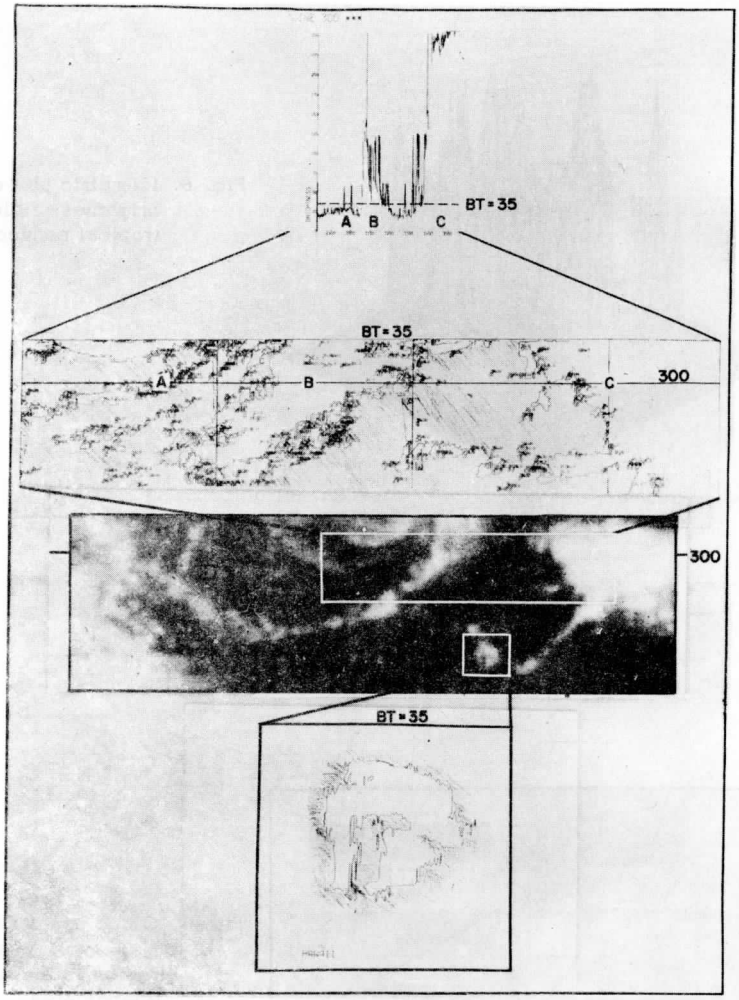

Fig. 5. Contour maps and scan line plot of Hawaiian Island region

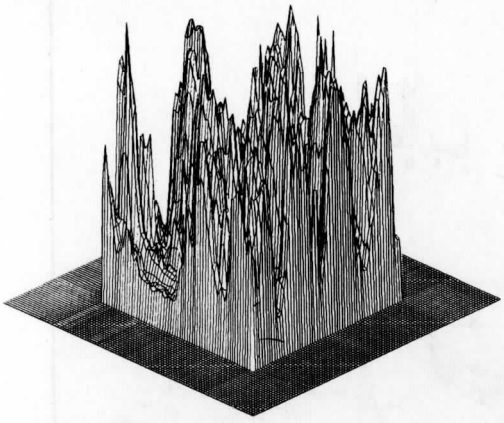

Fig. 6. Isometric plot of the brightness field over tropical convection.

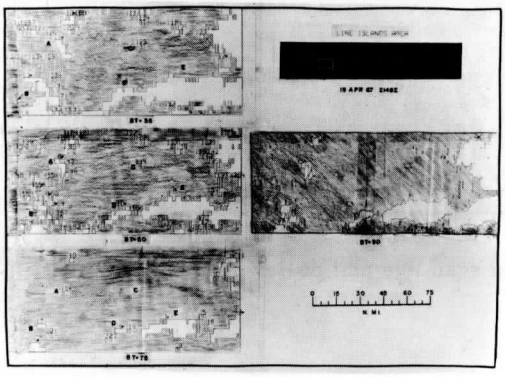

Fig. 7. Cloud population maps of a small region in the Line Islands area.

have prepared from the three cloud information tables generated by the program, a specialized information table associated with all three cloud depiction maps. The column headed ID indicates the individual clouds, as they are found at the three thresholds, for each cloud mass. The mean brightness and area is given for each of these clouds. For example, at BT = 35, cloud mass A is identified by ID = 11* and has a mean brightness of 59 digital counts and an area of 56 square nautical miles. The two brightest portions of this mass are shown at the BT = 75 level to have areas of 2 and 4 sq. n.mi. These small bright areas may identify the thick convective towers from the high and low level clouds associated with them. The letter C marks two small clouds at BT = 35, but at the next level (BT = 50) only one remains and neither of the clouds are brighter than the equivalent of 75 digital counts. Points D and E are related to a large cloud-covered region about 900 sq. n.mi. at the lower brightness threshold. Display at a higher level (BT = 75) yields a 75% reduction in area together with a 25% increase in mean brightness. This indicates that the cloud mass is rather uniform with a slightly brighter center portion and thinning toward the edges. At the right of the figure, a contour analysis at BT = 50 is seen. Although this product is visually more pleasing, it does not provide the wealth of quantitative information that is available with our cloud population process. The region we have displayed is seen in the upper right-hand corner of the figure (outlined in white). The advantage of the display techniques over the standard ATS picture is quite obvious.

By using this technique over time sequenced pictures, change in cloud positions can be measured very accurately. This offers another possibility of inferring the wind field from cloud motion. The advantage of this method over that of a correlative displacement technique for measuring cloud motion, is that the meteorologist can apply human decision during the process. This advantage becomes apparent when studying meso-scale activity, such as individual cloud growth and decay or wave patterns in convergence or divergence regions, when meteorological decision-making is not easily programmable.

6. SUMMARY

The display and analysis techniques discussed in this paper have been developed to aid the scientific utilization of quantitative ATS satellite observations. They have already saved thousands of man-hours of data plotting and analysis. At the same time their flexibility allows and requires frequent input judgment from the scientific users.

Detailed information regarding these techniques and the programs is available from the authors. A program time-cost summary is shown in Table 2.

Table 1. Cloud Statistics Table Associated with Figure 7

(BT = brightness threshold, ID = cloud identification number, $\bar{B}$ = cloud mean brightness, A = cloud area)

REGION	BT	ID	$\bar{B}$	A (Sq. n. mi.)
A	35	11*	59	56
	50	6*	61	32
		143	79	8
		146	56	2
	75	13	79	2
		14	101	4
B	35	13*	64	210
	50	8*	87	78
		9*	73	18
		Others		
	75	17	95	12
		20	89	4
		21	125	2
		5*	112	34
C	35	129	59	2
		130	50	2
	50	144	54	2
	75			

(continued next page)

Table 1 - continued

REGION	BT	ID	$\bar{B}$	A (Sq. n. mi.)
		12*	79	898
	35			
		10*	74	60
D	50	165	55	2
		166	62	2
		4*	93	16
	75	19	119	2
		12*	79	898
	35			
		7*	101	504
E	50			
		3*	119	184
	75			

Table 2. Program Time-Cost Summary

(Valid for a 100 scan line × 300 element grid of ATS data input to the CDC 3600 computer)

Technique	Program Name	Input/Output Time (sec)	Processing Time (sec)	Cost[a] ($)
Numeric or Character Display	ATSDSPLY	10[c]	10	$5[d]
Scan-line Plot[b]	ATSPLOT	2[c]	20	$5[d]
2-Dimensional Objective Contour Analysis	ATSCNTUR	10[c]	20	$6[d]
Isometric Plot	ATSMPLT	10[c]	25	$6.50[d]
Cloud Population Depiction and Statistics	CLOUDPOP	10[c]	25	$6.50[d]

a. total time rate of $400

b. refers to a 7000 element scan, not a grid

c. assumes data block is at beginning of tape

d. this is an average cost representing handling charges, program load time, and tape skip time not included in above table

7. ACKNOWLEDGMENTS

Programmers in the Space Science and Engineering Center of the University of Wisconsin have contributed to the display routines and to the associated data reduction techniques.

This work was supported by U.S. Department of Commerce, ESSA, under WBG-27.

8. REFERENCES

1. Hanson, K. and T. Vonder Haar, 1968: Cloud motion and modeling information in ATS-1 digital data (submitted for publication in Weather Motions From Space, U.W. Press).

2. Levanon, N., 1968: Studying the statistical geometry of the sea surface from a synchronous satellite utilizing the sun glitter (submitted for publication in Weather Motions From Space, U.W. Press).

3. Peekna, S., R. Parent and T. Vonder Haar, 1968: Possibilities for quantitative radiance measurements in the 450 - 650 nm region from the ATS-1 satellite (submitted for publication in Weather Motions From Space, U.W. Press).

4. Vonder Haar, T., K. Hanson, V. Suomi and U. Shafrir, 1968: Phenomenology of convective ring clouds in the tropics as derived from geosynchronous satellite observations. Proceedings of the International Conference on Cloud Physics, Toronto.

Scanner's note:

This page is blank.

SCIENTIFIC OBJECTIVES AND DATA REQUIREMENTS FOR RADIATION STUDIES DURING BOMEX[1]

by[2]

Stephen Cox
Kirby Hanson
Verner Suomi
Tom Vonder Haar

CONTENTS

The purpose of this document is to summarize our thoughts on the scientific objectives and data requirements for radiation experiments during the BOMEX program. We have not considered at this time the additional questions of what instrumentation should be employed and who will carry out the work.

Scientific Objectives: Radiation Studies

A considerable amount has been written in GARP documents concerning the scientific objectives of radiation studies in the tropics. An excellent discussion

---

[1]Submitted to BOMEX Project Office, ESSA, March, 1968.

[2]Authors have made equal contributions to this document.

is contained in the GARP Report.[1] The important underlying factor in those considerations is that a relationship exists between radiative and dynamical processes operating within the atmosphere. It is generally known that certain atmospheric variables represent the mechanisms through which the radiative forcing function and air motions are related. These variables are: the distribution and amount of cloud, water vapor, ozone, dust and haze; the temperature distribution; and the state of the lower boundary of the atmosphere. Although we know the relationship exists and the variables involved, we do not have an adequate understanding of how these variables effectively modulate atmospheric heating and cooling by radiation.

In view of this fact, it is indeed surprising that so few measurements exist in which radiation was measured simultaneously with the important atmospheric variables. As indicated in the GARP Report,[2] "this kind of (simultaneous) experiment is essential as a final check on radiation theory." An example of the importance of this check on theory is the need to determine the vertical distribution of absorption in the atmosphere. With clear sky, we know how the energy is distributed; however, with clouds there is multiple scattering and the problem becomes extremely complex. There is no way of checking the theory except by observations. It is vital to studies of the tropics that the vertical distribution of absorption with clouds be verified because the atmospheric stability depends critically on where the energy is absorbed.

There are a number of other useful objectives such measurements would serve. One is that radiation measurements within the atmosphere are essential in attempts to determine the radiative heating or cooling from indirect (satellite) measurements. The success of such indirect measurements depends very critically on knowing the angular and spectral dependence of radiation reflected or emitted outward from the atmosphere. Complete radiation measurements during BOMEX clearly would fill this need.

Another useful objective is to obtain measured radiation values which will serve as controls on calculated radiation values in numerical models. Comparisons of this sort are invaluable in testing radiation approximating equations in numerical models.

There is perhaps an additional opportunity available for BOMEX—it is radiation climatology obtained in a different way. Both long and short wave radiation budgets in the tropics are mainly controlled by clouds. This is especially so for a restricted region of the tropics such as the Barbados area. The sampling problems for a truly representative radiation climatology are very severe—

---

[1] Global Atmospheric Research Programme (GARP), Report of the Study Conference held at Stockholm, 28 June–11 July 1967. ICSU/IUGG-Committee on Atmospheric Sciences, COSPAR, WMO.

[2] Op. cit., p. 46.

perhaps not obtainable when the constraint of a reasonable budget is imposed. One would get enormously better radiation climatology if good radiation data on cloud systems were available. In order to compile the data on cloud systems, radiation measurements should be made not only as a function of time, but according to the presence or absence of identifiable cloud systems. Then a radiation climatology may be constructed by combining the radiation data, classified by cloud system, and satellite photographs of cloud systems. This technique will allow compilation of a radiation climatology even after the completion of BOMEX and over larger area than the proposed BOMEX data network.

Ideally we would like to see an effort made in BOMEX toward a complete radiation program together with simultaneous measurements of the important variables mentioned earlier. Although this task may be larger than possible for BOMEX, an attempt to obtain a "closed solution" radiation experiment during BOMEX will be valuable in itself, for it will provide the experience and problem definition for more sophisticated radiation experiments in the future of the GARP program.

Radiation Program

The overall objectives of a radiation program within BOMEX will be satisfied to a degree that depends on the resources committed to these goals. With this in mind, the remainder of this section contains a discussion of the various practical options regarding the content and distribution of the radiation observing net. They were derived with primary emphasis on the scientific requirements, although economic factors played a secondary role in the definition of the options.

Figures 1a and 1b contain a schematic description of the four major options that were examined. Both the solar and infrared observing networks are considered in each case. In this figure, the fundamental difference between the possible options is in the capability for measuring the vertical variation of the radiation parameters. In short, Option I provides observations throughout the entire atmosphere, and Option IV provides data only at the upper and lower boundaries. Since the spatial coverage will be limited to a large extent by the available facilities and the temporal sampling by operational and manpower considerations, these points are given special attention in the next section.

1. Vertical Distribution of Observations

Before considering the details and tradeoffs of the four options, some comments on the choice of the levels of observation noted at the left of Figure 1a are necessary.

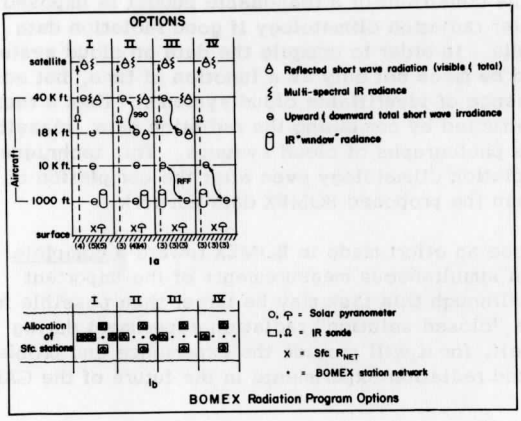

Fig. 1

a) Satellite observations

Radiation measurements from satellites would complement aircraft and surface observations, but the lack of satellite data would not adversely affect the radiation program considered in this document. To be useful, such satellite observations must have high spatial resolution and thus sensors flown on the ATS and NIMBUS satellite could provide the data. ATS-III (launched November 1967) and NIMBUS-B (scheduled for spring 1968) will carry a variety of total and narrow spectrum sensors useful for obtaining quantitative radiation measurements as well as video depictions of day and nighttime cloud cover. If the lifetimes of these satellites extend into the BOMEX time period, all data reduction techniques will have been optimized and the measurements would be available to users in a satisfactory format. Under the assumption that some type of satellite data will be available, it is included in each of the four program options, but did not influence the choice of the other observations.

b) Aircraft measurements at 40,000 feet

A well-equipped aircraft (such as NASA's 990) flown near 40,000 feet would provide a wealth of solar and infrared radiation data near the upper boundary of the troposphere. From this altitude, bi-directional reflectance measurements over the clear ocean and cloudy regions within the BOMEX observational network would be most valuable. Together with satellite observations, these data could be used to examine the radiation regime in the tropical stratosphere.

c) Aircraft measurements at 18,000 and 10,000 feet

Upward and downward solar radiation measurements from these levels would yield data on the vertical distribution of the absorption and scattering of shortwave energy by the atmosphere. The higher observations (near 500 mb) would be useful when tropical radiation data are considered relative to a simple two-layer numerical model. Near the top of the trade inversion (10,000 ft) solar radiation data could be obtained above the active moist region of the tropical troposphere and most probably above a majority of the clouds.

d) Aircraft measurements at 1000 feet

At this lower level, above the boundary layer, the aircraft radiation measurements significantly add resolution to the total vertical structure and also complement the surface observation network by yielding values near the lower boundary over a wide region. In addition to upward and downward shortwave measurements, this aircraft should carry a conventional infrared system for measuring sea surface temperature.

e) Surface observations

These measurements fit ideally into the BOMEX plan of air-sea interaction studies. At land and shipboard locations both IR and solar radiation instruments would measure the net radiation budget at the surface. Aside from their use in total surface energy budget work, the surface measurements and satellite (or high altitude aircraft) data will provide the net radiation budget of the atmosphere alone.

f) Balloon-borne radiometersondes

Nocturnal radiometersonde ascents offer a proven capability for obtaining the upward and downward total IR radiation profiles. These measurements are used to examine net radiation divergence and atmospheric cooling in various layers and can be used to infer the existence of thin layers of cloud and particulates. When combined with solar radiation observations at several altitudes the total atmospheric cooling by radiation can be examined within each layer.

2. Possible Options

The observations suggested for various levels and the recommended distribution of surface measurements within the BOMEX array are shown in Figures 1a and 1b in the form of four options. These options represent different measurement configurations that may be analyzed in order to assess the scientific return from a radiation program in BOMEX against the costs involved in obtaining the observations.

OPTION I

This most inclusive option, from the standpoint of scientific data and resources committed, includes:

a) a full vertical stack of instrumented aircraft,
b) five surface radiation sites, and
c) radiometersonde launches from four locations.

With this type of program, the vertical and horizontal radiation coverage is optimized within practical bounds. If the important meteorological variables were also measured, output from such a radiation program would satisfy the stated objectives, namely: a check of radiation theory with observations; to determine atmospheric heating and cooling by indirect (satellite) measurements; and to provide control radiation data for numerical models.

OPTION II

A reduction in the radiation program as detailed under Option I includes:

a) elimination of the aircraft at the 18,000 foot level, with the option of flying a high-altitude aircraft at this level,
b) a reduction in radiometersonde facilities to three, and
c) surface radiation measurements at only four sites.

Under Option II, the primary objectives would still be attained, but to a lesser extent. For example, the vertical variation of solar radiation above 10,000 feet could not be studied as well, and the infrared soundings would no longer bound a closed grid. The placement of the balloon sites under this option anticipates primarily a north-south orientation of weather phenomena across the BOMEX array.

OPTION III

The diminished program under this option:

a) cuts the number of instrumented aircraft to two (from a maximum of four in Option I), but retains a low and a high altitude capability,
b) reduces the number of surface and radiometersonde facilities to three.

Although a sufficient climatology of the BOMEX area is still attainable under this option, the vertical resolution is considerably reduced. In addition, the flexibility of the radiation program to seek out and observe specific phenomena is hampered. The surface and balloon program presented in Option III is the minimum required to adequately cover the BOMEX array.

OPTION IV

The radiation observing network listed under this option is the lower bound on a system that can still be called a useful radiation program. Eliminated from the previous option is the high altitude aircraft. Thus, no information on the vertical variation of solar radiation can be observed above 10,000 feet and since the remaining aircraft will be used extensively at 1000 feet for near-surface observations we have essentially the shortwave energy measurements only at the upper (from a satellite) and lower boundaries of the atmosphere. Of course, if the single aircraft were unavailable during any time period, even the crude climatology would contain gaps. As mentioned above, three surface and radiometersonde sites represent a minimum network also. This option is insufficient for the stated objectives.

Density of Observations

In order to determine the amount of equipment and manpower required to collect the radiation data, we must examine the required temporal and spatial density of the measurements. Table 1 divides the radiation data required by the program objectives into two convenient categories: phenomenological, with the goal of studying the radiative character of various spatial scales of tropical weather patterns, and climatological, with its purpose of establishing mean radiation budget parameters for the maritime tropical location. The reason a distinction has been made between the two categories is that a rigid schedule, tailored to climatological requirements, may deny data coverage of an interesting situation. There must be the option of real time control of data collected on a noncontinuous basis, namely the balloon soundings and aircraft. The phenomenology category refers to all situations where the real-time decision regarding when, where, and how often, aircraft and balloons are flown to observe phenomena of interest.

1. Time Sampling

We recommend that the solar and net radiation at the surface be collected continuously. Since the primary investment is in the instrumentation and recording systems and not in operation and maintenance, a large amount of data will not cost significantly more than a small amount. It would be desirable to have surface radiation data integrated over five minute intervals.

For the shortwave and infrared data as a function of height, the cost of acquiring frequent data is a primary consideration. Unlike the surface data where the initial equipment was the primary investment, the cost of additional operation of aircraft and support personnel becomes important. Here again the climatology-phenomenology designation becomes useful. For shortwave radiation as a function of height, we recommend the radiation detectors be in operation whenever the aircraft is airborne during daylight hours—this fulfills the

Table 1

Temporal Distribution

	Climatological	Phenomenological
Satellite, Shortwave and infrared	Whenever satellite observations are available	Whenever satellite observations are available
Infrared as a function of height	1 ascent/station-day W/3 periods of nocturnal serial ascents	Serial ascents through selected situations
Shortwave as a function of height	Whenever aircraft are airborne	Have ability to divert aircraft to area of special interest between 0900-1500 for two days out of each week
Net radiation at surface	Continuous	
Shortwave radiation at surface	Continuous	

climatological requirement. The phenomenology requirement is somewhat more restrictive. We recommend that the aircraft be available to divert to areas of special interest between 0900 and 1500LST for two days each week.

Infrared data as a function of height will be gathered by balloon-borne radiometers. Even though the cost of an individual instrument is small, when we talk about hundreds of soundings, the total cost is significant. In order to fulfill the climatological requirements we suggest one radiation sonde ascent per station per day with several periods of serial ascents to determine the presence or absence of variations on the order of hours. If chosen discriminately, the serial ascents mentioned above could also serve as serial ascents through interesting phenomena. If desired or dictated by economy, the climatological soundings could be scheduled approximately every 36 hours instead of every 24 hours or scheduled as a function of cloud systems.

Since it is unlikely that we will be able to dictate satellite coverage of experiment area, we can only specify that we receive data, both infrared and solar reflected, as often as possible. If ATS-III is still operational, it may be possible to make use of the back-to-back scan mode of the spin scan camera, thus allowing almost continuous daytime photographic coverage of the Barbados area.

2. Spatial Sampling

So far we have discussed the temporal density of radiation observations. Now let us turn to the spatial density. Figure 1b represents the suggested network of surface and radiation sonde data stations, the most desirable at left and the right. The positions of surface data stations were determined with two requirements in mind. First, we desire maximum North-South to detect significant latitudinal differences in radiative effects. Second, we wish to have adequate spatial resolution to complement the air-sea interaction study, the primary goal of the BOMEX experiment.

The spatial density of the aircraft data requires special consideration. While the data requirements will vary depending on the phenomenon of interest, in general we recommend the aircraft stacked vertically and coordinated so that measurements are taken at different levels at the same time. Optimally we would prefer an aircraft at 1000 feet (already indicated in BOMEX Bulletin) at 10,000 feet (already assigned in BOMEX Bulletin), at 20,000 (additional) and at 40,000 feet (NASA Convar 990). In lieu of this optimum configuration, the same aircraft could fly the 10,000 foot and 20,000 foot legs sequentially. Figure 1a represents the feasible configurations for aircraft radiation measurements. The wavy arrow indicates the use of a single aircraft to make measurements sequentially at two levels.

The spatial density of satellite data is again perhaps beyond your control, however let us stress that the maximum density available be utilized.

Scanner's note:

This page is blank.

THE INSPACE, ABSOLUTE CALIBRATION OF ATS-1 CLOUD CAMERA

by

Kirby J. Hanson and Verner E. Suomi

CONTENTS

DEFINITION OF TERMS

a	—Calibration constant [millivolts]
a*	—Angular field of view of ATS-1 camera [m rad.]
A_c	—Aperature-area of the ATS-1 camera [cm^2]
A_f	—Ratio of area of spot photometer field of view filled by the brightness source to the total area of the photometer field of view [dimensionless]
AU	—Earth-sun distance [cm]
b	—Calibration constant [sr^{-1}]
B	—Luminance associated with radiance (N_r), assuming maximum luminous efficiency of 680 [lumens $watt^{-1}$]. Units of B are [lumens M^{-2} sr^{-1}] or [ft. L.]
B_M	—Brightness of the moon, measured by a narrow beam photometer [ft. L.]
B_P	—Brightness of Kodak White Paper, measured by a narrow beam photometer [ft. L.]
c	—Calibration constant [WM^{-2}]
c_1	—Instrument constant, for narrow beam photometer
"camera output"	—This term indicates the gain on the camera. It has also been named "wide-band-data-mode" in NASA (1966). It is defined as: "camera output" #1 = 0 db. gain "camera output" #2 = 10 db. gain
DN	—Digitizer value on a scale from 0 to 255. The DN values are proportional to brightness or input power to the camera.
$(DN)_{1,0}$	—Digital value that would result with "nominal gain settings"
F_α	—Phase angle function of the moon [dimensionless]
"Ground station gain"	—Adjustable gain on the video signal induced within the ground equipment. The various gain factors are given by Peekna, et al. (1968), and in Appendix 4 of this paper.
H	—Irradiance of the sun at the earth's mean distance [WM^{-2}]

H' —Effective irradiance [WM^{-2}]

m^* —Optical air mass [dimensionless]

MV —Millivolt output of the ATS-1 camera [millivolts]

$[MV]_{1,0}$ —Millivolt output that would result with "nominal gain settings" [millivolts]

"Nominal gain settings" —Arbitrarily defined as the lowest gain settings possible (see Appendix 4). These are:
"camera output" #1, and
"Ground Station Gain" #0.

N_r —Radiance of the earth and atmosphere [$WM^{-2}\ sr^{-1}$]

N_r' —Effective radiance of the earth and atmosphere [$WM^{-2}\ sr^{-1}$]

$N_{r\lambda}$ —Spectral radiance of the earth and atmosphere [$WM^{-2}\ sr^{-1}\mu^{-1}$]

$N_\odot$ —Radiance of the sun [$=M^{-2}\ sr^{-1}$]

$N_\odot'$ —Effective radiance of the sun [$WM^{-2}\ sr^{-1}$]

$N_{\odot\lambda}$ —Spectral radiance of the sun [$WM^{-2}sr^{-1}\mu^{-1}$]

$N_{r\odot}$ —Radiance of the earth and atmosphere, but having the same spectral distribution as $N_{\odot\lambda}$ [$WM^{-2}\ sr^{-1}$]

P_r' —Effective radiant power into the ATS-1 camera aperture [W]

R_λ —Spectral sensitivity of ATS-1 camera [dimensionless]

sr —[Steradian]

V_m —Visual magnitude

α —Phase angle of the moon. That is, the angle made by the sun, moon and "observor." (Note: In determining a value for α, the "observor" is the ATS-1 camera.) [degrees]

γ —Zenith angle of the ATS-1 satellite as determined at the earth's surface and center of ATS-1 field-of-view [degrees]

δ —Zenith angle of the sun, determined at same point as for γ [degrees]

ρ' —Bidirectional reflectance [sr^{-1}]

ρ_λ' —Bidirectional spectral reflectance [sr^{-1}]

ρ_M' —Bidirectional reflectance of the moon [sr^{-1}]

$\rho_{m\lambda}'$ —Bidirectional spectral reflectance of the moon [sr^{-1}]

ρ_P' —Bidirectional reflectance of Kodak White Paper [sr^{-1}]

$\rho_{P\lambda}'$ —Bidirectional spectral reflectance of Kodak White Paper [sr^{-1}]

ρ_P —Directional reflectance of Kodak White Paper [dimensionless]

$\bar{\rho}'$ —Bidirectional reflectance (of the medium in the field-of-view) which is independent of wavelength over the range of $\underline{R_\lambda}$.

$-\tau_\lambda$ —Spectral transmittance of the earth's atmosphere [dimensionless]

ϕ_1 —Azimuth angle of the sun, at the same point as for $\underline{\gamma}$ [degrees]

ϕ_2 —Azimuth angle of the ATS-1 satellite, at the same point as for $\underline{\gamma}$ [degrees]

ω_c —Solid angle field-of-view of the ATS-1 camera [sr]

$\omega_\odot$ —Solid angle subtended by the sun at the earth, and at mean distance from the sun [sr]

$\omega_\odot^*$ —Solid angle subtended by the sun at the moon, during full-moon [sr]

1. INTRODUCTION

In the history of satellite radiometer or photometer experiments on United States spacecraft there have been many attempts to obtain absolute radiation values from the measurements. These have met with varying degrees of success. The primary difficulty in obtaining absolute values is a result of degradation of the satellite sensor, or sensor optics, in space. Therefore, a suitable pre-launch calibration is of little value after degradation begins. With the ATS-1 cloud camera we are fortunate in having an inherent technique for performing the calibration in space. That is the subject of this paper.

The cloud camera experiments on ATS-1 and -3 used photomultiplier tubes as detectors. It is well known that photomultipliers tend to be unstable under

varying light conditions. Because of this, the tubes were "burned-in" for a number of hours before launch in an attempt to stabilize their sensitivity (Suomi and Parent (1967)). In the future it would be wise to incorporate inspace calibration schemes into the experiment. Two promising methods appear feasible, in addition to the calibration technique which was used for ATS-1 and is the subject of this paper. One method is to monitor the current output of the photocathode when the camera "sees" the sun. This is possible during the equinoxes. A second method of inspace calibration is to periodically view a Cerenkov Standard Source with the photomultiplier. These sources have previously been used in this way (NASA, 1964). In these sources, quartz or other transparent substance exposed to gamma radiation produces a weak, continuous spectrum from red to ultraviolet. These sources have reasonably constant output and the distribution and intensity of the continuum depends on the index of refraction of the transparent substance. Quartz is often used because its index of refraction is nearly independent of temperature.

The present paper considers the absolute calibration of the ATS-1 camera. We are able to obtain an absolute calibration on the moon in the following manner. It is possible to observe the moon with ATS-1 for about two days out of fourteen, as the moon traverses the earth's equatorial plane. Thus, the moon may serve as a passive brightness source on which to determine the response of the ATS-1 camera. The main requirement of this technique is to accurately determine the brightness of the lunar target which the ATS-1 camera is viewing. Its brightness can be determined a number of ways. For example, astronomers have measured the brightness-phase function of the moon. They have also measured the lunar reflectance. Both of these determinations could serve as the basis for calibrating the ATS-1 camera. However, the accuracy of such a calibration would depend on the precision of the astronomer's methods, instrument calibration, and measurement accuracy. These are difficult to reconstruct.

We have, therefore, decided to determine the bidirectional reflectance of the moon relative to a standard MgO_2 reflectance surface. This surface has well known reflectance properties [Richmond (1962) and NBS (1939)]. Our procedure was to first determine the absolute value of bidirectional reflectance for Kodak white paper by comparative measurements with a MgO_2 surface. This was accomplished in an integrating sphere. Second, we determined the absolute value of bidirectional reflectance of the moon (at the time it was viewed by ATS-1) using comparative measurement with the previously "calibrated" Kodak white paper. Thus, the Kodak paper served as a secondary-standard, reflectance surface with which to relate the relative lunar reflectance measurement to an absolute reflectance value. The second comparison mentioned above was carried out at Barcroft Laboratory, White Mountain, California in September, 1967 and is discussed in detail in a later section. Such comparisons could be carried out at frequent intervals if there is evidence the ATS-1 photomultiplier is degrading.

This paper is intended to show the theory of inflight calibration technique; this is given in Section 2. It is also our desire to show the calibration of ATS-1, obtained in September, 1967; this is given in Section 3. In addition, this paper discusses the use of equations, based on ATS-1 calibration, for determining the radiance of the earth and atmosphere, and for determining the bi-directional reflectance within the field of view of the camera. This is given in Section 4.

2. THEORY OF CALIBRATION

An excellent introductory development of the theory is given in the paper by Peekna, et al. (1968). The development given here is an extension of that given in their paper. For those readers who are unfamiliar with the notation used here, which is essentially that of Nicodemus (1963 and 1965), we recommend they follow the development of Peekna before continuing.

a. General Development

In her paper, Peekna has shown that the effective radiant power (P_r') into the ATS-1 camera aperture due to radiance from an earth target is

$$P_r' = A_c \cdot \omega_c \cdot \rho' \cdot H_\delta' \cdot \cos\delta \qquad (1)$$

All of these terms are illustrated in Figure 1, where: A_c and ω_c are the aperture-area and solid-angle-field-of-view of the ATS-1 camera respectively; ρ' is the bidirectional reflectance, that is, the fraction of radiance incident from direction (δ, ϕ_1) which is reflected in direction (γ, ϕ_2); H_δ' is the effective irradiance of the sun at the earth; and δ is the zenith angle of the sun at the center of the intersection of the cone ω_c and the earth.

Another convenient way of expressing the effective power to the ATS-1 camera is as a function of the sun's radiance, $N_\odot$. The radiance and irradiance of the sun are related by the solid angle subtended by the sun at the earth, $\omega_\odot$, that is,

$$H' = \omega_\odot \cdot N_\odot' \qquad (2)$$

as a result we may combine (1) and (2) to give

$$P_r' = A_c \cdot \omega_c \cdot \rho' \cdot \cos\delta \cdot \omega_\odot \cdot N_\odot' \qquad (3)$$

An even more basic form would be to write (3) to include the spectral radiance of the sun, $N_{\odot\lambda}$, and the spectral sensitivity of the ATS-1 camera, R_λ. This form is,

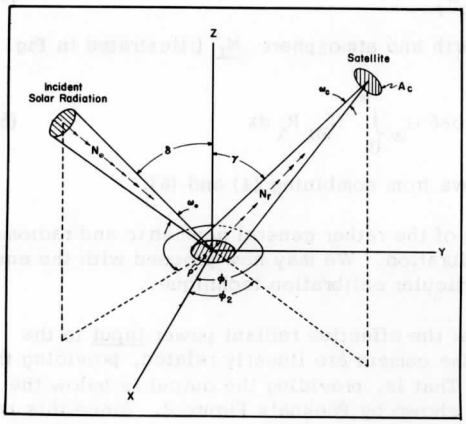

g. 1. Definition of notation, based on that of Nicodemus (1963 and 1965).

$$P_r' = A_c \cdot \omega_c \cdot \rho' \cdot \cos\delta\, \omega_\odot \int_0^\infty N_{\odot\lambda} \cdot R_\lambda \, d\lambda \qquad (4)$$

This is probably the most complete form of the effective power input to the camera, and one in which the power input is very clearly specified in terme of:

(1) a "throughput" term for the camera ($A_c \cdot \omega_c$), as defined by Nicodemus (1963). This term includes the camera aperture and solid angle field of view. Physically, it might be thought of as the "geometrical aperture" through which power may pass into the camera—hence, the term "throughput."

(2) The bidirectional reflectance of the earth and atmosphere within the field of view (ρ').

(3) geometry factors for the solar radiance impinging on the atmosphere within the field of view ($\cos\delta \cdot \omega_\odot$), and

(4) the integral of solar spectral radiance and spectral sensitivity of the ATS-1 camera. This integral is defined as the "effective" solar radiance. That is, that solar radiance which is sensed by the ATS-1 camera.

Perhaps the final useful form to express the effective radiant power into the camera is simply in terms of the radiance of the earth and atmosphere within the field of view. This form is

$$P_r' = A_c \omega_c N_r' \tag{5}$$

The effective radiance from the earth and atmosphere N_r' (illustrated in Fig. 1) is defined as

$$N_r' = \rho' \cos\delta \, \omega_\odot \int_0^\infty N_{\odot\lambda} R_\lambda \, d\lambda \tag{6}$$

Thus, it is apparent that (5) follows from combining (4) and (6).

This completes the definition of the rather general geometric and radiometric quantities required for the calibration. We may now proceed with the equations which are unique to this particular calibration technique.

Peekna et al. have shown that the effective radiant power input to the camera and millivolt output from the camera are linearly related, providing the photomultiplier is not saturated. That is, providing the output is below the "knee" of the response curve, as shown by Peekna's Figure 2. Since this is true, we know that millivolt output (MV) is proportional to the effective power input, P_r'. That is,

$$MV \propto P_r' \tag{7}$$

Therefore, by (5) and (7), we can also write that

$$MV \propto A_c \omega_c N_r' \tag{8}$$

or,

$$MV \propto A_c \omega_c \rho' \cos\delta \, \omega_\odot \int_0^\infty N_{\odot\lambda} R_\lambda \, d\lambda \tag{9}$$

This proportionality is the key to the in-space calibration. We may write equation (9) for some time, t_0, as the denominator in equation (10), and for some later time, t_1, as the numerator.

$$\frac{[MV]_{t_1}}{[MV]_{t_0}} = \frac{[A_c \omega_c \rho' \cos\delta \, \omega_\odot \int_0^\infty N_{\odot\lambda} R_\lambda \, d\lambda]_{t_1}}{[A_c \omega_c \rho' \cos\delta \, \omega_\odot \int_0^\infty N_{\odot\lambda} R_\lambda \, d\lambda]_{t_0}} \tag{10}$$

Now let the designation t_0 be the time of inflight calibration of the satellite camera. It will be shown later that during the calibration we measure the millivolt output of the camera $[MV]_{t_0}$, when the camera is viewing the moon; using another photometer, we also measure the bidirectional reflectance of the moon $[\rho']_{t_0}$, at that time. Thus, two terms in the denominator are measured.

The remaining terms in the denominator are known; their numerical values are given in the Appendix. So we may logically rewrite (10) by treating the denominator terms as constants of the calibration. Let us also drop the subscript t_1 and recognize that the numerator terms in (10) apply to any time after t_0. Thus, equation (10) becomes,

$$MV = \frac{a}{b \cdot c} \cdot \rho' \cdot \cos\delta \cdot \omega_\odot \int_0^\infty N_{\odot\lambda} \cdot R_\lambda \, d\lambda \tag{11}$$

where:

$$\left.\begin{aligned} a &\equiv [MV]_{t_0} \\ b &\equiv [\rho']_{t_0} \\ c &\equiv \left[\omega_\odot \int_0^\infty N_{\odot\lambda} \cdot R_\lambda \, d\lambda\right]_{t_0} \end{aligned}\right\} \tag{12}$$

Equation (11) is a useful form of the calibration result which now specifies the camera output in MV as a function of the variables, ρ' and $\cos\delta$. The remaining terms on the right hand side of (11) may be treated as constants. Thus, in (11) the camera output depends on the bidirectional reflectance in the camera field of view. This equation is written with ρ' outside the integral and therefore assumes it is independent of λ. However, it could have been written inside the integral, if this is desired in order to treat λ as spectrally dependent. Equation (11) also assumes the bidirectional reflectance of the moon is independent of λ within the spectral range of the camera (0.45 - 0.65 microns). In actual practice, one would use equation (11) to solve for ρ', given the ATS-1 camera output in MV and the solar zenith angle δ.

Another form of writing this equation is to specify camera output as a function of the earth's radiance, N_r'. By equations (6) and (11), this is,

$$MV = \frac{a}{b \cdot c} \cdot N_r' \tag{13}$$

Again, in practice, one would use equation (13) to solve for N_r', given the ATS-1 camera output in MV. The assumptions going into (13) are that:

1. the bidirectional reflectance of the moon is independent of wavelength within the spectral range of the camera,
2. the bidirectional reflectance of the earth and atmosphere within the field of view is independent of wavelength for the spectral range of the camera, and
3. that we know the effective solar radiance, $N'_\odot$, to suitable accuracy.

So equations (11) and (13) are the useful equations for working with ATS-1 digital data in order to obtain absolute radiance values, or bidirectional reflectance values, given the camera output in millivolts and a suitable calibration of the camera. Which equation one should use, and how to use it, will depend on the particular application of the researcher.

Now that the general development has been completed, we must go back and look more carefully at one term—the bidirectional reflectance of the moon $[\rho']_{t_0}$, which appeared in equation (11), so we may examine the method by which it is determined. Much of the credibility of this calibration rests on establishing an accurate method for determining this quantity. Therefore a separate section of the theory has been given to this determination.

b. Bidirectional Reflectance of the Moon

In this section we will show how the bidirectional reflectance of the moon can be determined by comparative measurements with the bidirectional reflectance of a known reflectance surface. Solar radiance is the source of energy in both measurements and the problem is to eliminate the effects of the earth's atmosphere which intervenes.

If we have a narrow beam photometer on the earth's surface whose field of view is filled by a portion of the full moon's disc, then the brightness of the moon measured by the photometer can be given as,

$$B_M = C_1 \omega_\odot \int_0^\infty N_{\odot\lambda} \cdot \rho'_{M\lambda} \cdot e^{-\tau_\lambda} \cdot S_\lambda \, d\lambda \qquad (14)$$

where: C_1 is an instrument constant; $\omega_\odot$* is the solid angle subtended by the sun at the moon; $N_{\odot\lambda}$ is the solar radiance; $\rho'_{M\lambda}$ is the spectral bidirectional reflectance of the lunar surface within the field of view; $e^{-\tau\lambda}$ is the spectral transmittance of the earth's atmosphere; and $S\lambda$ is the spectral sensitivity of the photometer.

If the same photometer is used on the earth's surface to measure the brightness of a piece of Kodak white paper held normal to the direct solar beam, then the measured brightness would be given as,

$$B_P = C_1 \cdot \omega_\odot \int_0^\infty N_{\odot\lambda} \cdot \rho'_{P\lambda} \cdot e^{-\tau_\lambda} \cdot S_\lambda \, d\lambda \qquad (15)$$

Here the terms common to (14) are as defined there; $\rho'_{P\lambda}$ is the spectral bidirectional reflectance of the paper; and $\omega_\odot$ is the solid angle subtended by the sun at the earth.

Let us assume the bidirectional reflectance of both the moon and paper are not wavelength dependent in the spectral range of the photometer. With this assumption, $\rho'_{M\lambda}$ may be removed from the integral in (14); and $\rho'_{P\lambda}$ may be removed in (15). The remaining integral values are identical, then, in (14) and (15). By taking the ratio of (14) to (15) we obtain,

$$\frac{B_M}{B_P} = \frac{\omega^*_\odot}{\omega_\odot} \cdot \frac{\rho'_M}{\rho'_P} \tag{16}$$

This can be rewritten as,

$$\rho'_M = \rho'_P \cdot \frac{\omega_\odot}{\omega^*_\odot} \cdot \frac{B_M}{B_P} \tag{17}$$

With this result it is apparent that the bidirectional reflectance of the moon ρ'_M, can be determined from the ratio of only relative brightness measurements of the moon surface and a known reflectance surface; absolute brightness measurements of the moon surface and a known reflectance surface; absolute brightness measurements are not required. The omega ratio term corrects for the fact that the moon and earth may not be the same distance from the sun when the measurements are made. Notice also that the attenuation of the earth's atmosphere cancels from the equation because it appears with both measurements. However, the observations must be made with the same optical air mass and the same meteorological conditions in order for the $e^{-\tau\lambda}$ terms to be identical and cancel. Thus, equation (7) would serve very well for the photometer described and measurements made at the time of full moon.

We have found it necessary to generalize (17) so that measurements may be made at times other than full moon. We have also found it necessary to generalize (17) so that measurements may be made with a photometer whose field of view is such that the moon fills only a portion of the field of view. This simply means two additional terms are included in (17), so that the more generalized form is,

$$\rho'_M = \rho'_P \cdot \frac{1}{A_f \cdot F_\alpha} \cdot \frac{\omega_\odot}{\omega^*_\odot} \frac{B_M}{B_P} \tag{18}$$

Here A_f is a ratio of the area of the photometer field of view filled by the brightness source to the total area of the photometer field of view. This is easily determined experimentally. F_α is the lunar phase function which is used by astronomers; a recent discussion is given by Gehrels, et al., (1964). This term, which is defined in the next section, corrects the brightness to its equivalent full moon value.

The calibration work reported in the next section of this paper used a 1.5 degree field of view spot photometer and measurements were not made at full moon. Therefore, equation (18) has been used in the present work in order to determine ρ'_M. This term was then used as the value of the calibration constant b in equation (12). Thus we may make use of the calibration equations (11) or (13) which requires this constant. This is the subject of the following two sections.

3. CALIBRATION OF SEPTEMBER, 1967

a. Description of the Experiment

The purpose of this calibration is to determine numerical values of the constants a and b in equation (12), where, you will recall

$$a \equiv [MV]_{t_0}$$

$$b \equiv [\rho']_{t_0}$$

and t_0 is the time of calibration. Now, in reality, it is usually not possible to determine a and b simultaneously. Yet these two quantities must be evaluated for the same time, t_0. Since they both depend on the integral brightness of the moon, it is convenient to calculate their equivalent values for full moon using lunar brightness vs. phase angle relation. The relation used in this study is that of Gehrels, et al., (1963), as shown in Fig. 2.

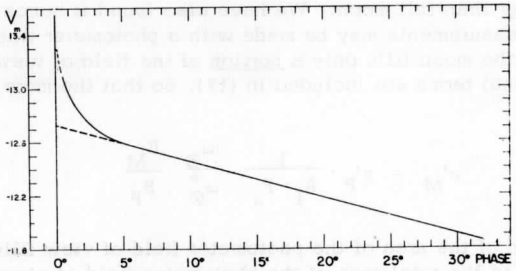

Fig. 2. The phase function of the moon. Abscissas, the phase angle in degrees. Ordinates, magnitudes V on the U, B, V system, reduced to 1 AU distance from the sun and 384,400 km from the earth (after Gehrels, et al. (1964)). The dashed linear extrapolation to phase angle (α) = 0 has been added for the present study so that our value may be normalized to a "full moon" equivalent. A V_m value of 12.74 at α = 0 was adopted for this purpose.

The task of calibration has two parts, the first is to determine a, the camera response in millivolts in viewing the moon. This was carried out by NASA at the Mojave tracking station. The quantitative measurements were digitized and stored on magnetic tapes. These tapes were read and evaluated at Wisconsin.

The second portion of the calibration, that of determining b, was conducted at Barcroft Laboratory, White Mountain, California. This is an excellent facility because its altitude (12,470 ft.) is above much of the atmospheric haze. It is located 18 miles NNE of Bishop, California, and is a part of the University of California at Berkeley.

b. Calibration Constants a, b and c

The constant a has been determined from ATS-1 picture 261-7-162755 which was obtained on September 18, 1967. The original data was digitized and recorded on magnetic tape with the following two gain settings:

$$\left.\begin{array}{l}\text{Camera output} = 2\\ \text{Ground Station Gain} = 6\end{array}\right\} \qquad (19)$$

The moon occupied 64 scan lines and a maximum of 202 elements near its equator. A computer display of the moon's disc, using a program described by Smith and Vonder Haar, is shown in Fig. 3. The isolines are digital numbers (DN) of 35, 50 and 75; the 35 value approximates the lunar limb. Considerable detail is available in the data which is not shown in Fig. 3. For example, the average brightness of some scan lines in the lower portion of the moon's disc are near DN's of 160.

There are 10,316 elements on the moon's disc in picture 261-7-162755 (Fig. 3), and the average DN is 109.74 on a scale of 0-255 DN. The digitizer conversion is given by Parent (1967) as,

$$MV = (1.96076)\cdot(DN) \qquad \text{[Millivolts]} \qquad (20)$$

Thus the measured digital value of 109.74 is equivalent to a camera output of 215.17 [MV]. However, this output is for amplifier gain setting indicated in (19), which is much higher than nominal because of the relatively low brightness of the moon.

A more logical way of expressing the numerical value of a is by determining the equivalent output for nominal gain settings. These settings are,

$$\left.\begin{array}{l}\text{Camera output} = 1\\ \text{Ground Station Gain} = 0\end{array}\right\} \qquad (21)$$

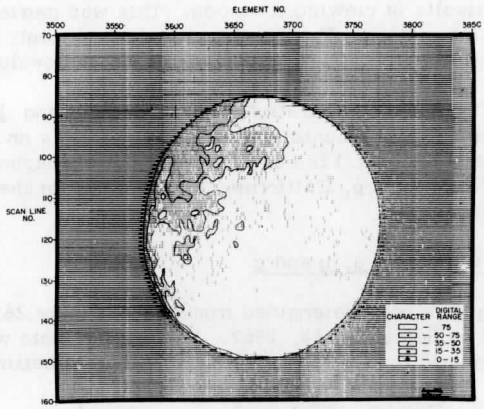

Fig. 3. Computer display of the ATS-1 picture of the moon, 261-7-162755. The lightest areas of the picture correspond to the brightest areas on the moon. The isolines correspond to digital numbers of 35, 50, and 75—the 35 value is approximately on the lunar limb.

As shown in Appendix 4, the amplification for gain setting in (19) is greater than for (21) by a factor of 6.324. Therefore the equivalent millivolt output at nominal gain settings is

$$MV = 215.17/6.324$$

or,

$$MV = 34.02 \text{ [millivolts]} \tag{22}$$

The final adjustment that must be made to this value is that of determining its equivalent full moon value, so that the camera output as well as input has been normalized to its equivalent at full moon. Using Gehrel's phase angle function (Fig. 2), we find the phase angle of 6.5 degrees requires a factor of 1.192 in order to determine the camera output at full moon. Thus,

$$a = 1.192 \times 34.02$$

$$a = (40.55)_{0,1} \text{ [millivolts]} \tag{23}$$

This, then, is the camera output at calibration, normalized to its equivalent value at full moon, and nominal gain settings, which are indicated in eq. 21.

To clearly indicate the gain settings are nominal, let us adopt the subscript notation indicated in (23) and continue this through the paper. The reason is, as will be apparent later, any camera output value must be normalized to this common base if the calibration equations are to be used to infer radiance or bidirectional reflectance.

The constant b is evaluated with eq. 18 and is based on the comparative measurements at White Mountain and other constants. You will recall that this equation is

$$\rho'_M = \rho'_P \frac{1}{A_f \cdot F_\alpha} \cdot \frac{\omega_\odot}{\omega^*_\odot} \cdot \frac{B_M}{B_P}$$

The five terms on the right hand side of this equation will be evaluated in order.

1. ρ'_P. This term is the bidirectional reflectance of Kodak white paper (Gray-scale card) at zenith angle of 60 degrees. This angle corresponds to the direction in which B_p has measured. The value of this term is,

$$\rho'_P = \frac{0.919 \times \rho_P}{\pi} \qquad (24)$$

We have determined the (total) directional reflectance (ρ_P) of Kodak white paper by comparison with MgO_2 surfaces and found $\rho_P = 0.90$. The factor 0.919 is the non-Lambertian reflectance of this surface at a zenith angle of 60 degrees. Evaluating (24) gives,

$$\rho'_P = 0.2633 \qquad (25)$$

2. A_f. This term, previously defined, was evaluated experimentally and found to be 1/8.263. This is in close agreement with the theoretical value of 1/8.466 for the moon (0.5181 degrees) in a 1.5 degree field of view photometer; we have therefore used

$$A_f = 1/8.263 \qquad [-] \qquad (26)$$

3. F_α. This factor is to correct the observed moon bidirectional reflectance at t_0 to its full moon equivalent. It is defined as

$$[V_M]_{t_0} - V_m = -2.512 \log (F_\alpha) \qquad (27)$$

where $[V_m]_{t_0}$ is the visual magnitude at its time of calibration and V_m is the visual magnitude at full moon. Therefore, F_α has values between zero and unity.

For the calibration at White Mountain on September 20, 1967, the measurement of ρ'_M at air mass = 1 was obtained at 06086MT. The phase angle (α) at this time was 19.87 degrees. Again using Gehrel's phase angle functioning (Fig. 2), we find that

$$F_\alpha = 0.6096 \qquad [-] \tag{28}$$

4. $\omega_\odot / \omega^*_\odot$. Since we are comparing the measured brightness of the moon with that of white paper on the earth, we must have the same distance between the sun and each of these surfaces. This omega ratio term corrects the irradiance on the moon at full moon distance from the sun to what the irradiance will be at the earth's mean distance from the sun.

Using the distance given in Appendix A, it is easy to show that

$$\frac{\omega_\odot}{\omega^*_\odot} = 0.9948 \qquad [-] \tag{29}$$

5. B_M / B_P. The measurements made at White Mountain on September 20, 1967, are illustrated in Fig. 4. These were obtained with a model SB, 1.5 degree Spot Photometer of the Photo Research Corporation. The Regulated Brightness Source for this instrument was calibrated by the manufacturer prior to obtaining the White Mountain series of measurements. The Brightness source was subsequently checked and found to be in calibration following the series of measurements. Because the instrument was calibrated, we are giving the measurements in foot Lamberts (ft. L.) in Fig. 4 and also in the following equations. However, the reader will recall from the theory that absolute measurements, such as ft. L., are not required for this series of measurements; relative measurements would be sufficient.

If we evaluate the curves in Fig. 4 at an optical air mass equal to 1 ($m^* = 1$), we find

$$B_M = (98.4)_{m^*=1} \quad [\text{ft. L.}]$$

$$B_P = (10,700)_{m^*=1} \quad [\text{ft. L.}]$$

These two measurement values give the ratio,

$$\frac{B_M}{B_P} = 0.9196 \times 10^{-2} \quad [-] \tag{30}$$

This completes evaluation of the five terms in eq. (18). Now, if we solve (18) with these particular constants at the time of calibration, t_0, we find the bidirectional reflectance of the full moon is,

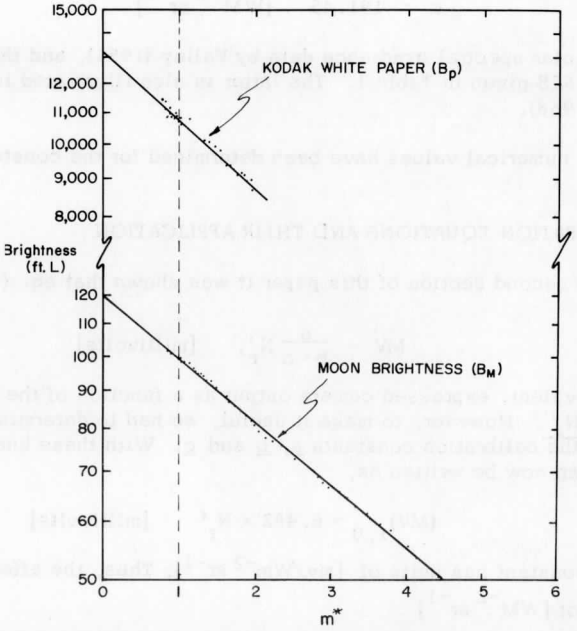

Fig. 4. Measurements at White Mountain on September 19, 1967. Abscissas, the optical air mass above 12,470 ft. (station height). Ordinates, measured brightness of Kodak white paper, 1001 to 1723 PDT (top illustration), of the moon, 1947 to 2400 PDT (bottom illustration). Brightness units are foot-Lamberts.

$$[\rho']_{t_0} = 0.03265 \qquad [sr^{-1}]$$

In addition, by eqs. (12) and (18), the numerical value for the constant b is,

$$b = 0.03265 \qquad [sr^{-1}] \tag{31}$$

The only remaining constant to be determined is c. The constant c is defined in eq. (12) as $\omega_\odot \int_0^\infty N_{\odot\lambda} R_\lambda \, d\lambda$. If we assume the solar spectral radiance $N_{\odot\lambda}$ and spectral sensitivity of the ATS-1 camera are both constant with time—which is a good assumption—then c is truly a constant at t_0. A numerical integration of this term gives,

$$c = 191.45 \quad [WM^{-2}\,sr^{-1}] \tag{32}$$

based on solar spectral irradiance data by Valley (1956), and the spectral sensitivity of ATS given in Table 1. The latter is also illustrated in Peekna's Figure 1 (1968).

Thus, numerical values have been determined for the constants a, b and c.

4. CALIBRATION EQUATIONS AND THEIR APPLICATION

In the second section of this paper it was shown that eq. (11),

$$MV = \frac{a}{b \cdot c} N_r', \quad [\text{millivolts}]$$

or its equivalent, expressed camera output as a function of the effective input radiance N_r'. However, to make it useful, we had to determine numerical values of the calibration constants a, b and c. With these known values, eq. (11) can now be written as,

$$(MV)_{1,0} = 6.482 \times N_r' \quad [\text{millivolts}] \tag{33a}$$

Here the constant has units of $[mv/Wm^{-2}\,sr^{-1}]$; Thus, the effective radiance has units of $[WM^{-2}\,sr^{-1}]$.

This form is both simple and useful because it answers the question, "What is the effective radiance from the earth and atmosphere within the field of view, given the camera output with nominal gain settings ?" There are also other useful forms, of course, and these should be given for continuity. They are,

$$(MV)_{1,0} = 6.482 \int_0^\infty N_r R_\lambda \, d\lambda \tag{33b}$$

$$= 6.482 \rho' \cos\delta \, \omega_\odot \int_0^\infty N_{\odot\lambda} R_\lambda \, d\lambda \tag{33c}$$

$$= 6.482 \cos\delta \, \omega_\odot \int_0^\infty \rho'_\lambda N_{\odot\lambda} R_\lambda \, d\lambda \tag{33d}$$

a. Estimating Total Radiance from Effective Radiance

For many applications we wish to estimate the total radiance from our measurements of effective radiance which represent only a limited portion of the spectrum. Our only basis for making such an estimate is that we know these two quantities for the solar spectral distribution.

Table 1

Relative Spectral Responses ATS-1 Camera and Spot Photometer

Wavelength (μ)	Relative Response ATS-1 Camera	Wavelength (μ)	Relative Response ATS-1 Camera
.400	.000	.550	.820
.405	.000	.555	.770
.410	.000	.560	.720
.415	.000	.565	.675
.420	.000	.570	.610
.425	.000	.575	.560
.430	.000	.580	.500
.435	.000	.585	.440
.440	.000	.590	.350
.445	.010	.595	.275
.450	.015	.600	.200
.455	.020	.605	.145
.460	.020	.610	.120
.465	.040	.615	.085
.470	.095	.620	.060
.475	.210	.625	.050
.480	.440	.630	.030
.485	.840	.635	.025
.490	.900	.640	.020
.495	.930	.645	.015
.500	.960	.650	.010
.505	.980	.655	.005
.510	.995	.660	.000
.515	1.000	.665	.000
.520	1.000	.670	.000
.525	.980	.675	.000
.530	.950	.680	.000
.535	.925	.685	.000
.540	.900	.690	.000
.545	.860	.695	.000
		.700	.000

We can proceed by defining a quantity, $N_{r\odot}$, which is identical to N_r but has the additional constraint that the distribution of energy is the same as for the radiance of the sun. That is, the relative distribution of $N_{r\odot\lambda}$ is that of $N_{\odot\lambda}$; although their absolute values need not agree. From solar radiance data we know that

$$\frac{N_{r\odot}}{\int N_{r\odot\lambda} R_\lambda \, d\lambda} = 7.257 \quad [-] \tag{34}$$

This simply says that if the energy is distributed spectrally as for the sun, then the ATS-1 camera would "see" or sense only (1/7.257)th of the total amount of energy. Now by combining (34) with (33b) and rewriting, we have

$$N_{r\odot} \times \frac{\int N_{r\lambda} R_\lambda \, d\lambda}{\int N_{r\odot\lambda} R_\lambda \, d\lambda} = 1.120 \times (MV)_{1,0} \; [WM^{-2} \; sr^{-1}] \tag{35}$$

Equation (35) is useful for handling problems dealing with various spectral distributions of radiance from the atmosphere. These distributions are of two types for discussion purposes—solar distribution and nonsolar distribution—and they are discussed below.

1. Solar Spectral Distribution. This is a special case of (35) in which we require that the radiance from the earth and atmosphere is identical to the solar spectral distribution. This case might be expected to occur in nature when a bright, neutral reflectance surface is located high in the atmosphere—such as with deep convection. In this case, the numerator integral on the left-hand side of (35) approaches $\int N_{r\odot\lambda} R_\lambda d\lambda$ and equation (35) becomes simply,

$$N_{r\odot} = 1.120 \times (MV)_{1,0} \quad [WM^{-2} \; sr^{-1}] \tag{36}$$

Or, to write the equation with DN instead of MV,

$$N_{r\odot} = 2.196 \times (DN)_{1,0} \; [WM^{-2} \; sr^{-1}] \tag{37}$$

These are helpful equations to use for estimation of radiance, under the conditions assumed. The reader might also find it helpful to recall that the radiance, $N_{r\odot}$, from a perfect, Lambert reflector at the top of the atmosphere is 442.2 $[WM^{-2} \; sr^{-1}]$. This means that for Lambertian reflectance surfaces, the maximum camera output will be about 394.8 [millivolts] or a digital number of 201, assuming nominal gain settings of (0, 1) are used.

2. Nonsolar Spectral Distribution. If the distributive is something other than the solar distribution, then eq. (35) is a useful form. It is useful because the ratio of the integrals allows one to correct for the error in calculation of N_r, which results from $N_{r\lambda}$ having a nonsolar distribution. The equation is

$$N_r \times \frac{\int N_{r\lambda} R_\lambda \, d\lambda}{\int N_{r\odot\lambda} R_\lambda \, d\lambda} = 1.120 \, (mv)_{1,0} \quad [WM^{-2} \, sr^{-1}] \qquad (35)$$

This equation is particularly helpful if one knows or can estimate the spectral distribution of N_r ; and this is often available from aircraft or satellite measurement, or from radiation model estimates.

If, however, one knows or can estimate the spectral reflectance properties of the medium within the field of view, then it is desirable to write (35) in terms of the bidirectional spectral reflectance.

$$N_r \cdot \frac{\int N_{\odot\lambda} \rho'_\lambda R_\lambda \, d\lambda}{\bar{\rho}' \int N_{\odot\lambda} R_\lambda \, d\lambda} = 1.120 \times (MV)_{1,0} \quad [WM^{-2} sr^{-1}] \qquad (38)$$

5. SUMMARY

The ATS-1 cloud camera was calibrated by observing the moon on September 19, 1967. This paper presents both the theory and data for that calibration. In that case the moon served simply as a passive brightness source with which to determine the ATS-1 cloud camera response to reflected sunlight. The moon's bidirectional reflectance was found by comparing its brightness to a secondary-standard reflectance surface (Kodak white paper), which had been calibrated by comparison with a MgO_2 reflectance surface.

It also has been shown that the camera input and output are related by,

$$(MV)_{1,0} = 6.482 \times N_r' \quad [\text{millivolts}] \qquad (33)$$

where the input is N_r' , the effective radiance within the camera field of view, and the output is $(MV)_{1,0}$ in millivolts when the camera gain and ground station gain are nominal. The nominal gain settings are 1 and 0, respectively.

It is also possible to estimate the true radiance (rather than effective) within the field of view if one has some idea of the distribution of the spectral radiance reaching the camera. This is determined from

$$N_r \times \frac{\int N_{r\lambda} R_\lambda \, d\lambda}{\int N_{r\odot\lambda} R_\lambda \, d\lambda} = 1.120 \times (MV)_{1,0} \quad [WM^{-2} sr^{-1}] \qquad (34)$$

Here, $N_{r\lambda}$ is the normalized spectral radiance within the field of view, and

$N_{r\odot\lambda}$ is the same normalized spectral radiance, but having a solar distribution. That is, we require that the integral values of $\underline{N_{r\lambda}}$ and $\underline{N_{r\odot\lambda}}$ be equal, that is,

$$\int N_{r\lambda} d\lambda = \int N_{r\odot\lambda} d\lambda$$

however, the <u>distributions</u> of $\underline{N_{r\lambda}}$ and $\underline{N_{r\odot\lambda}}$ may differ. In this way the integral ratio in eq. (34) serves as a correction to account for <u>nonsolar</u> spectral distribution.

Consider the special case in which the radiance in the field of view does have a <u>solar</u> spectral distribution, e.g. with radiance from bright clouds high in the atmosphere. In this case the integral ratio in eq. (34) approaches unity; thus,

$$N_r = 1.120 \times (MV)_{1,0} \qquad [WM^{-2}\ sr^{-1}] \tag{35}$$

For users, it is somewhat more handy to determine the radiance from digital numbers (DN) on the digital data tapes, rather than from camera <u>MV</u> values. Therefore, eq. (35) is easily written in its other form as,

$$N_r = 2.196 \times (DN)_{1,0} \qquad [WM^{-2}\ sr^{-1}] \tag{36}$$

Both (35) and (36) have the limitations of this special case.

APPENDIX

<u>Significant Constants</u>

1. <u>Astronomical Constants</u>

AU —Earth-sun mean distance - 1.496×10^{13} [cm]

—Radius of the sun - 6.975×10^{10} [cm]

—Earth-moon mean distance - 3.844×10^{10} [cm]

$\omega_\odot$ —Solid angle subtended by the sun at the earth's mean distance - 6.793×10^{-5} [sr]

$\omega_\odot/\omega_\odot^*$ —Solid angle of sun at earth and full moon - 0.9948

2. ATS-1 and Related Constants

a	—Calibration constant	- $(40.55)_{1,0}$ [millivolts]
a^*	—Angular field of view of ATS-1 camera	- 0.1 [m rad.]
A_c	—Aperture area of ATS-1 camera	- 104. [cm^2]
A_f	—Area ratio	- 1/8.263
b	—Calibration Constant	- 3.265×10^{-2} [sr^{-1}]
B_M/B_P	—Measurement ratio	- 0.9196×10^{-2}
c	—Calibration constant	- 191.45 [WM^{-2}]
F_α	—Phase function value at $\alpha = 19.87$ deg.	- 0.6096
$\int N_{\odot\lambda} R_\lambda d\lambda$	—Effective solar radiance	- 2.818×10^6 [$WM^{-2}sr^{-1}$]
$\int H_{\odot\lambda} R_\lambda d\lambda$	—Effective solar irradiance	- 191.45 [WM^{-2}]
$\int N_{r\lambda} R_\lambda d\lambda$	—Effective radiance	- 60.94 [$WM^{-2}\ sr^{-1}$]
$P_{r(max)}$	—Maximum power input to ATS-1 camera aperture	- 36.5×10^{-9} [W]
$P'_{r(max)}$	—Maximum effective power input to ATS-1 camera	- 4.98×10^{-9} [W]
ρ'_M	—Bidirectional reflectance of full moon	- 0.03265 [sr^{-1}]
ρ'_P	—Bidirectional reflectance of Kodak white paper at specified angles	- 0.2633 [sr^{-1}]
ρ_P	—Directional reflectance of Kodak white paper	-0.90
ω_c	—Solid angle field of view of ATS-1 camera	- 0.786×10^{-8} [sr]

3. Radiation Constants

$N_\odot$	—Solar radiance	- 2.045×10^7 [$WM^{-2}\ sr^{-1}$]
$H_\odot$	—Solar irradiance, at earth's mean distance	- 1389.1 [WM^{-2}]

$N_{r(max)}$	—Maximum earth radiance	- 442.2 [WM^{-2} sr^{-1}]
	—Brightness associated with $N_{r(max)}$	- 44109. [lumens $M^{-2}sr^{-1}$]
		- 12873 [ft. L.]

APPENDIX 4

ATS-1 spacecraft and ground-station gain and the resulting signal amplification factor (from Peekna, et al., 1968).

Spacecraft Gain	Ground Station Gain	Amplification Factor Relative to Lowest Setting
Camera Output 1		
(Mode 2) 0 db	0 db	1.00 (nominal setting)
"	2 db	1.26
"	4 db	1.59
"	6 db	2.01
"	8 db	2.54
"	10 db	3.20
"	12 db	4.00
Camera Output 2		
(Mode 1) 10 db	0 db	3.16
"	2 db	3.98
"	4 db	5.02
"	6 db	6.35
"	8 db	8.03
"	10 db	10.10
"	12 db	12.64

REFERENCES

Gehrels, T., T. Coffeen and D. Owings, 1964. Wavelength Dependence of Polarization. III. The Lunar Surface. Astr. j., 69, 10, 826-852.

NASA, 1964. Tech-Center Division, Cook Electric Co., "Fundamental Description and General Reference Specifications for the Wisconsin Experiment Package, Orbiting Astronomical Observation A." NASA Contract 5-1348, sub. 1. Section 2, Page 4.

NASA, 1966. Operational Procedure, Spin Scan Camera Experiment ATS-B. p. 3. (copies available from authors).

NBS, 1939. Preparation and Colorimetric Properties of a Magnesium-Oxide Reflectance Standard. Letter Circular, LC-547. March 17, 1939, National Bureau of Standards, Washington, D.C.

Nicodemus, Fred E., 1963. Radiance. Am. j. phy., 31, 5, 368-377.

Nicodemus, Fred E., 1965. Directional Reflectance and Emissivity of an Opaque Surface. Applied Optics, 4, 7, 767-773.

Parent, Robert, 1967. Private Communication on ATS-1 Digitizer Conversion. Based on information from J. Luhzun (GSFC/NASA) on 9/11/67.

Richmond, Joseph C., Physical Standards of Emittance and Reflectance, pp. 142-153 in Radiative Transfer from Solids. MacMillan, New York. Edited by Henry Blau and Heinz Fisher.

Peekna, S., R. Parent and T. Vonder Haar, 1968. Possibilities for Quantitative Radiance Measurements in the 450-650 nm. Region from the ATS-1 Satellite (submitted for publication in Weather Motions from Space, U.W. Press).

Smith, E. and T. Vonder Haar, 1968: Some Display and Analysis Techniques for ATS Digital Data Users (submitted for publication in Weather Motions from Space, U.W. Press).

Suomi, V. and R. Parent, 1967. ATS Spin-Scan Cloud Camera and Prelaunch Calibration Procedure, in Studies in Atmospheric Energetics based on Aerospace Probings. Annual Report on WBG-27, amendment no. 1, 1966, pp. 1-40. Department of Meteorology, University of Wisconsin, Madison.

Valley, Shea L., 1965. Handbook of Geophysics and Space Environments. Air Force Cambridge Research Laboratories, Office of Aerospace Research, USAF (Chapter 16).

Scanner's note:

This page is blank.

DESIGN OF A FLAT PLATE RADIOMETER FOR TIROS-M SPACECRAFT

by

Robert J. Parent and David F. Nelson

CONTENTS

1. INTRODUCTION

During the initial discussions on the TIROS-M spacecraft, the University of Wisconsin was requested by the Environmental Science Services Administration to consider the requirements for a Flat Plate Radiometer System (FPR) for the new stabilized spacecraft configuration.

As a minimum requirement the system was to provide the basic data to maintain continuity in the Thermal Radiation Balance measurements which have been made in the past by the University of Wisconsin and ESSA on the TIROS and ESSA series of satellites. More specifically, a measurement using sensors as nearly identical as possible to those now on the ESSA series was the main requirement.

The initial study, design, coordination on spacecraft-experiment interfacing and some breadboarding of new or critical portions of the system was accomplished under Grant WBG-27. What follows is an outline of this effort.

2. SYSTEM DESCRIPTION

The radiometer sensor aboard the spin-stabilized TOS series (Nelson and Parent, 1967), consists of a flat aluminum disc which is thermally isolated from the spacecraft. The disc is in radiative equilibrium with the target, which in the case of the spin-stabilized spacecraft, is the time average of the radiation from the earth, sun and space, as the spacecraft spins, plus any contribution from the spacecraft due to imperfections in the thermal isolation. One of the requirements on the TIROS M radiometer system is that it provide a measurement using an identical radiative equilibrium (RE) sensor to provide continuity in the data over a period of years.

In addition to the RE sensors, a new sensor system has been designed. This system will have the following characteristics:

1. Provide a digital output which has a linear relationship to the incident power in the spectral region in which the sensor responds.
2. Include a radiation source which can be placed in front of the sensor for calibration on command.
3. Sensor surface coatings identical to those on the RE sensors so that degradation observed in the calibration mode can be applied to the RE sensor.

The reasons for including the additional sensors are two-fold:

1. Provide a means by which to calculate surface degradation of the RE sensors.
2. Evaluate the performance of the new sensor system, while retaining the older type for comparison.

Two sensors of each type will be used with spectral response of 7 to 30 microns (white), and 0.3 to 30 microns (black), respectively.

The appearance of the FPR system as proposed is shown in Fig. 1. The location of the FPR system on the spacecraft and orientation with respect to the earth is shown in the artist's drawing of Fig. 2.

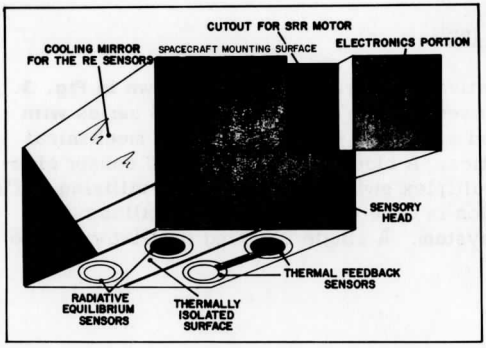

Fig. 1. Flat-Plate Radiometer Assembly (shown with thermal blanket removed).

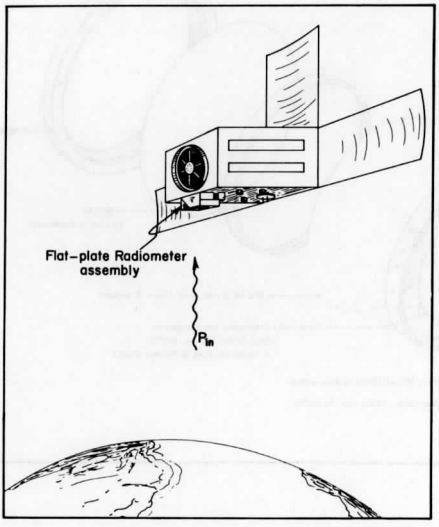

Fig. 2. Flat-Plate Radiometer Assembly on the Spacecraft.

3. SENSOR SUBSYSTEMS

a. Radiative Equilibrium Sensor (RE)

The configuration of the radiative equilibrium sensor is shown in Fig. 3. This sensor is identical to those used in the spin-stablized TOS series with the possible exception of improved surface coatings to increase mechanical strength and spectral characteristics. A block diagram of the RE sensor electronics appears in Fig. 4. The multiplex switch is solid state, utilizing FET's. The resistance to digital conversion is done with a blocking oscillator and counter, as in the previous TOS system. A single blocking oscillator will be

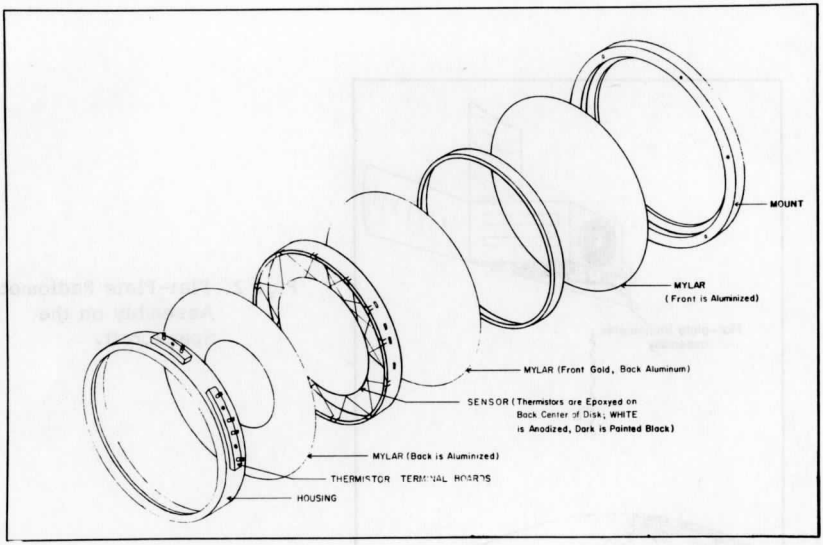

Fig. 3. Expanded View of Basic Radiometer Components.

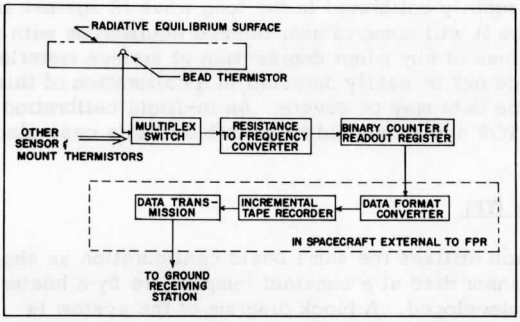

Fig. 4. Functions of the RE Sensor Electronics.

used for both RE sensors and the various mount and housing temperature measurements. The resolution in the RE sensor temperature measurement is to 10 bits and the auxiliary measurements to 7 bits.

The simplest form of the energy balance equation for the RE sensor is as follows:

$$P_{in} = \epsilon \sigma T_s^4 + f(T_s, T_m)$$

P_{in} = The power absorbed by the sensor surface (watts)

T_s = The sensor disc temp (°K)

T_m = The sensor mount temp (°K)

σ = Stefan-Boltzmann constant 5.6686×10^{-12} watts cm^{-2} $°K^{-4}$

ϵ = Emissivity of the sensor surface

The term $f(T_s, T_m)$ is an expression for the heat transfer between the mount and the sensor surfaces.

The temperatures T_s and T_m will be measured and telemetered. The desired quantity is P_{in}. Considerable calculation may be necessary to arrive at this number since the form of $f(T_s, T_m)$ may be complex and not easy to evaluate.

The RE sensor cannot be readily calibrated in the long wave IR against an on-board radiation target since it will come to near thermal equilibrium with a black radiation source regardless of any minor degradation of surface materials. The effect of degradation would not be easily detected in a calibration of this type, whereas the effect on the data may be severe. An in-flight calibration similar to that used with the TOS system should be possible in this case also.

b. Thermal Feedback Sensor (TF)

A new sensor system which utilizes the same basic configuration as shown in Fig. 1 but maintains the sensor disc at a constant temperature by a heater and a servo system has been developed. A block diagram of the system is shown in Fig. 5.

The resistance of the thermistor is compared to a precision resistor in a bridge circuit. The bridge error controls the frequency of a VCO and pulse generator. The pulse generator produces pulses which supply a known energy (watt seconds) per pulse to a resistance heater. The power input to the heater is thus proportional to the frequency of the pulse train. The heater is located on the back of the sensor disc in contact with the disc and the thermistor, thus closing the loop.

The electronics must operate continuously to maintain the sensor temperature even in the interval between sampling of a given sensor. Therefore, each sensor must have its own set of electronics with the multiplexing done at the counter input.

A simple form of the energy balance equation for the TF sensor surface is as follows:

$$E_p f_p + P_{in} = \epsilon \sigma T_s^4 + f(T_s, T_m)$$

E_p = Energy per pulse to resistance heater

f_p = Frequency of pulse train to heater.

The quantities telemetered by the system are f_p and T_m. Although T_s will be held constant by the servo loop, it will be telemetered to verify proper system performance.

A straight line relationship exists between f_p or counter reading and P_{in} (Fig. 6). The effect of T_m is to shift the curve slightly, but the effect is small, and can be corrected.

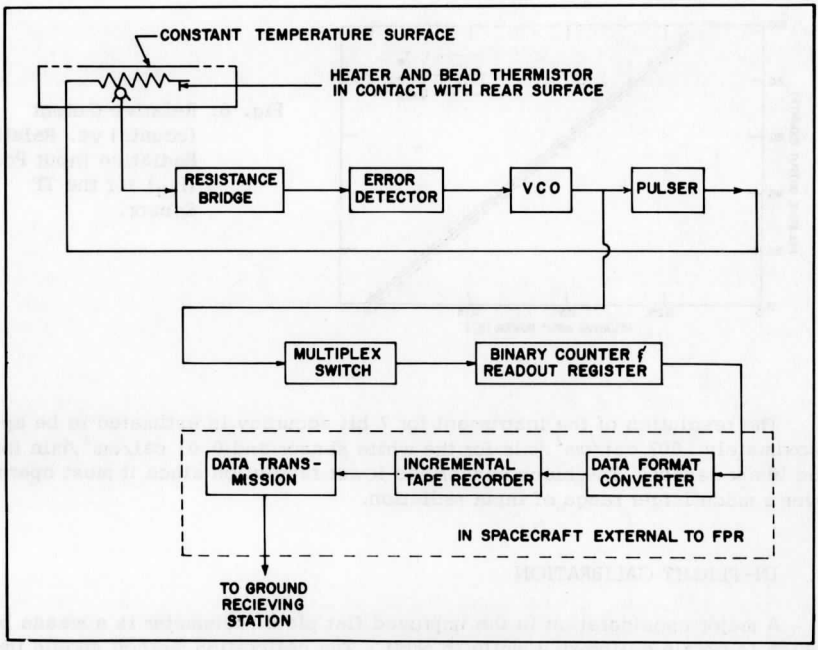

Fig. 5. Functions of the TF Sensor Electronics.

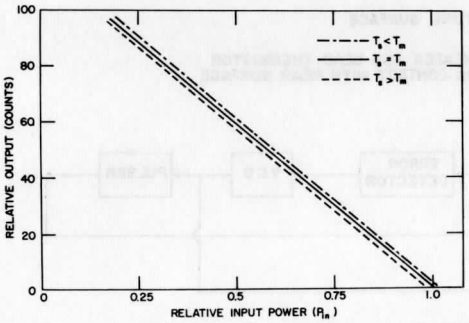

Fig. 6. Relative Output (counts) vs. Relative Radiative Input Power (P_{in}) for the TF Sensor.

The resolution of the instrument for 7 bit accuracy is estimated to be approximately .007 cal/cm^2/min for the white sensor and 0.01 cal/cm^2/min for the black sensor. The black sensor has lower resolution since it must operate over a much larger range of input radiation.

4. IN-FLIGHT CALIBRATION

A major consideration in the improved flat plate radiometer is a means by which to obtain calibration while in orbit. The calibration method should include a means of evaluating changes in the characteristics of the sensor surfaces and compensating for changes in the associated electronics.

a. RE Sensor Calibration

No radiometric calibrations will be applied directly to the RE sensors. Changes to the surfaces will be evaluated by calibrating the identical surfaces of the TF sensors. The electronics will be calibrated by switching a known precision reference resistor into the blocking oscillator circuit. If the reference reading deviates from the nominal value, a proportional correction must be made to all of the radiometer readings based on the relationship:

$$N' = \frac{R}{R_0} N$$

N' = Corrected sensor or auxiliary reading

R = Actual reference resistor reading

R_0 = Reference resistor reading at time of final calibration

N = Actual sensor or auxiliary reading

b. TF Sensor Calibration

The calibration of the TF sensors requires the evaluation of the emissivity and absorptivity of the sensor surfaces in the visible and infrared spectral regions and the energy supplied to the sensor surface per pulse (E_p). The three measurements listed below should make possible an in-flight calibration.

1. Rotate the sensors so that they look into a black body source of known temperature for evaluation of the sensor surface absorptivity in the infrared.

2. Utilize the direct solar input as the spacecraft goes in and out of eclipse to evaluate the sensor surface absorptivity in the visible portion of the spectrum (similar to present TOS in-flight calibration method).

3. Supply a known additional power from a DC-supply to the heater for short periods while the sensor is looking into the black source. The frequency of the pulse train will be reduced so that the total power dissipated in the heater remains the same. E_p can then be obtained from the relationship:

$$E_p = \frac{P_{dc}}{\Delta f}$$

P_{dc} = Power supplied to the sensor disc from a precision DC supply
Δf = Frequency change when P_{dc} is applied.

This measurement is designed to check calibration of the electronics portion of the system.

5. MOUNT TEMPERATURE THERMAL CONTROL

The surface to which the RE sensors are mounted will be cooled by radiation from the "cold" end of the spacecraft. It is anticipated that the mount temperatures will run at -60°C or lower and be quite constant. The cooling is done by coating the back side of the mounting surface with a high emissivity material and allowing it to radiate to space while minimizing any input radiation from the spacecraft or the earth.

The mount for the TF sensors will be operated at the temperature of the electronics package, expected to be in the range of 0 to +20 C.

6. MECHANICAL CONFIGURATION

The entire FPR package will mount to the spacecraft as a unit, i.e., there will be no separate electronics package. The sensor portion of the unit will separate from the electronics for calibration in the vacuum chamber. One side of the package will be open to expose the back side of the RE sensor mounting surface to space for cooling. The inside of the open end will be covered with aluminized mylar to form a reflecting surface. The back side of the RE sensor mounting plate will be black to provide a high emissivity surface while the front will be low emissivity to minimize radiation coupling to the earth.

The TF sensors will be mounted on bearings so that they will rotate 180° into the hemispherical black body radiation source. Several methods for providing a mechanical drive for the rotation were considered.

1. A linear or rotary solenoid and a mechanical linkage.

2. A motor and gear drive.

3. A bimetal device with a heater which is energized during the entire calibration period.

The first two tend to be heavy, complex, and may have a large uncompensated momentum, while the latter requires more total energy from the power system. A motor and gear drive probably will be used.

The weight of the package is expected to be approximately 5 pounds. The structure will weigh 3.5 pounds and the electronics 1.5 pounds.

7. DATA FORMAT

The FPR data will be presented to the spacecraft Data Format Converter (DFC) as 15 words of 8 bits each at 32 second intervals. The data will be presented at a 15 bit/second rate.

The 10 bit data from the RE sensors will be split into two words. The 7 least significant bits plus a sync bit will be recorded as 1 word and the 3 most significant bits included in another word. The 4 remaining bits in the second word will be zero except for the possibility of flag bits for telemetry. A summary of the data format appears below. The word order shown is as presented to the DFC, not as it appears on the ground.

Word Number	Assignment
1	7 LSB RE White
2	3 MSB RE White
3	7 LSB RE Black
4	3 MSB RE Black
5	7 LSB RE Calibrate
6	RE Mount-White
7	RE Mount-Black
8	TF White
9	TF Black
10	TF Mount
11	TF Cal Source White
12	TF Cal Source Black
13	TF Surface Temperature White
14	TF Surface Temperature Black
15	Electronics Temperature

MSB — Most significant bits
LSB — Least significant bits

It is expected that all data from the FPR will be processed by the Data Format Converter (DFC) and then stored on magnetic tape in the Incremental Tape Recorder provided on the spacecraft.

The FPR data will be read out on command and transmitted through a spacecraft data link to an appropriate ground station.

8. CONTINUING PROGRAM

Work on the FPR was formally transferred from the design and breadboarding under WBG-27 to the actual flight hardware phase under contract from ESSA effective 1 October 1967. The flight hardware is being fabricated at the Space Science and Engineering Center, University of Wisconsin, under the direction of Prof. Robert J. Parent, the Principal Investigator.

9. REFERENCES

Nelson, D. and R. Parent, 1967: The Prototype Flat-Plate Radiometers for the ESSA III Satellite. In Studies in Atmospheric Energetics Based on Aerospace Probings, annual report-1966 on WBG-27. Dept. of Meteorology, Univ. of Wisconsin, March 1967.

Scanner's note:

This page is blank.

APPENDIX 1

THE LINE ISLANDS EXPERIMENT AND ATS-1 DATA GUIDE

by

Terry L. Yonker

1. INTRODUCTION

Though many experiments have been conducted to observe the Intertropical Convergence Zone (ITC), few have had the large scope or have provided the opportunity to correlate surface, ship, aircraft, and satellite observations. The Line Islands Experiment of February through May, 1967, provided the time that observations of the tropical atmosphere were obtained simultaneously. The Experiment is a precursor to more extensive programs planned for the future (e.g. TROMEX), but it is valuable by itself as a basic study of the Intertropical Convergence Zone.

The Line Islands were chosen as the site for the Experiment because the mean geographic position of the Intertropical Convergence Zone lines within the region of that island chain during this period of the year. Table 1 gives the geographical position of the Line Islands. An equally important reason for choosing the Line Islands is that they lie very near the subsatellite point of the ATS-1 synchronous satellite (150° to 152° west on the Equator). Finally, the island chain is far from large continental land masses which would normally produce complicated effects on the weather.

Table 1

Island	Position	
Christmas	1° 55'N	157° 20'W
Fanning	3° 54'N	159° 23'W
Washington	4° 43'N	160° 25'W
Palmyra	5° 53'N	162° 05'W

2. PURPOSE OF THE DATA GUIDE

This data guide is intended to provide two kinds of information. One is to provide satellite pictures of the general meteorological conditions that existed in the area of the Line Islands for eacy day of the Experiment. The second requirement is to present a simple and convenient illustration of what supporting data are available during the Line Island Experiment period. A more comprehensive list of available Line Island Experiment data, its source, and a description of both the experiment and the instrumentation is given in the data catalog by Zipser and Taylor (1968).

3. STRUCTURE OF THE DATA GUIDE

A. The Once-a-Day ATS-1 Pictures

The area of observation, as shown in Fig. 1, is from 10° S to 20° N and from 140° W to 130° W. The ATS-1 satellite cloud pictures for each day of the Line Islands Experiment are shown in Fig. 2. The pictures have been gridded using an overlay technique described in the NASA ATS Data Catalog (NASA (1967)). The gridding is accurate to within approximately one degree latitude near the subsatellite point.

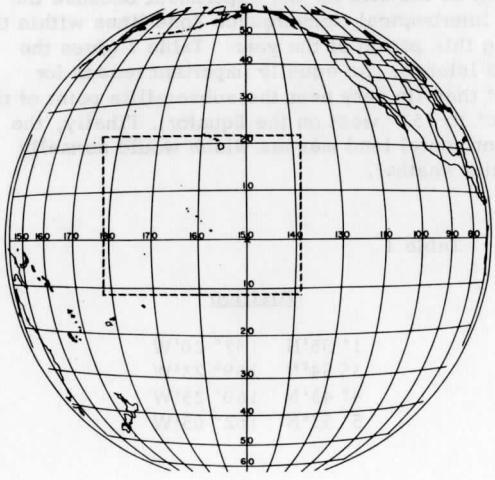

Fig. 1. Area of the Line Islands and Hawaiian Island region. The ATS-1 cloud pictures of this region are shown in Fig. 2

In the period from March 1 to March 27, the pictures are somewhat distorted, but mainly outside the Line Islands area. If the distortion of synchronization problem significantly affects the area, the gridding on the picture is discontinued. The date and local time (Hawaiian) appear under the picture. Every attempt has been made to provide a photograph as close to local noon as is possible. It should also be pointed out that some of the original detail was necessarily lost when the pictures were rephotographed for the data guide.

b. The Data Grid

A visual catalog of the Line Island Experiment data is illustrated in data grids which are shown in Fig. 3. The top margin of the grid gives the day and the time that the instruments on the left margin were operative. The ATS-1 data is listed first so that other observations can be referenced to it. Much of the information on the grids was taken from the data catalog by Zipser and Taylor. Table 2 is intended to aid the researcher in the use of the grids in Fig. 3.

Table 2

Symbol	Meaning
▬▬ ▬ ▮	Observations occurred during the inclusive period of time.
----------	Observations were intermittant or a single instrument of a unit did not function.
▬▬ ? ▬▬	C-97 aircraft made a flight but observation time is not known.
*	ESSA-III picture covers the entire area but the orbit time is not known.
+	ESSA-III picture covers only part of the area.
	(Surveyor oceanographic data observations were not available at the time of this writing)

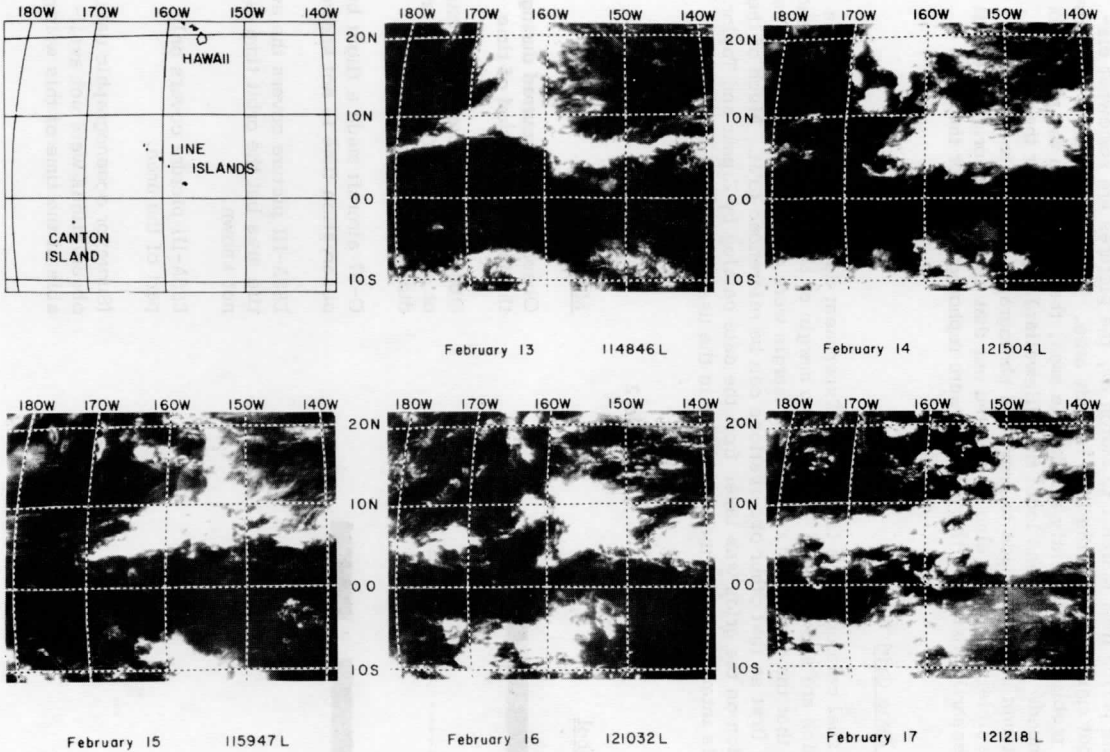

Fig. 2a

Fig. 2. ATS-1 cloud pictures of the Line Island and Hawaiian Island region for each day of the Line Island Experiment. The best picture nearest local noon is presented.

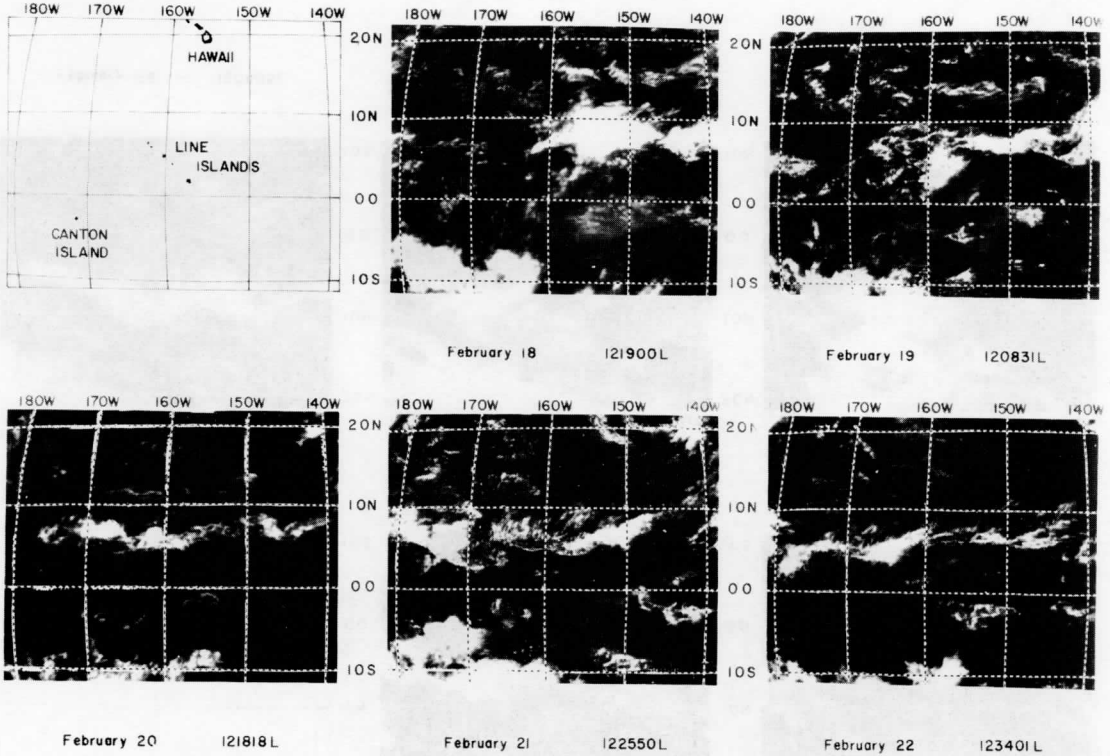
180W 170W 160W 150W 140W
20N
10N
00
10S
HAWAII
LINE
ISLANDS
CANTON
ISLAND
February 18 121900L
February 19 120831L
February 20 121818L
February 21 122550L
February 22 123401L

Fig. 2b.

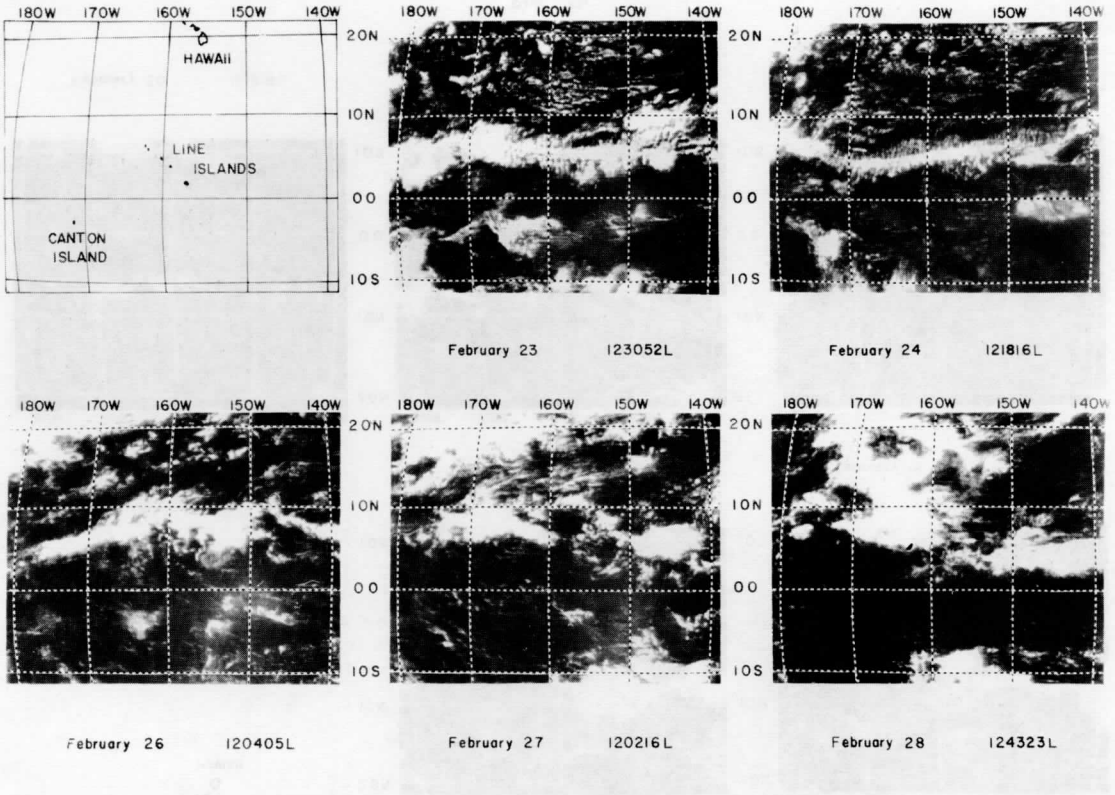
180W 170W 160W 150W 140W
20N
10N
00
10S
HAWAII
LINE
ISLANDS
CANTON
ISLAND
February 23 123052L
February 24 121816L
February 26 120405L
February 27 120216L
February 28 124323L

Fig. 2c

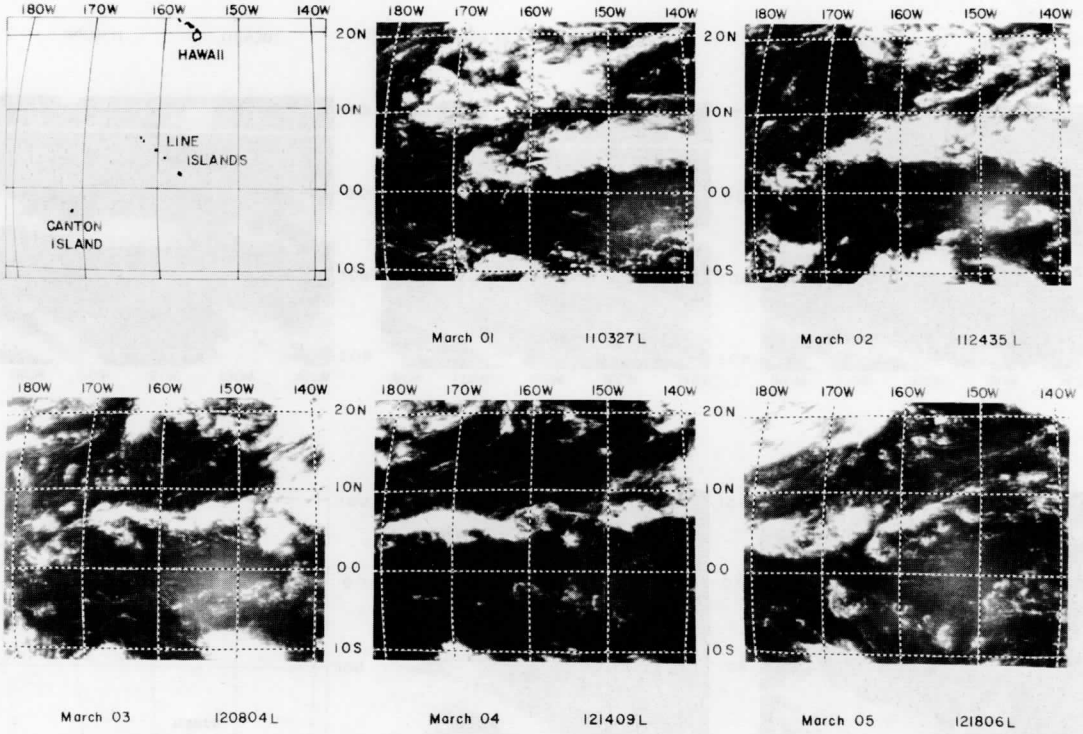
180W 170W 160W 150W 140W
20N
10N
00
10S
HAWAII
LINE
ISLANDS
CANTON
ISLAND
March 01 110327L
March 02 112435L
March 03 120804L
March 04 121409L
March 05 121806L

Fig. 2d

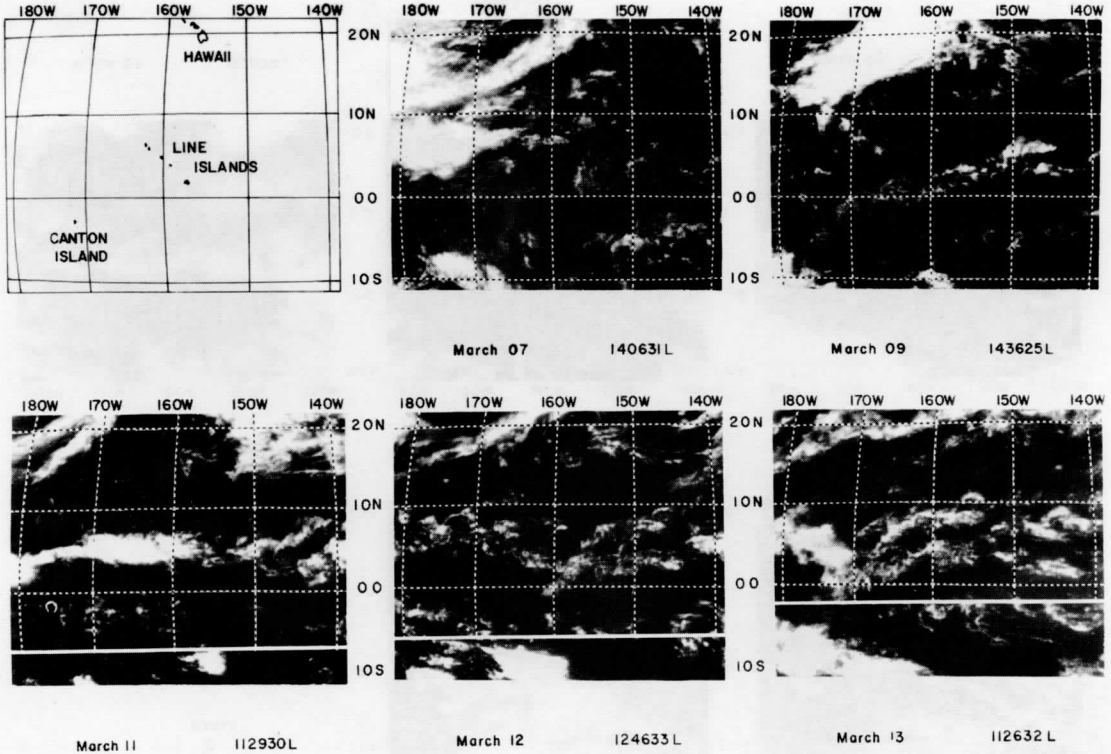
180W 170W 160W 150W 140W
20N
10N
00
10S
HAWAII
LINE
ISLANDS
CANTON
ISLAND
March 07 140631L
March 09 143625L
March 11 112930L
March 12 124633L
March 13 112632L

Fig. 2e

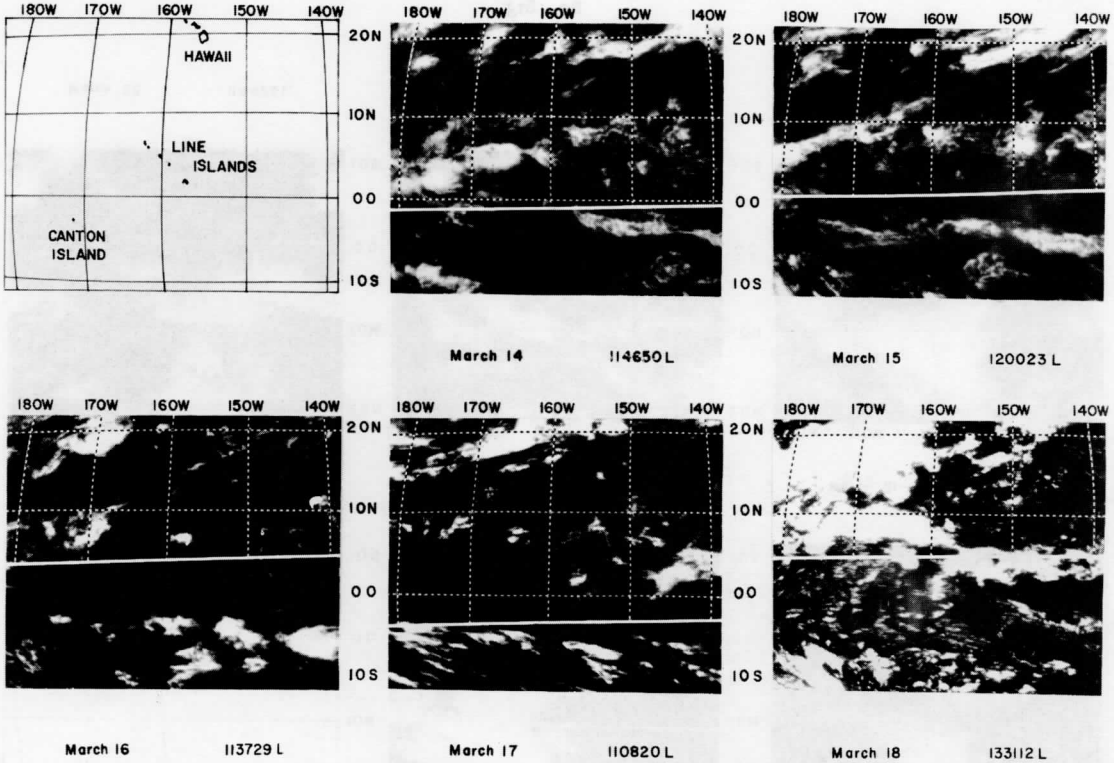
180W 170W 160W 150W 140W
20N
10N
00
10S
HAWAII
LINE ISLANDS
CANTON ISLAND
March 14 114650L
March 15 120023L
March 16 113729L
March 17 110820L
March 18 133112L

Fig. 2f

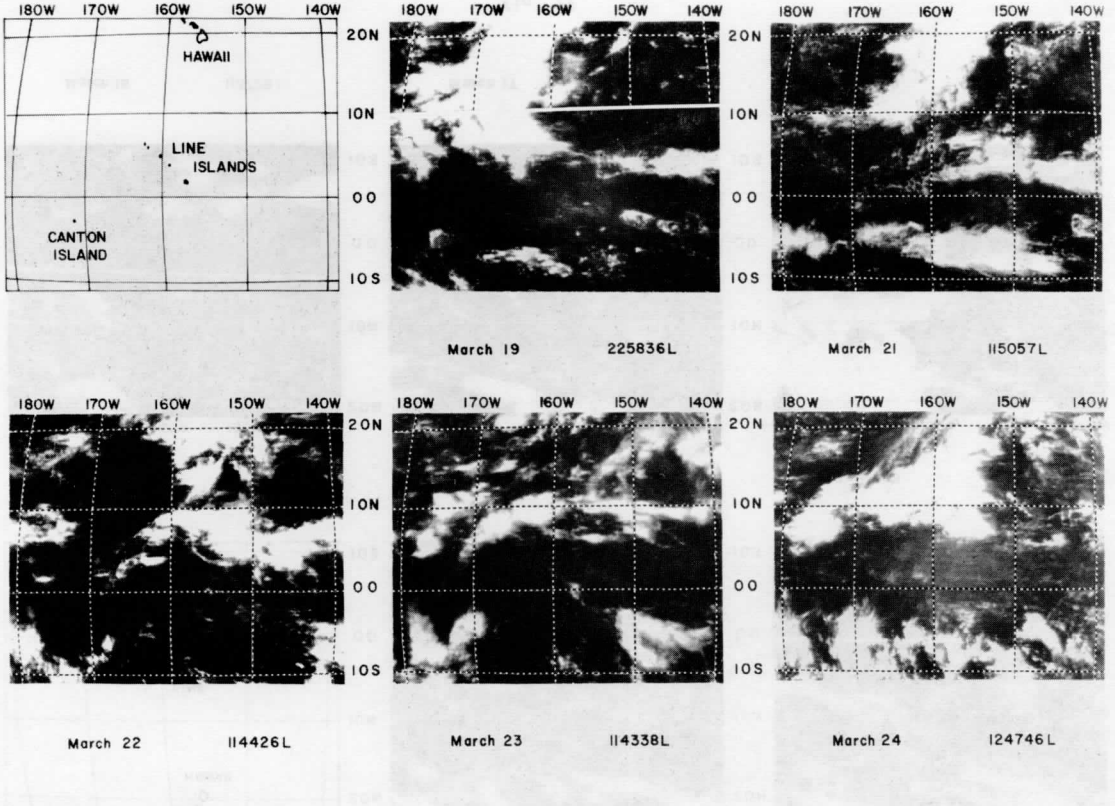
180W 170W 160W 150W 140W
20N
10N
00
10S
HAWAII
LINE ISLANDS
CANTON ISLAND
March 19 225836L
March 21 115057L
March 22 114426L
March 23 114338L
March 24 124746L

Fig. 2g

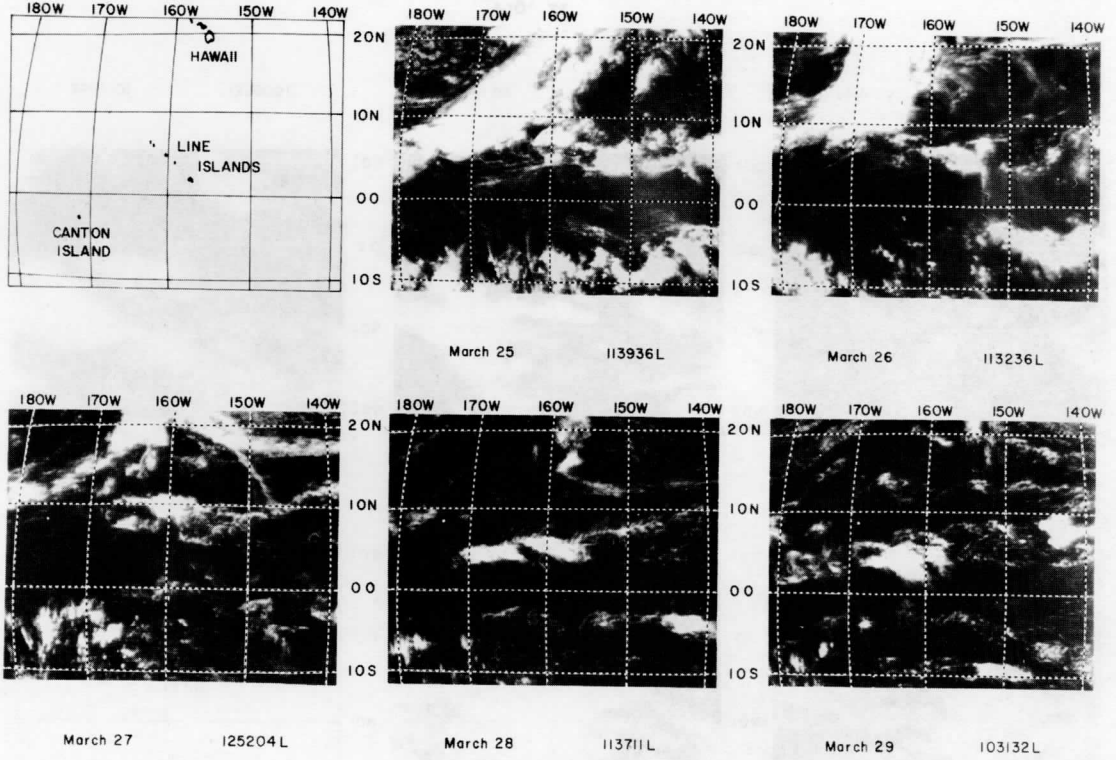
180W 170W 160W 150W 140W
20N
10N
00
10S
HAWAII
LINE
ISLANDS
CANTON
ISLAND
March 25 113936L
March 26 113236L
March 27 125204L
March 28 113711L
March 29 103132L

Fig. 2h

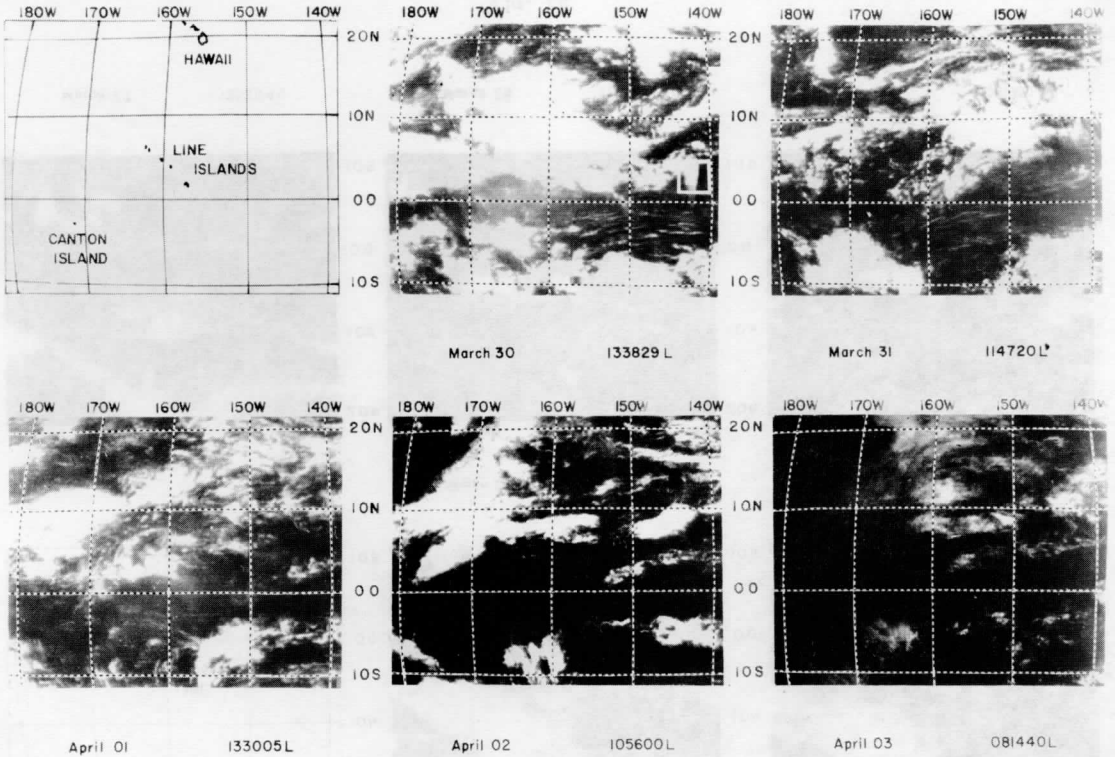
180W 170W 160W 150W 140W
20N
10N
00
10S
HAWAII
LINE
ISLANDS
CANTON
ISLAND
March 30 133829 L
March 31 114720 L
April 01 133005 L
April 02 105600 L
April 03 081440 L

Fig. 2i

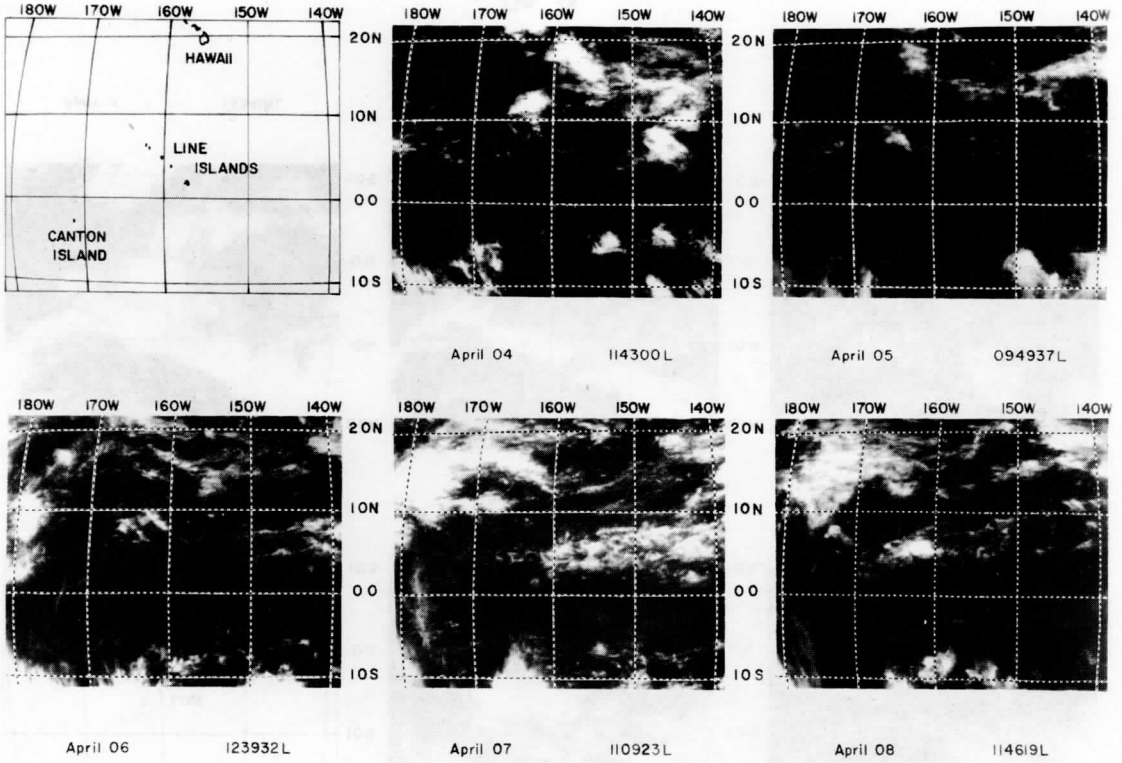
180W 170W 160W 150W 140W
20N
10N
00
10S
HAWAII
LINE
ISLANDS
CANTON
ISLAND
April 04 114300L
April 05 094937L
April 06 123932L
April 07 110923L
April 08 114619L

Fig. 2j

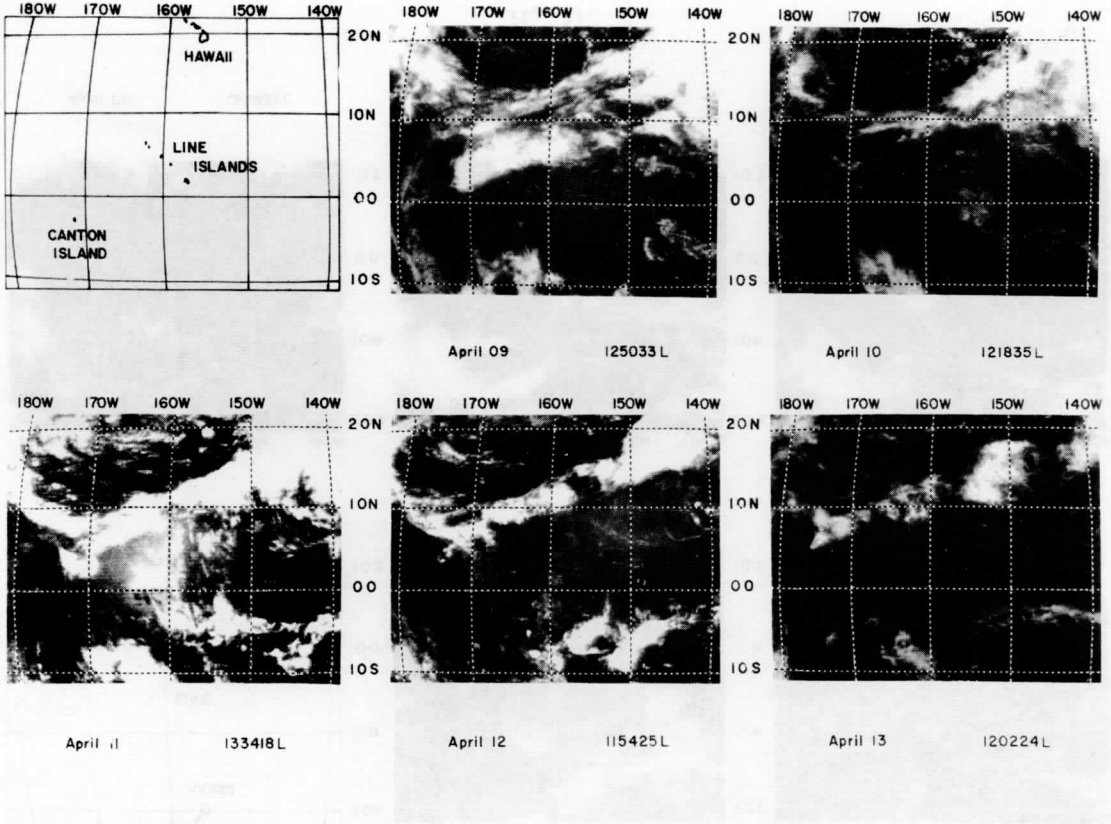
180W 170W 160W 150W 140W
20N
10N
00
10S
HAWAII
LINE ISLANDS
CANTON ISLAND
April 09 125033L
April 10 121835L
April 11 133418L
April 12 115425L
April 13 120224L

Fig. 2k

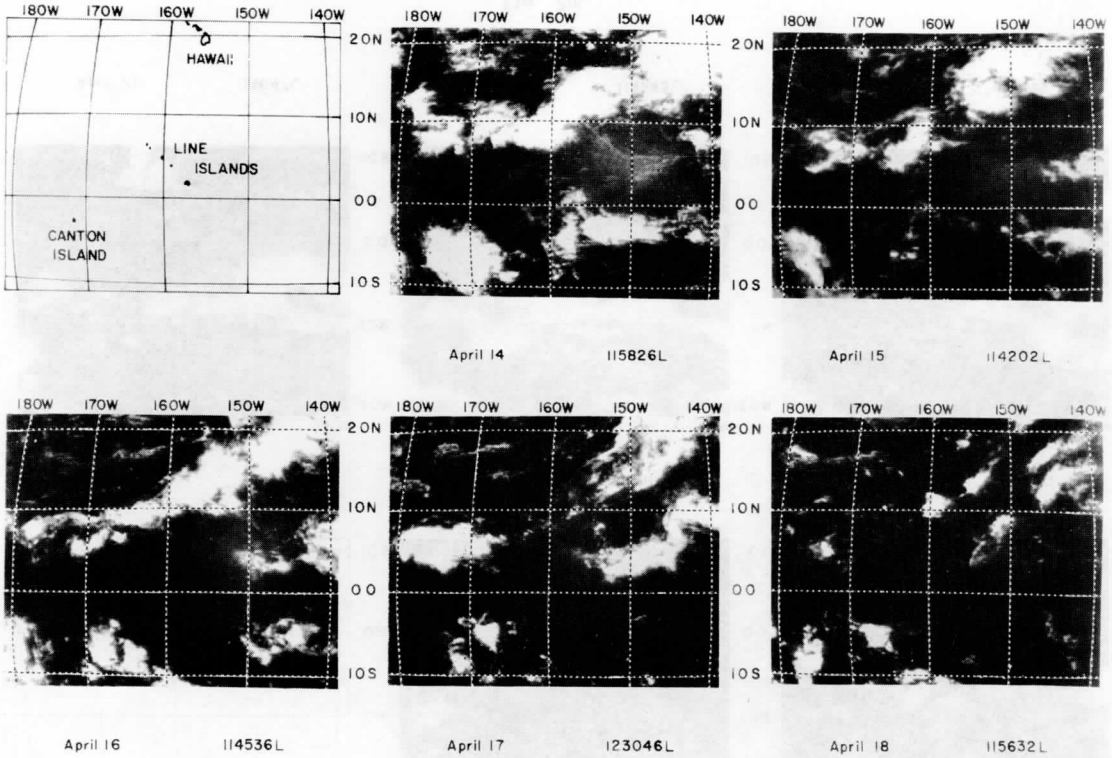
180W 170W 160W 150W 140W
20N
10N
00
10S
HAWAII
LINE
ISLANDS
CANTION
ISLAND
April 14 115826L
April 15 114202L
April 16 114536L
April 17 123046L
April 18 115632L

Fig. 21

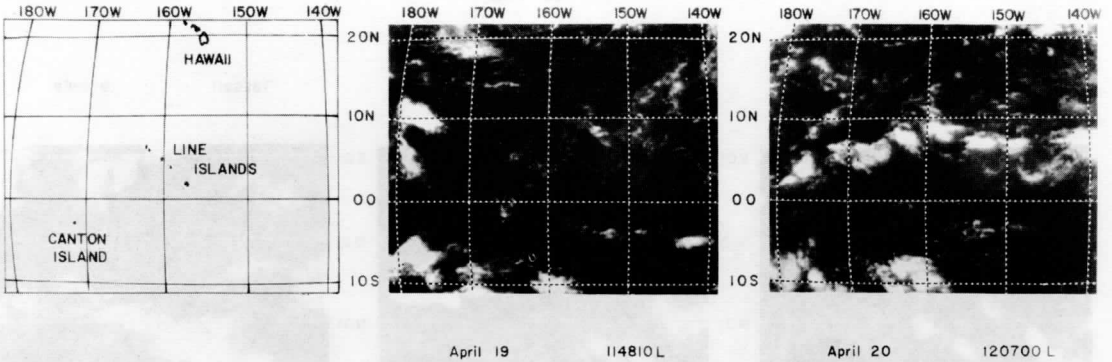
180W 170W 160W 150W 140W
20N
10N
00
10S
HAWAII
LINE ISLANDS
CANTON ISLAND
April 19 114810L
April 20 120700L
April 21 114647L
April 22 114243L
April 23 115959L

Fig. 2m

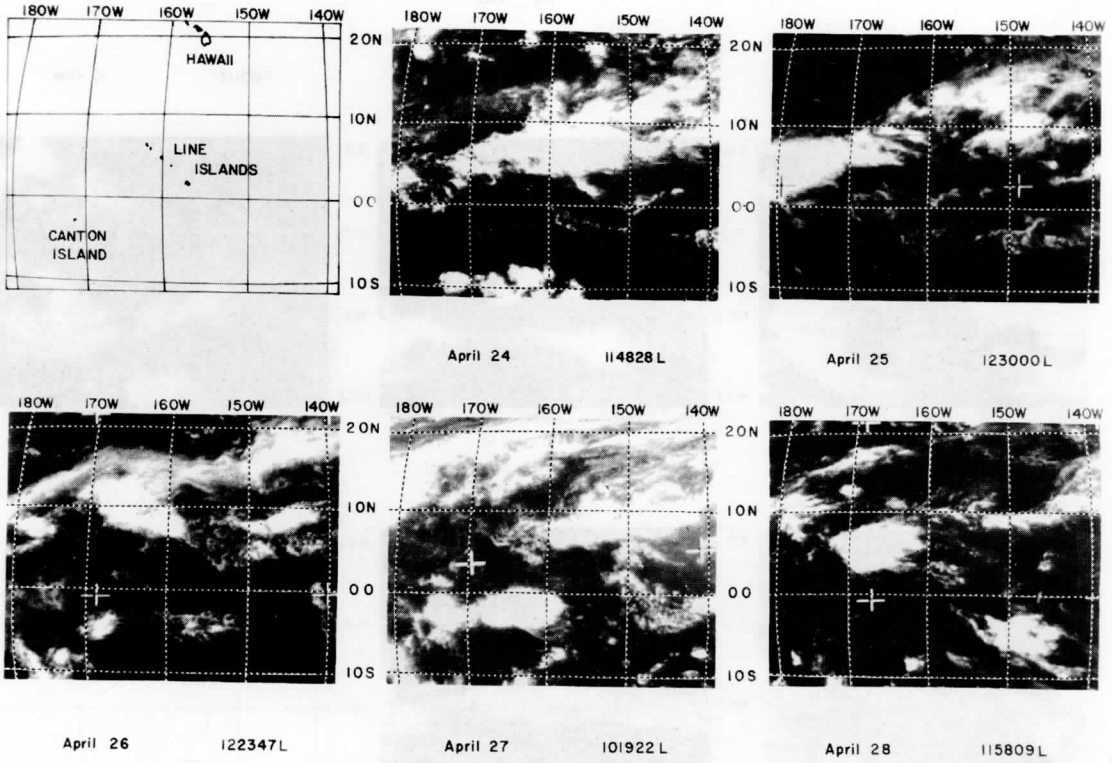
180W 170W 160W 150W 140W
20N
10N
00
10S
HAWAII
LINE
ISLANDS
CANTON
ISLAND
April 24 114828L
April 25 123000L
April 26 122347L
April 27 101922L
April 28 115809L

Fig. 2n

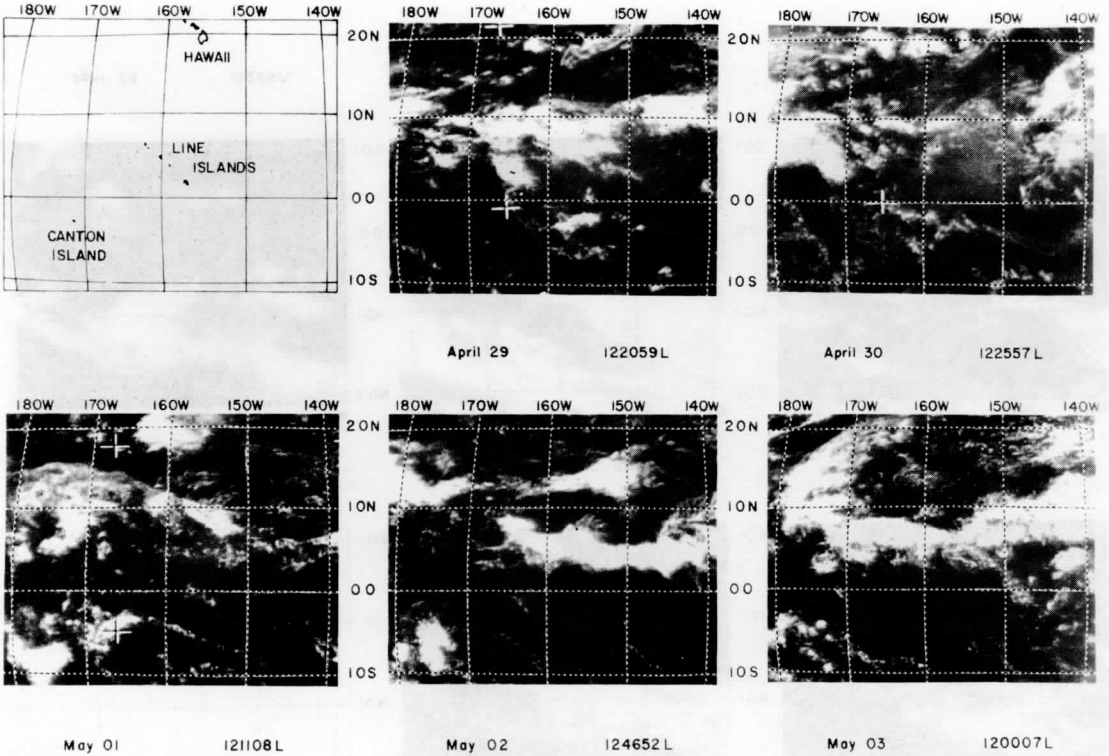
180W 170W 160W 150W 140W
20N
10N
00
10S
HAWAII
LINE ISLANDS
CANTON ISLAND
April 29 122059L
April 30 122557L
May 01 121108L
May 02 124652L
May 03 120007L

Fig. 2o

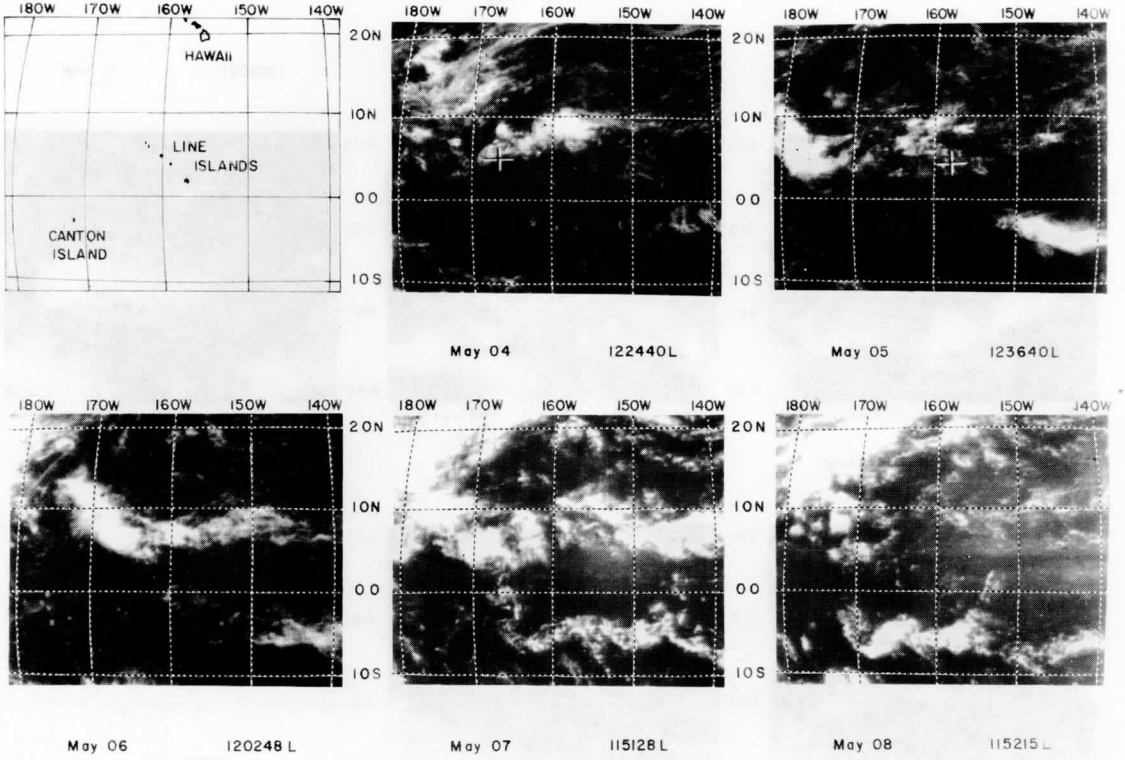
180W 170W 160W 150W 140W
20N
10N
00
10S
HAWAII
LINE
ISLANDS
CANTON
ISLAND
May 04 122440L
May 05 123640L
May 06 120248L
May 07 115128L
May 08 115215L

Fig. 2p

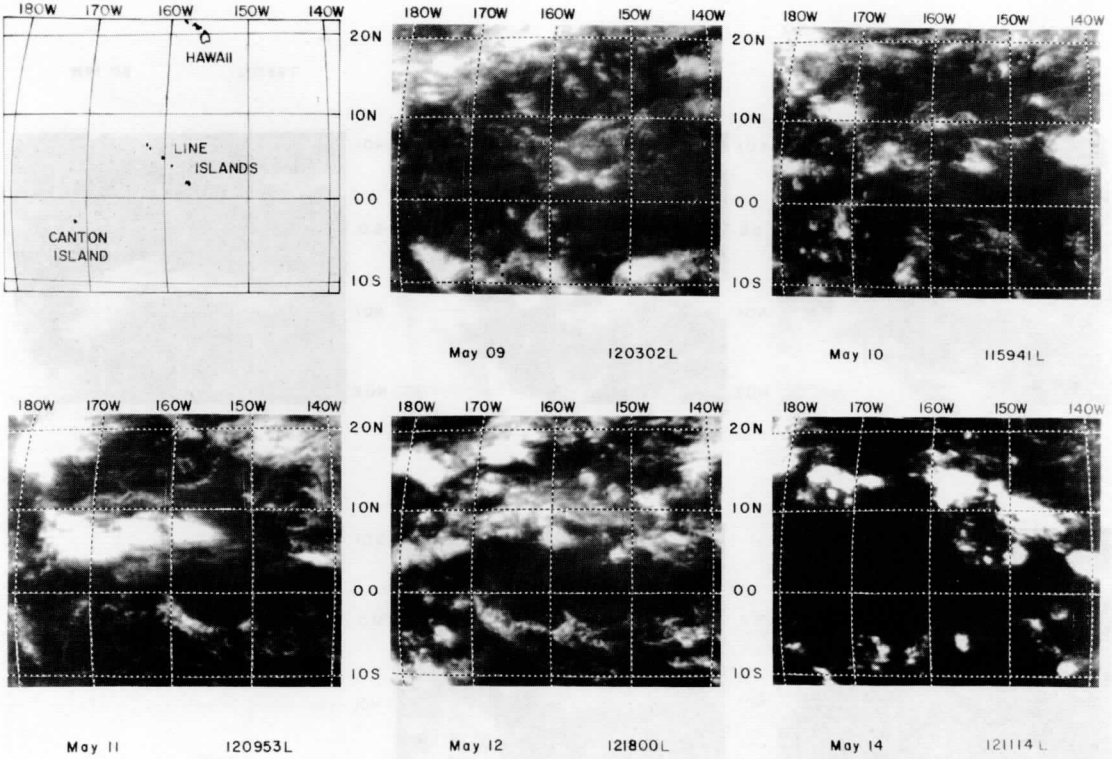
180W 170W 160W 150W 140W
20N
10N
00
10S
HAWAII
LINE
ISLANDS
CANTON
ISLAND
May 09 120302L
May 10 115941L
May 11 120953L
May 12 121800L
May 14 121114L

Fig. 2q

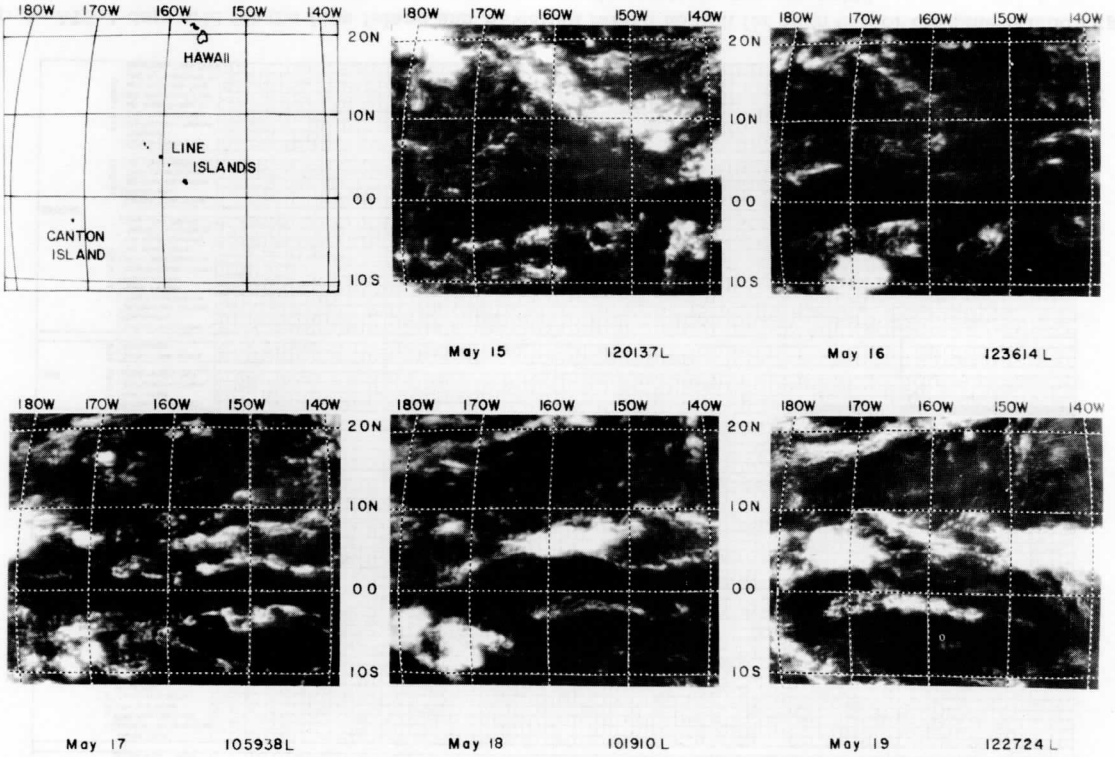
180W 170W 160W 150W 140W
20N
10N
00
10S
HAWAII
LINE
ISLANDS
CANTON
ISLAND
May 15 120137L
May 16 123614L
May 17 105938L
May 18 101910L
May 19 122724L

Fig. 2r

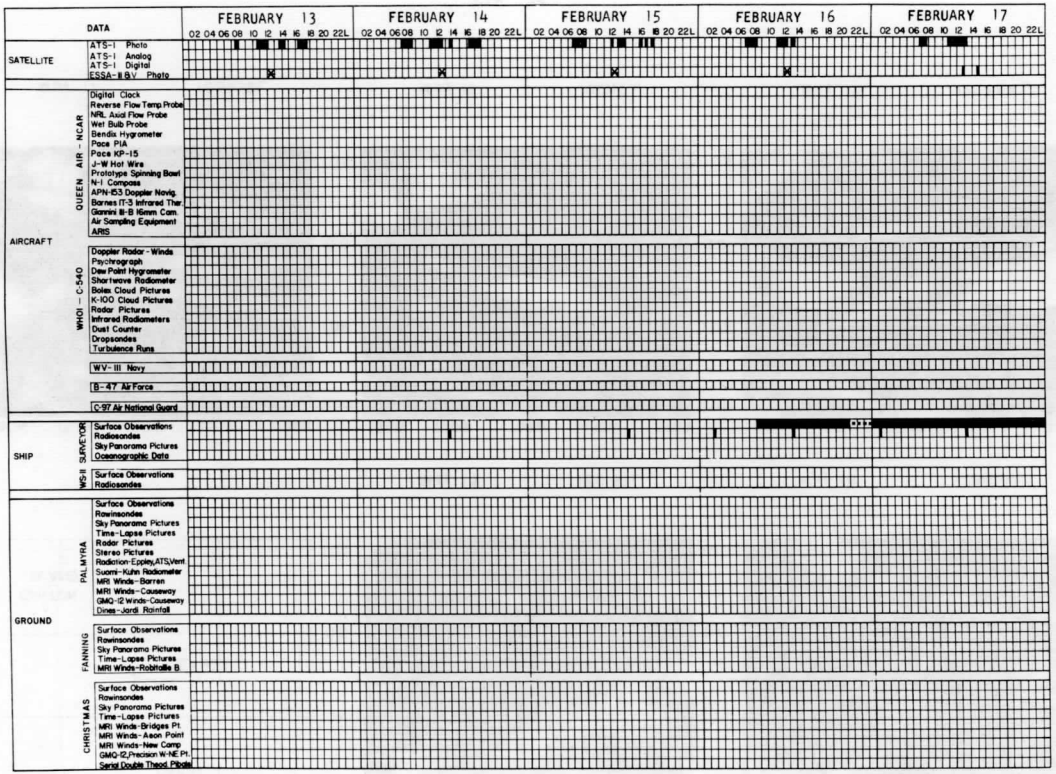

Fig. 3a

Fig. 3. ATS-1 data grid for the Line Island and Hawaiian Island Region for each day of the Line Island Experiment. The local time and the type of instrument observations are presented.

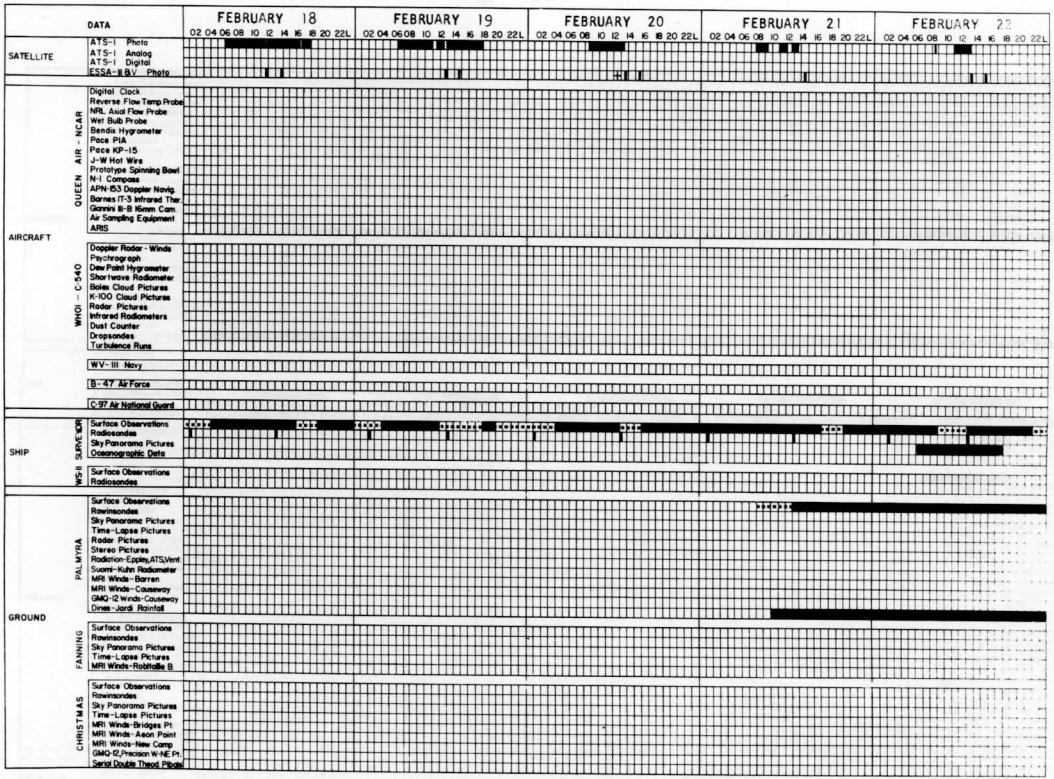
DATA
FEBRUARY 18
FEBRUARY 19
FEBRUARY 20
FEBRUARY 21
FEBRUARY 22
02 04 06 08 10 12 14 16 18 20 22L
SATELLITE
ATS-I Photo
ATS-I Analog
ATS-I Digital
ESSA-III&V Photo
AIRCRAFT
QUEEN AIR - NCAR
Digital Clock
Reverse Flow Temp Probe
NRL Axial Flow Probe
Wet Bulb Probe
Bendix Hygrometer
Pace PIA
Pace KP-15
J-W Hot Wire
Prototype Spinning Bowl
N-1 Compass
APN-153 Doppler Navig.
Barnes IT-3 Infrared Ther.
Gannini III-B 16mm Cam.
Air Sampling Equipment
ARIS
WHOI - C-540
Doppler Radar - Winds
Psychrograph
Dew Point Hygrometer
Shortwave Radiometer
Boles Cloud Pictures
K-100 Cloud Pictures
Radar Pictures
Infrared Radiometers
Dust Counter
Dropsondes
Turbulence Runs
WV-III Navy
B-47 Air Force
C-97 Air National Guard
SHIP
SURVEYOR
Surface Observations
Radiosondes
Sky Panorama Pictures
Oceanographic Data
WSB
Surface Observations
Radiosondes
GROUND
PALMYRA
Surface Observations
Rawinsondes
Sky Panorama Pictures
Time-Lapse Pictures
Radar Pictures
Stereo Pictures
Radiation-Eppley,ATS,Vent
Suomi-Kuhn Radiometer
MRI Winds-Barren
MRI Winds-Causeway
GMQ-12 Winds-Causeway
Dines-Jordi Rainfall
FANNING
Surface Observations
Rawinsondes
Sky Panorama Pictures
Time-Lapse Pictures
MRI Winds-Robitaille B
CHRISTMAS
Surface Observations
Rawinsondes
Sky Panorama Pictures
Time-Lapse Pictures
MRI Winds-Bridges Pt.
MRI Winds-Aeon Point
MRI Winds-New Camp
GMQ-12,Precison W-NE Pt.
Serial Double Theod. Pibals

Fig. 3b

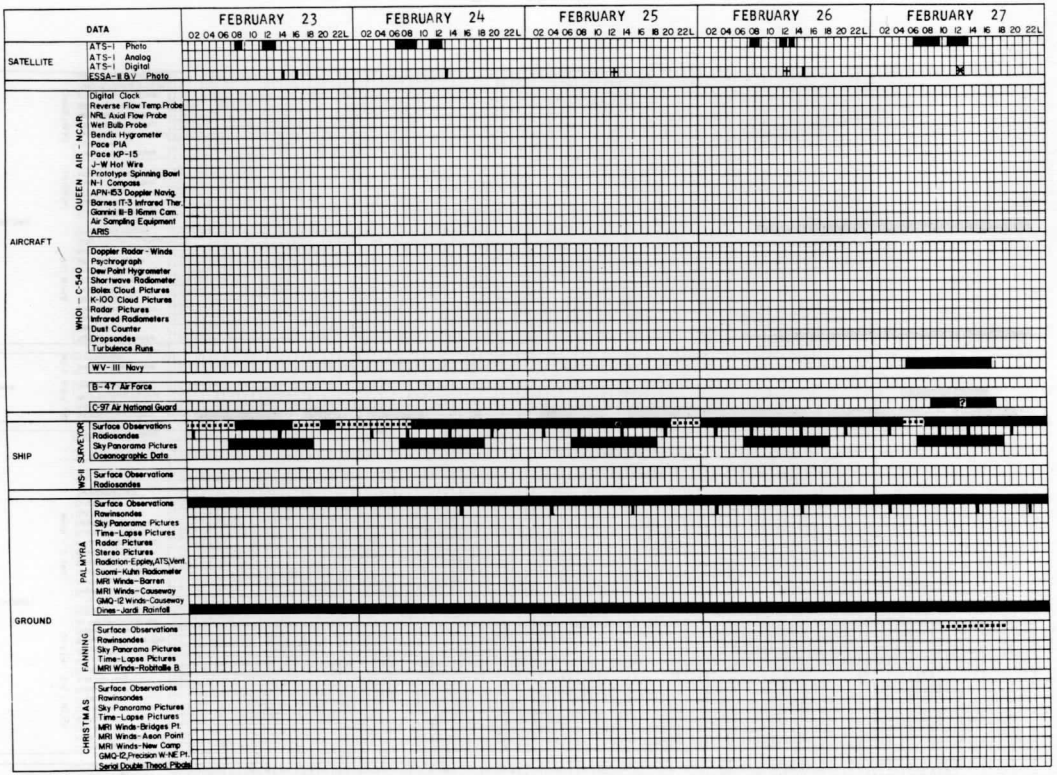
DATA
FEBRUARY 23
FEBRUARY 24
FEBRUARY 25
FEBRUARY 26
FEBRUARY 27
02 04 06 08 10 12 14 16 18 20 22L
SATELLITE
ATS-I Photo
ATS-I Analog
ATS-I Digital
ESSA-8 AVCS Photo
AIRCRAFT
QUEEN AIR - NCAR
Digital Clock
Reverse Flow Temp Probe
NRL Axial Flow Probe
Wet Bulb Probe
Bendix Hygrometer
Pace PIA
Pace KP-15
J-W Hot Wire
Prototype Spinning Bowl
N-1 Compass
APN-153 Doppler Navig.
Barnes IT-3 Infrared Ther.
Gianini 8-8 16mm Cam.
Air Sampling Equipment
ARIS
WHOI - C-540
Doppler Radar - Winds
Psychrograph
Dew Point Hygrometer
Shortreve Radiometer
Bolex Cloud Pictures
K-100 Cloud Pictures
Radar Pictures
Infrared Radiometers
Dust Counter
Dropsondes
Turbulence Runs
WV-III Navy
B-47 Air Force
C-97 Air National Guard
SHIP
SURVEYOR
Surface Observations
Radiosondes
Sky Panorama Pictures
Oceanographic Data
WSH
Surface Observations
Radiosondes
GROUND
PALMYRA
Surface Observations
Rawinsondes
Sky Panorama Pictures
Time-Lapse Pictures
Radar Pictures
Stereo Pictures
Radiation-Eppley,ATS,Vent
Suomi-Kuhn Radiometer
MRI Winds-Barren
MRI Winds-Causeway
GMD-12 Winds-Causeway
Dines-Jardi Rainfall
FANNING
Surface Observations
Rawinsondes
Sky Panorama Pictures
Time-Lapse Pictures
MRI Winds-Robitaille B.
CHRISTMAS
Surface Observations
Rawinsondes
Sky Panorama Pictures
Time-Lapse Pictures
MRI Winds-Bridges Pt.
MRI Winds-Aeon Point
MRI Winds-New Camp
GMD-12,Precision W-NE Pt.
Serial Double Theod. Pibals

Fig. 3c

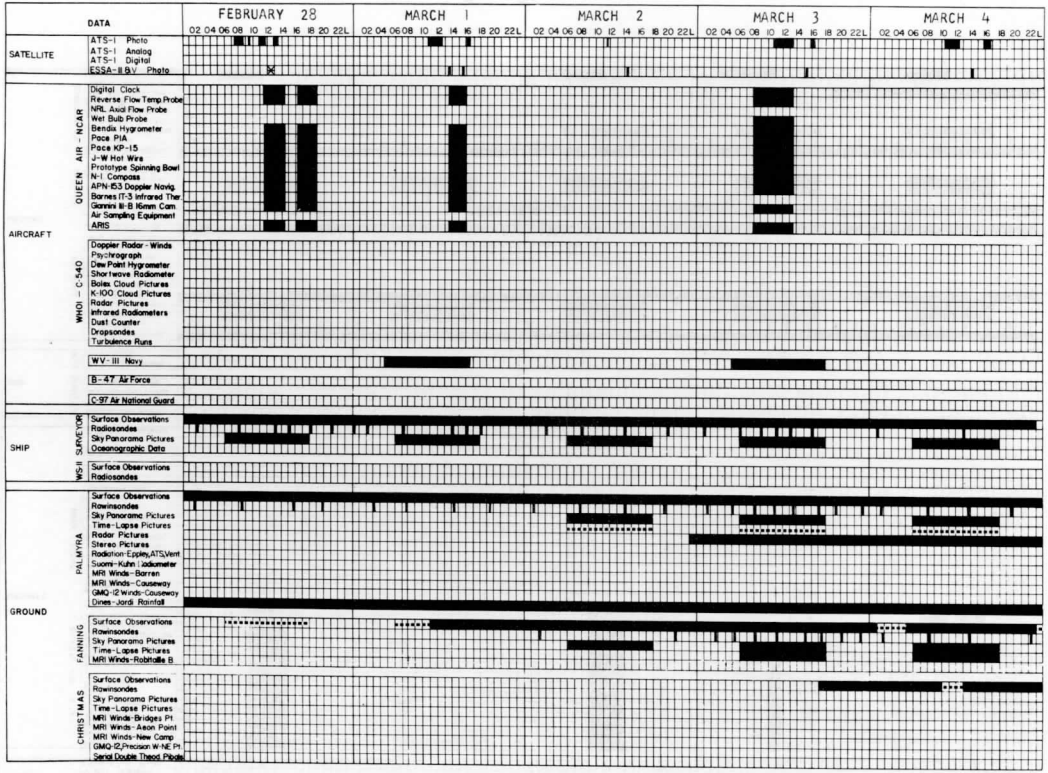
DATA
FEBRUARY 28
MARCH 1
MARCH 2
MARCH 3
MARCH 4
02 04 06 08 10 12 14 16 18 20 22L
SATELLITE
ATS-I Photo
ATS-I Analog
ATS-I Digital
ESSA-III & V Photo
AIRCRAFT
QUEEN AIR - NCAR
Digital Clock
Reverse Flow Temp Probe
NRL Axial Flow Probe
Wet Bulb Probe
Bendix Hygrometer
Pace PIA
Pace KP-15
J-W Hot Wire
Prototype Spinning Bowl
N-1 Compass
APN-153 Doppler Navig
Barnes IT-3 Infrared Ther
Gimmi III-B 16mm Cam
Air Sampling Equipment
ARIS
WHOI - C-540
Doppler Radar - Winds
Psychrograph
Dew Point Hygrometer
Shortwave Radiometer
Boles Cloud Pictures
K-100 Cloud Pictures
Radar Pictures
Infrared Radiometers
Dust Counter
Dropsondes
Turbulence Runs
WV - III Navy
B-47 Air Force
C-97 Air National Guard
SHIP
SURVEYOR
Surface Observations
Radiosondes
Sky Panorama Pictures
Oceanographic Data
WSII
Surface Observations
Radiosondes
GROUND
PALMYRA
Surface Observations
Rawinsondes
Sky Panorama Pictures
Time-Lapse Pictures
Radar Pictures
Stereo Pictures
Radiation-Eppley,ATS,Verf
Suomi-Kuhn Radiometer
MRI Winds-Barren
MRI Winds-Causeway
GMQ-12 Winds-Causeway
Dines-Jordi Rainfall
FANNING
Surface Observations
Rawinsondes
Sky Panorama Pictures
Time-Lapse Pictures
MRI Winds-Robitaille B
CHRISTMAS
Surface Observations
Rawinsondes
Sky Panorama Pictures
Time-Lapse Pictures
MRI Winds-Bridges Pt
MRI Winds-Aeon Point
MRI Winds-New Camp
GMQ-12,Precison W-NE Pt
Serial Double Theod Pibals

Fig. 3d

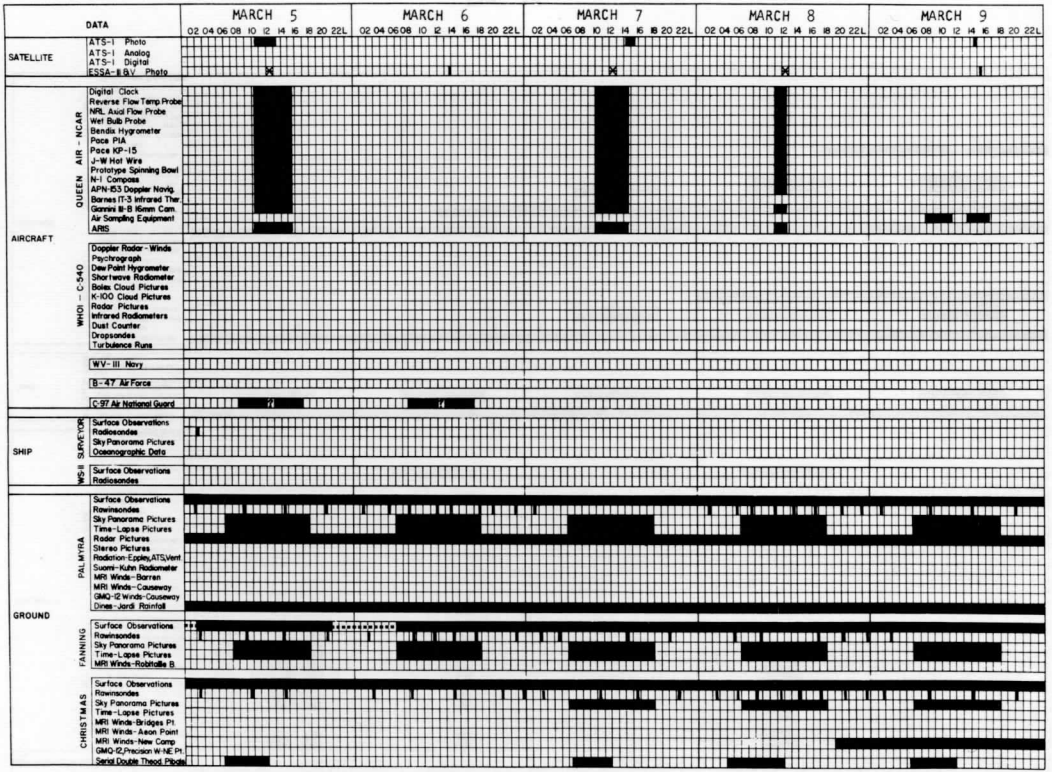
DATA
MARCH 5
MARCH 6
MARCH 7
MARCH 8
MARCH 9
02 04 06 08 10 12 14 16 18 20 22L
SATELLITE
ATS-I Photo
ATS-I Analog
ATS-I Digital
ESSA-8 & V Photo
AIRCRAFT
QUEEN AIR - NCAR
Digital Clock
Reverse Flow Temp Probe
NRL Axial Flow Probe
Wet Bulb Probe
Bendix Hygrometer
Pace PIA
Pace KP-15
J-W Hot Wire
Prototype Spinning Bowl
N-1 Compass
APN-153 Doppler Navig.
Barnes IT-3 Infrared Ther.
Gannis IR-B 16mm Cam.
Air Sampling Equipment
ARIS
WHOI - C-540
Doppler Radar - Winds
Psychrograph
Dew Point Hygrometer
Shortwave Radiometer
Bolex Cloud Pictures
K-100 Cloud Pictures
Radar Pictures
Infrared Radiometers
Dust Counter
Dropsondes
Turbulence Runs
WV-III Navy
B-47 Air Force
C-97 Air National Guard
SHIP
SURVEYOR
Surface Observations
Radiosondes
Sky Panorama Pictures
Oceanographic Data
WSR
Surface Observations
Radiosondes
GROUND
PALMYRA
Surface Observations
Rawinsondes
Sky Panorama Pictures
Time-Lapse Pictures
Radar Pictures
Stereo Pictures
Radiation-Epply,ATS,Vent
Suomi-Kuhn Radiometer
MRI Winds-Barren
MRI Winds-Causeway
GMQ-12 Winds-Causeway
Dines-Jardi Rainfall
FANNING
Surface Observations
Rawinsondes
Sky Panorama Pictures
Time-Lapse Pictures
MRI Winds-Robitaille B.
CHRISTMAS
Surface Observations
Rawinsondes
Sky Panorama Pictures
Time-Lapse Pictures
MRI Winds-Bridges Pt.
MRI Winds-Aeon Point
MRI Winds-New Camp
GMQ-12,Precison W-NE Pt.
Serial Double Theod. Pibals

Fig. 3e

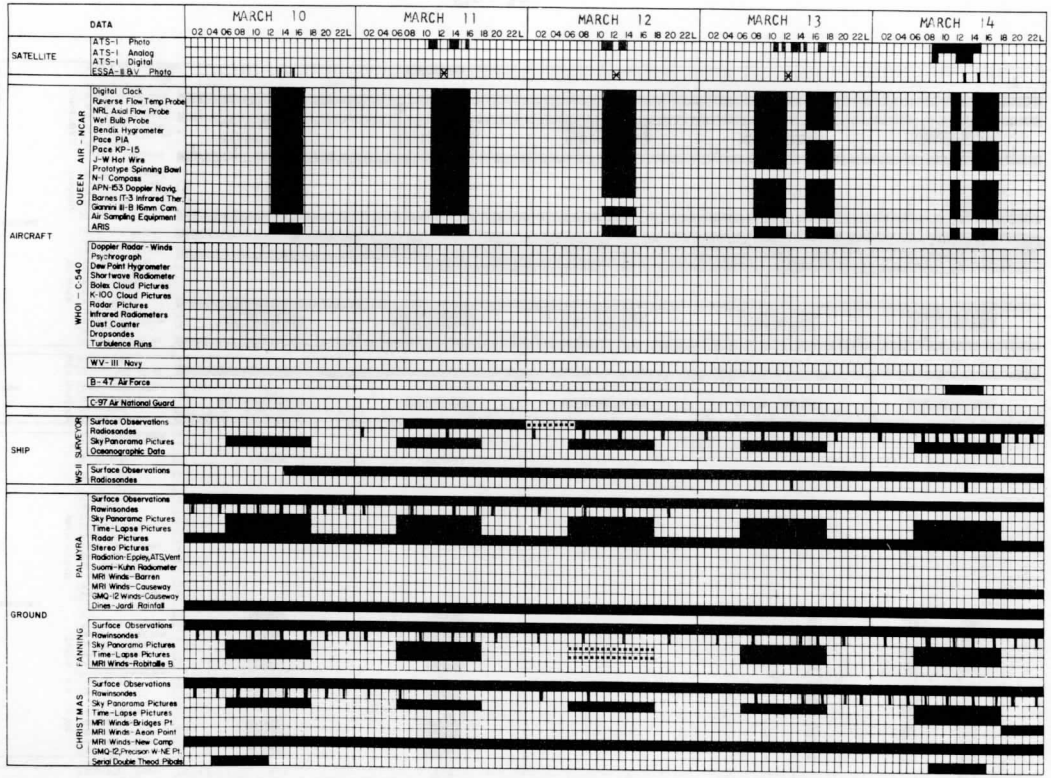
DATA
MARCH 10
MARCH 11
MARCH 12
MARCH 13
MARCH 14
02 04 06 08 10 12 14 16 18 20 22L
SATELLITE
ATS-1 Photo
ATS-1 Analog
ATS-1 Digital
ESSA-8 B/V Photo
AIRCRAFT
QUEEN AIR - NCAR
Digital Clock
Reverse Flow Temp Probe
NRL Axial Flow Probe
Wet Bulb Probe
Bendix Hygrometer
Pace PIA
Pace KP-15
J-W Hot Wire
Prototype Spinning Bowl
N-1 Compass
APN-153 Doppler Navig.
Barnes IT-3 Infrared Ther
Gannis III-B 16mm Cam
Air Sampling Equipment
ARIS
WMO - C-540
Doppler Radar - Winds
Psychrograph
Dew Point Hygrometer
Shortwave Radiometer
Boles Cloud Pictures
K-100 Cloud Pictures
Radar Pictures
Infrared Radiometers
Dust Counter
Dropsondes
Turbulence Runs
WV-III Navy
B-47 Air Force
C-97 Air National Guard
SHIP
SURFACE
Surface Observations
Radiosondes
Sky Panorama Pictures
Oceanographic Data
WSII
Surface Observations
Radiosondes
GROUND
PALMYRA
Surface Observations
Rawinsondes
Sky Panorama Pictures
Time-Lapse Pictures
Radar Pictures
Stereo Pictures
Radiation-Eppley,ATS,Vent
Suomi-Kuhn Radiometer
MRI Winds-Barren
MRI Winds-Causeway
GMQ-12 Winds-Causeway
Dines-Jordi Rainfall
FANNING
Surface Observations
Rawinsondes
Sky Panorama Pictures
Time-Lapse Pictures
MRI Winds-Robitaille 5
CHRISTMAS
Surface Observations
Rawinsondes
Sky Panorama Pictures
Time-Lapse Pictures
MRI Winds-Bridges Pt
MRI Winds-Aeon Point
MRI Winds-New Comp.
GMQ-12,Precison W-NE Pt.
Serial Double Theod Pibals

Fig. 3f

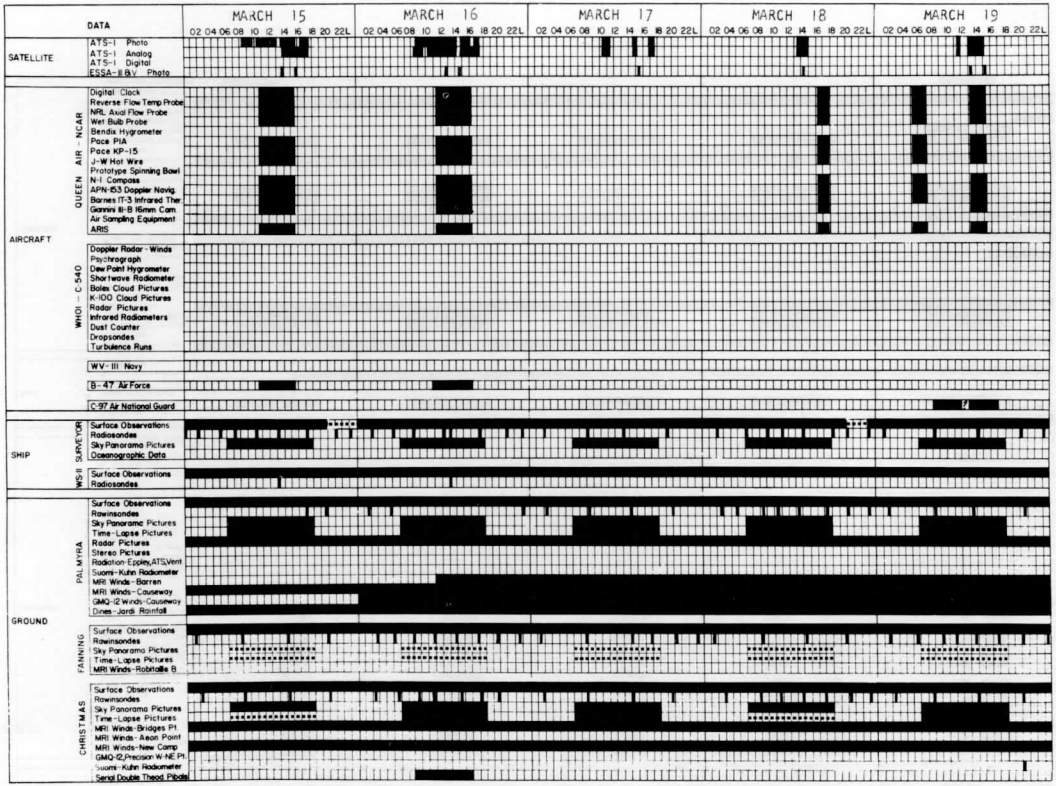
DATA
MARCH 15
MARCH 16
MARCH 17
MARCH 18
MARCH 19
02 04 06 08 10 12 14 16 18 20 22L
SATELLITE
ATS-1 Photo
ATS-1 Analog
ATS-1 Digital
ESSA-8 B/W Photo
AIRCRAFT
QUEEN AIR - NCAR
Digital Clock
Reverse Flow Temp Probe
NRL Axial Flow Probe
Wet Bulb Probe
Bendix Hygrometer
Pace PIA
Pace KP-15
J-W Hot Wire
Prototype Spinning Bowl
N-1 Compass
APN-153 Doppler Navig.
Barnes IT-3 Infrared Ther
Gamini III-B 16mm Cam.
Air Sampling Equipment
ARIS
WHOI - C 540
Doppler Radar - Winds
Psychrograph
Dew Point Hygrometer
Shortwave Radiometer
Bolex Cloud Pictures
K-100 Cloud Pictures
Radar Pictures
Infrared Radiometers
Dust Counter
Dropsondes
Turbulence Runs
WV-III Navy
B-47 Air Force
C-97 Air National Guard
SHIP
SURVEYOR
Surface Observations
Radiosondes
Sky Panorama Pictures
Oceanographic Data
WSII
Surface Observations
Radiosondes
GROUND
PALMYRA
Surface Observations
Rawinsondes
Sky Panorama Pictures
Time-Lapse Pictures
Radar Pictures
Stereo Pictures
Radiation-Eppley,ATS,Vent
Suomi-Kuhn Radiometer
MRI Winds-Barren
MRI Winds-Causeway
GMQ-12 Winds-Causeway
Dines-Jardi Rainfall
FANNING
Surface Observations
Rawinsondes
Sky Panorama Pictures
Time-Lapse Pictures
MRI Winds-Robitaille B
CHRISTMAS
Surface Observations
Rawinsondes
Sky Panorama Pictures
Time-Lapse Pictures
MRI Winds-Bridges Pt.
MRI Winds-Aeon Point
MRI Winds-New Camp
GMQ-12,Precison W-NE Pt.
Suomi-Kuhn Radiometer
Serial Double Theod. Pibals

Fig. 3g

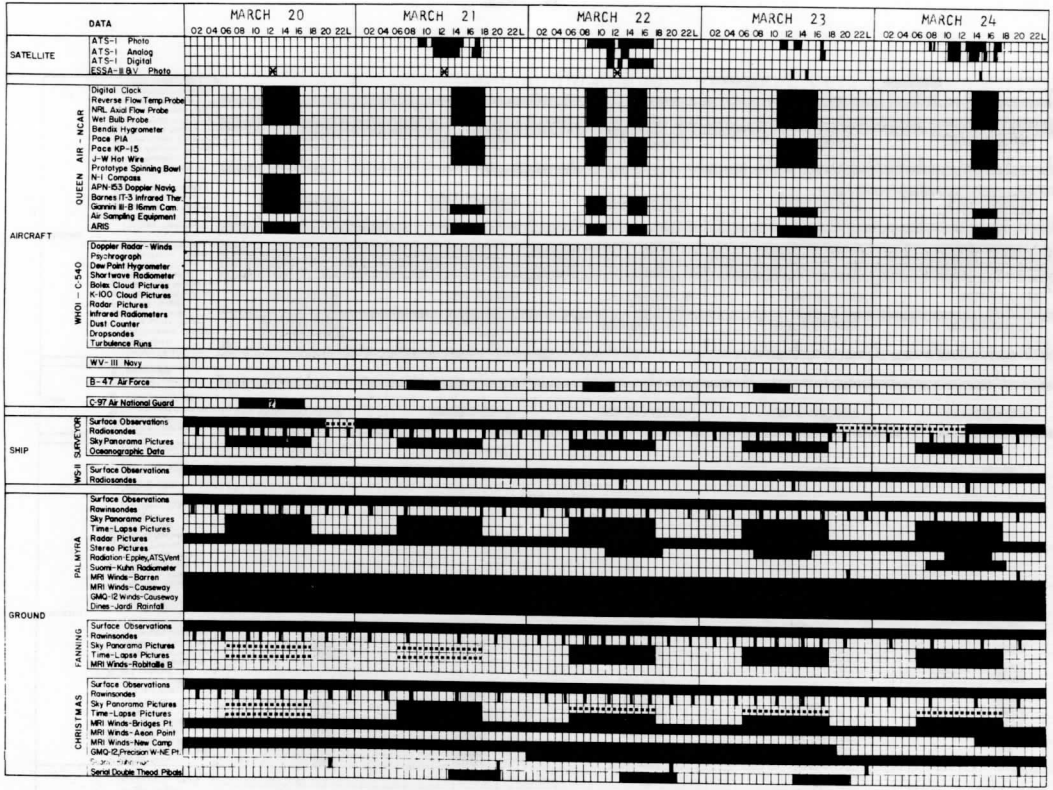
DATA
MARCH 20
MARCH 21
MARCH 22
MARCH 23
MARCH 24
02 04 06 08 10 12 14 16 18 20 22L
SATELLITE
ATS-I Photo
ATS-I Analog
ATS-I Digital
ESSA-II B&V Photo
AIRCRAFT
QUEEN AIR - NCAR
Digital Clock
Reverse Flow Temp Probe
NRL Axial Flow Probe
Wet Bulb Probe
Bendix Hygrometer
Pace P1A
Pace KP-15
J-W Hot Wire
Prototype Spinning Bowl
N-1 Compass
APN-153 Doppler Navig
Barnes IT-3 Infrared Ther
Gannis III-B 16mm Cam
Air Sampling Equipment
ARIS
WHOI - C-540
Doppler Radar - Winds
Psychrograph
Dew Point Hygrometer
Shortwave Radiometer
Boles Cloud Pictures
K-100 Cloud Pictures
Radar Pictures
Infrared Radiometers
Dust Counter
Dropsondes
Turbulence Runs
WV-III Navy
B-47 Air Force
C-97 Air National Guard
SHIP
SURVEYOR
Surface Observations
Radiosondes
Sky Panorama Pictures
Oceanographic Data
WSFI
Surface Observations
Radiosondes
GROUND
PALMYRA
Surface Observations
Rawinsondes
Sky Panorama Pictures
Time-Lapse Pictures
Radar Pictures
Stereo Pictures
Radiation Eppley,ATS,Vent
Suomi-Kuhn Radiometer
MRI Winds-Barren
MRI Winds-Causeway
GMQ-12 Winds-Causeway
Dines-Jardi Rainfall
FANNING
Surface Observations
Rawinsondes
Sky Panorama Pictures
Time-Lapse Pictures
MRI Winds-Robitaille B
CHRISTMAS
Surface Observations
Rawinsondes
Sky Panorama Pictures
Time-Lapse Pictures
MRI Winds-Bridges Pt
MRI Winds-Aeon Point
MRI Winds-New Camp
GMQ-12,Precision W-NE Pt
Serial Double Theod Pibals

Fig. 3h

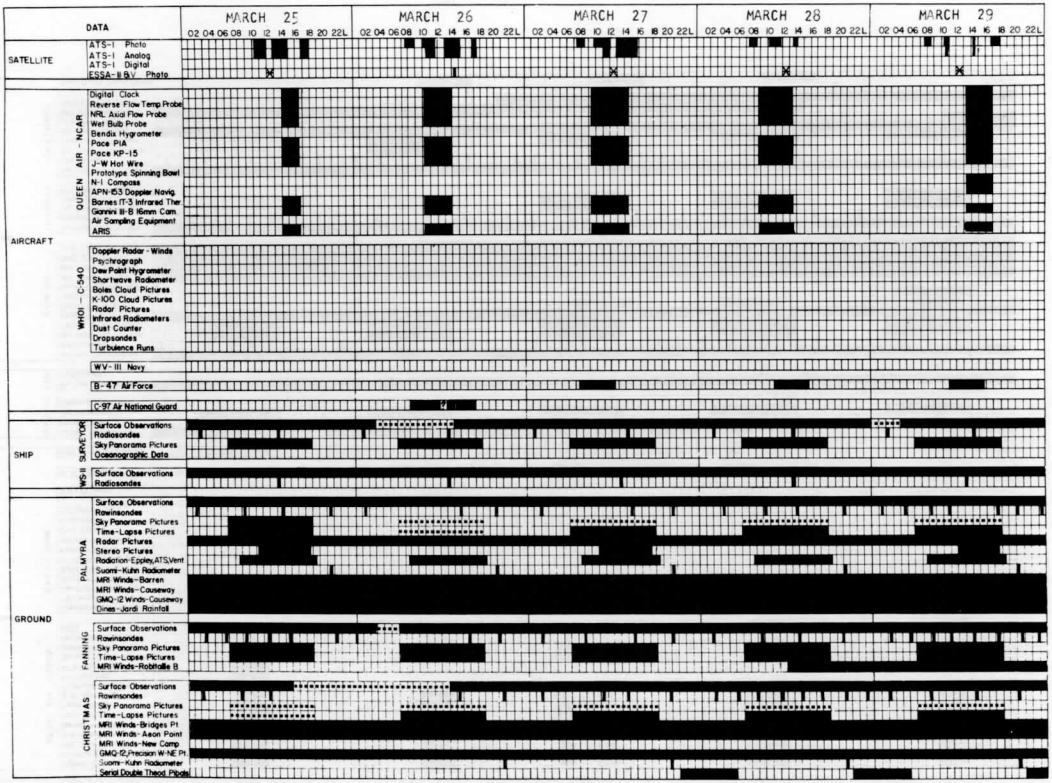
DATA
MARCH 25
MARCH 26
MARCH 27
MARCH 28
MARCH 29
02 04 06 08 10 12 14 16 18 20 22L
SATELLITE
ATS-1 Photo
ATS-1 Analog
ATS-1 Digital
ESSA-8 & V Photo
AIRCRAFT
QUEEN AIR - NCAR
Digital Clock
Reverse Flow Temp Probe
NRL Axial Flow Probe
Wet Bulb Probe
Bendix Hygrometer
Pace PIA
Pace KP-15
J-W Hot Wire
Prototype Spinning Bowl
N-1 Compass
APN-153 Doppler Navig.
Barnes IT-3 Infrared Ther.
Gianni's II-B 16mm Cam.
Air Sampling Equipment
ARS
WHOI - C-540
Doppler Radar - Winds
Psychrograph
Dew Point Hygrometer
Shortwave Radiometer
Boles Cloud Pictures
K-100 Cloud Pictures
Radar Pictures
Infrared Radiometers
Dust Counter
Dropsondes
Turbulence Runs
WV-III Navy
B-47 Air Force
C-97 Air National Guard
SHIP
SURVEYOR
Surface Observations
Radiosondes
Sky Panorama Pictures
Oceanographic Data
WSII
Surface Observations
Radiosondes
GROUND
PALMYRA
Surface Observations
Rawinsondes
Sky Panorama Pictures
Time-Lapse Pictures
Radar Pictures
Stereo Pictures
Radiation-Eppley,ATS,Vent
Suomi-Kuhn Radiometer
MRI Winds-Barren
MRI Winds-Causeway
GMQ-12 Winds-Causeway
Dines-Jordi Rainfall
FANNING
Surface Observations
Rawinsondes
Sky Panorama Pictures
Time-Lapse Pictures
MRI Winds-Robitaille B
CHRISTMAS
Surface Observations
Rawinsondes
Sky Panorama Pictures
Time-Lapse Pictures
MRI Winds-Bridges Pt
MRI Winds-Aeon Point
MRI Winds-New Camp
GMQ-12,Precison W-NE Pt
Suomi-Kuhn Radiometer
Serial Double Theod. Pibals

Fig. 3i

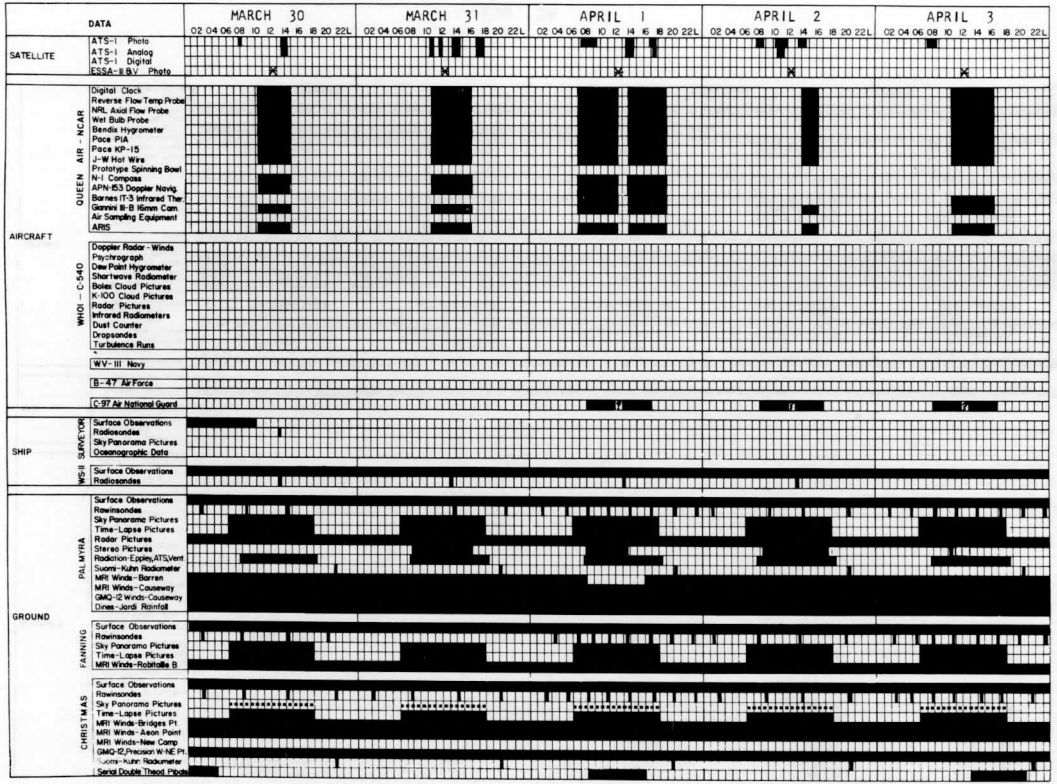
DATA
MARCH 30
MARCH 31
APRIL 1
APRIL 2
APRIL 3
02 04 06 08 10 12 14 16 18 20 22L
SATELLITE
ATS-I Photo
ATS-I Analog
ATS-I Digital
ESSA-II & V Photo
AIRCRAFT
QUEEN AIR - NCAR
Digital Clock
Reverse Flow Temp Probe
NRL Axial Flow Probe
Wet Bulb Probe
Bendix Hygrometer
Pace PIA
Pace KP-15
J-W Hot Wire
Prototype Spinning Bowl
N-1 Compass
APN-153 Doppler Navig.
Barnes IT-3 Infrared Ther
Gianini B-B 16mm Cam
Air Sampling Equipment
ARIS
WMO - C-540
Doppler Radar - Winds
Psychrograph
Dew Point Hygrometer
Shortwave Radiometer
Boles Cloud Pictures
K-100 Cloud Pictures
Radar Pictures
Infrared Radiometers
Dust Counter
Dropsondes
Turbulence Runs
WV-III Navy
B-47 Air Force
C-97 Air National Guard
SHIP
SURVEYOR
Surface Observations
Radiosondes
Sky Panorama Pictures
Oceanographic Data
WEST
Surface Observations
Radiosondes
GROUND
PALMYRA
Surface Observations
Rawinsondes
Sky Panorama Pictures
Time-Lapse Pictures
Radar Pictures
Stereo Pictures
Radiation-Eppley,ATS,Vent
Suomi-Kuhn Radiometer
MRI Winds-Barren
MRI Winds-Causeway
GMQ-12 Winds-Causeway
Dines-Jordi Rainfall
FANNING
Surface Observations
Rawinsondes
Sky Panorama Pictures
Time-Lapse Pictures
MRI Winds-Robitaille B
CHRISTMAS
Surface Observations
Rawinsondes
Sky Panorama Pictures
Time-Lapse Pictures
MRI Winds-Bridges Pt.
MRI Winds-Aeon Point
MRI Winds-New Camp
GMQ-12,Precision W-NE Pt.
Suomi-Kuhn Radiometer
Serial Double Theod. Pibals

Fig. 3j

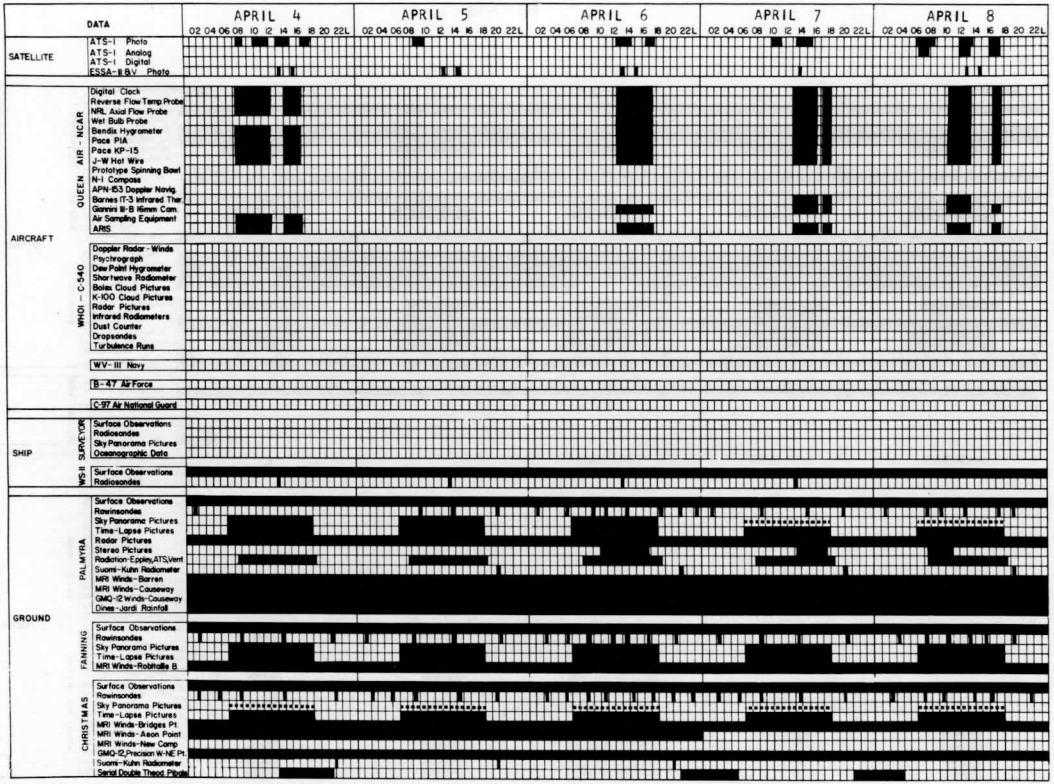
DATA
APRIL 4
APRIL 5
APRIL 6
APRIL 7
APRIL 8
02 04 06 08 10 12 14 16 18 20 22L
SATELLITE
ATS-1 Photo
ATS-1 Analog
ATS-1 Digital
ESSA-8 & V Photo
AIRCRAFT
QUEEN AIR - NCAR
Digital Clock
Reverse Flow Temp Probe
NRL Axial Flow Probe
Wet Bulb Probe
Bendix Hygrometer
Pace PIA
Pace KP-15
J-W Hot Wire
Prototype Spinning Bowl
N-1 Compass
APN-153 Doppler Navig.
Barnes IT-3 Infrared Ther.
Gannini III-B 16mm Cam.
Air Sampling Equipment
ARIS
WHOI - C-540
Doppler Radar - Winds
Psychrograph
Dew Point Hygrometer
Shortwave Radiometer
Boles Cloud Pictures
K-100 Cloud Pictures
Radar Pictures
Infrared Radiometers
Dust Counter
Dropsondes
Turbulence Runs
WV-III Navy
B-47 Air Force
C-97 Air National Guard
SHIP
SURVEYOR
Surface Observations
Radiosondes
Sky Panorama Pictures
Oceanographic Data
WSII
Surface Observations
Radiosondes
GROUND
PALMYRA
Surface Observations
Rawinsondes
Sky Panorama Pictures
Time-Lapse Pictures
Radar Pictures
Stereo Pictures
Radiation-Eppley,ATS,Vent
Suomi-Kuhn Radiometer
MRI Winds-Barren
MRI Winds-Causeway
GMQ-12 Winds-Causeway
Dines-Jordi Rainfall
FANNING
Surface Observations
Rawinsondes
Sky Panorama Pictures
Time-Lapse Pictures
MRI Winds-Robitaille B
CHRISTMAS
Surface Observations
Rawinsondes
Sky Panorama Pictures
Time-Lapse Pictures
MRI Winds-Bridges Pt.
MRI Winds-Aeon Point
MRI Winds-New Camp
GMQ-12,Precison W-NE Pt.
Suomi-Kuhn Radiometer
Serial Double Theod. Pibals

Fig. 3k

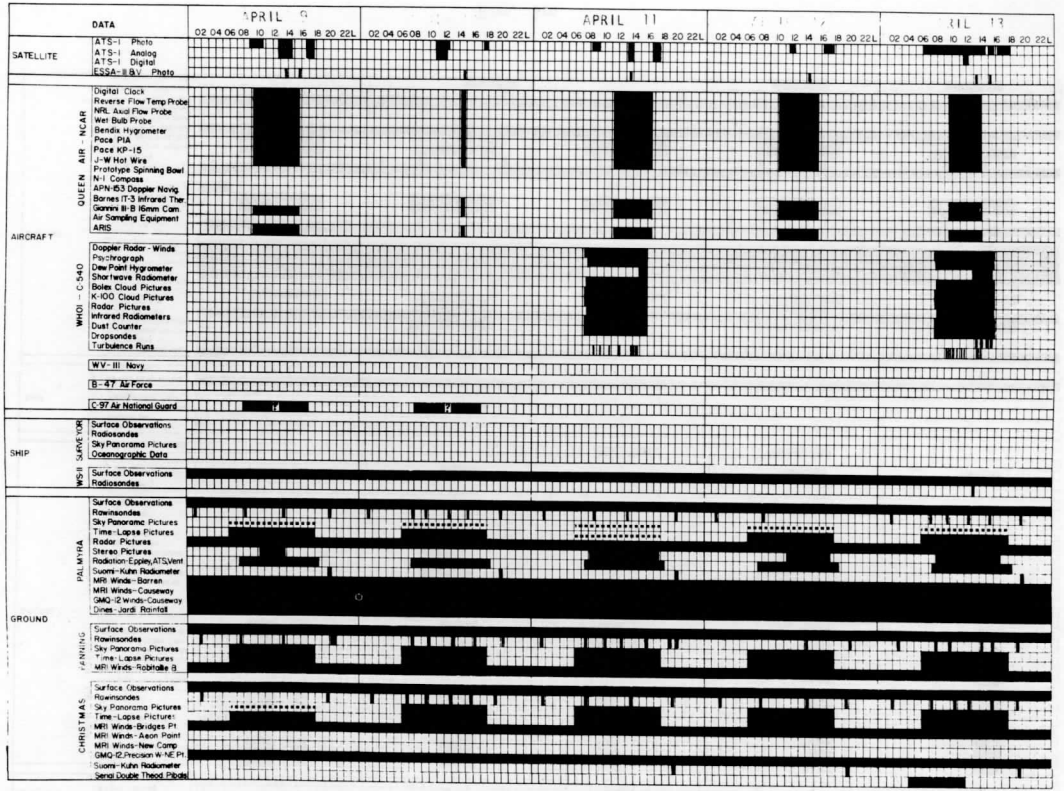
DATA
APRIL 9
APRIL 11
02 04 06 08 10 12 14 16 18 20 22L
SATELLITE
ATS-I Photo
ATS-I Analog
ATS-I Digital
ESSA-8 &V Photo
AIRCRAFT
QUEEN AIR - NCAR
Digital Clock
Reverse Flow Temp Probe
NRL Axial Flow Probe
Wet Bulb Probe
Bendix Hygrometer
Pace PIA
Pace KP-15
J-W Hot Wire
Prototype Spinning Bowl
N-1 Compass
APN-153 Doppler Navig
Barnes IT-3 Infrared Ther
Gamma III-B 16mm Cam
Air Sampling Equipment
ARIS
WHOI - C-540
Doppler Radar - Winds
Psychrograph
Dew Point Hygrometer
Shortwave Radiometer
Bolex Cloud Pictures
K-100 Cloud Pictures
Radar Pictures
Infrared Radiometers
Dust Counter
Dropsondes
Turbulence Runs
WV-III Navy
B-47 Air Force
C-97 Air National Guard
SHIP
SURVEYOR
Surface Observations
Radiosondes
Sky Panorama Pictures
Oceanographic Data
WSB
Surface Observations
Radiosondes
GROUND
PALMYRA
Surface Observations
Rawinsondes
Sky Panorama Pictures
Time-Lapse Pictures
Radar Pictures
Stereo Pictures
Radiation-Eppley,ATS,Vent
Suomi-Kuhn Radiometer
MRI Winds-Barren
MRI Winds-Causeway
GMQ-12 Winds-Causeway
Dines-Jardi Rainfall
FANNING
Surface Observations
Rawinsondes
Sky Panorama Pictures
Time-Lapse Pictures
MRI Winds-Rabbitts B
CHRISTMAS
Surface Observations
Rawinsondes
Sky Panorama Pictures
Time-Lapse Pictures
MRI Winds-Bridges Pt
MRI Winds-Aeon Point
MRI Winds-New Camp
GMQ-12,Precision W-NE Pt
Suomi-Kuhn Radiometer
Serai Double Theod Pibals

Fig. 31

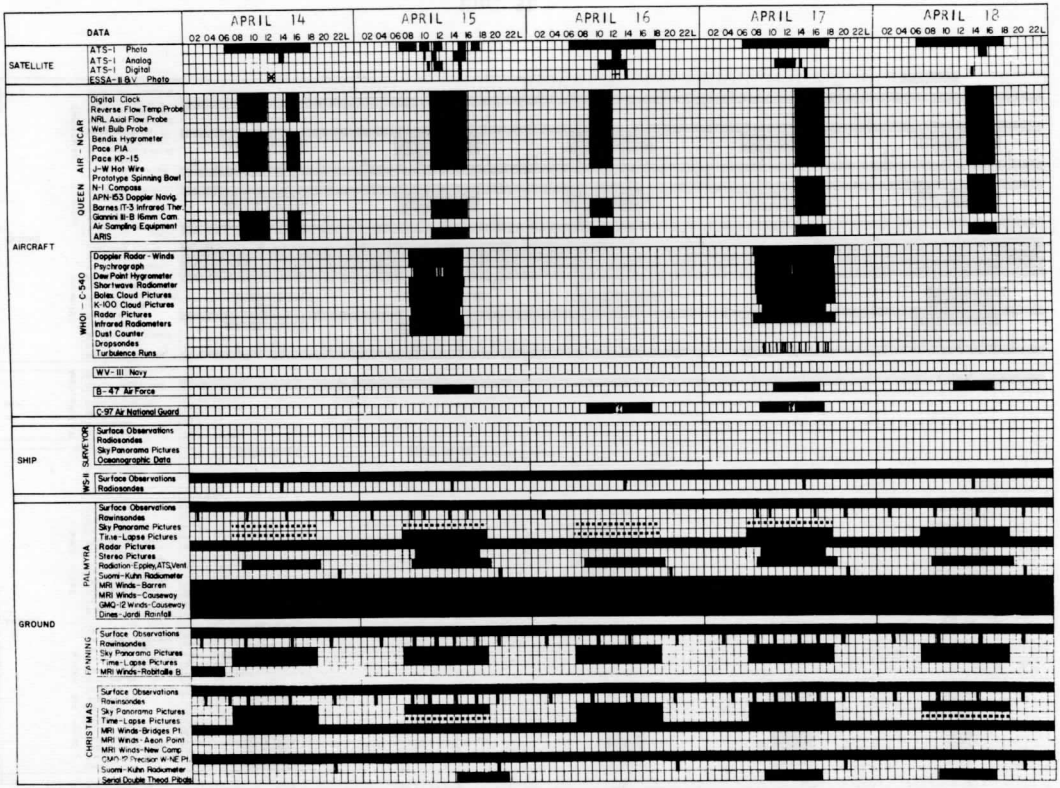
DATA
APRIL 14
APRIL 15
APRIL 16
APRIL 17
APRIL 18
02 04 06 08 10 12 14 16 18 20 22L
SATELLITE
ATS-1 Photo
ATS-1 Analog
ATS-1 Digital
ESSA-8 &V Photo
AIRCRAFT
QUEEN AIR - NCAR
Digital Clock
Reverse Flow Temp Probe
NRL Axial Flow Probe
Wet Bulb Probe
Bendix Hygrometer
Pace PIA
Pace KP-15
J-W Hot Wire
Prototype Spinning Bowl
N-1 Compass
APN-153 Doppler Navig.
Barnes IT-3 Infrared Ther.
Gianneri B-8 16mm Cam.
Air Sampling Equipment
ARIS
WHOI - C-540
Doppler Radar - Winds
Psychrograph
Dew Point Hygrometer
Shortwave Radiometer
Boles Cloud Pictures
K-100 Cloud Pictures
Radar Pictures
Infrared Radiometers
Dust Counter
Dropsondes
Turbulence Runs
WV-III Navy
B-47 Air Force
C-97 Air National Guard
SHIP
WSII SURVEYOR
Surface Observations
Radiosondes
Sky Panorama Pictures
Oceanographic Data
Surface Observations
Radiosondes
GROUND
PALMYRA
Surface Observations
Rawinsondes
Sky Panorama Pictures
Time-Lapse Pictures
Radar Pictures
Stereo Pictures
Radiation-Eppley,ATS,Vent
Suomi-Kuhn Radiometer
MRI Winds-Barren
MRI Winds-Causeway
GMD-2 Winds-Causeway
Dines-Jordi Rainfall
JANNING
Surface Observations
Rawinsondes
Sky Panorama Pictures
Time-Lapse Pictures
MRI Winds-Rabitaille Is
CHRISTMAS
Surface Observations
Rawinsondes
Sky Panorama Pictures
Time-Lapse Pictures
MRI Winds-Bridges Pt.
MRI Winds-Aeon Point
MRI Winds-New Comp.
GMD-2 Precise W-NE Pt.
Suomi-Kuhn Radiometer
Sensi Double Theod. Pibals

Fig. 3m

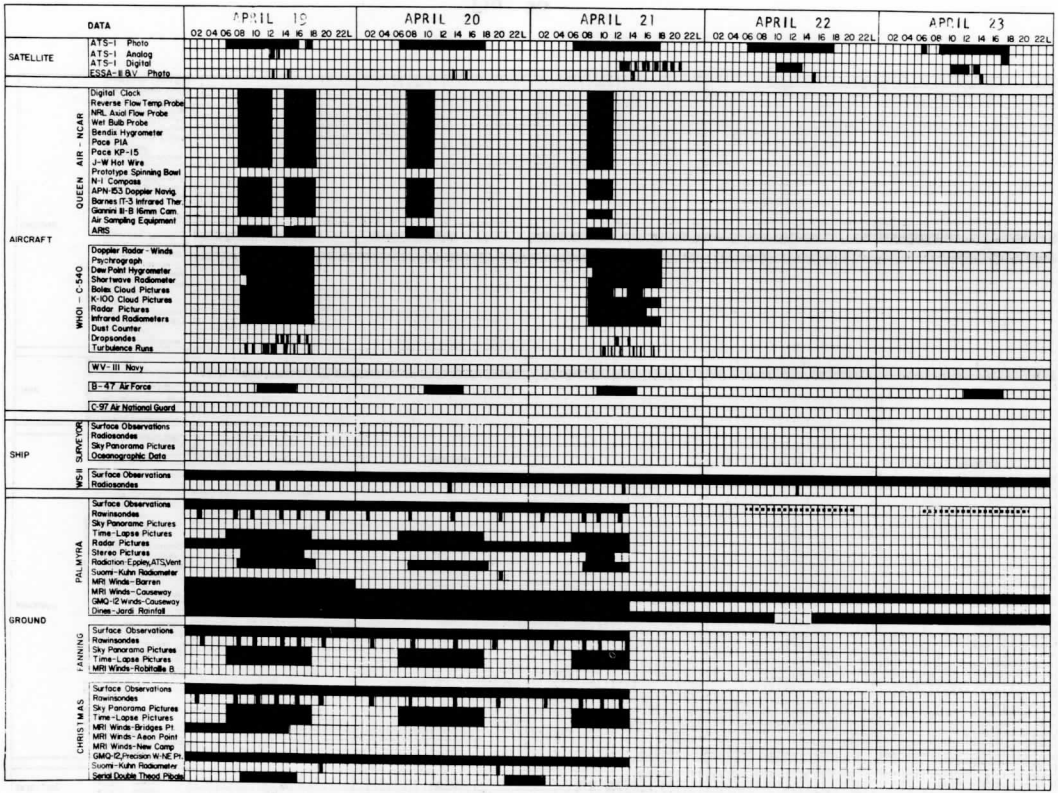
DATA
APRIL 19
APRIL 20
APRIL 21
APRIL 22
APRIL 23
02 04 06 08 10 12 14 16 18 20 22L
SATELLITE
ATS-I Photo
ATS-I Analog
ATS-I Digital
ESSA-II B.V. Photo
AIRCRAFT
QUEEN AIR - NCAR
Digital Clock
Reverse Flow Temp Probe
NRL Axial Flow Probe
Wet Bulb Probe
Bendix Hygrometer
Pace PIA
Pace KP-15
J-W Hot Wire
Prototype Spinning Bowl
N-1 Compass
APN-153 Doppler Navig.
Barnes IT-3 Infrared Ther
Gannini II-B 16mm Cam
Air Sampling Equipment
ARS
WHOI C-540
Doppler Radar - Winds
Psychrograph
Dew Point Hygrometer
Shortwave Radiometer
Bolex Cloud Pictures
K-100 Cloud Pictures
Radar Pictures
Infrared Radiometers
Dust Counter
Dropsondes
Turbulence Runs
WV-III Navy
B-47 Air Force
C-97 Air National Guard
SHIP
SURVEYOR
Surface Observations
Radiosondes
Sky Panorama Pictures
Oceanographic Data
WSN
Surface Observations
Radiosondes
GROUND
PALMYRA
Surface Observations
Rawinsondes
Sky Panorama Pictures
Time-Lapse Pictures
Radar Pictures
Stereo Pictures
Radiation: Eppley, ATS, Vent
Suomi-Kuhn Radiometer
MRI Winds - Barren
MRI Winds - Causeway
GMQ-12 Winds - Causeway
Dines - Jordi Rainfall
FANNING
Surface Observations
Rawinsondes
Sky Panorama Pictures
Time-Lapse Pictures
MRI Winds - Robitaille B
CHRISTMAS
Surface Observations
Rawinsondes
Sky Panorama Pictures
Time-Lapse Pictures
MRI Winds - Bridges Pt.
MRI Winds - Aeon Point
MRI Winds - New Camp
GMQ-12, Precison W-NE Pt.
Suomi-Kuhn Radiometer
Serial Double Theod Pibal

Fig. 3n

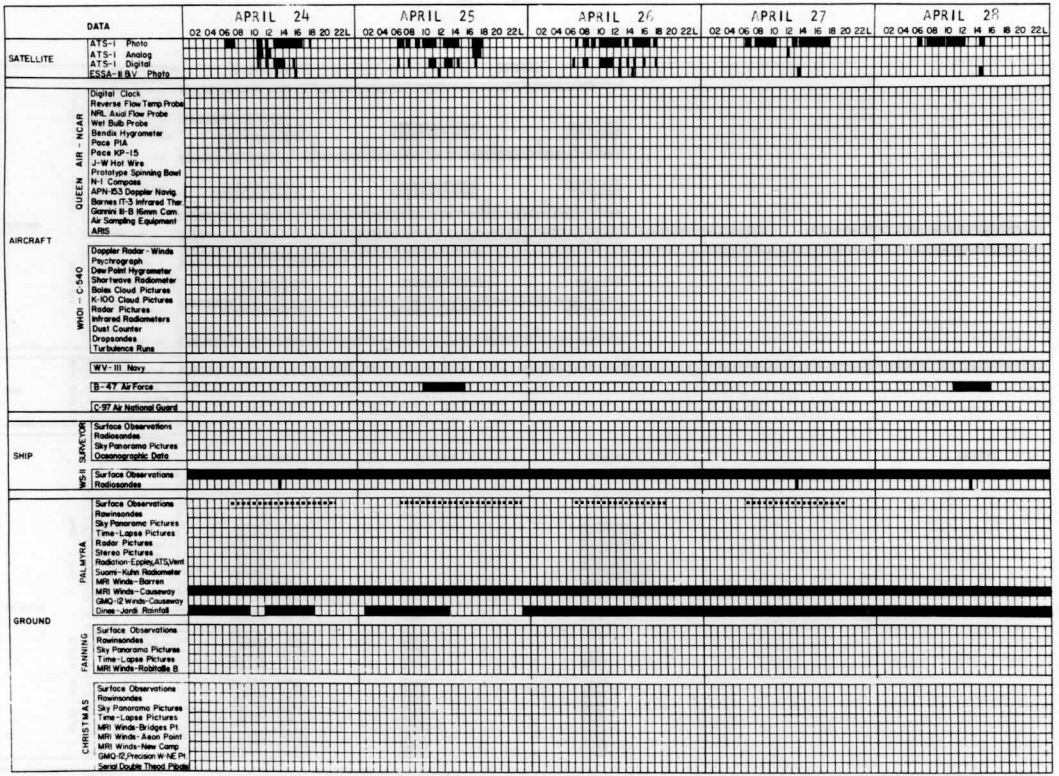
DATA
APRIL 24
APRIL 25
APRIL 26
APRIL 27
APRIL 28
02 04 06 08 10 12 14 16 18 20 22L
SATELLITE
ATS-1 Photo
ATS-1 Analog
ATS-1 Digital
ESSA-III B.V. Photo
AIRCRAFT
QUEEN AIR - NCAR
Digital Clock
Reverse Flow Temp Probe
NRL Axial Flow Probe
Wet Bulb Probe
Bendix Hygrometer
Pace PIA
Pace KP-15
J-W Hot Wire
Prototype Spinning Bowl
N-1 Compass
APN-153 Doppler Navig.
Barnes IT-3 Infrared Ther.
Gannini III-B 16mm Cam.
Air Sampling Equipment
ARIS
WHOI - C-54O
Doppler Radar - Winds
Psychrograph
Dew Point Hygrometer
Shortwave Radiometer
Bales Cloud Pictures
K-100 Cloud Pictures
Radar Pictures
Infrared Radiometers
Dust Counter
Dropsondes
Turbulence Runs
WV-III Navy
B-47 Air Force
C-97 Air National Guard
SHIP
SURVEYOR
Surface Observations
Radiosondes
Sky Panorama Pictures
Oceanographic Data
WSB
Surface Observations
Radiosondes
GROUND
PALMYRA
Surface Observations
Rawinsondes
Sky Panorama Pictures
Time-Lapse Pictures
Radar Pictures
Stereo Pictures
Radiation-Eppley,ATS,Vent
Suomi-Kuhn Radiometer
MRI Winds-Barren
MRI Winds-Causeway
GMQ-12 Winds-Causeway
Dines-Jordi Rainfall
FANNING
Surface Observations
Rawinsondes
Sky Panorama Pictures
Time-Lapse Pictures
MRI Winds-Robitaille B
CHRISTMAS
Surface Observations
Rawinsondes
Sky Panorama Pictures
Time-Lapse Pictures
MRI Winds-Bridges Pt.
MRI Winds-Ason Point
MRI Winds-New Camp
GMQ-12,Precison W-NE Pt.
Serial Double Theod. Pibals

Fig. 3o

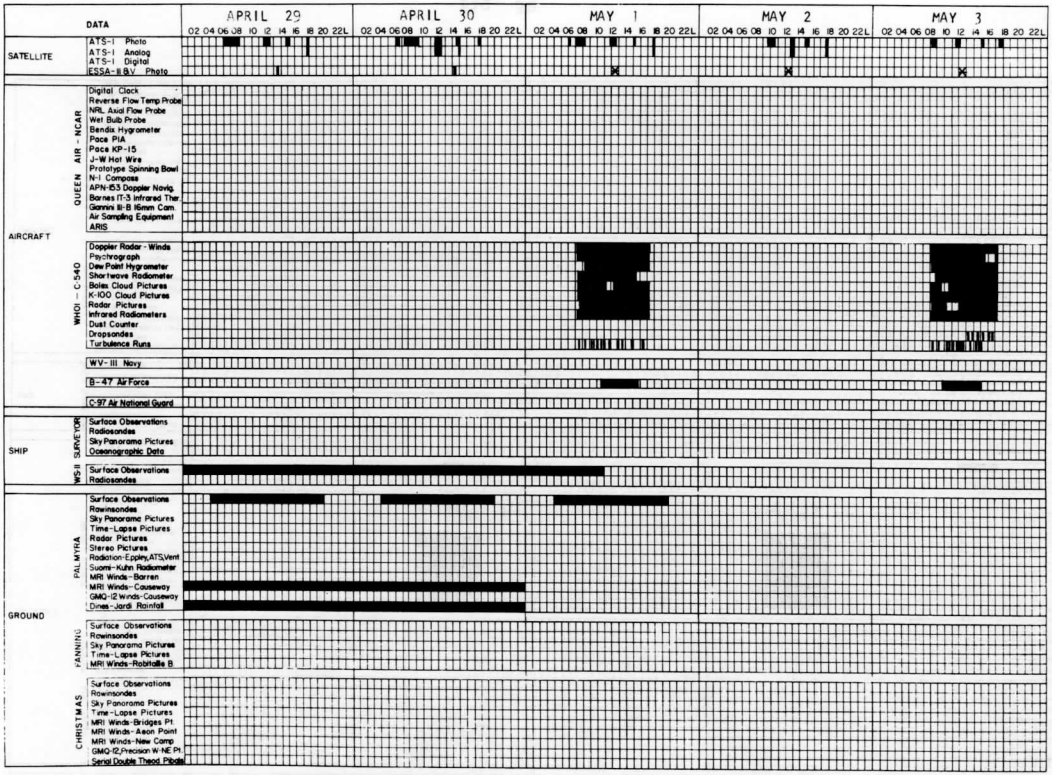
DATA
APRIL 29
APRIL 30
MAY 1
MAY 2
MAY 3
02 04 06 08 10 12 14 16 18 20 22L
SATELLITE
ATS-I Photo
ATS-I Analog
ATS-I Digital
ESSA-8 B/W Photo
AIRCRAFT
QUEEN AIR - NCAR
Digital Clock
Reverse Flow Temp Probe
NRL Axial Flow Probe
Wet Bulb Probe
Bendix Hygrometer
Pace PIA
Pace KP-15
J-W Hot Wire
Prototype Spinning Bowl
N-1 Compass
APN-153 Doppler Navig.
Barnes IT-3 Infrared Ther
Gannin Bi-B 16mm Cam
Air Sampling Equipment
ARIS
WHOI - C-540
Doppler Radar - Winds
Psychrograph
Dew Point Hygrometer
Shortwave Radiometer
Boles Cloud Pictures
K-100 Cloud Pictures
Radar Pictures
Infrared Radiometers
Dust Counter
Dropsondes
Turbulence Runs
WV-III Navy
B-47 Air Force
C-97 Air National Guard
SHIP
SURVETOR
Surface Observations
Radiosondes
Sky Panorama Pictures
Oceanographic Data
WSH
Surface Observations
Radiosondes
GROUND
PALMYRA
Surface Observations
Rawinsondes
Sky Panorama Pictures
Time-Lapse Pictures
Radar Pictures
Stereo Pictures
Radiation-Eppley,ATS,Vent
Suomi-Kuhn Radiometer
MRI Winds-Barren
MRI Winds-Causeway
GMQ-12 Winds-Causeway
Dines-Jardi Rainfall
FANNING
Surface Observations
Rawinsondes
Sky Panorama Pictures
Time-Lapse Pictures
MRI Winds-Robitaille B
CHRISTMAS
Surface Observations
Rawinsondes
Sky Panorama Pictures
Time-Lapse Pictures
MRI Winds-Bridges Pt
MRI Winds-Axon Point
MRI Winds-New Camp
GMQ-12,Precision W-NE Pt
Sensi Double Theod. Pibals

Fig. 3p

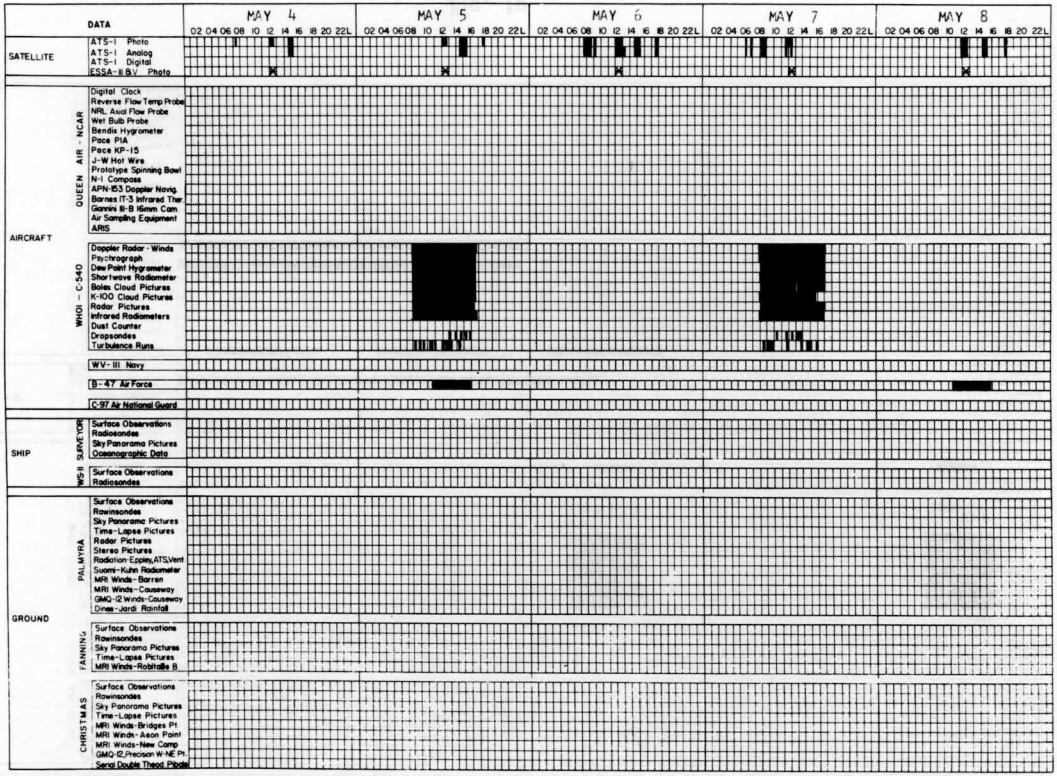
DATA
MAY 4
MAY 5
MAY 6
MAY 7
MAY 8
02 04 06 08 10 12 14 16 18 20 22L
SATELLITE
ATS-1 Photo
ATS-1 Analog
ATS-1 Digital
ESSA-8 BV Photo
AIRCRAFT
QUEEN AIR - NCAR
Digital Clock
Reverse Flow Temp Probe
NRL Axial Flow Probe
Wet Bulb Probe
Bendix Hygrometer
Pace PIA
Pace KP-15
J-W Hot Wire
Prototype Spinning Bowl
N-1 Compass
APN-153 Doppler Navig
Barnes IT-3 Infrared Ther
Gannin III-B 16mm Cam
Air Sampling Equipment
ARIS
WHOI - C-540
Doppler Radar - Winds
Psychrograph
Dew Point Hygrometer
Shortwave Radiometer
Boles Cloud Pictures
K-100 Cloud Pictures
Radar Pictures
Infrared Radiometers
Dust Counter
Dropsondes
Turbulence Runs
WV-III Navy
B-47 Air Force
C-97 Air National Guard
SHIP
SURVEYOR
Surface Observations
Radiosondes
Sky Panorama Pictures
Oceanographic Data
WSB
Surface Observations
Radiosondes
GROUND
PALMYRA
Surface Observations
Rawinsondes
Sky Panorama Pictures
Time-Lapse Pictures
Radar Pictures
Stereo Pictures
Radiation-Eppley,ATS,Vent
Suomi-Kuhn Radiometer
MRI Winds-Barren
MRI Winds-Causeway
GMQ-12 Winds-Causeway
Dines-Jordi Rainfall
FANNING
Surface Observations
Rawinsondes
Sky Panorama Pictures
Time-Lapse Pictures
MRI Winds-Robitaille B
CHRISTMAS
Surface Observations
Rawinsondes
Sky Panorama Pictures
Time-Lapse Pictures
MRI Winds-Bridges Pt
MRI Winds-Ason Point
MRI Winds-New Camp
GMQ-12,Precison W-NE Pt
Serial Double Theod Pibals

Fig. 3q

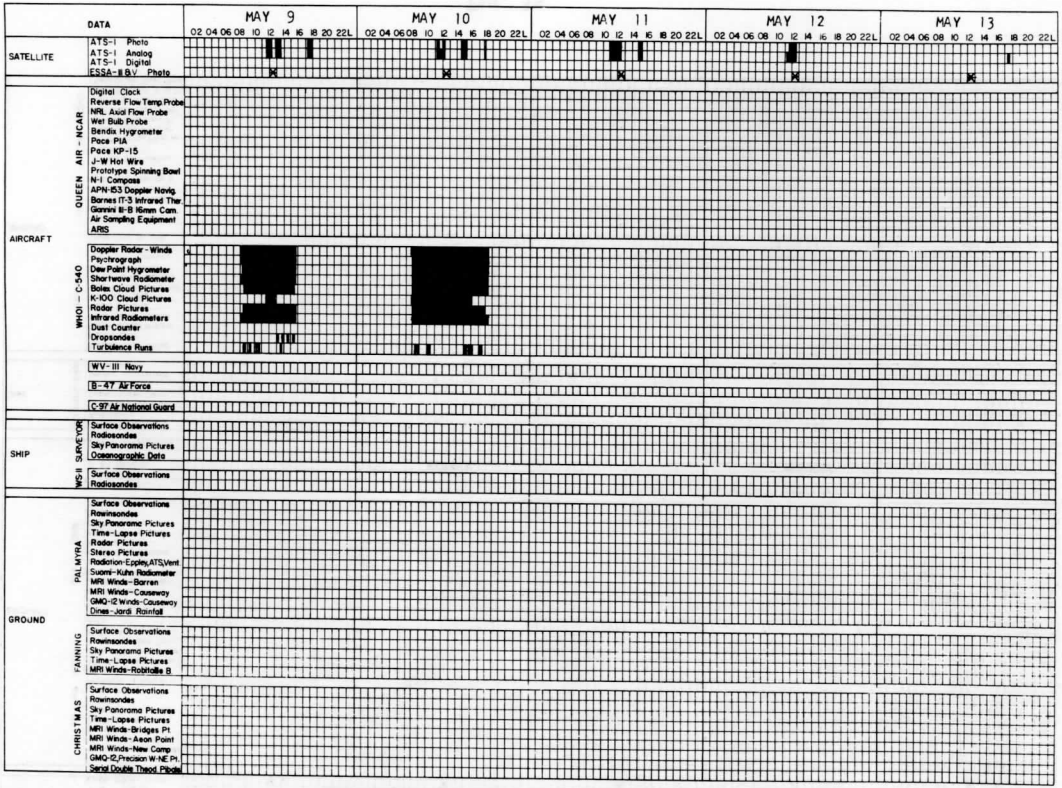
DATA
MAY 9
MAY 10
MAY 11
MAY 12
MAY 13
02 04 06 08 10 12 14 16 18 20 22L
SATELLITE
ATS-I Photo
ATS-I Analog
ATS-I Digital
ESSA-8 8V Photo
AIRCRAFT
QUEEN AIR - NCAR
Digital Clock
Reverse Flow Temp Probe
NRL Axial Flow Probe
Wet Bulb Probe
Bendix Hygrometer
Pace PIA
Pace KP-15
J-W Hot Wire
Prototype Spinning Bowl
N-I Compass
APN-153 Doppler Navig.
Barnes IT-3 Infrared Ther
Gimmi B-B 16mm Cam
Air Sampling Equipment
ARIS
WHO - C-540
Doppler Radar - Winds
Psychrograph
Dew Point Hygrometer
Shortwave Radiometer
Boles Cloud Pictures
K-100 Cloud Pictures
Radar Pictures
Infrared Radiometers
Dust Counter
Dropsondes
Turbulence Runs
WV-III Navy
B-47 Air Force
C-97 Air National Guard
SHIP
SURVEYOR
Surface Observations
Radiosondes
Sky Panorama Pictures
Oceanographic Data
WSH
Surface Observations
Radiosondes
GROUND
PALMYRA
Surface Observations
Rawinsondes
Sky Panorama Pictures
Time-Lapse Pictures
Radar Pictures
Stereo Pictures
Radiation-Eppley,ATS,Vert
Suomi-Kuhn Radiometer
MRI Winds-Barren
MRI Winds-Causeway
GMQ-12 Winds-Causeway
Dines-Jardi Rainfall
FANNING
Surface Observations
Rawinsondes
Sky Panorama Pictures
Time-Lapse Pictures
MRI Winds-Robitalle B
CHRISTMAS
Surface Observations
Rawinsondes
Sky Panorama Pictures
Time-Lapse Pictures
MRI Winds-Bridges Pt
MRI Winds-Aeon Point
MRI Winds-New Camp
GMQ-12,Precision W-NE Pt
Serial Double Theod Pibals

Fig. 3r

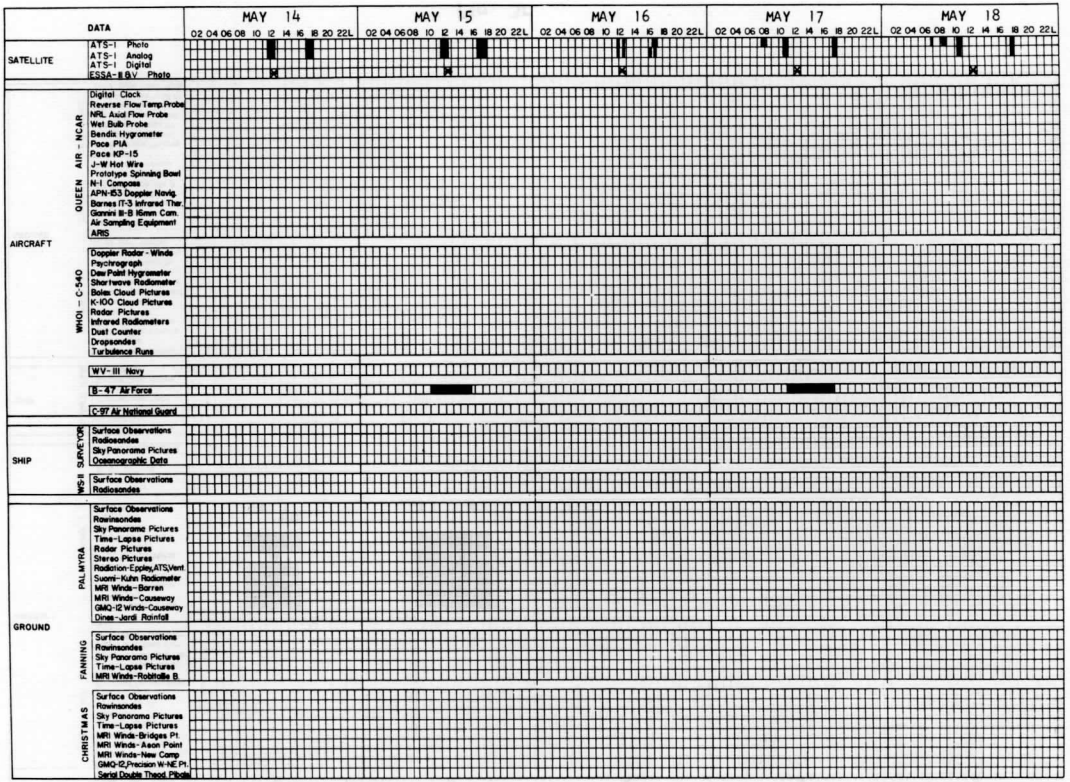
DATA
MAY 14
MAY 15
MAY 16
MAY 17
MAY 18
02 04 06 08 10 12 14 16 18 20 22L
SATELLITE
ATS-I Photo
ATS-I Analog
ATS-I Digital
ESSA-8 B.V. Photo
AIRCRAFT
QUEEN AIR - NCAR
Digital Clock
Reverse Flow Temp.Probe
NRL Axial Flow Probe
Wet Bulb Probe
Bendix Hygrometer
Pace PIA
Pace KP-15
J-W Hot Wire
Prototype Spinning Bowl
N-1 Compass
APN-153 Doppler Navig.
Barnes IT-3 Infrared The
Gannini III-B 16mm Cam.
Air Sampling Equipment
ARIS
WHOI - C-540
Doppler Radar - Winds
Psychrograph
Dew Point Hygrometer
Shortwave Radiometer
Boles Cloud Pictures
K-100 Cloud Pictures
Radar Pictures
Infrared Radiometers
Dust Counter
Dropsondes
Turbulence Runs
WV-III Navy
B-47 Air Force
C-97 Air National Guard
SHIP
SURVEYOR
Surface Observations
Radiosondes
Sky Panorama Pictures
Oceanographic Data
WSB
Surface Observations
Radiosondes
GROUND
PALMYRA
Surface Observations
Rawinsondes
Sky Panorama Pictures
Time-Lapse Pictures
Radar Pictures
Stereo Pictures
Radiation-Eppley,ATS,Vert
Suomi-Kuhn Radiometer
MRI Winds-Barren
MRI Winds-Causeway
GMD-12 Winds-Causeway
Dines-Jordi Rainfall
FANNING
Surface Observations
Rawinsondes
Sky Panorama Pictures
Time-Lapse Pictures
MRI Winds-Robitaille B
CHRISTMAS
Surface Observations
Rawinsondes
Sky Panorama Pictures
Time-Lapse Pictures
MRI Winds-Bridges Pt.
MRI Winds-Asan Point
MRI Winds-New Camp
GMD-12,Precison W-NE Pt.
Serial Double Theod. Pibals

Fig. 3s

REFERENCES

1. NASA, ATS Project 1967: User's Guide, ATS-1: The Applications Technology Satellite Meteorological Data Catalog, Volume 1, Goddard Space Flight Center, Greenbelt, Maryland, 4-3.

2. Zipser, E. J. and B. C. Taylor, 1968: A Catalog of Meteorological Data Obtained During the Line Islands Experiment, February-April, 1967. NCAR TN-35, National Center for Atmospheric Research, Boulder, 362 pp.